ATMOSPHERIC POLLUTION MEASUREMENTS WITH TUNABLE LASERS EMPLOYING RESONANCE ABSORPTION

by

© M. M. Elsherbiny, B.Sc., M.Sc.

A Thesis
Submitted to the School of Graduate Studies
in Partial Fulfilment of the Requirements
for the Degree
Doctor of Philosophy

McMaster University
1980

ATMOSPHERIC POLLUTION MEASUREMENTS WITH TUNABLE LASERS EMPLOYING RESONANCE ABSORPTION

TO SAMIA, SHERIN, AND AIMY

DOCTOR OF PHILOSOPHY (1980)
(Electrical and Computer Engineering)

McMaster University
Hamilton, Ontario

TITLE: ATMOSPHERIC POLLUTION MEASUREMENTS WITH TUNABLE LASERS EMPLOYING RESONANCE ABSORPTION

AUTHOR: Mohamed Mahmoud Elsherbiny, B.Sc. (E.E.)
(Alexandria University)

M.Sc. (E.E.)
(Alexandria University)

SUPERVISORS: C. K. Campbell, Professor of Electrical and Computer Engineering, and
J. Shewchun, Professor of Engineering Physics

NUMBER OF PAGES: xxv, 224

ABSTRACT

Theoretical and experimental techniques, which are useful in molecular spectroscopic studies and in the development of Laser Absorption Spectrometers (LAS), are described. Both fixed-frequency and tunable lasers have been employed. All the measurements reported are based on either direct or second harmonic absorption techniques.

A commercial CO/CO_2 line-tunable laser has been used to obtain useful criteria for air pollution monitoring via the direct absorption scheme. CO_2 laser absorption measurements on ozone at reduced pressures are reported. Measurements on seventeen NO absorption lines with a CO laser are described. For these, the absolute absorption as a function of pressure has been determined. As a result we have been able to establish accurate values for the absorption of NO at the pertinent CO laser wavelengths. From the best fit between experimental measurements and theoretical calculations we have deduced the separation between the appropriate NO and CO wavelengths, the NO/N_2 pressure broadening, the NO band strength, and the individual NO line strengths.

Using a tunable lead-salt semiconductor diode laser, and employing the direct absorption technique, we have developed a simple method for accurate frequency measurements of ozone absorption lines. This technique is based on employing a tunable semiconductor diode laser, an etalon, and a White cell. We report accurate frequency

measurements of over 100 absorption lines of ozone in the ν_3 band, which are near the CO_2 laser transitions. Despite the relative simplicity of the technique, we achieved an accuracy of better than 10 MHz in our measurements. This accuracy compares well with that achieved by the more complicated heterodyne techniques of high-resolution spectroscopy. However, these are the first measurements over an entire absorption band using the full resolution of a tunable diode laser.

A LAS, which combines the sensitivity of the acousto-optical methods with the convenience of direct, long-path optical detection, is described. The diode laser is wavelength modulated and the second harmonic detection technique is applied. This technique enables us to detect atmospheric pollutant gases with extremely high sensitivity (3 ppb of a weak absorbing pollutant such as SO_2 in its ν_1 band or 3×10^{-3} ppb of a strongly absorbing molecule such as CO). This sensitivity is achieved using a frequency-locking technique for the diode. We report on the detection of O_3, SO_2, NH_3, and N_2O pollutants at their ambient levels in air. A very high specificity and virtual elimination of interference effects are obtained by sampling the atmospheric air at reduced pressures.

A remote LAS station, which is considered to be adjunct to the above LAS, has been built. A remote retroreflector and an off-axis telescope near the laser have been employed to achieve a total pathlength of 1.2 km in the atmosphere. We report theoretical and experimental investigations of SO_2, H_2O, NH_3 and H_2O absorption in the region 1100 - 1200 cm^{-1} at atmospheric pressure. This enabled us to develop a technique, based on the second harmonic detection scheme, to detect SO_2 in the atmosphere with a sensitivity of 50 ppb employing a diode laser emitting in the ν_1 band of SO_2. We report also on spectroscopic studies and absorption measurements for SO_2 and H_2O in the region 1300 - 1400 cm^{-1}. These studies indicate that it is possible to detect SO_2 with ambient levels in the atmosphere by employing a diode laser radiating in the ν_3 band of SO_2, near 1331.5 cm^{-1}.

In all the above mentioned techniques, theoretical calculations of laser transmission through the atmosphere must be predicted prior to applying such techniques. For this reason, a computer package has been developed and tested. This package generates the absorption line parameters of any molecule, even asymmetric-top molecules, in the vibration-rotation infrared region. The absorption (transmission) can be calculated at any pressure.

ACKNOWLEDGEMENTS

The author wishes to express his sincere appreciation to Professor C. K. Campbell for his guidance and supervision in the writing of this thesis. His personal loyalty and friendliness have done much to make the work on this thesis enjoyable.

The guidance, suggestions, and supervision of Professor J. Shewchun during the research are gratefully acknowledged. The author also expresses his deep personal appreciation to Professor E. A. Ballik, for his continuing interest, guidance, and scientific acumen throughout the course of this work.

Thanks are due to Dr. J. Reid for many stimulating discussions and for the use of some of his experimental results in Chapters 7 and 9. The author is grateful to Professor B. K. Garside for his co-operation in the work presented in Chapter 5. The author acknowledges useful discussions with G. Hogenkamp, N. Dalaceu, and I. Rabenda, of the Air Pollution Laboratory at McMaster University.

The financial assistance provided by the Department of National Health and Welfare, Environment Canada, Ontario Ministry of the Environment, and Atmospheric Service, Environment Canada through their grants, and by the Department of Electrical and Computer Engineering through a Teaching Assistantship, are gratefully acknowledged.

The author also expresses his appreciation to Ms. L. Hunter for her expert typing of this manuscript.

TABLE OF CONTENTS

TABLE OF CONTENTS (continued)

TABLE OF CONTENTS (continued)

TABLE OF CONTENTS (continued)

LIST OF FIGURES

LIST OF FIGURES (continued)

LIST OF FIGURES (continued)

LIST OF FIGURES (continued)

LIST OF FIGURES (continued)

LIST OF FIGURES (continued)

LIST OF FIGURES (continued)

LIST OF FIGURES (continued)

LIST OF FIGURES (continued)

LIST OF TABLES

Symbols, Parameters, and Conversion Factors

In the following we have listed the used Conversion factors, constants and definitions in this thesis.

(1) **Physical Constants**

$h = 6.626 \times 10^{-34}$ Js	Planck's constant
$e = 1.602 \times 10^{-19}$ As	Charge of an electron
$k = 1.381 \times 10^{-23}$ JK^{-1}	Boltzmann constant
$c = 299\,792\,460$ ms^{-1}	speed of light in vacuum

(2) **Conversion Factors**

$1\text{J} = 10^{7}$ erg = 0.239 Cal

$1\text{eV} = 1.602 \times 10^{-12}$ erg $= 1.602 \times 10^{-19}$ J

$1\text{W} = 10^{7}$ erg s^{-1}

1 Web / m^{2} = 10^{4} G

1 bar = 10^{6} dyne cm^{-2}

1° = 17.45 mrad

(3) Conversion of transmission, T, to optical density, D;

$T = 10^{-D}$

(4) Conversion of linewidth given in wavelength ($\Delta\lambda$) or wavenumber ($\Delta\nu$) to bandwidth Δf

$\Delta f/f = \Delta\lambda/\lambda = \Delta\nu/\nu$

(4) cont'd.

$$\Delta f = c\Delta\nu$$

$$\Delta\lambda = \Delta\nu\ \lambda^2 = \Delta f\ \lambda^2 / c$$

(5) Units in common usage

$$\lambda\ (\mu m) = 10^4 / \nu\ (cm^{-1})$$

$$E\ (eV) = 1.24 \times 10^{-4}\ \nu\ (cm^{-1})$$

$$f\ (Hz) = 3 \times 10^{10}\ \nu\ (cm^{-1})$$

$$E\ (eV) = 1.24 / \lambda\ (\mu m)$$

$$f\ (Hz) = 3 \times 10^{14} / \lambda\ (\mu m)$$

$$E\ (eV) = 4.14 \times 10^{-15}\ f\ (Hz)$$

Following conventional usage, the terms "wavenumber" and "frequency" are used interchangeably, but the individual symbols are quite explicit in their meaning.

(6) Glossary of Symbols

A	Area [cm^2]
A_e	Molecular rotational constant [cm^{-1}]
B	Magnetic flux density [G]
B_e	Molecular rotational constant [cm^{-1}]
c	Speed of light in vacuum [cm/s]
C_e	Molecular rotational constant [cm^{-1}]
d	Mode spacing [cm^{-1}]
e	Electronic charge [C]
E_i	Energy level of quantum state i [cm^{-1}]

(6) cont'd.

f	Frequency [Hz]
g	Nuclear spin statistics
g_i	Statistical weight
G	Vibrational energy level [cm^{-1}]
h	Planck's constant [J s]
I	Laser Drive current [A]
I (z, ν)	Laser beam intensity [W / cm^2]
J	Rotational quantum number
k	Boltzmann's constant [J/k]
k (ν)	Extinction coefficient [cm^{-1}]
K_o	Oblate pseudo-quantum number
K_p	Prolate pseudo-quantum number
L	Depth of pollutant layer [cm, km]
L	Pathlength [m, km]
L	Cell length [cm]
m	Molecular weight [gm]
n	Refractive index
N	Number density of molecules [cm^{-3}]
p	Pressure [atm, Torr]
P	Laser power [W]
q	Electron charge [C]
Q	Total partition function
Q_r	Rotational partition function
Q_v	vibrational partition function

(6) cont'd.

R	Reflectivity
R_{ij}	Transition dipole matrix element between states i and j [$erg^{1/2}$ $cm^{3/2}$]
S	Integrated spectral line intensity [cm^{-2} atm^{-1}]
T	Absolute temperature [K]
T	Transmission
v	Vibrational quantum number
V	Voltage [V]
x	Semiconductor alloy composition
y	Variable
z	Pathlength variable [km]
$\alpha(\nu)$	Absorption coefficient [m^{-1} ppb^{-1}] or [cm^{-1} atm^{-1}]
$\lvert\beta\rvert^2$	Vibrational matrix element
$\beta(\nu)$	Total extinction coefficient [cm^{-1}]
γ_L	Lorentz broadening (HWHM) [cm^{-1}]
γ_D	Doppler broadening (HWHM) [cm^{-1}]
§	Thermal diffusivity [cm^2/s]
η_i	Internal quantum efficiency
k	Asymmetric rotor parameter
λ	Wavelength [μm]
$\lvert\mu\rvert^2$	Rotational matrix element
ν	Wavenumber (or "frequency") of electromagnetic radiation [cm^{-1}]
ν_o	Wavenumber at line center [cm^{-1}]

(6) cont'd.

ν_s	Spontaneous - emission frequency [cm^{-1}]
ξ	Parameter controlling the emission frequency of semiconductor laser [cm^{-1}]
ω	Central vibrational frequency [cm^{-1}]

(7) PM and LPM definitions

Point monitoring (PM), is where the monitor is placed at one location in the field and it samples the surrounding ambient air. However, the monitor itself contains a long-path absorption cell (White cell).

Long-path monitoring (LPM). Here the monitoring technique is based on long-pathlengths in the atmosphere. This long path is given by twice the distance between the laser source and a remote retroreflector. Hence, the detectable parameter is the average concentration of a pollutant gas over the atmospheric path, and not the concentration at one point into the atmosphere, as in the case of PM.

CHAPTER 1

INTRODUCTION

1.1 Need for a Pollution Monitor

With the increase in industrialization and mechanization, the world has witnessed over the past fifty years a corresponding increase in the pollution of the environment. The atmosphere in particular has been contaminated to an alarming degree by waste from innumerable industrial processes and, especially, the internal combustion engine. Because pollution sources are so diverse, the atmosphere contains hundreds of "unnatural" gases, many of which produce measurable effects on the biological and physical environment.

At this point in time, the degree of pollution in the atmosphere is serious enough to have precipitated government legislation regulating the maximum permissible amounts of pollution levels of industry and vehicles. This requires monitoring the atmosphere to ascertain levels of at least the particularly harmful pollutants.

In Ontario, the Ministry of the Environment compiles an Air Pollution Index for several large urban centres based on the continuous measurement of sulphur dioxide, telemetered from remote stations, and suspended particulate concentrations, determined from 24 hour average values of the soiling index. For a downtown Toronto location (the Index varies according to the character of the particulates), the Index I is given by:

$$I = 0.2\ (30.5\ \mathrm{COH} + 126.0\ \mathrm{SO_2})^{1.35} \qquad (1.1)$$

where COH is the 24 hour running average of the soiling index expressed as a coefficient of haze per 1000 feet of air, while SO_2 is the 24 hour running average of sulphur dioxide concentration in parts per million (ppm).

In Hamilton, the Urban Air Environment Group at McMaster University Medical Center is presently conducting a project looking at the effect of environment factors on the respiratory health of school children. It has been found that the combined effect of SO_2 and particulates in the ambient air has the more severe effect on respiratory health as compared to the individual effects. It was for this reason that SO_2 was monitored (by the McMaster University Air Pollution Laboratory) as a representative of pollutant gases, along with the particulate monitoring. The instrument currently used (by the Ministry of Environment and the group of McMaster University) for SO_2 monitoring is based on secondary coulometry and dynamic iodimetric titration. This instrument is a point sampling device in the form of a Beckman Model 906A SO_2 analyzer.

Generally, it has been found that the highest levels of pollution can be found in the North-East segment of the City of Hamilton, usually recognized as the industrial sector. When there are prevailing North East or Easterly winds, then the remainder of the city also has high SO_2 levels.

Techniques for monitoring other gases are available, but all these monitoring instruments are usually based on chemical reaction and laboratory procedures. This limited the applicability of such monitors to one gas or at most an undiscriminated group of gases and is costly in terms of time. Other developments brought about monitors utilizing radiation sources instead of chemical reagents; however, these systems suffered from a lack of suitable sources.

Today, with increased concern over the rapidly deteriorating environment, there is a definite need for a system that is capable of performing far better than the traditional ones. A monitoring system is required that is capable of giving instantaneous measurements of at least four chemically different pollutants on either point or long-path basis. It also should be inexpensive, reasonably mobile, rugged in construction, and simple to operate.

At this time, such a system does not exist. However, the development of the laser, especially, the tunable one, has sparked much interest in solving the problem since, potentially, it can serve as a suitable radiation source.

1.2 The Use of Lasers in Pollution Monitoring

Optical techniques for the monitoring of atmospheric pollution have advantages over the presently-used wet chemical methods, since they can be used for remote sensing and also because they are instantaneous by comparison. Of greatest interest is the infrared (ir) spectral region from about 2 to 20 μm, because nearly all of the gaseous pollutants have vibration-rotation resonances in this region which can be useful for both absorption and emission measurements [1]. Due to strong absorption of the principal polyatomic constituents of a clean atmosphere, CO_2 and H_2O, certain bands in this region (2.5 to 2.9 μm, 4.2 to 4.4 μm, 5.5 to 7.5 μm, and 14 to 16 μm) may have to be avoided.

A number of classical optical methods, including the use of selective filters, spectrographs, interferometers, optical correlation and derivative techniques have been explored and shown to hold promise for certain applications [2]. A new dimension to the optical techniques is added by making use of the unique properties of lasers, particularly their high power, directionality, spectral purity, and wavelength tunability.

Three techniques, which involve the use of lasers for various modes of point sampling and remote sensing, have been employed. These techniques are based on 1) Raman scattering, 2) resonance flourescence, and 3) absorption. These laser methods have been compared by Kildal and Byer [3], who concluded that the resonance absorption scheme is the least complex and costly one and requires minimal laser power. It lacks depth resolution, but it is the only scheme sensitive enough to detect dispersed pollutants. A more detailed analysis of this scheme, over that performed in [3], has been reported by Rosegren [4].

1.3 Resonance Absorption Scheme

The absorption technique has perhaps the widest range of application because it can be used both for point sampling and remote sensing. For remote long distance measurements, one possible disadvantage is the necessity for a remote detector, retroreflector, or scatterer. Wherever this requirement can be met, the technique is advantageous because it is the most sensitive and requires the least amount of laser power, consequently, it promises to be the simplest and least expensive system. For point sampling, laser powers as low as 1 μW can be used, whereas for remote sensing 1 mW should be quite sufficient.

In recent years, a great deal of attention has been given to the use of infrared lasers to measure molecular absorptions over long pathlengths. In general, line-tunable sources (CO_2, CO, DF), have been employed to monitor those gases which have absorption lines in close coincidence with the available output wavelengths of the lasers [5-7]. Semiconductor diode lasers which can readily provide powers in the range mentioned above have proven to be particularly convenient for the absorption technique [8], [9]. To date, the minimum detectable absorption reported using such optical techniques is $> 0.1\%$. This has resulted in applications being limited to gases which occur naturally at high concentrations.

An air pollution detection system must be able to identify and measure the concentration of pollutants. The characteristic resonance frequencies at which a polluting molecule absorbs laser radiation can be used to identify the molecule if there is no ambiguity due to overlapping absorption of other molecules in the atmosphere. The magnitude of the absorbed power of a laser beam propagating through the sample or in the atmosphere at an absorption frequency of a molecule, is then used to determine the mean concentration of such molecules along the measuring path.

Every absorption line of a molecule in the atmosphere has its own value of center position, width, and intensity. Without a precise knowledge of these parameters, a theoretical determination of absorption coefficient is out of the question, even with a correct knowledge of the dispersing contour. Furthermore, the line parameters depend in a complicated manner on the variable macroconditions of the medium; notably, temperature and pressure (total and partial) of the component gases. All this creates exceptional difficulties in making a quantitative estimate of energy loss of an optical wave due to an individual absorption line. These theoretical calculations along with experimental investigation are required as a starting point in the design of a pollution monitoring system. Hinkley's monograph [10] contains comprehensive theoretical and experimental techniques for atmospheric pollutants monitoring which have been employed during the time period 1968 to 1976.

1.4 Object and Scope of Thesis

Long-path Laser Absorption Spectroscopy (LAS) applications to the detection and spectroscopic studies of pollutant gases are covered in this Thesis. The LAS is used for point sampling of pollutant gases, and provides an important tool for determining the average concentration of atmospheric pollutants.

Both fixed-frequency and tunable lasers are used and proposed for atmospheric pollution monitoring. Chapter 2 describes these lasers used in this Thesis: fixed-frequency lasers (CO, CO_2) are described briefly, while the theory and operation of the tunable Lead-salt Semiconductor Diode Lasers (SDL) are described in detail. Chapter 2 also includes an experimental method for determining diode laser characteristics; including spectral region, tuning ranges, tuning rates, region of single mode operation, and frequency stability. These experimental investigations must be carried out prior to employing the diode laser.

In general, to utilize the LAS technique adequately, it is necessary to accurately know the band spectra of both pollutants and normal atmospheric absorbing gases, together with values of their ir absorption coefficients, α. Therefore, a comprehensive compilation of ir absorption line parameters of the atmosphere constituents, (especially absorbing gases), must be provided. The important line parameters are: central position (ν_o), intensity (S^o), broadening coefficient (γ), and line shape, $f(\nu, \nu_o)$. Most of this data is coded on two 7 track magnetic tapes, written on a CDC 800 computer, and is available from the Air Force Cambridge Research Laboratory (AFCRL). Also, for a laser spectroscopy air pollutant monitoring station, it is necessary to have a computer package to generate the individual line parameters of the target gas from its molecular constants, especially if the required data is not available or it is, but not accurate enough. The theory used in constructing such a computer package is described in Chapter 3.

Chapters 4, 5, and 6 provide theoretical calculations and experimental measurements for obtaining the required data mentioned above. This data is useful for the design of any pollutant monitor, based on the resonance absorption scheme. Chapter 4 describes measurements with line-tunable laser (CO_2) on a pollutant gas (O_3) in order to establish some useful criteria for air pollution monitoring via the "direct" absorption scheme. Chapter 5 describes a method for determining the absorption line parameters of a nearest pollutant (NO) line to a line-tunable laser (CO) line. This method is based on the best match between experimental absorption data and theoretical calculations.

In some pollution detection techniques employing line-tunable lasers (e.g., heterodyne radiometers), the separation between the laser line used, and the nearest pollutant absorption line ($\Delta\nu_n$) must be known to better than 10 MHz. Chapter 6 describes a simple technique for accurate frequency (wavenumber), ν, measurement of over 100 lines in the ν_3 band of ozone. These measurements are based on the use of a diode laser, White cell, and etalon. The accuracy of these measurements is compared with those obtained using the more complicated laser heterodyne techniques.

Up to this point, experimental and theoretical tools have been examined, for spectroscopic studies of pollutant gases. These studies must be performed (especially in the atmosphere) prior to the design of a detection instrument. Chapter 7 describes the developed Point Monitoring (PM) technique at the McMaster University Air Pollution Laboratory. This technique is based on LAS and second harmonic detection methods. In this Chapter, the applications of the LAS to the detection of SO_2, N_2O, NH_3, and O_3 are described. The LAS sensitivity is compared with the most accurate recent optical techniques. Chapter 7 additionally describes necessary improvements needed to increase the absorption coefficient detection sensitivity from 10^{-7} m^{-1} to 3×10^{-8} m^{-1}.

Remote Long-path Monitoring (LPM) yields values for the average pollutant concentration over the path, which are generally more meaningful for regional models than point monitoring. However, LPM is not generally considered to be a substitute for point monitoring, but an adjunct to it. Chapter 8 describes a remote long-path monitoring station for SO_2 detection in the atmosphere. This station employs a semiconductor diode laser which radiates in the ν_1 band of SO_2, a launching telescope, corner cubes retroreflector, and a second harmonic detection system. The present detection technique enabled us to detect an SO_2 concentration as low as 50 ppb in a total pathlength of 1.2 km in the atmosphere. The basic concept shows promise for measuring SO_2 concentration as low as 10 ppb in the ν_1 band. This can be achieved by improving the present optical system, and the data processing. Chapter 8 also contains the results of experimental and theoretical investigations which indicate that it is possible to achieve additional improvement in the detection sensitivity by employing a diode laser which radiates in the ν_3 band of SO_2.

Chapter 9 describes the LAS system noise and methods for eliminating such noise.

Finally, Chapter 10 contains the summary and conclusions of the presented work in this thesis.

CHAPTER 2

LASERS USED IN THIS THESIS

2.1 Introduction

Resonance absorption pollutant detection can be performed with line-tunable or broadly tunable lasers. Two different schemes for long-path absorption monitoring and spectroscopic investigation have been used in this thesis. One involves the use of line-tunable lasers (CO_2 and CO lasers). The other involves the use of tunable lead-salt semiconductor diode lasers. The theory and operation of gas lasers are well known and described elsewhere [11], therefore, in section 2.2, only the CO/CO_2 system components and specifications will be described. On the other hand, tunable lead-salt diode lasers, at their present stage, have a variety of important and realizable applications. As the state-of-the-art is advanced, their application range will be expanded considerably. Improved output powers and higher operating temperature appear quite feasible for the near future [12]. In section 2.3 the fundamental theory and operation of such lasers will be described, and a comprehensive comparison between the semiconductor lasers and the other tunable lasers will be demonstrated.

2.2 Line-Tunable Lasers: CO/CO_2 Laser

The gas laser is one type of device that is capable of generating coherent electromagnetic radiation at wavelengths shorter than those generally considered to be microwave frequencies. The other devices that have this property employ, as an active medium, crystalline solids, glasses, liquids, or semiconductors. The first two experiments in this thesis have been performed with the commercial Molectron C250 CO/CO_2 laser. Table 2.1 shows the system component and the laser specifications, while Fig. 2.1 displays a view of the laboratory facility showing the CO/CO_2 laser. These two experiments will be described in Chapters 4 and 5 in detail.

2.3 Tunable Lasers

2.3.1 Introduction

Since the development of the first laser in the early 1960's most applications have relied on their high power and low beam divergence. Wavelength tuning has been of secondary importance. Now the laser has become a powerful tool of spectroscopy over a range extending from submillimeter waves to the vacuum ultraviolet region. The following subsections review the fundamental properties of a lead-salt semiconductor diode laser, which has been used to obtain the data, and to develop the pollutant monitoring techniques in this thesis. A number of tunable lasers can be used for this purpose, these include: spin-flip raman lasers [13], sum and difference frequency generators [14], parametric oscillators [15], and high pressure gas lasers [16]. Characteristics and properties of this variety of lasers are outside the scope of the thesis. For comparison, Table 2.2 contains the characteristics of some tunable lasers emitting in the infrared (ir) region.

2.3.2 Lead-Salt Semiconductor Diode Lasers (SDL)

Semiconductor diode lasers are the simplest of the tunable lasers, providing modest continuous powers with narrow line-widths, good frequency stability, and with capabilities for tuning over a wide spectral region. Since the first publication in 1970 of Doppler - limited spectra within the 10.6 µm band of SF_6 by E. D. Hinkley [17], lead-salt semiconductor diode lasers have been employed for high resolution infrared spectroscopy [18], [19].

Over fifteen years ago, J. Butler fabricated the first lead-salt laser [20]; for a number of years subsequently, researchers investigated lead-salt lasers on an R & D basis. But it was not until 1970 that these devices began to be used for ultra-high-resolution spectral measurements.

Structurally, the lead-salt lasers are quite similar to the familiar GaAs lasers, although the wavelength coverage and uses are quite different. The devices are formed using a stripe geometry (Fig. 2.2) to make them lossy in the transverse direction. The diode lasers are fabricated from vapor-grown single crystals of $Pb_{1-x}Sn_xTe$, $Pb_{1-x}Sn_xSe$, $PbS_{1-x}Se_x$, $Pb_{1-x}Ge_xTe$, or $Pb_{1-x}Cd_xS$ semiconducting material by cleaving the crystals into rectangular parallelepipeds of approximate overall dimension 0.12 by 0.05 by 0.03 centimeter. By choosing the alloy composition, x, tunable lasers with wavelengths from less than 3 µm to more than 30 µm can be fabricated.

TABLE 2.1 System Component and Specifications of CO/CO_2 Laser

SYSTEM COMPONENTS

MODEL	DESCRIPTION
C-250	CO/CO_2 Laser head
CPS-N	Power supply system
SD-21	Grating sine drive

Specifications	CO_2 Laser Grating sine drive	CO Laser Grating sine drive
Power Output	10 W	1-4 W
Output wavelengths	9.17-9.39, 9.43-9.80, 10.13-10.38, 10.44-10.91 μm	5.1-6.5 μm
Mode	TEM_{oo}	TEM_{oo}
Cooling	water	LN_2
Power Stability long term (4 hours) short term (1 sec.)	 ± 2% ± .2%	 ± 4% ± .4%
Beam diameter $1/e^2$ intensity	8 mm	6 mm
Beam divergence far field, full angle	< 4 m rad	< 3 m rad

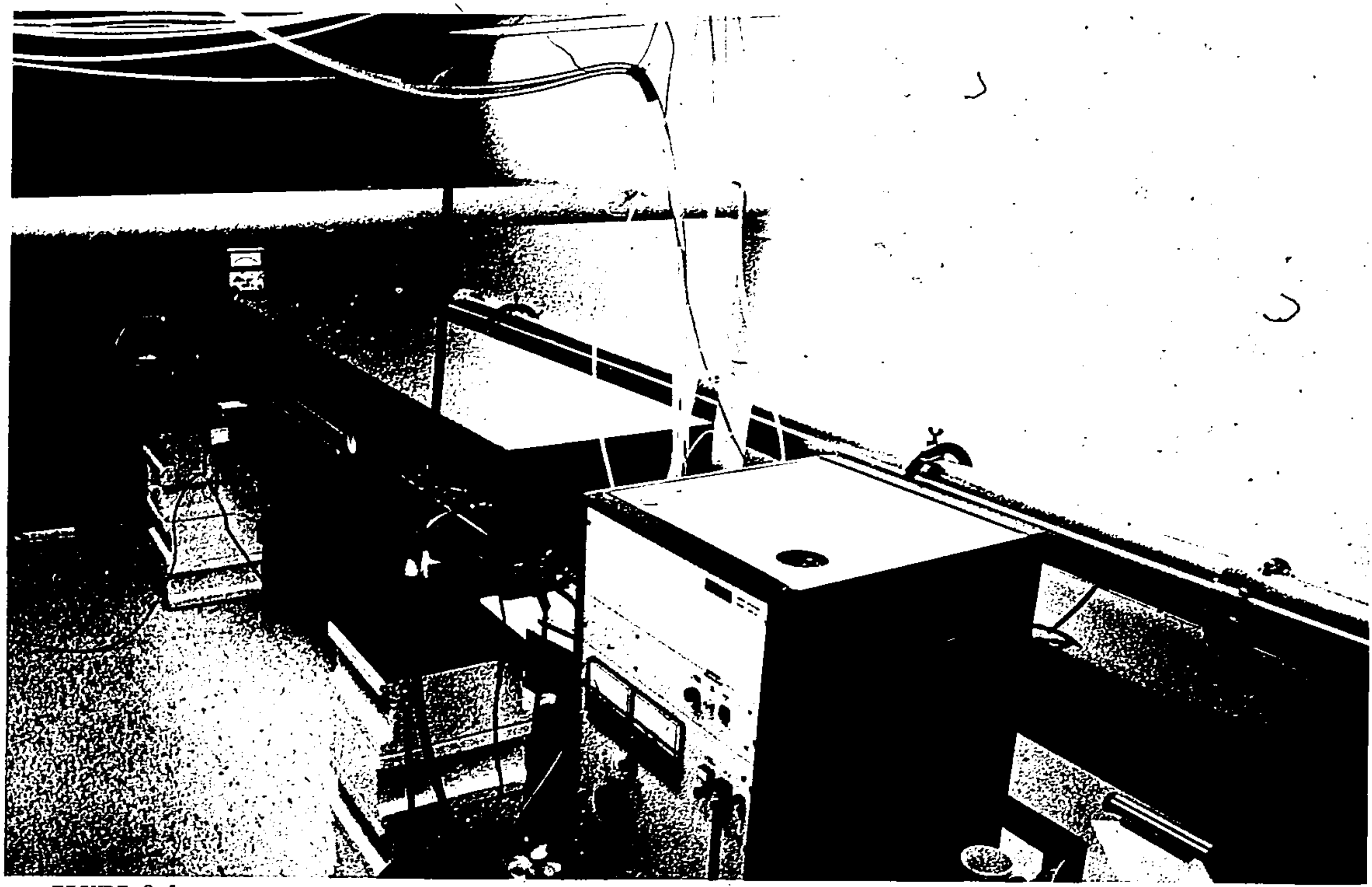

FIGURE 2.1
OVERALL VIEW OF THE LASER LAB Laser power supply is in the foreground, laser is in left centre, optical table is in the background. Behind the laser along the wall is the multiple reflection long path cell.

TABLE 2.2 Properties of Infrared Tunable Lasers

Type		Tuning Mechanism	Pump Laser	Active Medium	Wavelength Coverage μm	Highest Resolution cm^{-1}
Semiconductor Diode Laser	(SDL)	T,p,B	-----	Semiconductor	< 1-34	$3x10^{-6}$
Spin-Flip-Raman Lasers	(SFR)	B	CO, CO_2	InSb	5-6 9-11	$3x10^{-5}$
Nonlinear Optical Devices						
Parametric Oscillators	(OPO)	T,Θ	YAG,RUBY	Nonlinear Material	<1-11	$3x10^{-2}$
Diff.-Freq. Generators	(DFG)	ν_{pump}	RUBY,Dye,CO_2,Klyst.	......	3-6	$2x10^{-3}$
Two-Photon Mixer	(TPM)	ν_{pump}	....	......	9-11	$3x10^{-5}$
Four-Photon Mixer	(FPM)	ν_{pump}	....	......	2-24	$1x10^{-1}$
Gas Lasers						
Zeeman-Tuned	(ZTG)	B	-----	He-Ne,He-Xe	3-9	$3x10^{-3}$
High-Pressure CO_2	(HPG)	Θ,δ	-----	CO_2	9-11	$3x10^{-2}$

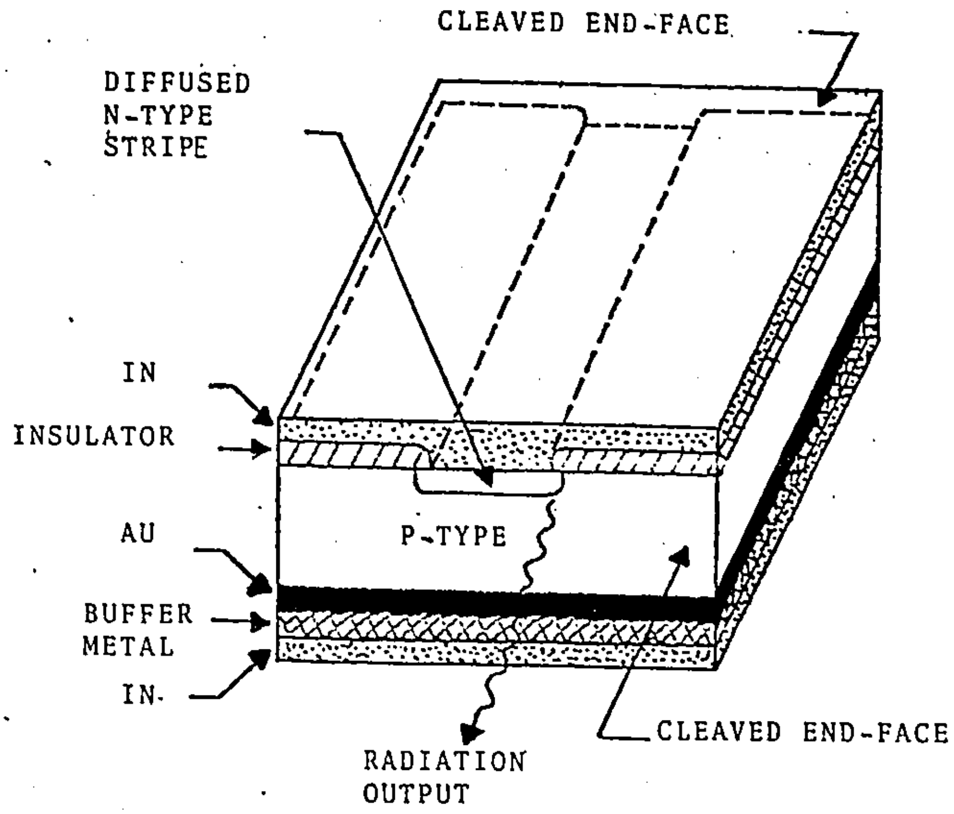

Figure 2.2 Schematic diagram of stripe geometry diode laser.

2.3.2.1 Laser Action

Forward bias current flow through a pn junction diode produces a density of minority carriers in excess of the thermal equilibrium density on either side of the pn junction. Laser action results from radiative recombination of these injected minority carriers. The injection luminescence process is illustrated in the energy band diagram of Fig. 2.3. Only a fraction of the injected excess of minority carriers recombine radiatively. The remainder are lost through non-radiative processes such as Auger recombination at impurity or defect-induced centers. Furthermore, a fraction of the generated photons is reabsorbed within the crystal and does not reach the external world. The transitions involved take place between continuous energy bands, rather than discrete states. As a result, the spontaneous emission of semiconductor lasers is much broader than that of atomic or molecular lasers. At low current levels, spontaneous emission is produced, as the current is increased, a threshold current is reached at which stimulated emission gain outweighs electromagnetic loss in one or more modes and laser action occurs. The threshold current density I_t may be expressed as [11]:

$$\frac{I_t}{A} = \frac{8\pi\nu^2 q d n^2 \Delta\nu}{c^2 \eta_i}\left[\alpha + (1/L)\ell n(1/R)\right] \tag{2.1}$$

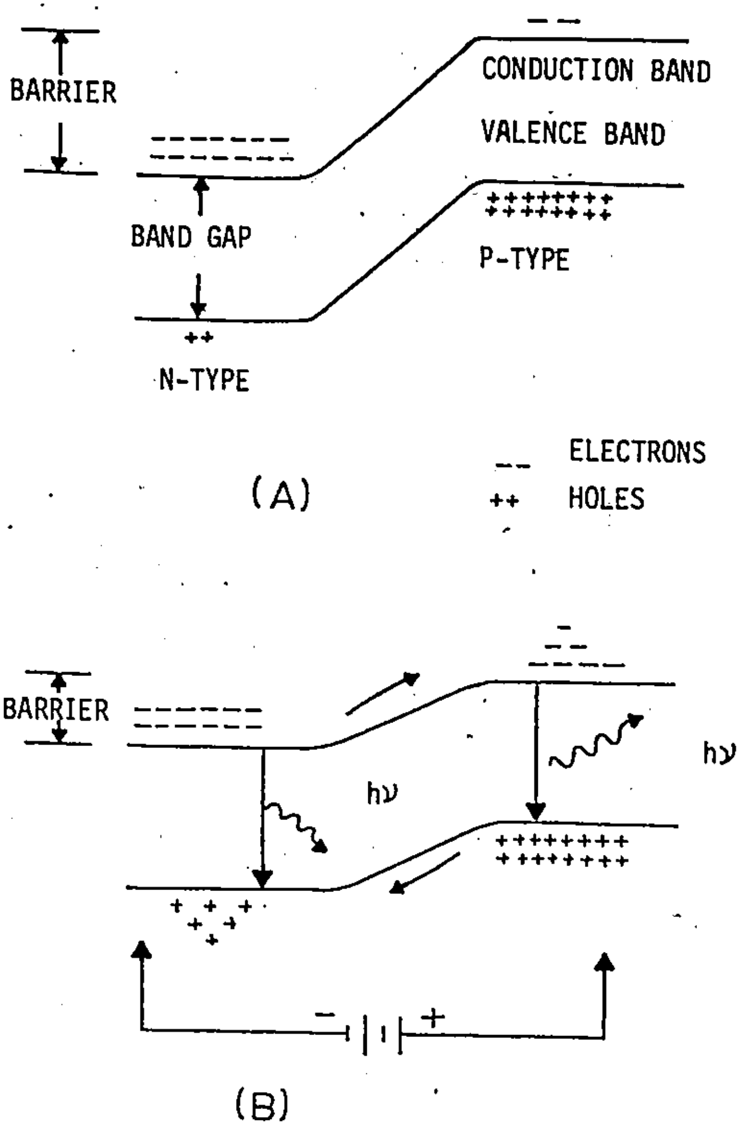

Figure 2.3 Injection luminescence of a pn junction.
A- Zero bias.
B- Forward bias.

where

ν = laser mode wavenumber

d = mode width

$\Delta\nu$ = spontaneous emission line-width

n = refractive index

α = loss constant

L = distance between end faces

R = end face reflectivity

η_i = internal quantum efficiency

The output power of an injection laser is given by

$$P_o = \frac{(I - I_t)\ \eta_i\ h\nu}{q} \left[\frac{(1/L)\ \ell n\ (1/R)}{\alpha + (1/L)\ (\ell n\ 1/R)} \right] \qquad (2.2)$$

Experimentally, it is apparent that the output power of the laser increases much faster than linearly with current. It may be inferred from this observation that since α does not vary significantly, η_i increases rapidly with current. Maximum observed output power for a single mode was P = .5 mW.

2.3.2.2 Tuning Methods

The lead-salt compounds which are available and have been used for spectroscopy in the 3 µm to 15 µm region are shown in Fig. 2.4, along with compositional tuning ranges of the semiconductors and locations of some of the molecular-absorption bands which have been studied. Spontaneous-emission frequency ν_s varies almost linearly with the alloy composition factor x across most of an alloy's range in the form [21].

$$\nu_s = \nu_o + \xi x \tag{2.3}$$

The values ν_o and ξ in Table 2.3 for the semiconductor can be used to select the appropriate crystal composition to match a particular wavelength. After the wavelength region is selected, the laser may be tuned during its operation by various methods which are described below.

The method chosen for a particular application will depend on factors such as resolution requirements, desired tuning range, cost and convenience. The tuning of a diode laser occurs quasi-continuously with individual modes shifting typically 1-5 cm^{-1}. An expression which describes the continuous tuning of a laser mode by varying some external parameter "y" may be described as follows. The wavelength of the m^{th} mode is given by:

$$\lambda = \frac{2nL}{m} \tag{2.4}$$

Differentiating,

$$\frac{d\lambda}{dy} = \left[1 - \frac{2L}{m} \frac{\partial n}{\partial \lambda} \right]^{-1} \left[\frac{2L}{m} \frac{\partial n}{\partial y} + \frac{2n}{m} \frac{\partial L}{\partial y} \right]$$

$$= \frac{2\Delta\lambda}{\lambda} \left[L \frac{\partial n}{\partial y} + n \frac{\partial L}{\partial y} \right] \qquad (2.5)$$

where $\Delta\lambda$ is the mode spacing. The term containing $\frac{\partial L}{\partial y}$ is generally negligible.

Magnetic field tuning has been demonstrated in many Pb-salt semiconductors [22], [23]. For example, the tuning rate of $^{df}/_{dB}$ has been measured and found to vary from 0.4 to 2.0 MHz/G.

The widest tuning range in a single tunable laser has so far been achieved with hydrostatic pressure variation. The tuning limit was established by damage to the crystal, and a tuning rate of $8.4\ 10^{-6}$ eV/bar was obtained [24].

Temperature tuning utilizes the temperature dependence of the bandgaps of Pb-salt. It is complicated by the fact that, with the present state-of-the-art, pulsed operation of Pb-salt semiconductor lasers is generally required for temperatures greater than about 20°K [101]. To eliminate the need for liquid-helium cooling, a closed-cycle cryogenic cooler has been developed that lowers the temperature to 10°K in 60 minutes. This cryogenic system has been built by Cryogenic Technology Inc., and has been used to control the temperature of the Pb-salt diode lasers employed in this thesis.

TABLE 2.3 Composition-tuning Characteristics of Lead-Salt Lasers [21].

Material	$\nu_o(cm^{-1})$	$\xi(cm^{-1})$	Composition Range	Wavenumber Range (cm^{1})
$Pb_{1-x}\,Sn_x\,Te$	1,540	-3,837	$0 \leq x \leq 0.32$	1,540 - 312
$Pb_{1-x}\,Ge_x\,Te$	1,540	14,600	$0 \leq x \leq 0.05$	1,540 - 2,270
$Pb_{1-x}\,Sn_x\,Se$	1,190	-8,780	$0 \leq x \leq 0.10$	1,190 - 312
	1,190	5,552	$0.19 \leq x \leq 0.40$	312 - 1,562
$Pb\,S_{1-x}\,Se_x$	2,295	-1,105	$0 \leq x \leq 1$	2,295 - 1,190
$Pb_{1-x}\,Cd_x\,S$	2,295	29,396	$0 \leq x \leq 0.058$	4,000 - 2,295

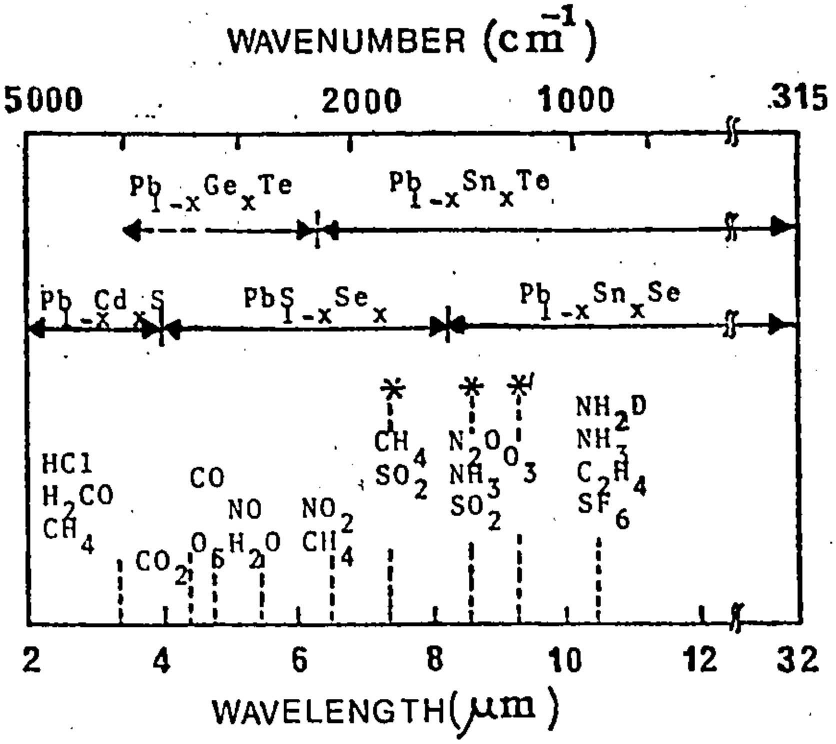

Figure 2.4 Wavelength coverage for several lead-salt diode lasers. Also shown are some gases that have been studied with diode lasers (present work are marked by *).

Current tuning is a manifestation of temperature tuning which utilizes the joule heating caused by the diode current flow. Continuous tuning of a single mode has been achieved, and a continuous tuning range of about 1 cm^{-1} is observed during the present research. Current tuning may be used in conjunction with other tuning methods as a fine tuning control or to extend the tuning range.

The usefulness of the current tuning may be enhanced by superimposing a small ac ripple onto the dc bias current. The ac component allows synchronous detection to be used, or the resulting small laser frequency variation may be applied to differential spectroscopy.

In a typical monitoring application, several Pb-salt diode lasers would be used, each tailored to emit in a strongly absorbing infrared region of one of the pollutant gases. This arrangement is necessary because of the limited current tuning range of these lasers, and desirable because it provides for increased specificity. The small size of these lasers makes it possible for several to be mounted into the same cold head.

2.3.2.3 The Lead-Salt Diode Laser System

An operating system has been assembled to provide a convenient source of tunable radiation from any diode laser system. A block diagram of the system assembly is given in Fig. 2.5. The major components consist of a closed-cycle liquid helium temperature cryocooler (CTi Model 21), a laser diode temperature control unit (Lake Shore Cryotronics Model DTC 500) and a laser power supply and control unit (Laser Analytics Model LPS-2). This overall package allows the temperature of the laser diode mounting system to be controlled to within a few millidegrees at average temperatures ranging upwards from 11°K. At present, a particular PbSnSe diode laser (acquired from Laser Analytics) is mounted on the cold head of the cryocooler (see Figures 2.6 and 2.7), but the system is sufficiently versatile to permit the easy installation of other alloy lead-salt combination diode lasers directly into the system. The particular diode presently installed in the cryocooler package has an alloy composition (1% Sn) selected to produce laser wavelengths spectrally matched to some strong absorption lines in the ν_1 band of SO_2. The characteristics of this particular diode have been investigated, and are reported below. It is expected that the output power, laser mode and tuning characteristics will be typical of those obtained with diodes operating at other wavelengths (e.g., O_3 monitoring diode).

The conjunction of laser and cryocooler control units permits the average temperature of the cold head to be selected, independent of the drive current applied to the continuously operating diode laser. This feature is crucial to the provision of a convenient, repeatable means of tuning the wavelength of the laser mode output. The base temperature of the cold head broadly determines the average wavelength of the diode laser output. Relatively small changes in the current drive to the diode subsequently provide the means of "fine tuning" the wavelength of laser emission about the base value fixed by the cold head temperature. The necessary electronic systems to

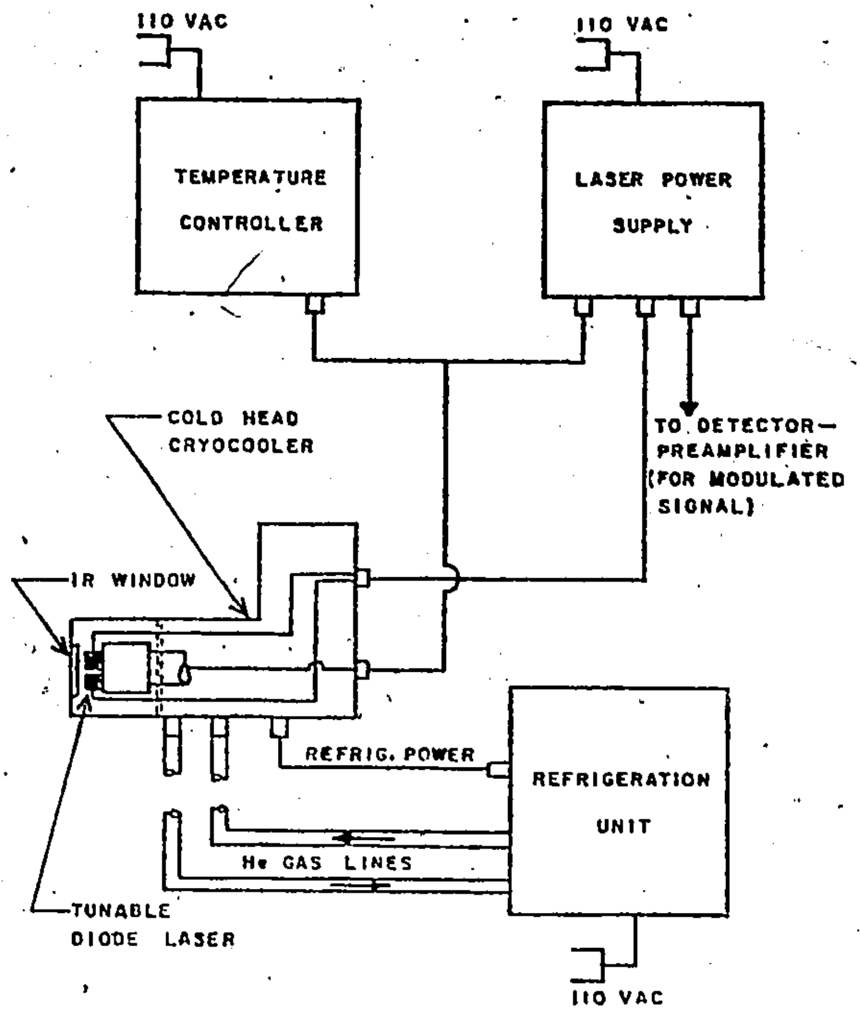

Figure 2.5 Block diagram of tunable diode laser system showing three major components: refrigeration unit and cold head, temperature controller, and laser power supply.

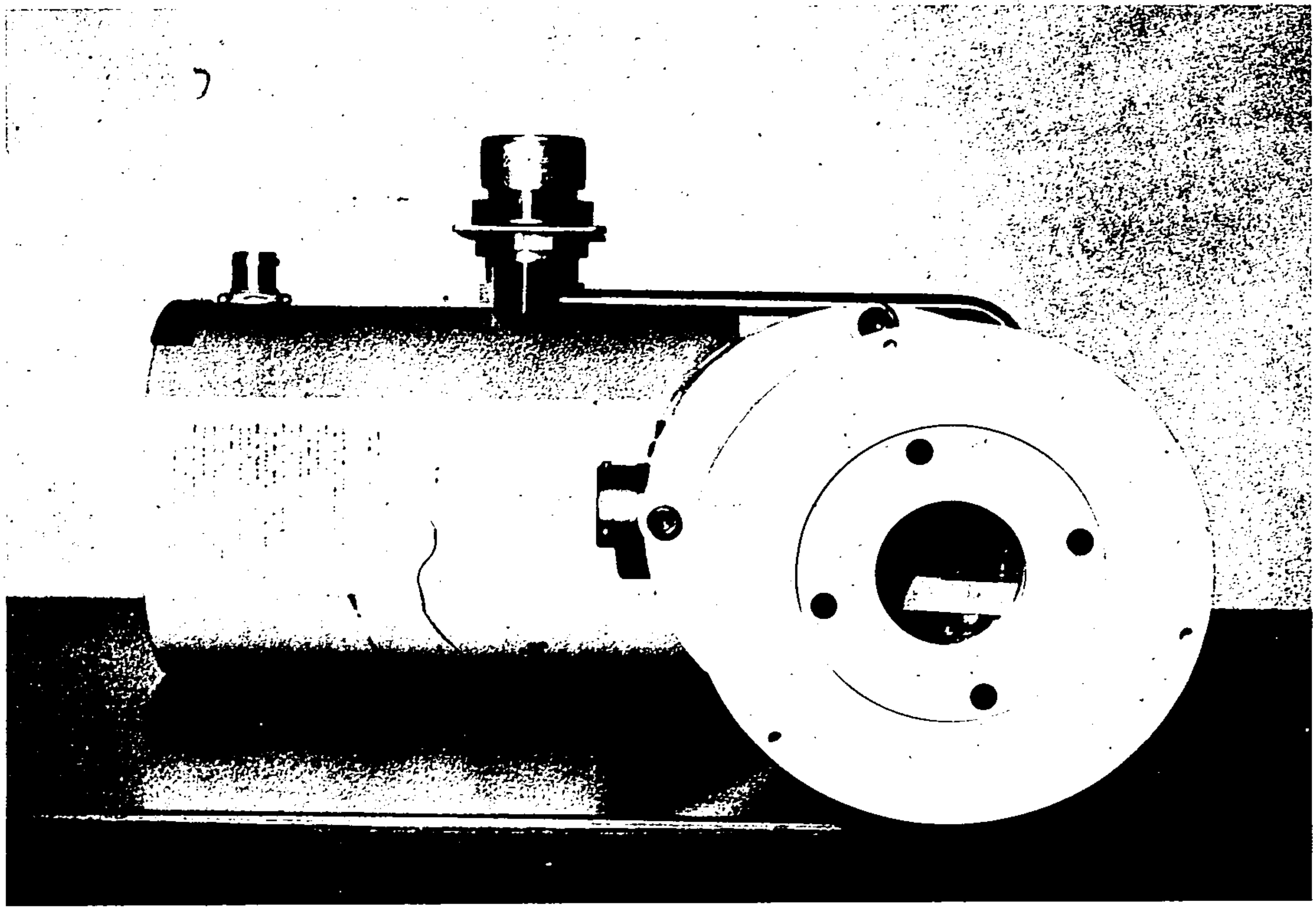

Figure 2.6 A view of the cryocooler head in which the semiconductor diodes are located. The infrared transmitting window through which the laser output is emitted can be seen in the background.

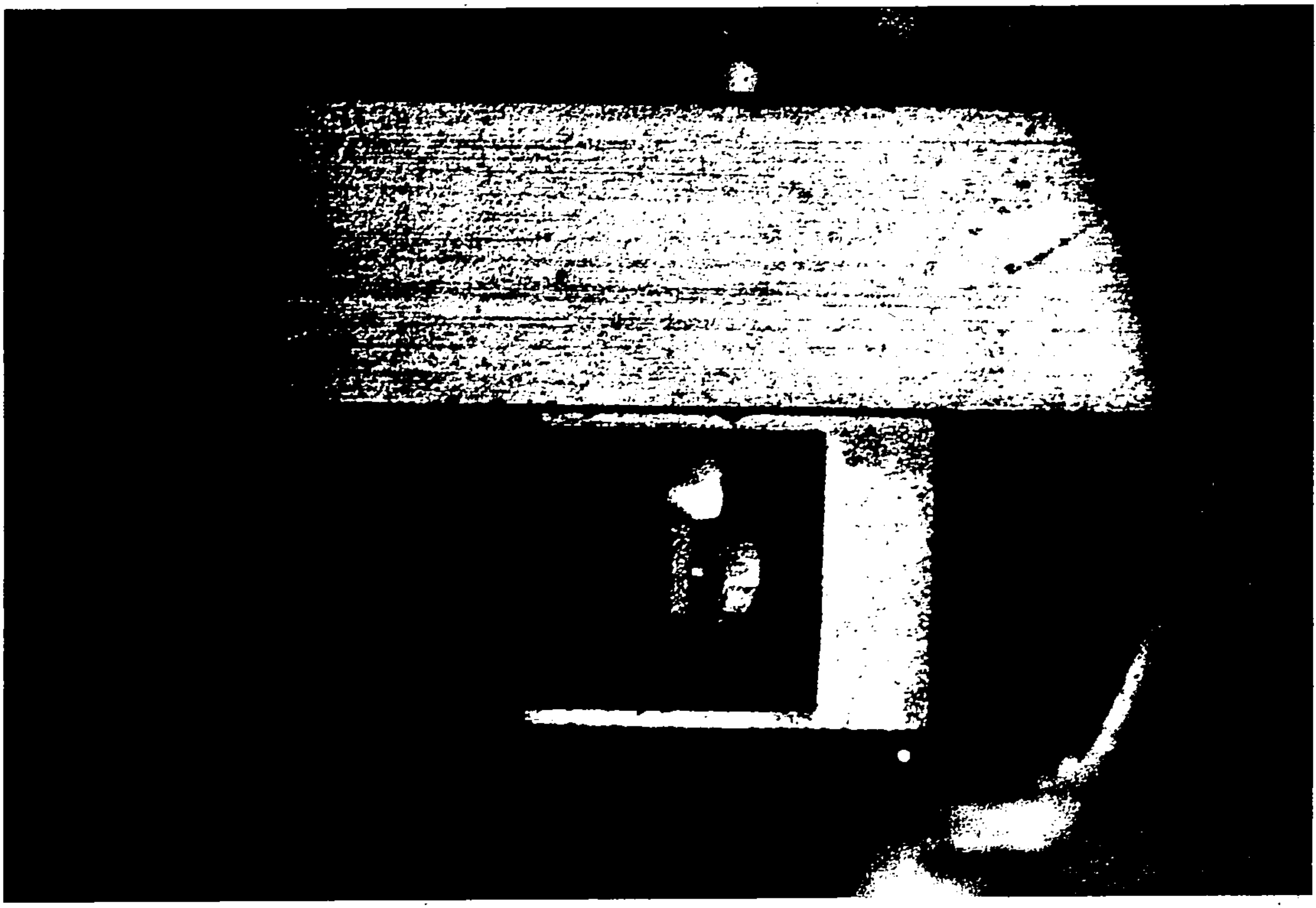

Figure 2.7 A close-up of the cryocooler cold head, taken from the direction of the output window. The lead-salt diode laser can clearly be seen highlighted in its mounting in the lower central part of the photograph.

provide the base temperature of the diode and the current drive for fine tuning are shown in Fig. 2.8 which also illustrates the compactness of the system. The small changes in diode current are generated by the laser drive unit; two modes of operation are available: a slow scan mode in which the current is slowly varied over a range of up to 200 mA (the drive current itself is from 0.6 to 2A), or a modulation mode in which a sawtooth, triangular or sinusoidal current modulation can be applied at a rate varying from 50 Hz to 1 kHz. The latter mode of operation is particularly suitable for the sensing of rapid changes in laser radiation absorption, such as would be employed in a fast-time response detection system for monitoring small scale fluctuations in atmospheric pollutant gases. The base temperature range from 11°K to 40°K allows an overall change in average (inverse) wavelength of diode emission by approximately 80 cm^{-1} (1080 cm^{-1} to 1160 cm^{-1}). Fine tuning by variation of diode drive current produces a tuning range for a particular mode of roughly 1 cm^{-1} at a given cold head temperature. The threshold current of the laser diode is a function of the base operating temperature. The threshold bias current was found to increase from 0.65 to 1.5 amps as the base temperature was increased from 11°K to a maximum of 40°K. Under typical operating conditions the laser output was measured with a HgCdTe infrared detector (see Fig. 2.9).

Figure 2.10 shows the output obtained from the diode laser as a function of wavelength. The diode was operated at low base temperature (16°K) and a high drive current. As expected under these circumstances, a number of laser modes operate simultaneously. The laser mode spectrum so produced was measured with a 1/2 metre Jarrell/Ash scanning spectrometer (Model 82-000). The width of the peaks shown in Fig. 2.10 reflect the resolution setting of the spectrometer (~75Å). Of course, this does not reflect the width of each individual laser mode, which is a great deal smaller (~10^{-4} cm^{-1} which is ~0.01Å) than the spectral resolution. Observe that, even for operation well above threshold, only a few laser modes oscillate. Furthermore, these modes are well separated in wavelength and so one of them can easily be selected using a spectrometer with a very modest resolution.

Figure 2.11 shows the output of the diode laser at a higher temperature (25°K) and relatively high drive current. Nevertheless, only a single mode oscillates. Once more, the width of the peak shown in the figure merely reflects the resolution of the spectrometer. In this Figure, the single mode output is shown for several different currents. Observe the change in wavelength of the peak as the diode drive current is changed, directly reflecting the "fine tuning" of the laser diode wavelength.

Finally, a particularly important characteristic of the diode laser is the extent to which, at a given base temperature and drive current, the output wavelength remains constant. Figure 2.12 shows the results of a direct test of this stability obtained on an X-Y recorder. In this experiment, the laser beam was used to probe the multi-pass White cell (see Chapter 4) which contained a trace of SO_2 in a few Torr of nitrogen. The diode current was fine-tuned until a particular, sharp resonance line was detected. At some point, tuning was discontinued and the X-Y recorder was switched to time base. Any tendency of the laser wavelength to drift would show up as a decrease or increase in the absorption as a coincidence is lost between the laser radiation and that point on the resonant absorption line. No such effect was observed over a period of several seconds. Three different diode lasers are used in this thesis. Table 2.4 contains the listing of these diodes along with its applications.

TABLE 2.4 Listing of the Diode Lasers Used in this Thesis

SDL	Range cm^{-1}	Application	Chapter
PbSnSe	1050 - 1160	Atmospheric Monitoring of SO_2	8
		Point Monitoring of SO_2, NH_3, and N_2O	7
PbSnSe	1030 - 1070	Point Monitoring of O_3	7
		High resolution spectroscopy of O_3	6
PbSnSe	1300 - 1380	Laboratory Studies of atmospheric SO_2 monitoring possibility.	8

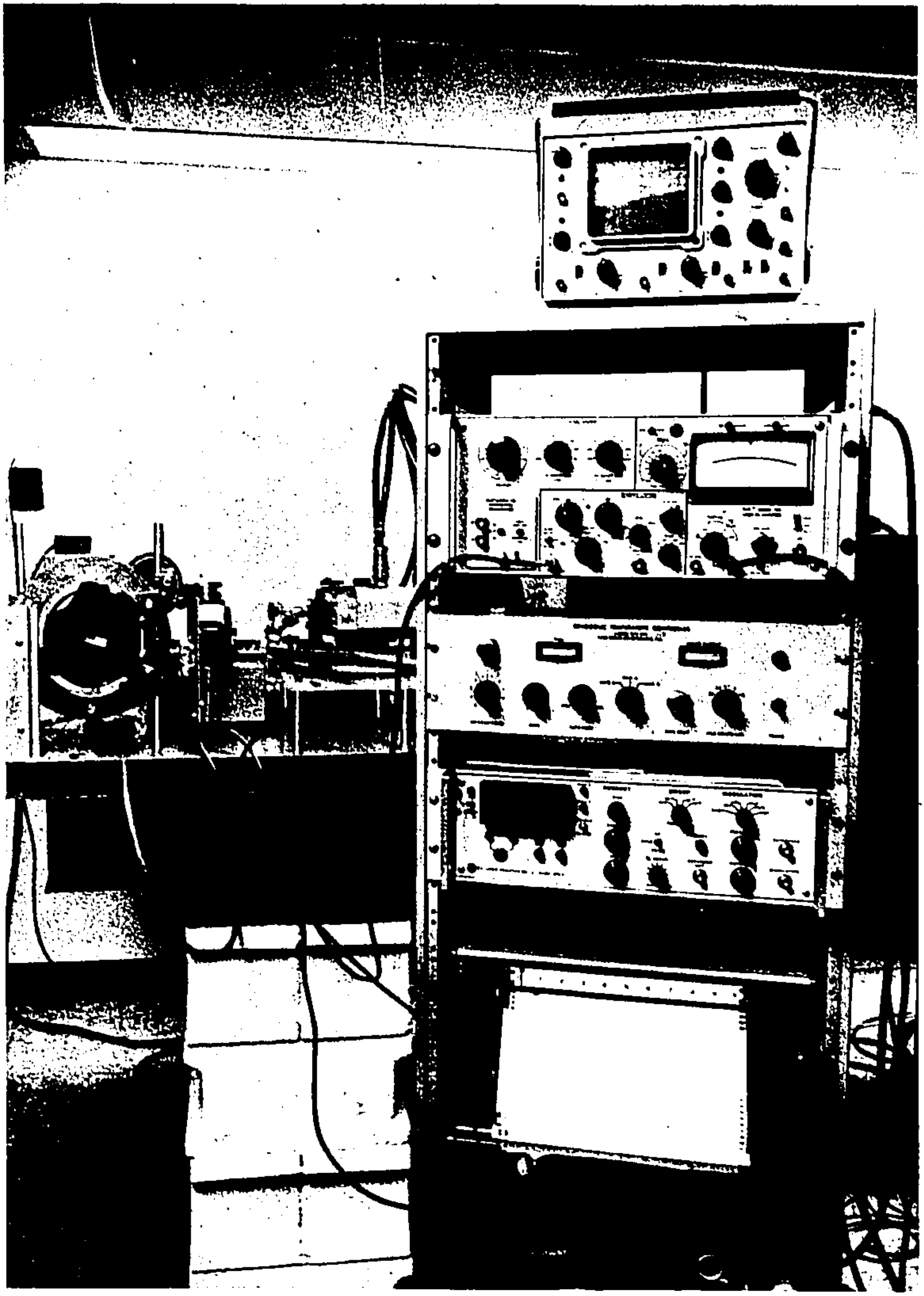

Figure 2.8 A view of the lead-salt diode laser control system. The helium transfer lines and cryocooler head can be seen on the optical table behind the controller.

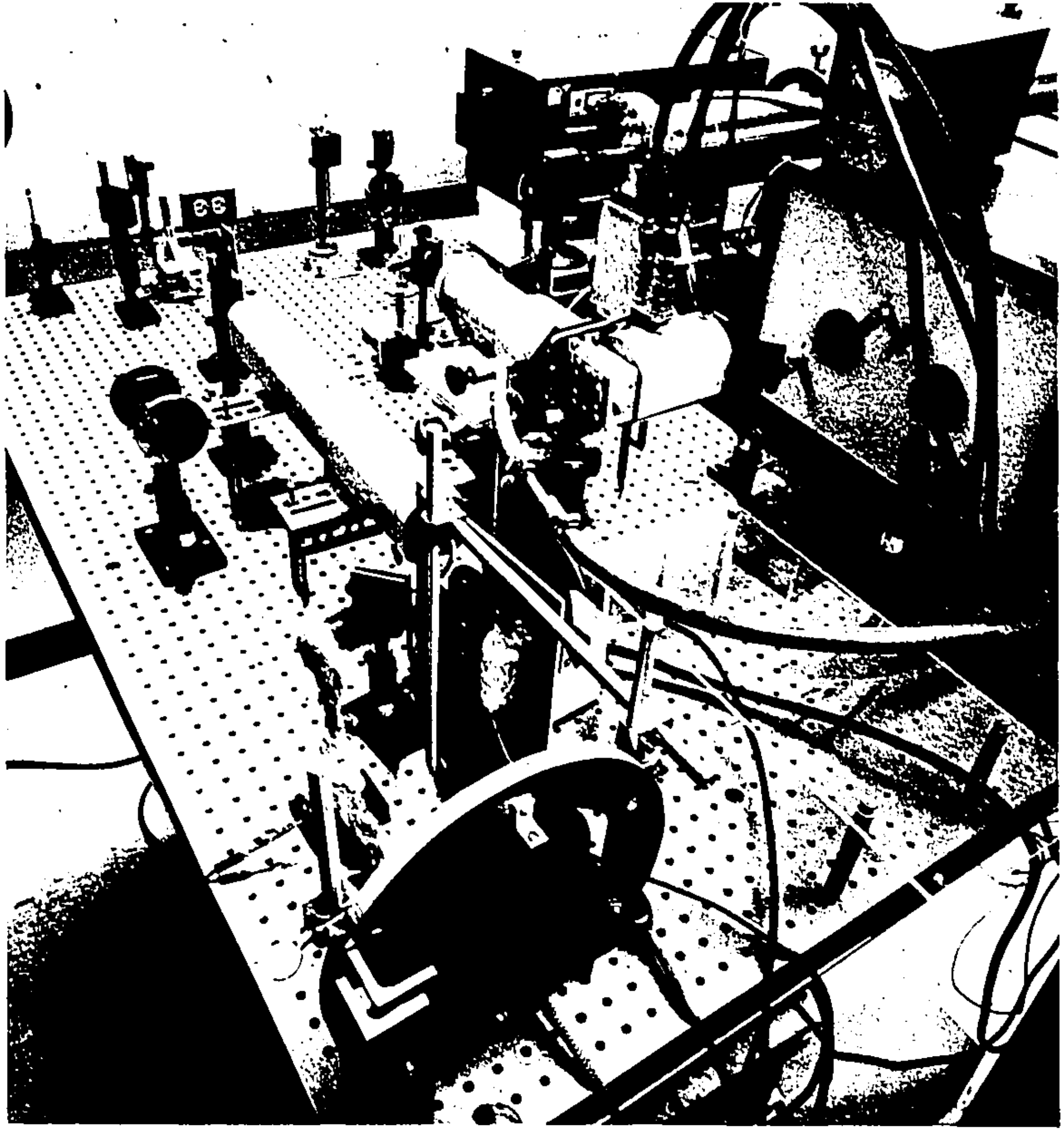

Figure 2.9 A view of the optical table showing the beam transport systems for both the semiconductor diode and the CO/CO_2 lasers. The He-Ne laser is used for optical alignment and the spectrometer for wavelength determination.

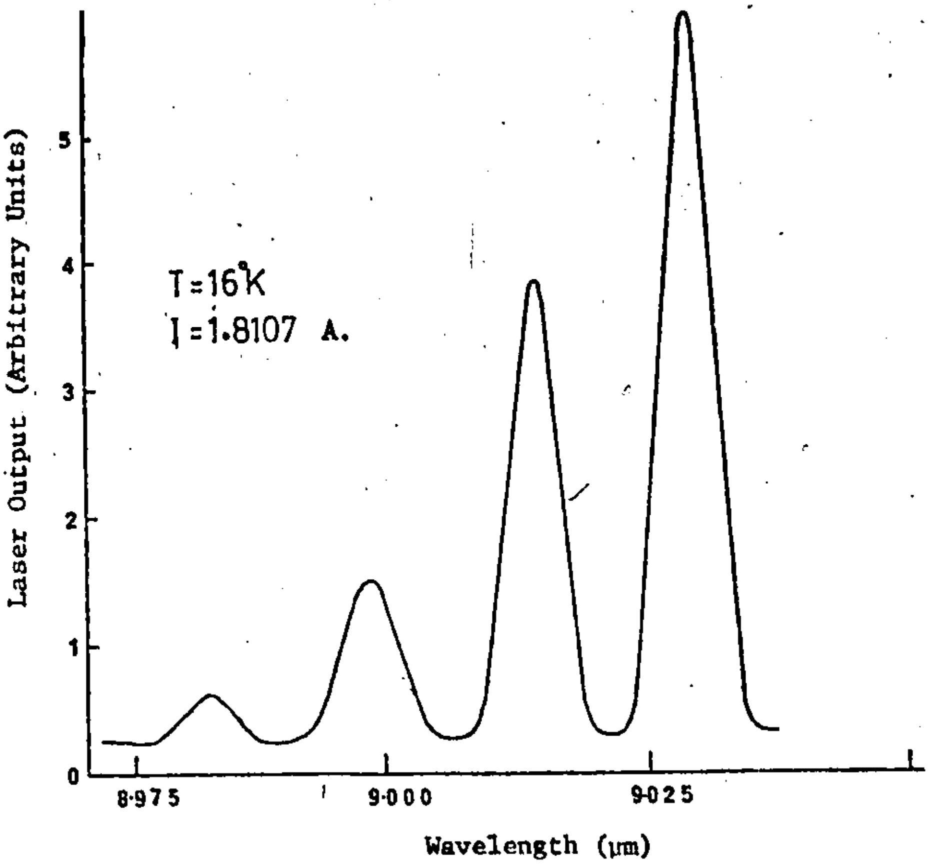

Figure 2.10 Output spectrum from PbSnSe diode laser operating at 16 °K and diode current of 1.8107 A.

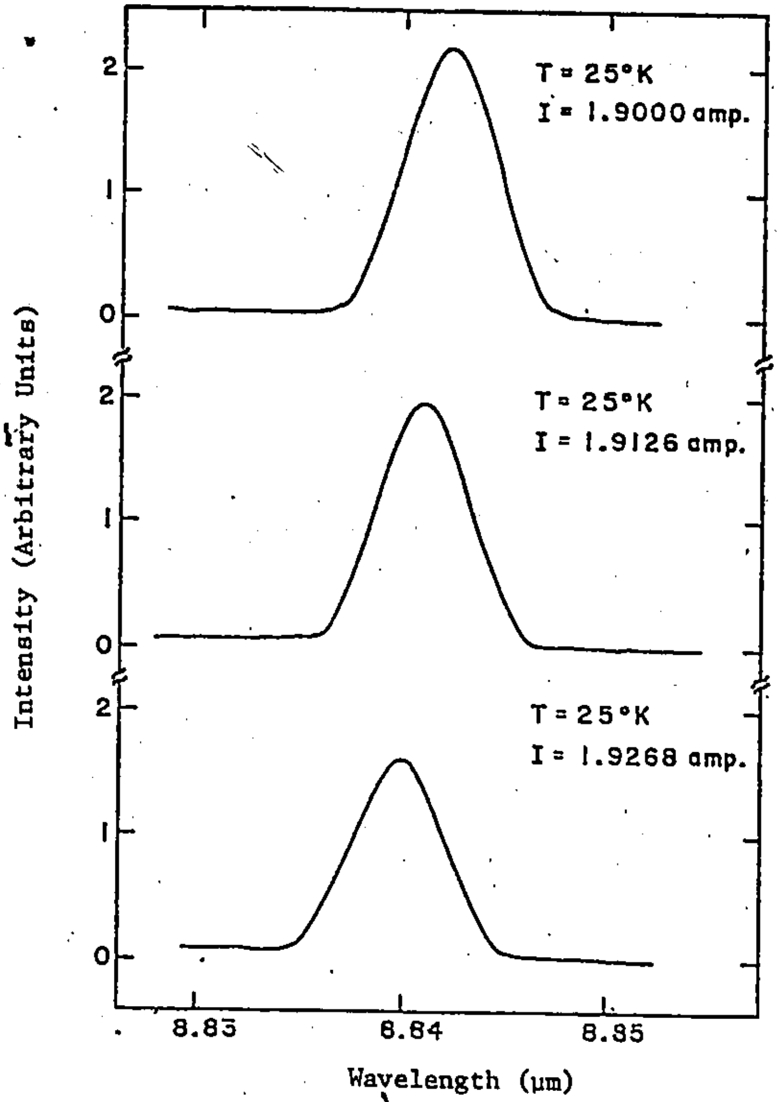

Figure 2.11 Output spectrum from PbSnSe diode laser operating at 25°K and for various diode currents as shown.

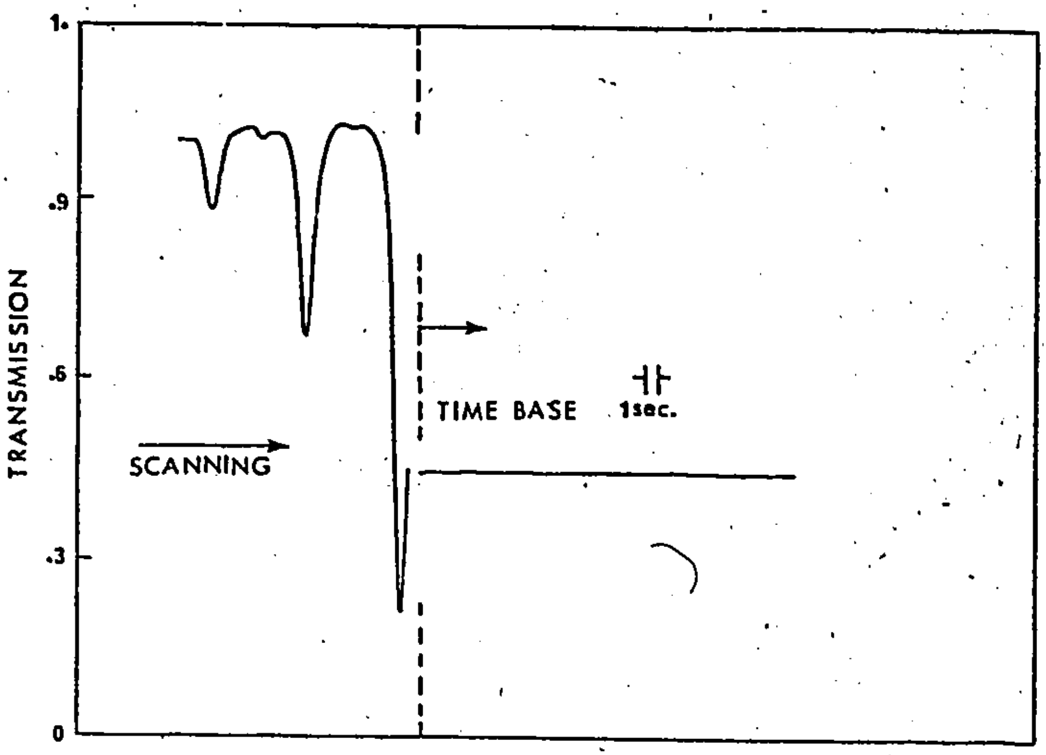

Figure 2.12 Typical result of diode-laser frequency stability experiment. The laser is scanned first through gas absorption lines (left part). Then , the scanning is stopped and the recording apparatus(X-Y recorder) is switched to time base. Note that in 20s the stability is better than 0.25 MHz.

CHAPTER 3

THEORY OF MOLECULAR ABSORPTION OF INFRARED LASER RADIATION

3.1 Introduction

In this Chapter, we consider the required data and modelling, necessary to predict the molecular absorption of narrow linewidth laser radiation.

Beer's law for the linear propagation of monochromatic radiation of frequency (wavenumber) ν in a homogeneous and isotopic medium is of the form

$$\frac{d}{dz} I(z, \nu) = -\beta(\nu) I(z, \nu) \tag{3.1}$$

Where z is the direction of propagation, I(z, ν) is the intensity of the radiation, and β(ν) is the extinction coefficient. The extinction coefficient is the sum of the total absorption coefficient and total non-forward scattering coefficient. The transmittance, T, over a path of length L is then given from the above Equation by

$$T(L, \nu) \equiv I(L, \nu) / I(o, \nu) = \exp\left[-\beta(\nu) L \right] \tag{3.2}$$

The effects of aerosol absorption and scattering or the effects on propagation due to refractive index changes arising from turbulence will not be considered. Also, only the region from 1 to 25 μm will be considered. Here the molecular absorption is primarily due to vibrational overtones and combination bands at the short wavelength end, vibrational fundamental in the middle of this range, and pure rotation at the long wavelength end. The principal absorbers are the most abundant isotopes of H_2O and CO_2 and secondarily, but important in those regions away from strong absorptive transitions of the above molecules, are CH_4, CO, O_3, N_2O, NO, NO_2, SO_2, and HNO_3 as well as the less abundant isotopes of H_2O and CO_2.

The important parameters of a calculation of molecular absorption in the atmosphere relate to a detailed knowledge of line positions, intensities, pressure broadening coefficients, and line shapes. This data has been accumulated and refined since the inception of infrared molecular spectroscopy in the 1930's. The improvement in available data has over the years been most significant. With accurate spectroscopic information one can calculate for various model atmospheres the expected laser transmittance.

Data on individual vibration-rotation lines that are useful for atmospheric transmission calculations in the infrared have been compiled in a systematic fashion over the last ten years. The most accurate data on spectral line parameters has been compiled on magnetic tapes by AFCRL [25]. The molecules included in the compilation are H_2O, CO_2, O_3, N_2O, CO, CH_4, O_2, and recently SO_2, NO, NO_2, and HNO_3 [26].

Since the improvement of accuracies in the molecular constants have become more and more significant over the years, it has been found that for a laser spectroscopy air pollution monitoring station, it is necessary to have a Computer package to generate the individual line parameters of the target gas from its molecular constants, especially if the required data is not available or it is, but not accurate enough. In the following sections, the wavelength regions of different gases and their mixing ratios in the atmosphere, the theory of evaluating the individual line parameters, and the transmittance calculations will be considered.

3.2 General Characteristics of Absorption Spectra of Atmospheric Gases

The main absorbing gases in the atmosphere in the infrared are water vapor, carbon dioxide, ozone, and oxygen. The atmosphere contains minor constituents that also absorb radiation in the infrared region. These are primarily carbon monoxide, methane, and nitrogen oxides. In addition, various gases of industrial origin are present in localized regions, and these can absorb optical radiation. In this section the absorption spectra and the mixing ratios of gases existing in the atmosphere on a planetary scale will be considered [10].

H_2O, mixing ratio of 1.3×10^{-7} to 4.5×10^{-2}

The vibrational-rotational spectrum of H_2O contains three main bands ν_1, ν_2, and ν_3 with centers at 3657.05, 1594.78, and 3755.92 cm^{-1}, respectively, and overtones, combination, and hot bands in the infrared. The most intensive and broad vibration-rotation band of H_2O is the main ν_2 band with center near 6.3 μm. The laser used for pollutant monitoring must be tuned away from the completely absorbing regions (non-window) : 5.5 - 7.5 μm, and 2.6 - 3.3 μm by H_2O.

$\underline{CO_2}$: mixing ratio at sea level: 3.18×10^{-4}

The vibration of CO_2 contains three main modes ν_1, ν_2, and ν_3. ν_1 is optically inactive - because of symmetry its dipole moment remains constant during vibrations. Centers of the main ν_2 and ν_3 vibration-rotation bands are located near 667.40 and 2349.16 cm^{-1}, respectively. The non-window regions are from 13.5 to 16.5 μm, and from 4.2 to 4.4 μm.

$\underline{O_3}$: mixing ratio: $(2 - 7) \times 10^{-8}$

All three main vibration frequencies of O_3 are active in absorption. $\nu_1 = 1110$ cm^{-1}, $\nu_2 = 710$ cm^{-1}, and $\nu_3 = 1043$ cm^{-1}. The ν_1 band is very weak and completely overlaps the ν_3 band. The strongest absorption band of ozone, with its center near 9.6 μm, with a width of approximately 1 μm, absorbs half the solar radiation (non-window).

$\underline{N_2O}$: mixing ratio: $(2.7 - 3.5) \times 10^{-7}$

All three main oscillation frequencies of N_2O: $\nu_1 = 1285.6\ \text{cm}^{-1}$, $\nu_2 = 588.8\ \text{cm}^{-1}$, and $\nu_3 = 2223.5\ \text{cm}^{-1}$, are active in the infrared.

$\underline{CH_4}$: mixing ratio: $(1.0 - 1.4) \times 10^{-6}$

A high degree of molecular symmetry causes strong degeneracy of the vibrational energy levels. The molecule has only four basic oscillations differing in frequencies while the ν_1 and ν_2 frequencies are optically inactive. The centers of the basic ν_3 and ν_4 vibration-rotation bands are close to $3020.3\ \text{cm}^{-1}$ and $1306.2\ \text{cm}^{-1}$, respectively.

$\underline{CO}$: mixing ratio: $(0.5 - 2.5) \times 10^{-7}$

The basic vibration-rotation band is close to $2143.2\ \text{cm}^{-1}$, centers of the second, third, and fourth overtones are near 4260.1, 6350.4, and $8414.5\ \text{cm}^{-1}$, respectively. Other minor constituents [27] are:

$\underline{NO}$: mixing ratio: $10^{-8} - 10^{-6}$

Band 1-0 : $1876\ \text{cm}^{-1}$

$\underline{NO_2}$: mixing ratio: $10^{-9} - 10^{-6}$

Band ν_3 : $1621\ \text{cm}^{-1}$

HNO_3: mixing ratio: 2.8×10^{-9}

Band $2\nu_9$: $896\ cm^{-1}$

NH_3: mixing ratio: $<10^{-6}$

Band ν_2 : $933\ cm^{-1}$

SO_2: mixing ratio: $(0.5 - 7.2) \times 10^{-9}$

Bands: $\nu_1 = 1151\ cm^{-1}$

$\nu_2 = 518\ cm^{-1}$

$\nu_3 = 1362\ cm^{-1}$

3.3 Calculation of Absorption Coefficients

The absorption of laser radiation by a gas may be expressed in terms of the absorption coefficient, $\alpha(\nu)$. For frequencies (wavenumbers) ν near a resonant absorption centered at frequency ν_o, $\alpha(\nu)$ is given by

$$\alpha(\nu) = S^o\, p\, f(\nu, \nu_o) \tag{3.3}$$

where S^o is the line intensity (to be defined below), p is the partial pressure of the absorber, and $f(\nu, \nu_o)$ is the normalized lineshape function, which expresses the fact that the resonance has finite width.

At atmospheric pressure (in the lower region of the atmosphere), broadening of spectral lines is mainly due to collisions between molecules. The line contour determined by these effects is called dispersion and, in the absence of power saturation, may be written as [28].

$$f(\nu, \nu_o) = (1/\pi) \frac{\gamma_L}{(\nu-\nu_o)^2 + \gamma_L{}^2} \qquad (3.4)$$

Where γ_L is the line-halfwidth, which is one-half the linewidth between points ν_1 and ν_2 satisfying the condition

$$\alpha(\nu_1) = \alpha(\nu_2) = \alpha(\nu_o) / 2 \qquad (3.5)$$

This linewidth is caused by collisions between the molecules and is proportional to the pressure and temperature. For the case of a gas mixture,

$$\gamma^o = \sum_j \gamma_j^o p_j , \qquad (3.6)$$

where γ_j^o is the pressure broadening constant of the jth component of the mixture for the spectral line in question, and p_j is the partial pressure of the jth component. The values of γ_L^o for atmospheric gases are of the order of 0.01 - 0.1 cm^{-1}.

Since the line intensity, $S^o p$, is also proportional to the pressure, the peak absorption at resonance $\alpha(\nu_o)$, obtained by combinations of Equations 3.4 and 3.3, is pressure independent. It is therefore a convenient parameter to characterize the magnitude of absorption.

Under these conditions, the peak absorption is given by

$$\alpha(\nu_o) = S^o / (\pi\gamma_L^o) \qquad (3.7)$$

Spectral line broadening is also produced by the Doppler effect. At reduced pressures, and assuming thermodynamic equilibrium for the translational degrees of freedom of a molecule, and Maxwellian velocity distribution of the molecules, then for spectral line contour for which broadening is due to the Doppler effect only, the following expression is obtained [28].

$$f(\nu, \nu_o) = (1/\gamma_D)\,(\ell n\ 2/\pi)^{\frac{1}{2}}\ \exp\left[-(\nu - \nu_o)^2 (\ell n\ 2)/\ \gamma_D{}^2\right] \qquad (3.8)$$

where,

$$\gamma_D \equiv (\text{HWHM}) = (\nu_o/c)\ (2kT\ \ell n\ 2\ /\ m)^{\frac{1}{2}} \qquad (3.9)$$

$$\cong 3.58 \times 10^{-7}\ (T/m)^{\frac{1}{2}}\ \nu \quad \text{cm}^{-1}.$$

Calculations show that the value of γ_D for atmospheric gases is approximately within the limits from $\gamma_D = 6 \times 10^{-2}$ cm^{-1} (for O_2 lines near .2 μm) to $\gamma_D = 3 \times 10^{-4}$ cm^{-1} (H_2O vapor lines near 50 μm).

In the stratosphere (between 15 and 30 km), the ambient pressure varies from 10 to 90 Torr, such that the spectral lines in the infrared are for the most part, neither fully Lorentzian nor Gaussian in shape, but a convolution of the two-known as the Viogt lineshape, and may be written as [28]:

$$\alpha(\nu, \nu_o) = \frac{\alpha_o A}{\pi} \int_{-\infty}^{\infty} \frac{\exp(-x^2)}{A^2 + (\omega - x)^2} dx \qquad (3.10)$$

where,

$$\alpha_o = \frac{S^o p}{\gamma_D} \left(\frac{\ln 2}{\pi}\right)^{\frac{1}{2}},$$

$$A = \frac{\gamma_L}{\gamma_D} (\ln 2)^{\frac{1}{2}},$$

$$\omega = \frac{\nu - \nu_o}{\gamma_D} (\ln 2)^{\frac{1}{2}}.$$

For the limiting case where $|\nu-\nu_o| >> \gamma_L$ and γ_D

$$\alpha(\nu_o) = \frac{S^o p \gamma_L}{\pi(\nu - \nu_o)^2} \left[1 + \left(\frac{3}{2A^2} - 1\right)\left(\frac{\gamma_L}{\nu - \nu_o}\right)^2 + \left(\frac{15}{4A^2} - \frac{5}{A^2} + 1\right)\left(\frac{\gamma_L}{\nu - \nu_o}\right)^4 + \ldots \right]$$

(3.11)

In the case of a number of overlapping lines, the absorption coefficient is the sum over all the individual contributing lines.

The intensity of a spectral line is expressed as an integral of the absorption coefficient over all frequencies

$$S = \int_{-\infty}^{\infty} \alpha(\nu)\, d\nu \tag{3.12}$$

In principle, the intensity may be evaluated by the application of quantum theory of Einstein transition probabilities. Thus the intensity of absorption for the transition i to j is [29].

$$S_{ij} = \left(\frac{8\pi^3 \nu_{ij}}{3hc}\right) \left(\frac{N_i}{g_i N}\right) \left[1 - \exp\,(hc\nu_{ij} / kT)\right] \times |R_{ij}|^2 \tag{3.13}$$

where ν_{ij} is the transition frequency (wavenumber), N_i/N is the fractional number density in state i with statistical weight g_i, $|R_{ij}|^2$ is the square of the matrix element of the dipole moment. The fractional number density may be rewritten in terms of energy level E_i of state i and the total partition function Q as

$$N_i / g_i N = Q^{-1} \exp \left[-E_i / kT\right] \tag{3.14}$$

The partition function is given as the product of the vibrational and rotational partition function, i.e.

$$Q = Q_v Q_r. \tag{3.15}$$

Using the harmonic oscillator approximation, the vibrational partition function is expressed by

$$Q_v = \prod_{i}^{d_i} \left[1 - \exp\left(-h\omega_i/kT\right) \right]^{-1} \tag{3.16}$$

where ω_i is the fundamental vibrational frequencies of degeneracy d_i.

The calculation of absorption coefficients for specific molecules, using Eqn. (3.3), depends upon the molecular symmetry. The appropriate line intensity formulas for the asymmetric top and linear molecules are described in the following subsections.

3.3.1 Asymmetric Top Molecules

A number of atmospheric gases are asymmetric top rotors with C_{2v} molecular symmetry. For these molecules, the rotational states are identified by the quantum numbers $J(K_p, K_o)$, where J is the rotational quantum number and K_p and K_o are pseudo-quantum numbers describing the projection of J on the symmetry axis for the limiting prolate and oblate symmetric tops respectively.

The energy levels associated with these states cannot be obtained in closed form but can be calculated by a Computer diagonalization of the rotational Hamiltonian. A subroutine subprogram has been developed in this study, and proved to be very efficient. This program calculates the energy levels and hence the frequency of any transition from J = 0 up to J = 45 for any asymmetric molecule following the general theory described by King et al [30]. In order to obtain results of sufficient accuracy, it is necessary to include contributions to the Hamiltonian due to centrifugal distortion [31].

In calculating the absorption coefficient due to individual lines, the most difficult problem in line intensity calculations is the determination of $|R_{ij}|^2$. Neglecting the interaction between vibration and rotation we obtain the dipole matrix element as the product of the vibrational and rotational matrix element:

$$|R_{ij}|^2 = |\mu|^2 \ |\beta|^2 \tag{3.17}$$

The rotational matrix element $|\mu|^2$ cannot be given as a simple function of the rotational quantum number because of the asymmetric nature of the molecule. A subroutine subprogram has been developed in this study which calculates the matrix element for arbitrary κ and for any transition. The theory used is the same as that described by Cross et al [32].

The vibrational matrix element $|\beta|^2$ for a complex molecule is very difficult to calculate and it is customary to obtain the matrix element through a measured quantity. This matrix element is related to the integrated absorption coefficient through the relations

$$|\beta|^2 = (v_i + 1) \ |\beta_o|^2 \tag{3.18}$$

where $|\beta_o|^2$ for the fundamental transition, and the integrated absorption coefficient at temperature of T_o may be expressed as

$$\alpha^{obs} = \frac{8\pi^3}{3hc} \frac{N_{To}}{Q_v} |\beta_o|^2 \sum_{v_1 v_2 \ldots = 0}^{\infty} \omega_o (v_i + 1) \exp\left[-\frac{hcG_o(v_1 v_2 \ldots)}{k T_o}\right] x$$

$$\left[1 - \exp\left(\frac{-hc\,\omega_o}{k T_o}\right)\right] \qquad (3.19)$$

As an example, consider the first band v_1 in the three bands v_1, v_2, and v_3 of a triatomic molecule

$$G_o (v_1 v_2 v_3) = G (v_1 v_2 v_3) - G(000),$$

where $G(v_1 v_2 v_3)$ is the vibrational energy [33] , and

$$\omega_o = G_o (1 v_2 v_3) - G_o (0 v_2 v_3)$$

The rotational partition function can be written to sufficient accuracy using the semi-classical expression

$$Q_r = \left[\exp(\sqrt{B_e C_e}\ \ hc/4kT)\right]\sqrt{\frac{\pi}{A_e B_e C_e}\left(\frac{kT}{hc}\right)^3}\left[1 + \frac{1}{12}\left(1 - \frac{\sqrt{B_e C_e}}{A_e}\right)\frac{hc\sqrt{B_e C_e}}{kT}\right] \quad (3.20)$$

where A_e, B_e, and C_e are the rotational constants.

Finally, it is necessary to consider the effects of the nuclear spin statistics on the level population. In the case of the molecules SO_2, O_3, and NO_2, this factor is unity for the allowed states which are J(e, e) and J(o, o), where e and o specify the parity of K_p and K_o. In the case of H_2S and H_2O the factor is g = 1/4 for the states (e, e) and (o, o) and is g = 3/4 for the states (e, o) and (o, e).

These factors, the molecular constants, the total band strength, and the selection rules are the input data to run the two subroutine subprograms for the line position and intensity calculations.

The Computer program for such evaluations, as devised by the author, contains three main subroutines:

(1) A subroutine for generating line positions,

(2) A subroutine for generating line intensities,

(3) A subroutine for calculating the absorption coefficient at any selected wavenumber, and any pressure due to all the contributing absorption lines.

3.3.2 Linear Molecules

For diatomic and linear polyatomic molecules the calculations of the individual line positions and intensities are straightforward

4

and available elsewhere [31].

3.3.3 Linewidths

Calculations of the linewidth parameter γ_L based on collisional models are quite complex and available for only a few cases of interest. Hence, if accurate absorption coefficients are desired, it is usually necessary to use experimentally determined values for γ_L. Because of the limitations of the available data, in most of the calculations reported in this thesis, average values of γ_L were assumed for each molecule independent of the transition involved. Calculations and/or measurements of linewidth for N_2 and air diluted mixtures have been given for a number of gases in the literatures [34 - 38].

3.4 Results and Discussion

In the wavelength range from 2 to 20 μm, absorption by atmospheric gases is mainly due to vibration-rotation bands, the strongest of which are in the infrared spectral region. It is clear that very intensive absorption in the center of certain bands practically excludes the possibility of applying these regions for the purpose of laser monitoring of the atmosphere, irrespective of whether the wavelength of the laser radiation is near the central part of the absorption line of the gas, or is between strong lines of central part of the absorption band. Within strong absorption bands, laser monitoring can be accomplished only in the upper layers of the atmosphere or by point monitoring (extracting an air sample at reduced pressures). In both cases the neighbouring lines are separated and there is no overlapping.

The most useful wavelengths for laser monitoring are generally those in intervals between absorption bands, or microwindows of atmospheric transparency. In order to perform laser monitoring of the atmosphere, it is necessary to have quantitative information on absorption coefficients in the very atmospheric transparency microwindows located close to the wavelength of the laser radiation, along with information on absorption due to nearly spectral lines of atmospheric gases. Figure 8.7 (see Chapter 8) shows the required quantitative information about the atmospheric gases for the region from 1100 cm^{-1} to 1200 cm^{-1}. These traces in Fig. 8.7 are the output of our computer package. The upper trace is the transmission due to 1% of H_2O in the air at total pressure of one atmosphere, and with total pathlength of L = 1 km. The other traces are the absorption coefficient for different atmospheric gases absorbing in this region. The optimum laser wavelength regions are determined first, in order to avoid strong absorption due to H_2O, Secondly the selected wavelength region must be at maximum absorption due to the target gas and minimum absorption due to the other gases. This Figure will be used for SO_2 monitoring in the atmosphere in Chapter 8.

CHAPTER 4

RESONANCE ABSORPTION MEASUREMENTS WITH FIXED-FREQUENCY LASERS: USEFUL CRITERIA

4.1 Introduction

As mentioned in Chapter 3, every absorption line of a molecule in the atmosphere has, generally speaking, its own value of center position, width, and intensity. Without precise knowledge of these parameters, a theoretical determination of absorption coefficient is out of the question, even with correct knowledge of the broadening contour. The measurements of absorption coefficients of different gases, or performing high resolution spectroscopic studies with tunable lasers seem to be good solutions to this problem. A laser beam has a very low divergence and can thus be passed through a sample of target gas many times to enhance its absorption at concentrations equal to the ambient levels.

In this Chapter, measurements with line-tunable CO_2 laser, whose emission wavelengths are stable and well known, will be demonstrated. Section 4.2 contains measurements with a CO_2 laser on ozone in order to establish some useful criteria for pollution monitoring via the direct absorption scheme. The measurements of absorption coefficient α and the pressure dependence of the extinction coefficient k_ν (p) at frequencies ν corresponding to the P(8) to P(36) vibration-rotation lines of the CO_2 laser will be described and compared with theory.

Of the laser techniques mentioned in Chapter 1, the resonance absorption approach appears to be the least sophisticated in experimental design, least costly, and most straightforward in providing optical information on gaseous pollutants. However, the applicability of this approach has appeared to be limited for two reasons: (a) the lack of frequency matching of available laser lines from fixed frequency lasers with lines from the vibrational-rotational spectrum of the target gas; (b) interference with the absorption signal by neighboring lines of other gas species as a result of Lorentz broadening of absorption lines at atmospheric pressure. The first of these problems has been potentially removed with the development of tunable lasers (as described in Chapters 6, 7 and 8). In the second area, the question of line interference has not been answered because of a lack of experimental and theoretical investigation. It is this second area that this Chapter is addressed to. The following questions are the main object of this Chapter: (1) If a fixed frequency laser is used, how close a line match is required to the principal gas species absorption line? (2) What is the width of the frequency band around the laser line in which spectral line absorptions due to other gases will cause a significant error in concentration measurements? (3) What is the minimum absorption intensity of foreign gas species lines above which they will play a significant part, if they are in the range described in (2)? (4) If fixed frequency detection is employed, is more than one line required in order to ensure that the absorption reading is solely due to the gas species, and if so, how many such lines are required?

To answer such questions a "tunable" CO_2 laser has been employed as a light source. This laser is tunable in the sense that it employs a diffraction grating for line selection and thus offers a large number of lines that can be matched up in varying degrees with the absorption lines of target gas.

The growing concern about the hazardous effects of ozone on human respiratory [39] and visual systems [40] has pointed to the need for an efficient scheme for monitoring this pollutant gas in the atmospheric ambient. Due to the overlap between the ozone absorption band and the CO_2 laser emission band, the CO_2 laser has been employed in some optical monitoring investigations on ozone [41 - 43]. However, ozone is a complicated molecule and has a concomitant complex multiline absorption spectrum. An examination of the ozone vibrational-rotational spectrum [44] indicates that at room temperature and pressure there can be significant absorption due to lines with centers as far away as 0.1 cm^{-1}.

Therefore, the observed absorption of a laser line can be due to contributions from several ozone lines. The effects due to frequency mismatch, line broadening, and numbers of lines contributing are then all mingled together. A study of the ozone system in more detail was expected, therefore, to shed light on the various questions raised in the previous paragraph. Although the frequency mismatch between the CO_2 laser lines and the ozone lines is fixed, the line broadening can be reduced by lowering the pressure of the gas. This will be employed to yield useful information on the establishment of criteria for monitoring pollutants with lasers.

4.2 Experimental Technique

Room temperature measurements of resonance absorption were made on ozone in the 9.4 μm wavelength region using CO_2 laser radiation. A schematic diagram of the apparatus is shown in Figs. 4.1 and 4.2. The CO_2 laser used was a Molectron model C250 (see Fig. 2.1), coupled with a model SD-20 diffraction grating for spectral line selection. The spectral lines used in this work were P(8) - P(36) in the $00^{0}1 - 02^{0}0$ band. The designation of each line was confirmed by using an Optical Engineering model 16-A CO_2 laser spectrum analyzer.

The absorption chamber (see Fig. 4.3) was a multipass White-type cell [45] consisting of a 5 m long stainless steel tube of 15 cm diam. Both the entrance and exit windows were made of BaF_2. A mechanical assembly at the chamber ends supported the concave gold-plated mirrors of 5 m radius of curvature. Orthogonal kinematic mounts on these mirrors allowed the adjustments of the optical path, with lengths from 20 m to 1000 m in intervals of 20 m. However, for optimum SNR and stability of the optical path, a pathlength of 400 m was used for most measurements in this Chapter. The absorption chamber was equipped with vacuum facilities to permit measurements at controlled pressures in the 0.015 - 1 atm. range.

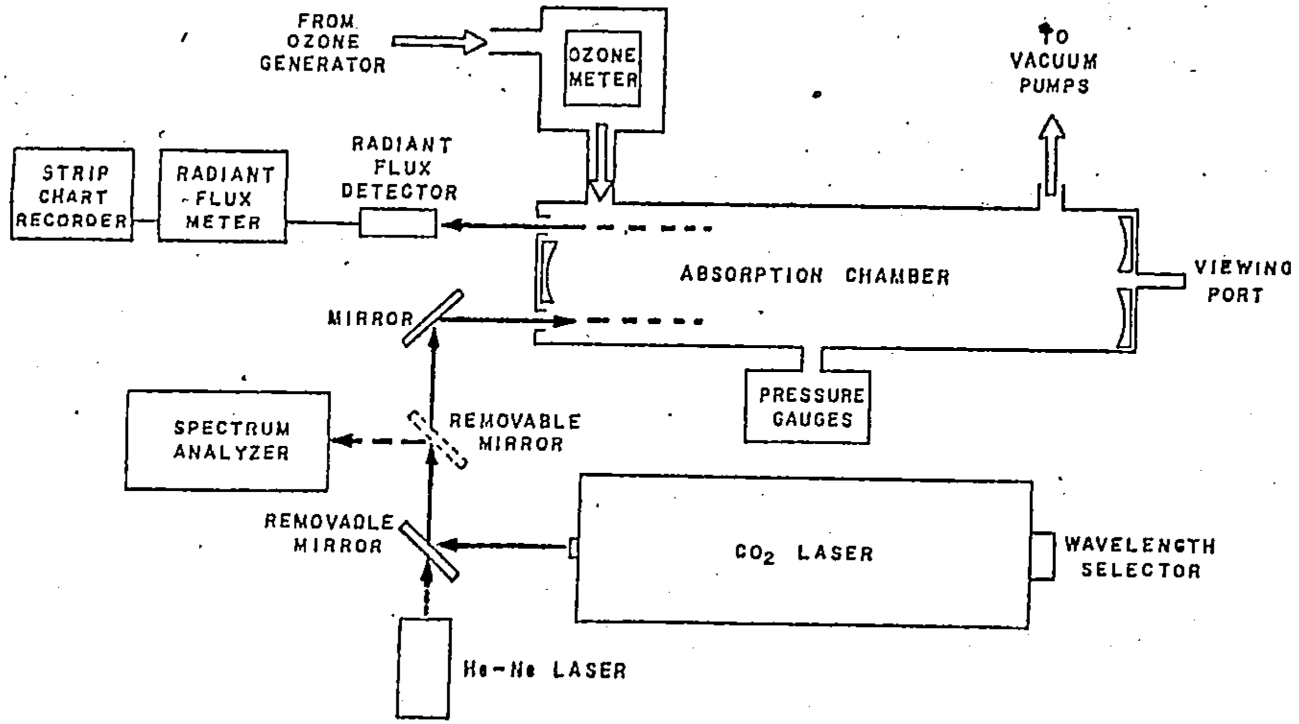

Figure 4.1 Schematic digram of the system used for resonance absorption measurements on ozone.

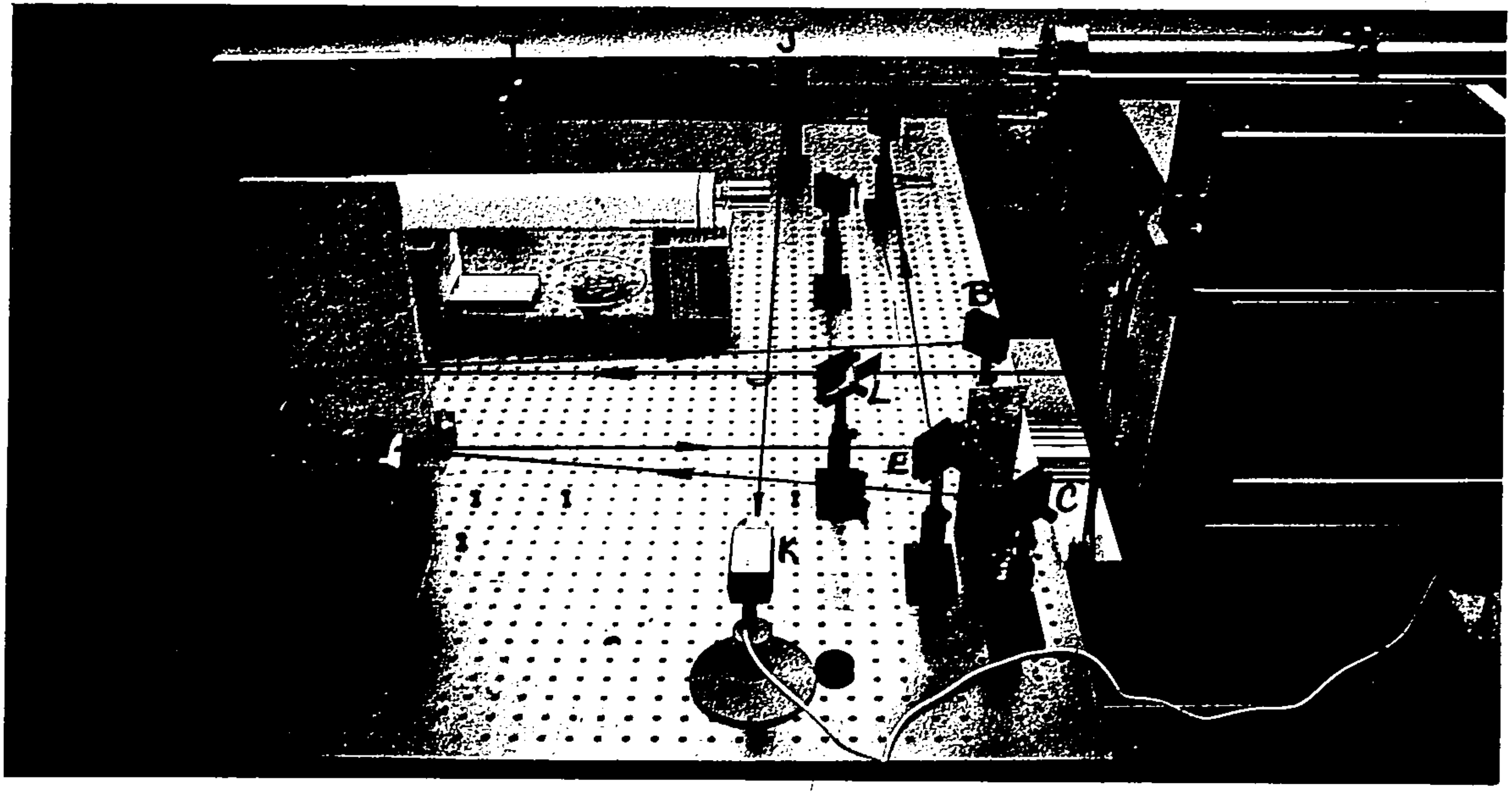

FIGURE 4.2

OPTICAL BENCH IN THE LASER LAB Laser light follows the path drawn in: past the alignment mirror(normally withdrawn) to concave mirror A, to B, through the asbestos pinhole,to C,to concave mirror D, to E,to F, then to concave mirror G (which focusses the beam into the long path cell H). It re-emerges to concave mirror I, to J, and finally to the detector K.

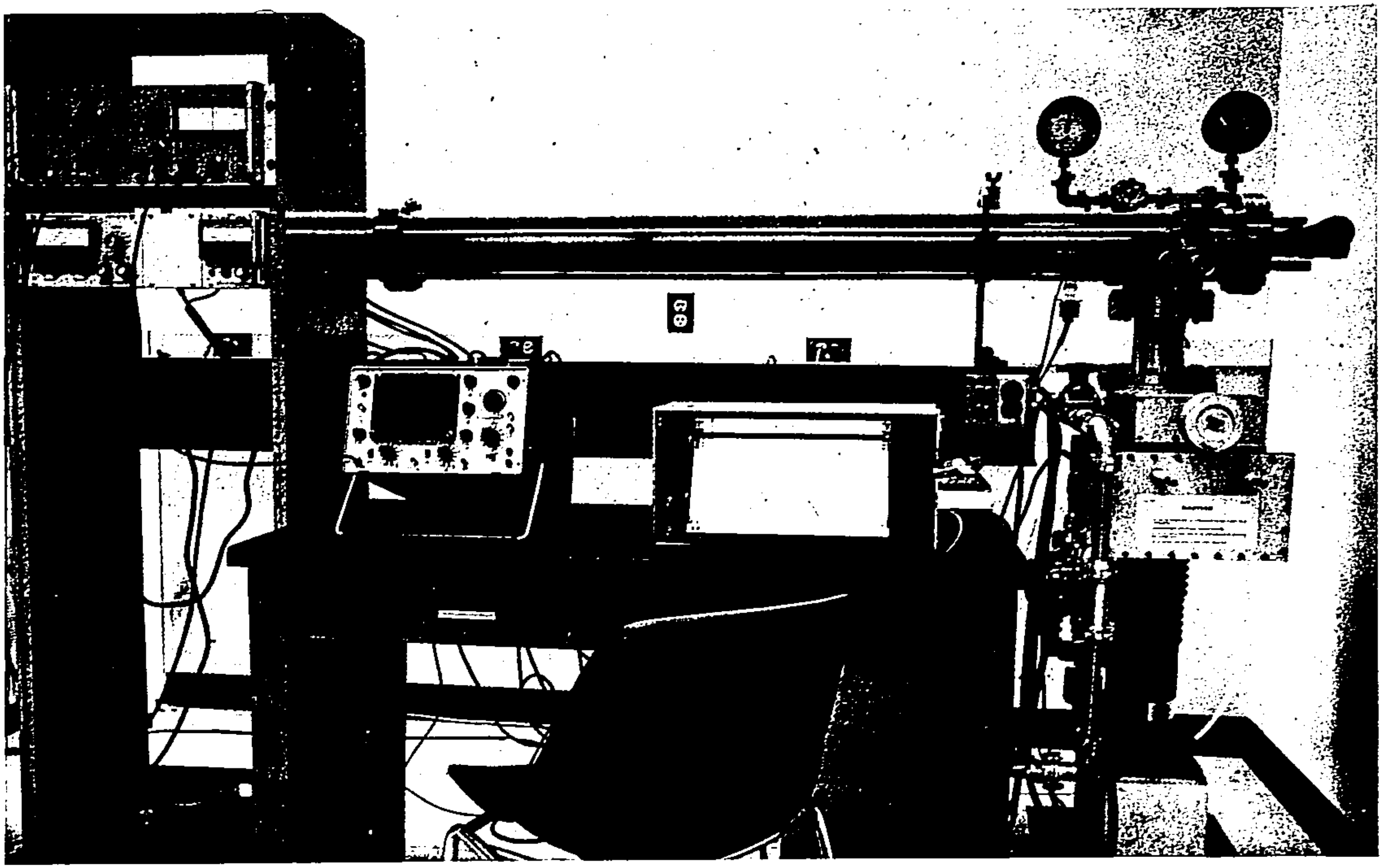

Figure 4.3 View of laboratory facility showing stainless steel absorption chamber (variable path length, multiple-reflection White Cell) in which various atmospheres are simulated, as well as instrumentation for absorption detection and data processing.

Optical alignment for the system was achieved by using a He - Ne (6328-Å) laser whose optical path was made to coincide with that of the CO_2 laser, (see Figure 4.2). The CO_2 laser radiation was attenuated before being detected by a Hewlett-Packard (H-P) Model 8334 A radiation flux detector that was coupled with a H-P Model 8330 A radiant flux meter.

Ozone was generated by an electrical discharge across pure oxygen. The ozone was then diluted with room air in a chamber. The concentration of ozone in the resultant mixture used for this work was in the 0.05 - 2 ppm range. Ozone-air mixtures and pure N_2 were alternatively introduced into the absorption chamber in order to determine the transmitted radiation intensity. Since ozone decayed with time, a continuous flow method was used. The ozone concentration was monitored by a MAST model 724-2M ozone meter that was calibrated against a neutral buffered KI method. For resonance measurements at 1 atm pressure, the ozone meter placed at either the gas inlet or outlet line showed no observable change in its reading. For measurements at reduced pressures, the ozone meter was placed at the gas inlet line where the pressure was 1 atm. The error in ozone concentration determination was within ± 3%.

4.3 Data Analysis and Results

The transmission $T(\nu)$ was obtained from the ratio of measured transmitted light intensities for the ozone-air mixture and for pure N_2. Using the following expression

$$-\ell n\, T(\nu) = k(\nu)\, L \qquad (4.1)$$

experimental values of the extinction coefficient k(ν) were deduced for a total pathlength L. The absorption coefficient

$$\alpha(\nu) = k(\nu) / p_{O_3} \quad (\mathrm{cm}^{-1}\ \mathrm{atm}^{-1}) \qquad (4.2)$$

of ozone was then determined for each of the P(8) - P(36) laser lines in the $00^{0}1$ - $02^{0}0$ band. For each laser frequency, α was found to be constant over the ozone concentration range of 0.05 - 2 ppm. The variation of α with ν for measurements at 1 atm is shown in Fig. 4.4 Patty et al, [42] have reported similar results for ozone. Despite some differences in the experimental approach and the range of ozone concentrations used (the range used by Patty was 10 - 80 ppm) the absorption coefficients obtained in both cases were in agreement to within the experimental error of ± 10%.

Using the theoretical considerations in Chapter 3, α(ν) was calculated using only the nearest ozone line to the corresponding P branch laser line. These results, which are presented in Fig. 4.4, indicate that significant absorption is present due to other neighboring ozone lines. For these calculations, CO_2 wavelengths given by Baird et al [46] and ozone wavelength compilations by Clough and Kneizys [47] were used. Further calculations were carried out using up to six neighboring ozone lines with frequencies separated from

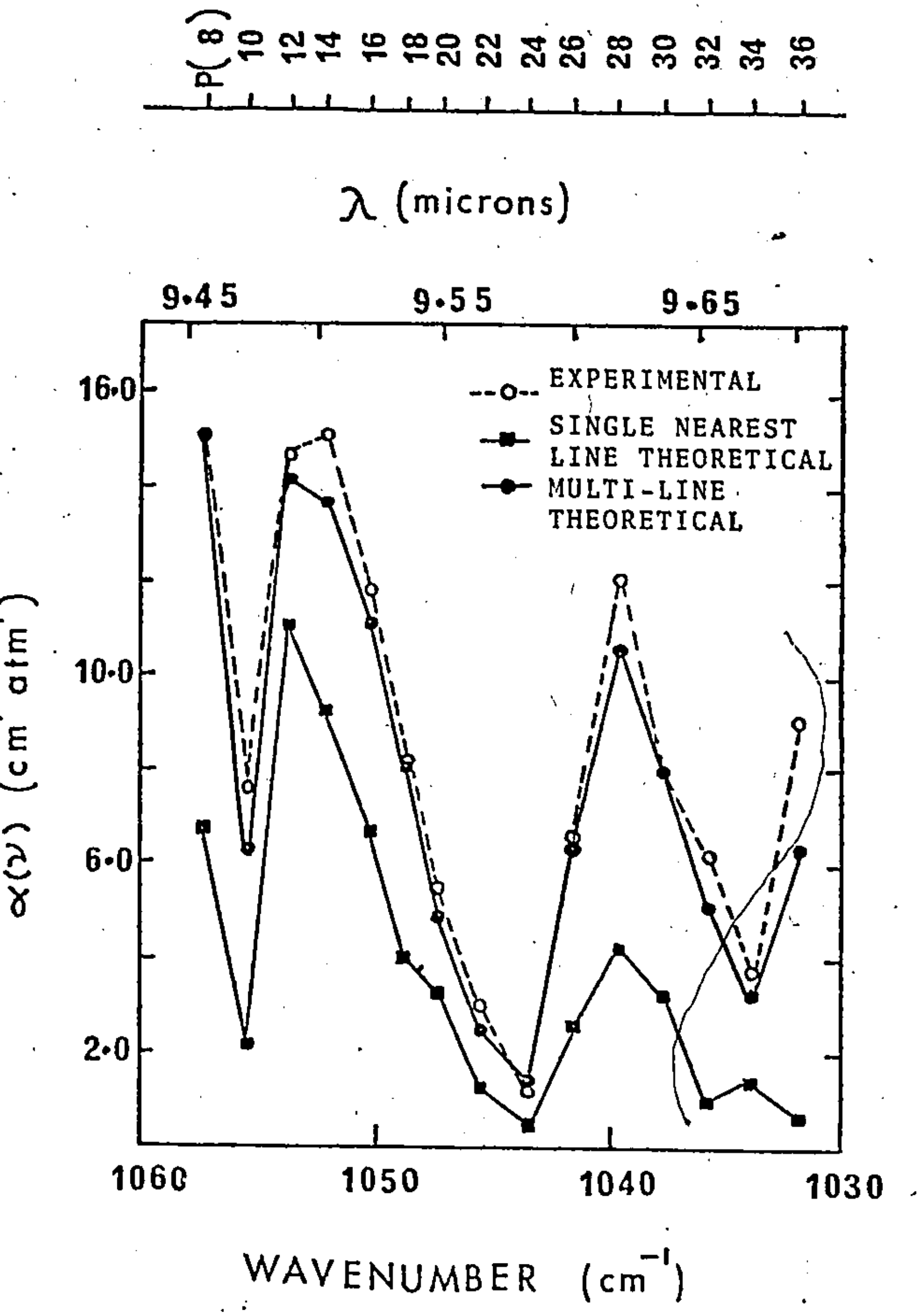

Figure 4.4 Experimental and theoretical plots of absorption coefficients as a function of CO_2 laser wavelength for P(8) to P(36) lines in the $00^{0}1-02^{0}2$ band. Temperature=22°C and pressure=1atm. The multi-line theoretical curve has been normalized to the experimental curve of P(8) and the single nearest line curve is appropiately scaled with respect to that point.

the laser line by as much as 0.25 cm^{-1}. The ozone lines used are given in Table 4.1. The results are also presented in Fig. 4.4 and indicate good agreement (to within experimental error) between experiment and theory. Note that the multiline theoretical curve has been normalized to the experimental curve at P(8) and the single nearest neighbor curve appropriately scaled with respect to that point. Calculations of absolute absorption coefficients always lead to numerical values higher than observed. The implications of these data, insofar as considerations for a practical pollution monitoring system using direct absorption with single line lasers are concerned, is that even with an exact laser-pollutant absorption line match, absorption lines of any species within about 0.1 cm^{-1}, can contribute significantly to the absorption process if their absorption intensity is not more than an order of magnitude below that for the nearest neighbor line. Consequently, in constructing a pollution monitoring system using fixed frequency detection, care must be exercised in the selection of the laser line and gas absorption frequency so as to ensure that there are no other neighboring absorption lines of significant strength within about ±0.10 cm^{-1}. In practice this may be difficult to realize as the ozone data presented here seem to indicate. To test this hypothesis further, measurements as function of pressure were also carried out and are presented next.

Typical experimental results of resonance absorption measurements at pressures in the 0.015 - 1 atm range are shown in Figs. 4.5 - 4.7. The extinction coefficient $k(\nu)$ has been normalized with

TABLE 4.1 Listing of CO_2 Laser Lines from the P Branch of the 00°1-02°2 Band Along with Nearest Neighbor Ozone Lines.

CO_2 Laser Line Frequency in cm^{-1}	Difference of Nearest Ozone Line Frequency to CO_2 Laser Line in cm^{-1} (Intensity of Ozone Line in cm^{-2} atm^{-1} at T = 300°K)					
P(8): 1057.3001	+0.0002 (0.33)	+0.0077 (0.81)	+0.0710 (0.78)			
P(10):1055.6251	-0.0032 (0.01)	+0.0428 (0.15)	+0.0846 (0.96)	+0.0940 (0.03)		
P(12):1053.9235	+0.0008 (0.90)	+0.0220 (0.21)	+0.0546 (1.35)			
P(14):1052.1956	-0.0659 (0.25)	-0.0493 (0.72)	+0.0614 (0.35)	+0.0640 (0.52)	+0.0765 (1.16)	
P(16):1050.4413	-0.0445 (1.48)	+0.0978 (0.92)				
P(18):1048.6609	+0.0175 (0.60)	+0.0509 (0.12)	+0.0690 (0.96)			
P(20):1046.8545	-0.0588 (0.03)	-0.0534 (0.15)	-0.0521 (0.15)	+0.0429 (0.39)		
P(22):1045.0219	+0.1295 (0.48)	+0.1539 (0.66)				
P(24):1043.1635	-0.1190 (0.03)	+0.0244 (0.03)				
P(26):1041.2791	-0.0964 (0.01)	-0.0587 (1.38)	-0.0215 (0.24)			
P(28):1039.3693	-0.0403 (0.25)	-0.0229 (0.55)	-0.0179 (0.25)	-0.0130 (0.12)	+0.0385 (0.08)	+0.0724 (0.68)
P(30):1037.4342	-0.0824 (0.42)	-0.0323 (0.03)	-0.0106 (0.12)	+0.0112 (0.27)	+0.0326 (0.01)	+0.0598 (0.06)
P(32):1035.4737	-0.0694 (0.06)	-0.0617 (0.01)	-0.0461 (0.03)	+0.0285 (0.01)	+0.0343 (0.03)	+0.0438 (0.01)
P(34):1033.4883	-0.0541 (<0.01)	-0.0430 (<0.01)	-0.0104 (0.02)	+0.0087 (0.01)	+0.0465 (<0.01)	
P(36):1031.4776	-0.1054 (1.40)	-0.0999 (<0.01)	-0.0191 (<0.01)	-0.0186 (0.38)	-0.0175 (0.82)	-0.0158 (<0.01)

respect to the value at 1 atm. Although data were obtained for all fifteen lines in the P(8) - P(36) band, it was found that the curves could be sorted according to their shapes into three categories. These categories were determined basically by the magnitude of the frequency separation of the laser line from its nearest neighbor ozone line ($\Delta\nu_n$) provided the absorption strength of the nearest neighbor was greater than 0.1 cm^{-2} atm^{-1}. In those situations where the absorption strength was less than 0.1 cm^{-2} atm^{-1} there were two cases: (a) the next nearest neighbor would be chosen provided it also was within the criterion and (b) the nearest neighbor would still be chosen in spite of the criterion because other nearest neighbors also had low absorption strengths. The categories and lines in each are enumerated in Table 4.2.

The special cases are marked with an asterisk. For example, for P(10) $\Delta\nu_n = 0.0032$, but the absorption strength $S^o = .01$, whereas the next nearest neighbor $\Delta\nu_n = 0.0428$ along with a strength of $S^o = 0.15$, and so it is chosen. Typical curves for each category are given in Figs. 4.5 - 4.7.

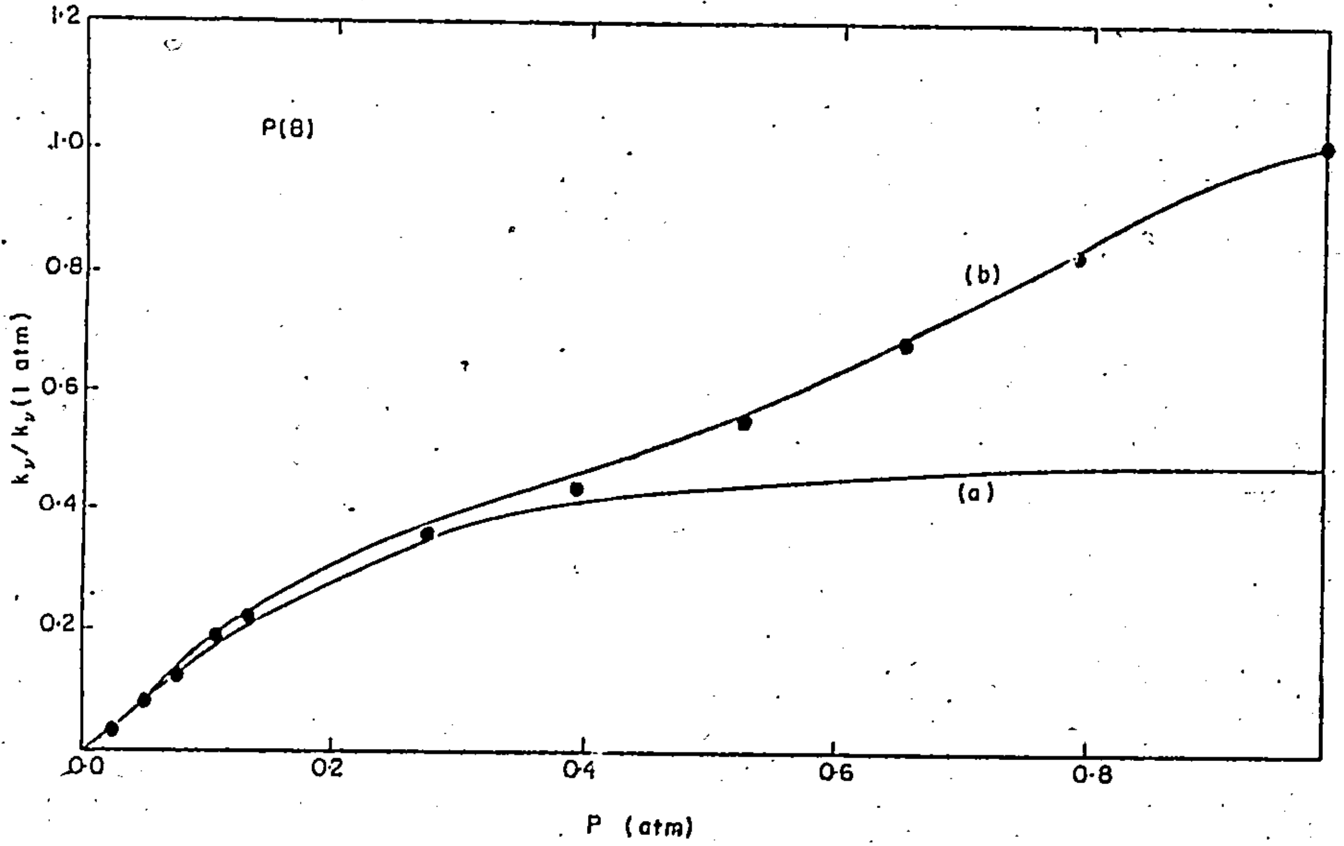

Figure 4.5 Plot of normalized extinction coefficient, k_ν/k_ν(1atm), as a function of ozone partial pressure for the P(8) CO_2 line: (a) theoretical curve using nearest neighbor ozone line only; (b) theoretical curve using neighbors listed in Table 4.1 and experimental points. Temperature=22°C.

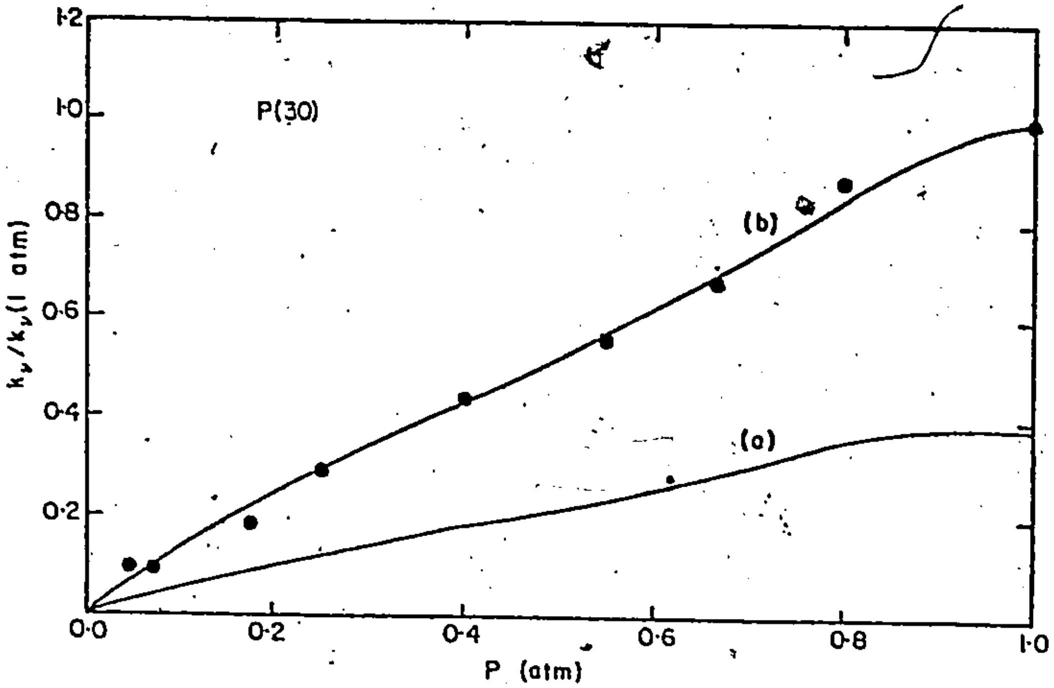

Figure 4.6 Plot of normalized extinction coefficient, k_ν/k_ν(1atm), as a function of ozone partial pressure for the P(30) CO_2 line : (a) theoretical curve using nearest neighbor ozone line only; (b) theoretical curve using neighbors listed in Table 4.1 and experimental points. Temperature is 22°C.

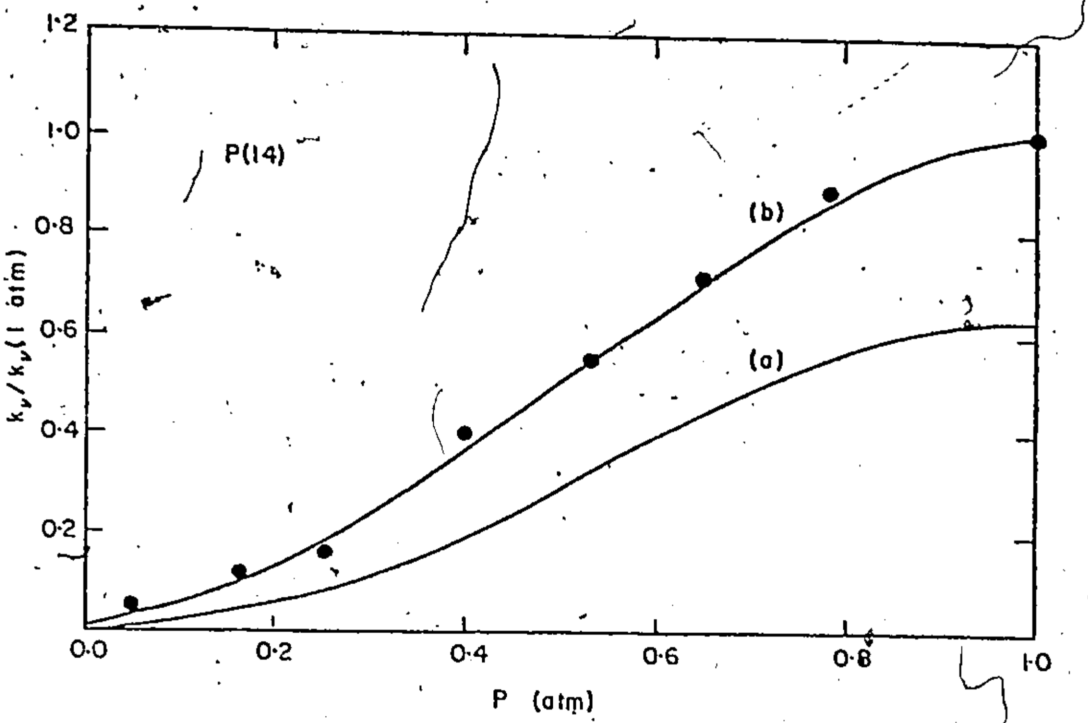

Figure 4.7 Plot of normalized extinction coefficient, k_ν / k_ν(1atm), as a function of ozone partial pressure for the P(14) CO_2 line : (a) theoretical curve using nearest neighbor ozone line only; (b) theoretical curve using neighbors listed in Table 4.1 and experimental points. Temperature is 22°C.

TABLE 4.2 Categories and Lines

$\Delta\nu_n < .001$ cm^{-1}	0.001 cm$^{-1} < \Delta\nu_n$ and $\Delta\nu_n < .01$ cm^{-1}	$\Delta\nu_n > .01$ cm^{-1}
P(8)	P(30)	*P(10)
P(12)	*P(34)	P(14)
		P(16)
		P(18)
		P(20)
		P(22)
		*P(24)
		P(26)
		P(28)
		P(30)
		*P(32)

A theoretical variation of $k(\nu)_p$ / $K(\nu)_{1\ atm}$ was generated for each laser line using the theory described in Chapter 3 with numerical values from Refs [46] and [47]. This was done first using only the nearest neighbor ozone line and then the neighboring lines listed in Table 4.1. The results of these calculations are shown in Figs. 4.5 - 4.7. In the calculations using only the nearest neighbor ozone line, the discrepancy between experimental data and theory is quite large. This again illustrates the hypothesis advanced earlier that neighboring lines within ± 0.1 cm^{-1} have a significant effect on total absorption even when the match between laser lines and nearest gas absorption line is quite close, as in the case of P(8). When lines within ±.1 cm^{-1} are included in calculations, the agreement between theory and experiment is quite good.

As seen in Figs. 4.5 - 4.7, when the pressure is reduced, the discrepancy between the nearest neighbor curve and the multiline curve is reduced. The number of ozone lines contributing to the absorption of a CO_2 laser line depends on the frequency separation of the ozone lines and on the Lorentz-half-width γ_L (which is ∿ .08 cm^{-1} at 1 atm). Since γ_L decreases approximately linearly with pressure, the ozone lines farthest from the laser line will, in sequence, become less important, and the nearest neighbor and multiline calculations must merge at low pressures. It should be noted that despite an uncertainty of approximately 0.003 cm^{-1} in each laser line, only the frequency corresponding to the center of the appropriate rotation line was used in the calculation of $k(\nu)_p$. This simplifying process did not affect the validity of the theory for the case of significant frequency mismatch of laser and ozone lines. Even for the case of closely matched lines, such as P(8) or P(12), the error due to neglecting the finite spread of the laser line would only be noticeable at $p < .1$ atm. However, the decreasing accuracy in the experimental determination of $k(\nu)_p$ at pressures below 0.1 atm may prevent one from making this observation.

4.4 Discussion

For all fifteen laser frequencies considered here, $k(\nu)_p$ was found to decrease monotonically with decreasing pressure. In the theoretical framework of collision and Doppler broadenings, the variation of $k(\nu)_p$ at high pressures can be interpreted primarily in terms of the changes in Lorentz half-width γ_L and in the partial pressures of the gases. Should the absorption of a laser line be due to a very closely matched ozone line alone, $k(\nu)$ would not decrease much with decreasing p until the onset of the Doppler broadening. This behaviour is shown in the calculated nearest-neighbor-only curve for P(8) in Fig. 4.5. On the other hand, should the absorption be mainly due to some poorly matched ozone lines, $k(\nu)$ would drop very rapidly as p decreases. This is illustrated in Fig. 4.7 for the single nearest neighbor curve of P(14).

The three categories depicted in Figs. 4.5 - 4.7 each show a characteristic curve shape with pressure. For the category of a closely matched laser-ozone-line pair as in Fig. 4.5 for P(8), the sign of $d^2k(\nu)/dp^2$ changes from negative to positive and then negative as p gradually decreases over the whole pressure range used. The reason for this is, of course, the contribution due to the two other nearest neighbors ($\Delta\nu_n$ = .008 cm^{-1} and $\Delta\nu_n$ = 0.071 cm^{-1}), which have strengths greater than the nearest neighbor ($\Delta\nu_n$ = .0002 cm^{-1}). The second category (0.001 cm^{-1} $<\Delta\nu_n<$0.01 cm^{-1}) yields curves that are similar to the category of closely matched lines, but the effect on $k(\nu)_p$ due to the larger frequency mismatch is readily noticeable. A frequency mismatch of ~ 0.01 cm^{-1} is not small enough to overcome the narrowing of the Lorentz half-width, but not large enough to cause a rapid decrease of $k(\nu)$ at low pressures. For either P(30) or P(34), the laser line is evenly sandwiched between its two nearest ozone lines. This coincidence helps to maintain their marginal contributions to $k(\nu)$ even at lower pressures. In the final category of a large mismatch ($\Delta\nu_n$ > .01 cm^{-1}) as in Fig. 4.7 for P(14), the sign of $d^2k(\nu)/dp^2$ changes from negative to positive as p decreases. For each laser line in this category, the frequency mismatch is large enough to cause a rapid decrease with reduced pressure. It is interesting to note that the absorption coefficient for P(14) at p = 1 atm (see Fig. 4.3) is comparable to P(8) or P(12) where $\Delta\nu_n$ < 0.001 cm . Again this supports the argument that absorption lines of any gas species within ± 0.1 cm^{-1} of the laser line will contribute significantly to the absorption process provided their intensities are not more than one order of magnitude below that of the main gas line being scrutinized.

CHAPTER 5

RESONANCE ABSORPTION MEASUREMENTS WITH A FIXED-FREQUENCY LASER: SPECTROSCOPIC DATA FOR POLLUTION MONITORING

5.1 Introduction

In Chapter 4 the matching between the line-tunable CO_2 laser and the ozone absorption lines was explored to establish some useful criteria for air pollution monitoring via the direct absorption scheme employing a fixed-frequency laser. This was achieved mainly because of the fact that, all the required knowledge about the laser line positions, and the individual pollutant gas absorption line parameters are well known to the desired accuracy. However, in the case where accurate values of the absorption line parameters, or a tunable laser with its calibration method are not available, the line-tunable laser with very accurately measured transition frequencies, can be employed to estimate the position, strength, and width of the nearest absorption line to a particular laser emission line with enough accuracy to perform studies or monitoring at atmospheric pressure.

In this Chapter, a line-tunable CO laser is employed to carry out laboratory measurements of NO absorption in a White cell. This laser is tunable in the sense that a diffraction grating is used for selecting discrete CO laser frequencies. Absorption by NO is observed on seventeen CO laser transitions. The absorption coefficients of these transitions are determined by measuring the transmission when the White cell was evacuated (or filled with pure N_2) and when filled with an appropriate NO - N_2 mixture. The separation ($\Delta\nu_n$) between each CO and relevant absorbing NO transition, the pressure broadening parameter (γ_L^o), and the integrated absorption (S^o) for the seventeen lines are determined by matching the experimental data to the theoretical calculation.

5.2 Theory

The theory is similar to that used for Chapter 4, and described in Chapter 3. The absorption coefficient for NO is evaluated using

$$\alpha(\nu) = k(\nu) / p_{NO} \tag{5.1}$$

where p_{NO} is the partial pressure of NO in the mixture.

The NO molecule is a simple molecule which has an odd number of electrons and a non-zero electron angular momentum. The electronic orbital and spin angular momenta are strongly coupled to give a total electron angular momentum of either 1/2 or 3/2. The electronic ground state is actually a doublet, and the substates, classified as ${}^2\Pi_{1/2}$ and ${}^2\Pi_{3/2}$ are separated by a spin orbit splitting of about 124 cm^{-1} [49]. The ir band of NO consists of two superimposed sub-bands, one associated with each ground substate. The rotational energies of these two substates can be represented by using different effective rotational constants for each substate; the conventional rotational constants of the molecule are just the average of the effective constants. The vibrational constants are not as well established, and there is disagreement between the various published values [50.-52]. These values are adequate for this technique, where it is only necessary to obtain reasonably accurate parameters for the target gas (NO). The wavenumbers are calculated using the approach outlined in Ref. [53]. This allows identification of relevant absorbing lines and provides a starting point for comparison between theory and experiment.

Individual line strengths are calculated using

$$S_{\nu,J} = S_1 H(\nu, J) \qquad (5.2)$$

which is derived from Ref. [53]. Here S_1 is the fundamental band strength of NO, and $H(\nu, J)$ is the appropriate weighting function of the transition. The fundamental band strength S_1 may be calculated using

$$\alpha(\nu) = S_1 H(\nu, J) f(\nu-\nu_o) / p_{NO}. \qquad (5.3)$$

derived from Eqs. 5.2, and 5.3.

5.3 Experimental

The instrumentation and alignment techniques used are identical to those described in Chapter 4, except that the liquid-nitrogen-cooled CO plasma tube was employed in the Molectron model C250 laser. Oscillation was observed on approximately fifty transitions in the 5.16 -

5.6 μm range. Significant absorption was observed on seventeen of these.

Measurements were carried out employing a 934 ppm (by volume) NO in N_2 mixture supplied by Matheson. This was diluted with high-purity N_2 as required. As a check on reliability, all measurements were repeated using a different cylinder (93.5 ppm) obtained from AIRCO.

5.4 Data Analysis and Results

The transmission $T(\nu)$ and the absorption coefficient $\alpha(\nu)$ were evaluated using Eqs. (4.2) and (5.1), respectively. Values of $\alpha(\nu)$ for the seventeen lines, shown in Fig. 5.1, are based on measurements taken at 1 atm total NO-N_2 pressure. Also shown in Fig. 5.1 are the two values obtained by Chackerian and Weisbach [54]. Despite some differences in experimental approach (the nitric oxide was placed in an intralaser-cavity absorption cell), the absorption coefficients obtained in the two cases are in reasonably good agreement.

Absorption measurements were also made using total gas pressures ranging from 20 Torr to 760 Torr. The following procedure was employed to give theoretical fit to the measured absorption coefficients. The separation of the NO lines [$R(1.5)_{1/2}$ and $R(1.5)_{3/2}$] from the CO-laser line [P(13) 9-8 band] are known to high precision [55] and consequently were taken as reference separations. These reference separations were used to determine the pressure broadening parameter (γ_L^o) by matching the theoretical and experimental normalized extinction coefficients. This normalization procedure avoids the need to know the individual line strengths. Data were taken over a range of pressures and were fitted by using the least squares technique. Results of this procedure are displayed as curve b in Fig. 5.2 and yield a value of $\gamma_L^o = 0.052 \pm 0.002$ cm^{-1} atm^{-1}. Note that the quoted error represents the limit for which there is no significant deviation in the fit between measurement and theory. The two other plots depicted in Fig. 5.2 correspond to a best fit of the theory presented earlier to the experimental data obtained for the $R(6.5)_{1/2}$ and $R(18.5)_{3/2}$ lines of NO. The three plots shown in the figure are representative of the types of variation of the extinction coefficient with pressure observed on the remaining lines. Curve a is typical of the variation obtained when the absorbing NO line and the CO laser wavelength are close to coincidence; curves b and c correspond to increasing separation between the laser wavelength and molecular resonance line. The best fits between experimental observation and the theoretical model illustrated in plots a and c, and those for all other absorbing transitions, were obtained as follows. The parameter γ_L^o was initially assumed to have the value $\gamma_L^o = 0.052$ cm^{-1} atm^{-1} determined above. Next, $\Delta\nu_n$ (separation between the NO and appropriate CO transitions) was adjusted until the best fit was obtained between theory and experiment. Finally, the procedure was repeated for small changes in γ_L^o. Both $\Delta\nu_n$ and γ_L^o were determined from the one curve giving the best fit to the experimental data. Results for the values of $\Delta\nu_n$ and γ_L^o obtained in this way were presented in Tables 5.1 and 5.2 respectively. For purposes of comparison values deduced from NO measurements by other workers are also displayed. The CO laser wavenumbers required for this have been measured directly using harmonic mixing techniques, and so they are known to high precision [56].

In general, the present results for $\Delta\nu_n$ are in reasonably good agreement with the more recent experimental work [57] and with the calculated values [58]. The latter values of $\Delta\nu_n$ were found from a new compilation of NO transition wavenumber obtained by fitting the molecular constants to the best available data. The generally good agreement between the values of $\Delta\nu_n$ deduced from our experiment and those determined from Johns' NO wavenumbers has motivated to the interpretation of the experimental data in an alternate fashion. The values of $\Delta\nu_n$ determined from Johns' work were taken to be correct. The best fit between theory and experiment was carried out by variation of the pressure-broadening parameter (γ_L^o) alone. In this way, the values of γ_L^o have been determined to an accuracy limited mainly by the precision of the wavelength data for the NO lines. The set of values of γ_L^o so determined, as well as those determined by the previous approach, is given in Table 5.2 [(ii) and (i), respectively]. The agreement obtained between the line broadening parameters determined by the two methods for treating the data is moderately good in most cases. However, for the line designated as $R(12.5)_{1/2}$ (using the Johns' NO wavelength tabulation), it was not possible to obtain a fit between theory and experiment for any reasonable line-broadening parameter. This indicates that the predicted position of this particular NO line is significantly in error. In a more general way, there is a lack of obvious correlation between the γ_L^o values obtained using the fixed $\Delta\nu_n$ approach and molecular state angular momenta. This is some indication that the present accuracy of the wavelength data for the NO lines is not sufficient to give high-precision values of γ_L^o . Better values for these parameters are expected from the present experimental data when more accurate values of the target gas resonance lines become available. However, a different technique, which is proved to be very accurate, is achieved and will be described in Chapter 6.

The measurements of extinction coefficient as a function of pressure were normalized to the values observed at atmospheric pressure before fitting to the theory. The value of the extinction coefficients, together with a knowledge of the partial pressure of NO, allows the various line strengths to be calculated using Eq. (5.3). Figure 5.3 is a plot of the line strengths obtained in this way against wavenumber. Also shown are experimental values from Abels and Shaw [59] and the relative variation of the line strength expected theoretically (using the computer program package described in Chapter 2). The theory has been normalized to agree with the experimentally determined band strength. As can be seen, the agreement between experiment and theory is very good. The value of the band strength obtained is given in Table 5.3, which also shows a sampling of values obtained by other investigators. The agreement with the earliest and more recently, reported measurement is good.

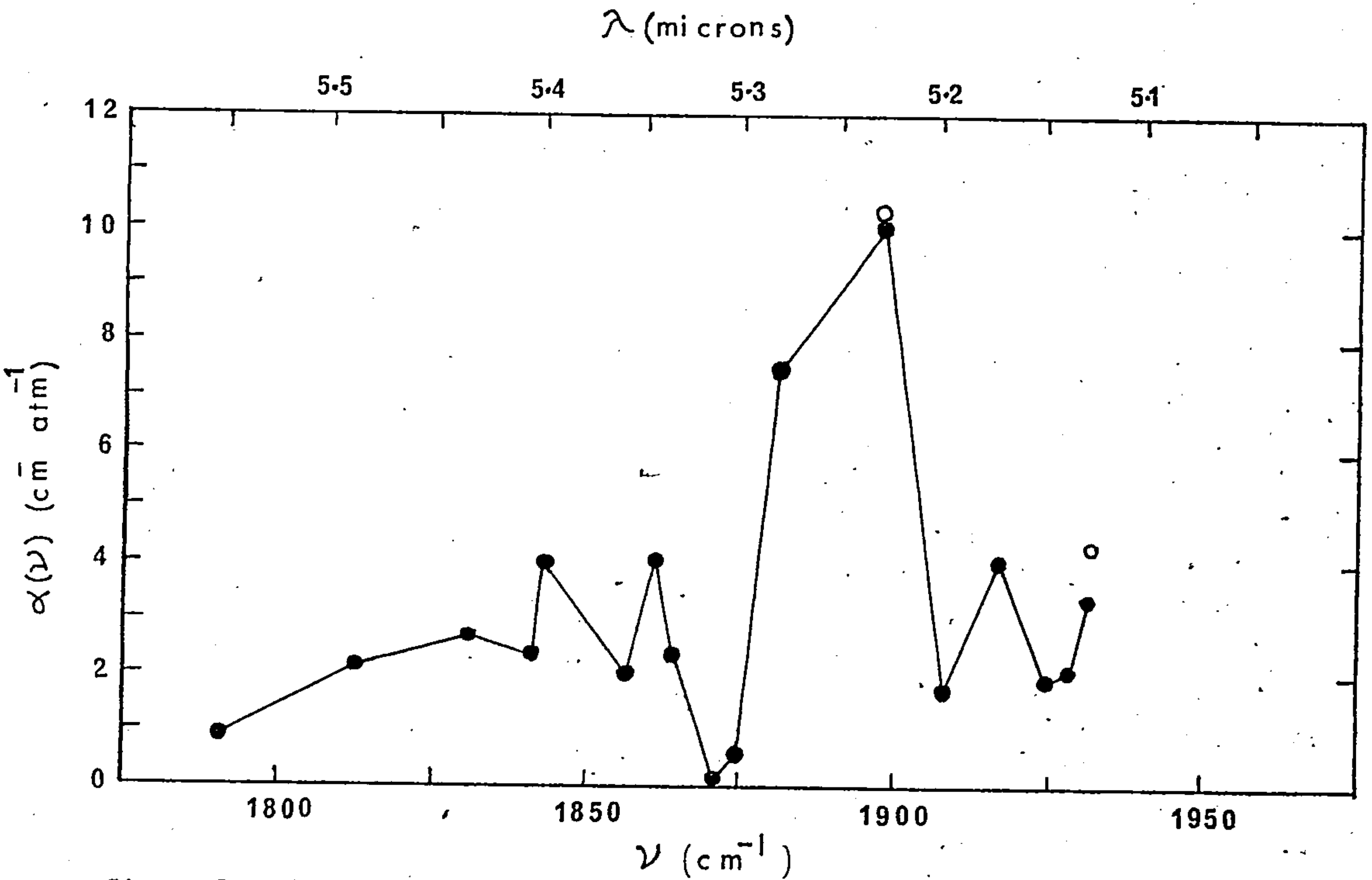

Figure 5.1 Absorption of the seventeen CO laser wavelengths. Present measurements are represented by ●; those of Chackerian and Weisbach[54] by o.

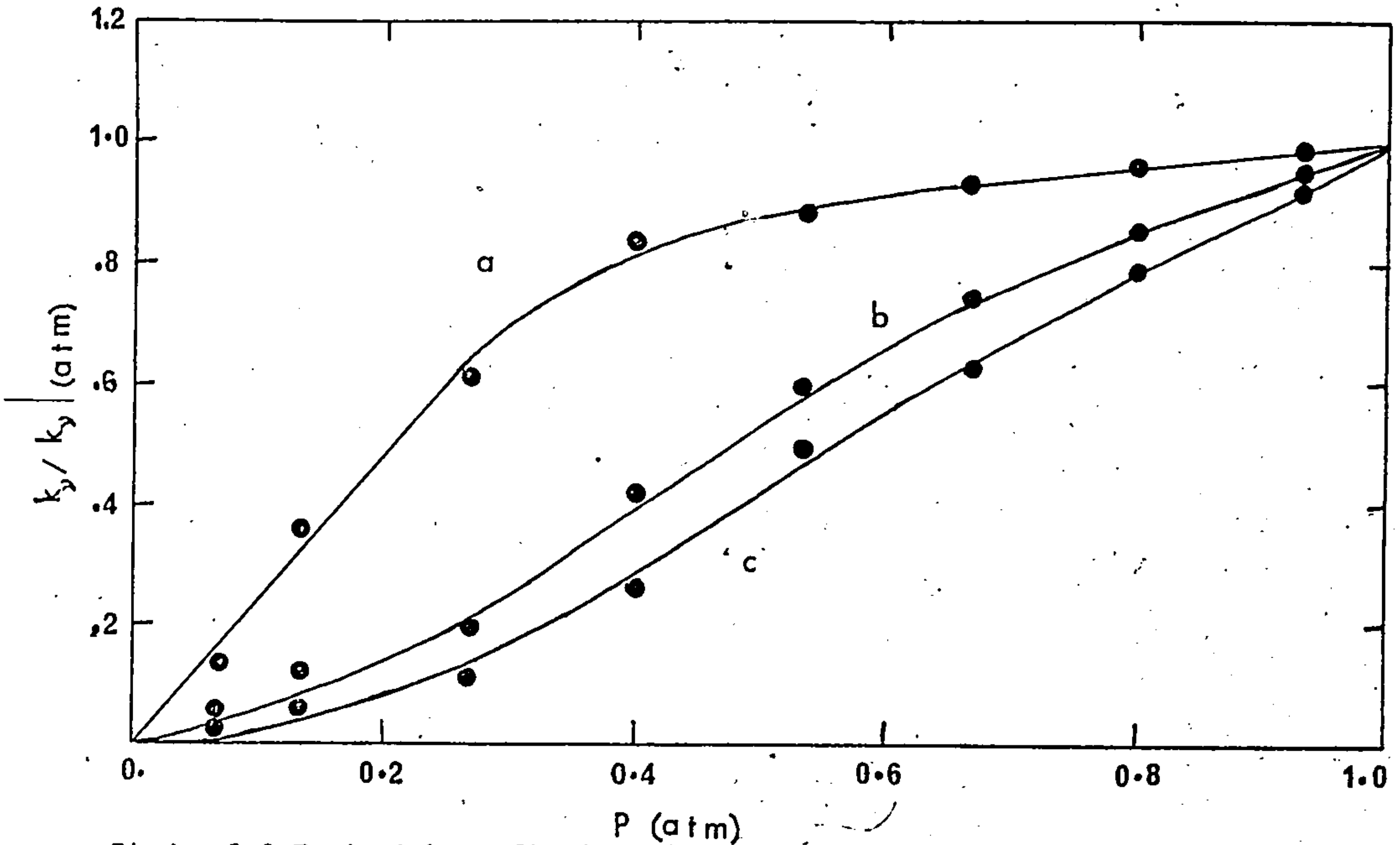

Figure 5.2 Typical best fit data for the normalized extinction coefficient. The plotted points are experimental, the solid curves theoretical. Curve b represents the combined $R(1.5)_{1/2}$ and $R(1.5)_{3/2}$ NO absorption. Curves a and c represent the $R(18.5)_{3/2}$ and $R(6.5)_{1/2}$ NO absorption, respectively.

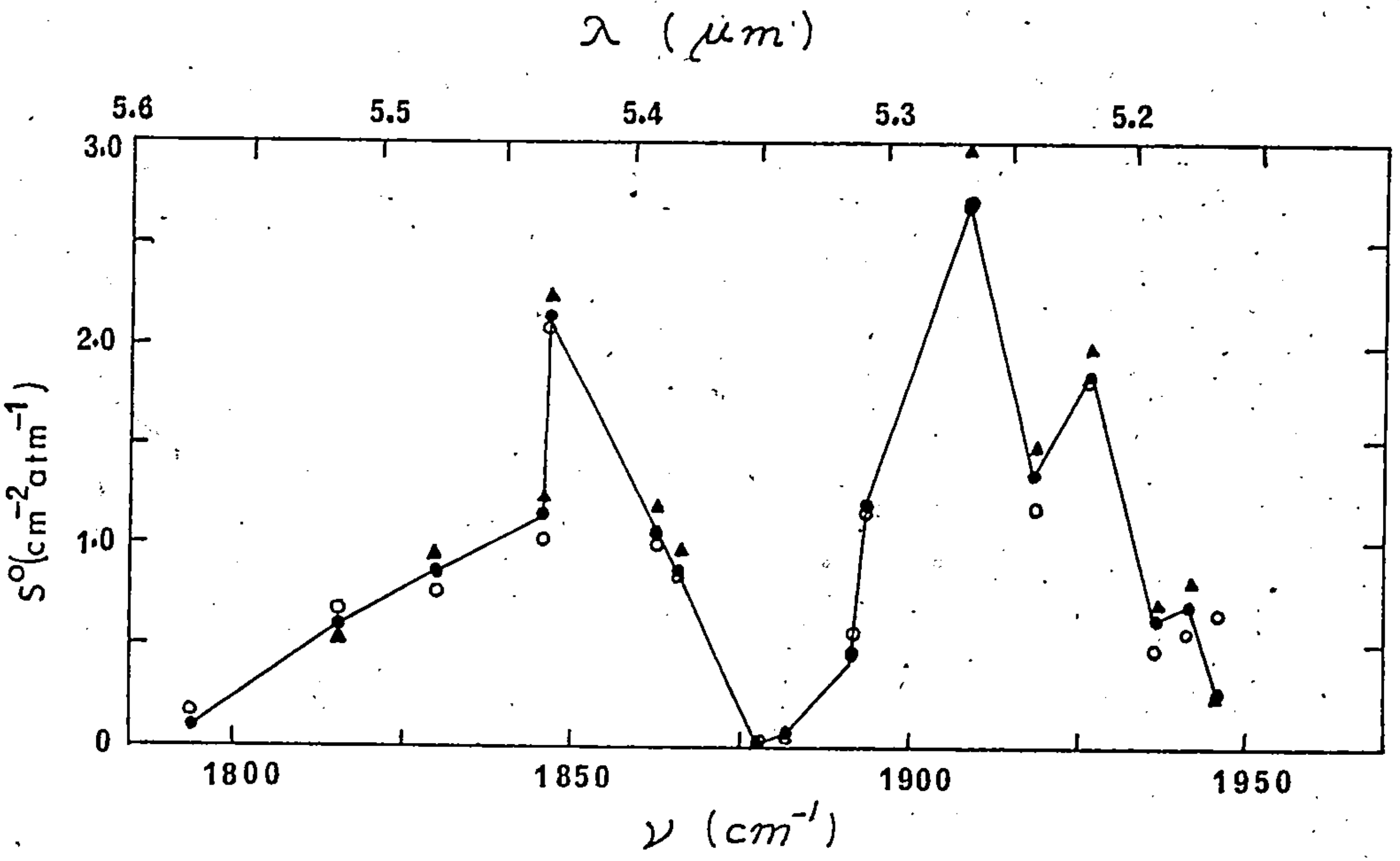

Figure 5.3 NO strengths at 300K. The solid line is based on suitably normalized values from Johns[58]. Present data points are represented by O; those of Abels and Shaw[59] by ▲.

TABLE 5.1 Different $\Delta\nu_n$ Values Between Selected CO Laser Lines and the Nearest NO line (in cm^{-1})

CO line[13] (cm^{-1})	NO line	Hakuta Vehara[57] (obs.)	Johns (calc.)[a] $\Delta\nu_n$ [58]	This work (obs.) $\lvert\Delta\nu_n\rvert$
1935.4818	$R(18.5)_{3/2}$	--	-.016	0.014
1931.6929	$R(17.5)_{1/2}$	--	-0.037	0.061
1927.2959	$R(15.5)_{3/2}$	--	+0.019	0.045
1917.8611	$R(12.5)_{1/2}$	--	-0.008	0.032
1909.8776	$R(9.5)_{3/2}$	--	+0.094	0.074
1900.0427	$R(6.5)_{1/2}$	--	-0.034	0.042
1884.3492	$R(1.5)_{1/2}$	--	+0.049	0.044
1884.3492	$R(1.5)_{3/2}$	0.0280[b]	+0.026	0.026
1874.4517	$Q(9.5)_{3/2}$	--	+0.026	0.041
1870.6135	$Q(17.5)_{3/2}$	--	-0.072	0.077
1863.6344	$P(3.5)_{3/2}$	0.0484[b]	-0.049	0.047
1860.1468	$P(4.5)_{3/2}$	0.0274[b]	+0.028	0.04
1856.4449	$P(5.5)_{3/2}$	--	-0.074	0.072
1842.8159	$P(9.5)_{1/2}$	--	-0.115	0.079
1841.8411	$P(9.5)_{3/2}$	--	+0.065	0.061
1830.4125	$P(12.5)_{3/2}$	--	+0.048	0.052
1812.7522	$P(17.5)_{1/2}$	--	+ .116	0.076
1794.4241	$P(21.5)_{3/2}$	--	+0.064	0.061

---

[a] The calculated difference is for the average value of the two Λ - doubled components.

[b] Measurements obtained from laser magnetic resonance spectroscopy.

TABLE 5.2 Experimental Halfwidths (HWHM) γ_L^o at 300°K(in cm^{-1} atm^{-1})

NO line	Abels and Shaw [59]	Richton [60]	Present work (i)	Present work (ii)
$R(18.5)_{3/2}$	0.050		0.053	0.055
$R(17.5)_{1/2}$	0.041		0.051	0.063
$R(15.5)_{3/2}$	0.056		0.048	0.065
$R(12.5)_{1/2}$	0.058		0.047	0.014
$R(9.5)_{3/2}$	0.058		0.054	0.043
$R(6.5)_{1/2}$	0.058	0.051[a]	0.050	0.066
$R(1.5)_{1/2}$	--	0.058[a]	0.050	0.052
$R(1.5)_{3/2}$	--		0.050	0.052
$Q(9.5)_{3/2}$	--		0.050	0.062
$Q(17.5)_{3/2}$	--		0.054	0.066
$P(3.5)_{3/2}$	0.055		0.050	0.05
$P(4.5)_{3/2}$	0.059		0.051	0.065
$P(5.5)_{3/2}$	0.058		0.049	0.045
$P(9.5)_{1/2}$	0.058		0.052	0.062
$P(9.5)_{3/2}$	0.059		0.05	0.050
$P(12.5)_{3/2}$	0.057		0.05	0.061
$P(17.5)_{1/2}$	0.061		0.05	0.062
$P(21.5)_{3/2}$	--		0.049	0.051

[a] Assuming the values in Ref.[60]are quoted for the full widths.

TABLE 5.3 Band Strength at 273°K (in cm^{-2} atm^{-1})

Investigator(s)	Band Strength cm^{-2} atm^{-1}	
Havens (1938)	121	
Dinsmore and Crawford (1949)	145	±29
Penner and Weber (1953)	70	±7
Vincent - Geisse (1954)	82	
Schurin and Clough (1963)	111	±7
James (1964)	138	±6
Breeze and Ferriso (1964)	76	±7
Fukuda (1965)	70	-77
Ford and Shaw (1965)	115	±9
Abels and Shaw (1966)[59]	122	±6
Varanasi and Penner (1967)[61]	128	±10
Present Study (1976)	124	±9

Note: The first nine values are taken from Varanasi and Penner [61] and are referenced therein.

CHAPTER 6

RESONANCE ABSORPTION MEASUREMENTS
WITH TUNABLE SEMICONDUCTOR DIODE LASERS:
HIGH RESOLUTION SPECTROSCOPIC TECHNIQUE

6.1 Introduction

The development of tunable lasers with emission between 1 and 30 micrometers has provided spectroscopists with much higher resolution than has been possible in the infrared "fingerprint" region, which is rich in characteristic molecular vibration-rotation lines.

This Chapter describes a developed technique for accurate frequency measurements. Over 100 lines in the ν_3 band of ozone have been measured. These measurements, taken with a laser absorption spectrometer based on a tunable semiconductor diode laser, are accurate within 3-10 MHz. Throughout this series of measurements, only those ozone lines that are important for monitoring instruments based on CO_2 lasers, are determined. Hence, measurements of the frequencies, of those reasonably strong ozone lines that lie within 6 GHz of the laser lines in the 9.4 μm region, have been made. These laser lines include most of the $^{12}C^{16}O_2$ lines and, in addition, selected isotopic and sequence lines, particularly those in close coincidence (<300 MHz) with ozone lines. Diode lasers have been used previously to measure some individual absorption lines with accuracies of 15 MHz [62] and to analyze absorption bands with much reduced accuracies [63].

However, this is one of the first reported measurements over an entire absorption band using the full resolution of the tunable diode laser.

Thus far, detection of ozone based on CO_2 lasers is discussed in Chapter 4. Such lasers are suitable if long pathlength propagation through the atmosphere is employed. For short pathlengths or for point monitoring of ozone (as will be described in next chapters), tunable diode lasers possess many advantages. For example, a tunable diode laser does not have to rely on chance coincidences between discrete laser lines and target gas absorption lines. An appropriate diode laser can be tuned to the line center of any strong ozone line and to a wavelength region that avoids interference from other atmospheric species, particularly CO_2 and water vapor (instruments based on CO_2 lasers usually probe the atmosphere at several different frequencies in order to allow for interfering species).

6.2 Experimental Method

Figure 6.1 is a schematic diagram of the laser absorption spectrometer. A PbSnSe diode (Laser Analytics, Inc.) is mounted on the tip of a cold head, which is cooled by a closed-cycle He refrigerator. The diode temperature, which determines the approximate laser emission wavelength, can be set and controlled accurately in the 10-70° K range (employing the technique described in Chapter 2). Fine tuning of the wavelength is obtained by varying the diode current. A 1030-1070 cm^{-1} range was readily available from the diode laser used in the present measurements. The laser output is collected by a 5 cm focal length lens, then chopped at 150 Hz by a mechanical chopper, and finally focused into the 5 m base-pathlength multiple traversal (White) cell (described in Chapter 4). The output beam from the White cell passes through the 0.5 m spectrometer (to separate the longitudinal modes of the diode) and is then focused onto a HgCdTe, LN_2 cooled, detector. A PAR-Lock-in Amplifier Model 126 and an HP (X-Y) recorder model 74004B are used to record the laser power as a function of diode current. As indicated in Fig. 6.1, a germanium etalon (described in Sec. 6.3) can be inserted in the laser beam to provide a series of wavelength calibration fringes. There is also a provision for using the CO_2 Molectron laser discharge tube in the laser beam. This allows one to use gain measurements on selected CO_2 sequence lines [64], for example, as a method of obtaining additional reference lines.

Generally, an optical pathlength of 300 m in the White cell was used. Although not essential, such a long pathlength allows the use of low concentrations of ozone. Ozone, generated by flowing air through a simple UV ozone generator, was introduced into the White cell at a reduced pressure (∿ 3 Torr). The ozone concentration in the cell was estimated to be 10 ppm, based on the measured absorption of the strong ozone lines. The diode laser beam passes through this mixture of ozone and air in the White cell, through the 0.5 m scanning spectrometer, and finally onto the detector. The spectrometer serves two functions. Initially, it is used to select a single diode mode in the wavelength region of interest. For example, the spectrometer is set to pass ir radiation at 1053.9 cm^{-1} [i.e., near the P(12) CO_2 laser line]. The diode temperature and current are then varied until maximum detector output is achieved. Finally, a recording is made of absorption vs diode laser current in this wavelength region. The spectrometer now acts as a filter to reject any undesirable laser modes that may be present (these are generally separated by at least 2 cm^{-1} and, therefore, are easily rejected by a 0.5 m spectrometer).

It is easy to produce high-resolution recordings with a good diode laser. The main problem in high-resolution diode-laser spectroscopy is the accurate calibration of the wavelength scale. The usual procedure is to measure the separation between an unknown absorption line and a known reference line [62, 63]. Fortunately, CO_2 provides numerous reference lines in the 9 μm wavelength region, and these have been measured with extremely high accuracy [65]. The upper traces in Fig. 6.2 show the P(12) CO_2 reference line together with ozone lines obtained by adding a trace of CO_2 to the air-ozone mixture entering the White cell. The high sensitivity of the apparatus also enables one to use isotopic variation of CO_2 to provide additional reference lines. Both the $^{13}C^{16}O_2$ and $^{16}O^{12}C^{18}O$ forms of CO_2 can easily be detected in absorption using a 300 m pathlength in naturally occurring CO_2 (∿ 5 Torr total pressure of CO_2). The frequencies of these isotopic laser lines have been measured to high accuracy by Freed et al. [66, 67]. In addition, the CO_2 Molectron discharge has been employed to generate the CO_2 sequence lines [68] as further references. As a result, it was very easy to find a CO_2 reference line within 0.4 cm^{-1} of any ozone line.

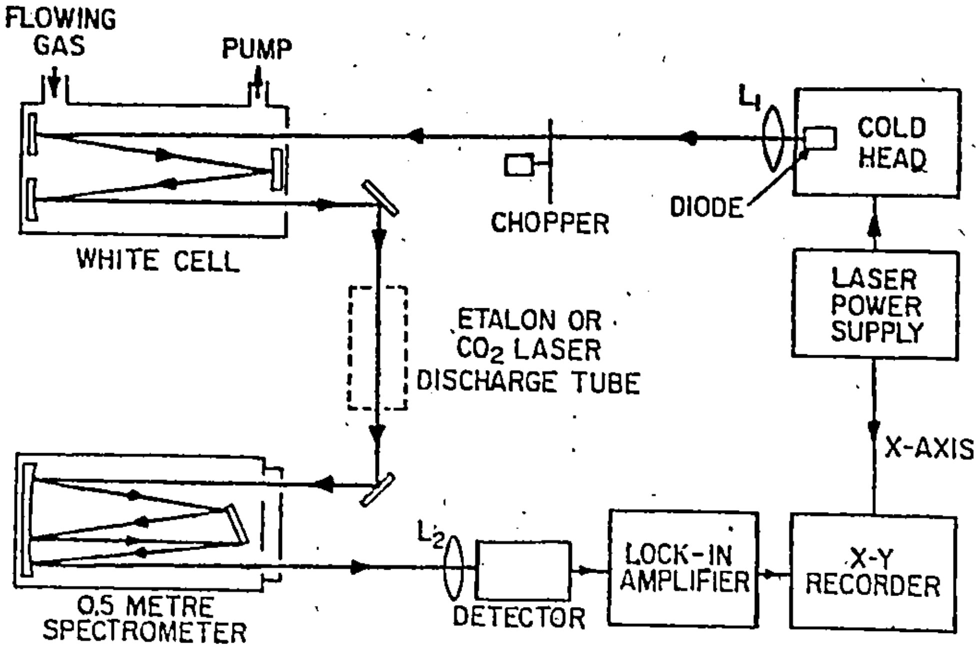

Figure 6.1 Schematic diagram of laser absorption spectrometer (LAS). L_1 and L_2 are the laser output and detector input lenses, respectively.

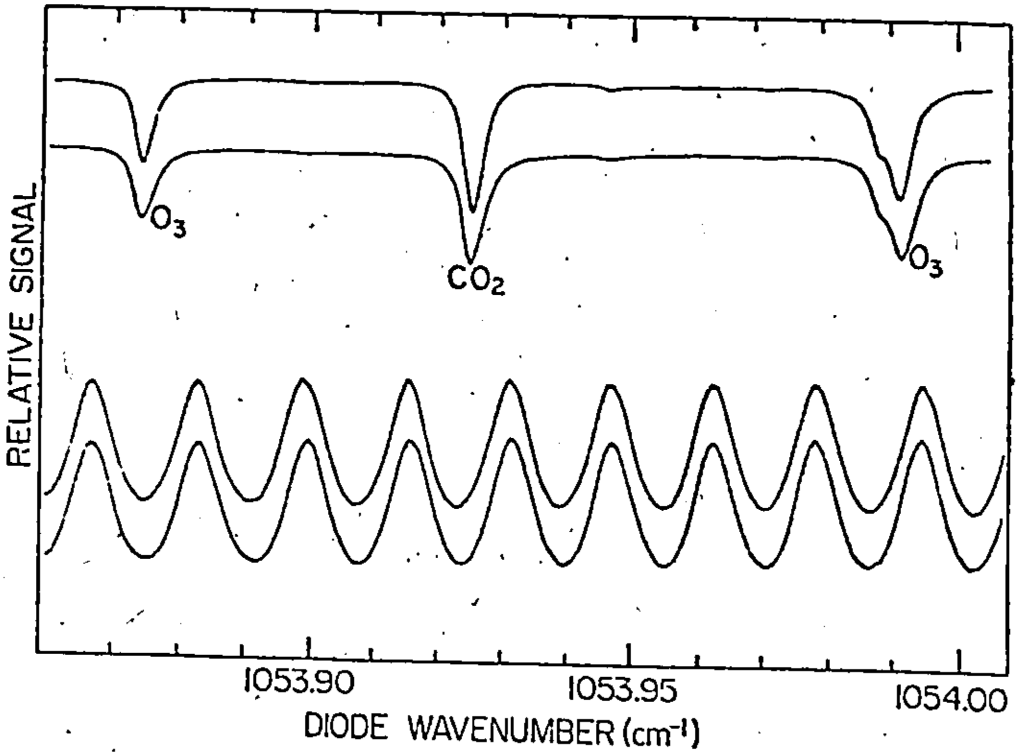

Figure 6.2 Typical example of data taken with the tunable diode laser. For the upper scans, a mixture of 10 ppm ozone in air, together with a trace of CO_2, flows at 3Torr total pressure through the White cell (300 m pathlength). The lower scans show reference fringes obtained with a germanium etalon.

6.3 Accuracy of Measurements

The final step in determining the accurate wavenumber of an ozone line, from data such as shown in Fig. 6.2, is to measure its separation from the reference CO_2 line. For this, an uncoated solid germanium etalon was employed, this solid germanium was nominally 7.650 cm long with a finesse of approximately 3. The etalon was placed in the diode laser beam and provided claibration fringes as shown at the bottom of Fig. 6.2. The separation between a pair of absorption lines was measured by counting the number of etalon fringes. The main aim was to measure the ozone line frequencies to an accuracy of better than 10 MHz, which corresponds to less than two hundredths of an etalon fringe. Care in etalon stabilization and systematic checking of the apparatus were, therefore, required.

First the stability of the laser, detector, and X-Y recorder were evaluated by comparing many successive traces of the type shown at the top of Fig. 6.2 or in Fig. 6.3. A comparison of the positions of the absorption lines on successive traces showed that the maximum uncertainty in the line was less than 3 MHz over a period of about an hour. Chapter 2 contains a different experiment to evaluate the laser stability (see Fig. 2.11). Next, the etalon stability was checked. Initially, it was found that thermal changes cause the fringes to drift as much as half a fringe (i.e., 240 MHz) from scan-to-scan. This corresponds to a 0.08°K temperature change, based on calculations using the data in Edwin et al. [69]. Consequently, the etalon was enclosed within a heavy copper cylinder whose temperature was stabilized by flowing water from a temperature controller through the cylinder walls. This resulted in a random shift of ∿ 0.05 fringes in periods of up to an hour, corresponding to the average etalon temperature remaining constant to better than 0.008° K. The very good reproducibility enabled the measurement of absorption lines and then etalon fringes on successive scans with negligible loss of accuracy. Figure 6.3 illustrates the scan of a reference CO_2 line in gain, an ozone absorption line, and the etalon fringes, using a single diode-laser beam. Note that the use of successive scans enables the placement of the etalon in the diode-laser beam before it enters the spectrometer. Placing the etalon after the spectrometer in a two-beam system can lead to errors due to a changing angle of incidence at the etalon as the diode wavelength is changed [62, 70]. A recent publication [71] describes a technique for the simultaneous recording of both the spectrum and the etalon fringes. This technique, which avoids errors due to changing angle of incidence, requires additional instrumentation but does not require such a high degree of stability from scan-to-scan.

The usual measurement procedure was to take several recorder scans with ozone or CO_2 in the White cell, then several scans with the cell evacuated and the etalon in the beam. Finally, the initial scans were repeated as a check of stability. The scans were carefully measured by hand, with an estimated accuracy of 0.01-0.02 fringes (depending on the quality of the lines). This accuracy is based on the reproducibility of many successive measurements. To check for systematic errors, initial series of measurements on CO_2 lines of known separation are made. The results of these measurements are given in Table 6.1. The etalon fringe separation [0.016271 (3) cm^{-1}] was calibrated by measuring the number of fringes between the P(16) and P(14) laser lines of $^{12}C^{16}O_2$ using a single diode-laser mode. The agreement between the present measurements and the values calculated from heterodyne data is very good, particularly as the available frequency measurements on the $^{13}C^{16}O_2$ isotope lines and the 00^o2 sequence lines may be in error by a few megahertz [66, 68]. Based on the above agreement and on the reproducibility of the measurements, the accuracy was estimated to range from ∿ 3 MHz for very closely separated lines to ∿ 10 MHz for absorption lines separated by about 25 fringes (0.4 cm^{-1}).

It is worthwhile to compare the accuracies using the present relatively simple technique with those obtained using laser heterodyne techniques. Accuracies of ± 15 MHz and ± 3 MHz have been achieved employing tunable lasers [72] and CO_2 lasers [73], respectively, to determine spectral line centers. The accuracy reported in this work compares favorably with these values. Note that the heterodyne techniques are limited to measurements of absorption lines that lie within a detector bandwidth (∿ 2 GHz) of the reference CO_2 lines [72, 73]. No such limitation exists with the present method.

The accuracy of the present measurements is still limited by residual drifts of the etalon fringes. Better temperature stabilization or the use of an air-spaced actively-locked etalon will remove this limitation. The estimated accuracy of a tunable diode laser, in combination with a stabilized etalon, would then be limited simply by the accuracy with which one can judge the line center (1-3 MHz). Finally, it should be possible to automate much of the measurement procedure.

6.4 Results and Discussions

The diode laser used in the present work was operated in the 1030-1070 cm^{-1} range. By using regular and isotopic forms of CO_2 as references, frequency measurements of over 100 ozone lines in this wavenumber region were made. These lines are more than sufficient for a detailed band analysis of the ν_3 band of ozone; such an analysis is underway but it is outside the scope of this thesis. Table 6.2 is a comprehensive list of relatively strong ozone lines that lie close to the important 9.4 μm laser lines of $^{12}C^{16}O_2$, to other CO_2 isotopes, and to the CO_2 sequence lines. These measured lines all lie within 0.4 cm^{-1} of the appropriate CO_2 lines and usually have intensities greater than 1×10^{-21} $mole.^{-1}$ cm^{-1}. The present technique enabled the measurements of approximately 55% of the lines satisfying these conditions at the listed CO_2 reference lines. The balance of the lines was either overlapped, or else the laser power was too low for carrying out accurate measurements. The listed line strengths are taken from Barbe et al. [74]. The measured wavenumbers are in good agreement with Barbe et al. when their experimental uncertainties (up to 0.003 cm^{-1}) are taken into account.

In the regions covered by the diode laser, it was found that all ozone lines with intensities greater than 1 x 10^{-21} $mole.^{-1}$ cm^{-1} (i.e., lines within 1/30th of the line strength of the strongest lines) could be identified with ν_3 lines listed by Barbe et al. There is no evidence of hot band or isotope lines with significant line strength. This observation agrees with the results of Barbe et al. [74].

The data in Table 6.2 is essential for comparing experimental and theoretical estimates of ozone absorption as a function of pressure (as described in Chapter 4), [75 - 77]. The wavenumbers in this table are also sufficiently accurate to be used with solar heterodyne radiometers in the measurement of both tropospheric and stratospheric ozone. Airborne instruments employing differential absorption based on CO_2 lasers require a close coincidence between the ozone line and the CO_2 laser line. Such CO_2 lines, which are indicated by an asterisk in Table 6.2, include various isotope and sequence lines. Despite the additional compexity in obtaining lasing on the rare isotope or sequence lines of CO_2, these may prove more practical for stratospheric monitoring of ozone, as they suffer negligible absorption by atmospheric CO_2.

The present sensitivity depends upon the accuracy of the reference lines. All the laser lines have been measured with accuracy better than 1 MHz, however, some absorption lines of particular gases has been measured with moderate accuracies. These measured lines could be used as reference lines to measure the inaccurate absorption lines which are in coincidences. Table 6.3 contains a listing of wavenumbers, and the estimated accuracy, that can be used as reference lines [78].

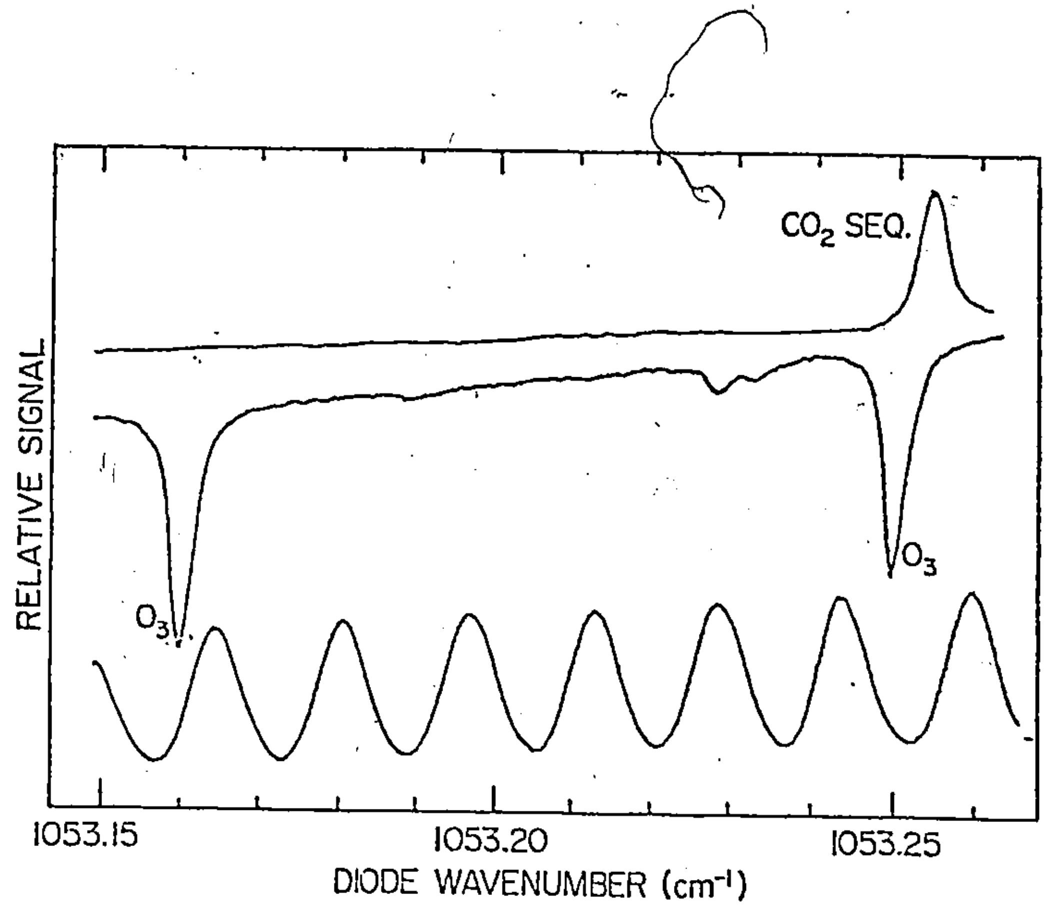

Figure 6.3 Represenţive diode scans. For these, the diode laser beam is passed through a CO_2 discharge, through an ozone-air mixture in the White cell, and finally through the germanium etalon.

TABLE 6.1 Measured Reference CO_2 Line Separation

CO_2 Lines	(A) Wavenumber Separation	No. Of Fringes (Our Work)	(B) Wavenumber Separation (Our Work)	DIFF. (A) – (B) Converted to MHz
P(28) 636 - P(30) Seq	.00425 (Ref.63,66)	.257	.00418	-2
P(20) 626 - P(31) 628	.405112 (Ref.62,63)	24.888	.404960	-4
P(28) 636 - P(30) 626	.267057 (Ref.62,63)	16.416	.267111	2
P(16) 626 - P(14) 626	1.754263 (Ref.62)	107.813	1.754263	0

TABLE 6.2 Measured Ozone Line Wavenumbers.

CO_2 REFERENCE LINE	OZONE LINE UPPER STATE			LOWER STATE			(A) CALC. 1/CM (REF.74)	ABS.INT. E-21 MOL.-CM (REF.74)	(B) MEAS. 1/CM (OUR WORK)	
R(4)626	39	3	36	38	3	35	1067.7369	5.18	1067.73480	
P(13)628	39	0	39	38	0	38	1062.6657	6.69	1062.66580	*
	38	8	31	37	8	30	1062.5998	2.49	1062.59998	
	36	7	30	35	7	29	1062.5905	4.05	1062.59036	
	32	4	29	31	4	28	1062.5818	10.55	1062.58266	
	32	3	30	31	3	29	1062.5778	11.82	1062.57773	
	33	1	32	32	1	31	1062.5313	11.86	1062.53142	
	34	2	33	33	2	32	1062.5252	10.63	1062.52614	
	29	2	27	28	2	26	1062.4932	16.39	1062.49392	
	40	9	32	39	9	31	1062.4224	1.44	1062.42053	
	31	4	27	30	4	26	1062.3895	11.56	1062.38968	
P(2)626	38	1	38	37	1	37	1062.3883	7.56	1062.38916	
	29	3	26	28	3	25	1062.2595	15.35	1062.25912	
	37	8	29	36	8	28	1062.1635	2.81	1062.16516	*
P(4)626	32	7	26	31	7	25	1060.6948	6.16	1060.69676	
	28	3	26	27	3	25	1060.6678	16.70	1060.66742	
	29	5	24	28	5	23	1060.5430	11.88	1060.54217	
P(17)628	27	5	22	26	5	21	1059.4495	13.79	1059.45283	
	29	0	29	28	0	28	1059.4497	18.49	1059.45283	
	25	1	24	24	1	23	1059.4327	22.84	1059.43514	
	26	4	23	25	4	22	1059.3880	17.12	1059.39049	*
	28	6	23	27	6	22	1059.3682	10.70	1059.37069	
P(6)626	23	2	21	22	2	20	1059.0351	24.54	1059.03409	
	28	1	28	27	1	27	1059.0109	19.92	1059.01115	
	25	4	21	24	4	20	1058.8898	18.19	1058.88916	
	26	5	22	25	5	21	1058.8820	14.73	1058.88153	
	30	8	23	29	8	22	1058.8669	5.72	1058.86700	
	27	6	21	26	6	20	1058.8293	11.48	1058.82874	
P(8)626	22	3	20	21	3	19	1057.3682	23.78	1057.36759	
	27	8	19	26	8	18	1057.3186	7.14	1057.31812	
	24	1	24	23	1	23	1057.2946	25.53	1057.29463	*
	31	10	21	30	10	20	1057.2293	2.77	1057.22781	
	22	2	21	21	2	20	1057.1907	25.99	1057.18828	
	23	5	18	22	5	17	1057.1631	17.32	1057.16175	
	24	6	19	23	6	18	1057.1557	13.69	1057.15467	
	34	11	24	33	11	23	1057.1308	1.35	1057.12353	
	22	4	19	21	4	18	1057.0529	21.09	1057.05130	
	21	3	18	20	3	17	1057.0421	24.66	1057.04049	
	25	7	18	24	7	17	1057.0350	10.41	1057.03416	
	23	0	23	22	0	22	1056.9442	26.85	1056.94258	

TABLE 6.2 Continued.

CO$_2$ REFERENCE LINE	OZONE LINE UPPER STATE			LOWER STATE			(A) CALC. 1/CM (REF.74)	ABS.INT. E-21 / MOL.-CM (REF.74)	(B) MEAS. 1/CM (OUR WORK)	
P(10)626	19	3	16	18	3	15	1055.7063	26.07	1055.70533	
	24	8	17	23	8	16	1055.6843	8.43	1055.68380	
	21	6	15	20	6	14	1055.3959	15.39	1055.39541	
	20	1	20	19	1	19	1055.3509	29.89	1055.35027	
	20	5	16	19	5	15	1055.3515	19.16	1055.35027	
	22	7	16	21	7	15	1055.3224	11.87	1055.32162	
	25	9	16	24	9	15	1055.3107	5.94	1055.30959	
P(12)626	25	10	15	24	10	14	1054.1965	4.15	1054.19462	
	19	6	13	18	6	12	1054.1729	16.02	1054.17213	
	20	7	14	19	7	13	1054.1303	12.48	1054.12951	
	18	5	14	17	5	13	1054.1103	16.99	1054.11298	
	17	0	17	16	0	16	1053.9664	31.66	1053.96577	
	21	8	13	20	8	12	1053.9606	9.33	1053.96025	
	17	4	13	16	4	12	1053.9203	23.50	1053.91944	*
P(24)628	17	5	12	16	5	11	1053.4580	19.84	1053.45470	*
P(9)SEQ	16	4	15	15	4	12	1053.2595	23.44	1053.25863	*
	22	12	11	21	12	10	1053.2498	1.35	1053.23969	
	26	11	16	25	11	15	1053.2418	2.45	1053.23570	
	16	1	16	15	1	15	1053.1685	31.55	1053.16756	
P(25)628	16	5	12	15	5	11	1052.8062	19.69	1052.80533	
	19	8	11	18	8	10	1052.7600	9.55	1052.75973	
	25	11	14	24	11	13	1052.7236	2.57	1052.71861	
	15	4	11	14	4	10	1052.5947	23.15	1052.59424	*
	22	10	13	21	10	12	1052.5618	4.62	1052.55940	
P(14)626	14	2	13	13	2	12	1052.3926	28.92	1052.39215	
	13	1	12	12	1	11	1052.3093	29.85	1052.30882	
	17	7	10	16	7	9	1052.2641	26.11	1052.26386	
	16	6	11	15	6	10	1052.2614	12.55	1052.26386	
	14	3	12	13	3	11	1052.2651	15.89	1052.26386	
	24	11	14	23	11	13	1052.1985	2.67	1052.19472	*
	18	8	11	17	8	10	1052.1439	9.52	1052.14361	
	15	5	10	14	5	9	1052.1438	19.35	1052.14361	
	13	2	11	12	2	10	1052.0436	28.17	1052.04254	
	21	10	11	20	10	11	1051.9984	4.70	1051.99680	
	14	1	13	13	1	13	1051.9856	30.96	1051.98448	
P(27)628	15	7	8	14	7	7	1050.9664	11.86	1050.96581	
	14	6	9	13	6	8	1050.9337	14.88	1050.93297	
	12	3	10	11	3	9	1050.8780	24.37	1050.87740	

TABLE 6.2 Continued.

CO_2 REFERENCE LINE	OZONE LINE UPPER STATE			LOWER STATE			(A) CALC. 1/CM (REF.74)	ABS.INT. E-21 MOL.-CM (REF.74)	(B) MEAS. 1/CM (OUR WORK)	
P(27)628	11	1	10	10	1	9	1050.8642	27.75	1050.86388	
	13	5	8	12	5	7	1050.7880	17.96	1050.78727	
	12	1	12	11	1	11	1050.7412	29.27	1050.74042	
P(16)626	17	9	8	16	9	7	1050.6560	6.65	1050.65565	
	11	2	9	10	2	8	1050.5456	25.95	1050.54453	
	12	4	9	11	4	8	1050.5329	20.80	1050.53194	
	11	0	11	10	0	10	1050.3859	28.48	1050.38494	
P(18)626	12	7	6	11	7	5	1048.9372	9.40	1048.93845	
	18	11	8	17	11	7	1048.9055	2.70	1048.90306	
	13	8	5	12	8	4	1048.8999	7.28	1048.89893	
	11	6	5	10	6	4	1048.8609	11.68	1048.86093	
	14	9	6	13	9	5	1048.7350	5.41	1048.73481	
	9	3	6	8	3	5	1048.7212	19.60	1048.72083	
	10	5	6	9	5	5	1048.6742	13.93	1048.67385	*
P(20)626	7	4	3	6	4	2	1046.8899	11.06	1046.88950	
	10	8	3	9	8	2	1046.8156	3.73	1046.81540	
	9	7	2	8	7	1	1046.8062	4.78	1046.80609	
	11	9	2	10	9	1	1046.7105	2.80	1046.71030	
	6	2	5	5	2	4	1046.6928	15.35	1046.69215	
	8	6	3	7	6	2	1046.6876	5.91	1046.68765	
	6	1	6	5	1	5	1046.6457	17.50	1046.64504	
R(44)636	5	4	1	4	4	0	1045.3567	4.42	1045.35660	*
P(22)626	4	1	4	3	1	3	1045.1643	11.72	1045.16408	
	4	2	3	3	2	2	1045.1408	8.96	1045.14060	
R(36)636	6	3	2	5	3	3	1041.4876	8.81	1041.48675	*
P(26)626	7	3	4	7	3	5	1041.3418	6.10	1041.34126	
	8	3	6	8	3	5	1041.2484	5.20	1041.24775	
P(30)626	16	8	9	16	8	8	1037.4342	5.50	1037.43452	*
R(28)636	4	3	2	5	3	3	1037.3419	8.55	1037.34157	
	20	7	14	20	7	13	1037.3217	3.13	1037.32131	
	12	9	4	12	9	3	1037.3132	9.07	1037.31297	
	23	6	17	23	8	18	1037.2395	1.86	1037.23780	
	17	8	9	17	8	10	1037.2318	4.83	1037.23133	
	13	9	4	13	9	5	1037.1478	7.94	1037.14746	

TABLE 6.2 Continued.

CO_2 REFERENCE LINE	OZONE LINE UPPER STATE			LOWER STATE			(A) CALC. 1/CM (REF.74)	ABS.INT. E-21 / MOL.-CM (REF.74)	(B) MEAS. 1/CM (OUR WORK)
P(29)SEQ	7	1	6	8	1	7	1034.8563	21.69	1034.85583
	7	2	5	8	2	6	1034.8250	19.82	1034.82485
	14	11	4	13	11	3	1034.8175	5.16	1034.81621
	29	7	22	29	7	23	1034.8603	.86	1034.80583
	19	12	7	19	12	8	1034.7898	1.70	1034.78876
	20	12	9	20	12	8	1034.7883	1.43	1034.78876
	18	12	7	18	12	6	1034.7857	2.01	1034.78507
	21	12	9	21	12	10	1034.7811	1.21	1034.78145
	6	5	2	7	5	3	1034.7774	6.83	1034.77711
	16	12	5	16	12	4	1034.7596	2.84	1034.76220
	15	12	3	15	12	4	1034.7371	3.38	1034.73941
	14	12	3	14	12	2	1034.7077	4.05	1034.71101
	13	12	1	13	12	2	1034.6711	4.88	1034.67318

TABLE 6.3 List of Wavenumber Regions Used As Reference, After Cole [78].

Substance and band	Region Covered (cm^{-1})	Estimated Absolute Accuracy (cm^{-1})
CO (2-0)	4350 - 4100	< 0.0002
C_2H_2 ($\nu_1 + \nu_5^1$)	4150 - 4015	0.005
H_2O	4050 - 3480	0.001
HCN (ν_3)	3410 - 3190	0.002
HCI (1-0)	3130 - 2515	0.005
HBr (1-0)	2750 - 2265	0.005
CO_2 (ν_3)	3390 - 2290	0.002
$^{13}CO_2$ (ν_3)	2300 - 2225	0.002
CO (1-0)	2260 - 1990	< 0.0002
DCL (1-0)	2240 - 1890	0.002
DBr (1-0)	1985 - 1630	0.002
HCN ($2\nu_2$)	1505 - 1330	0.005
C_2H_2 ($\nu_4 + \nu_5)^o$	1380 - 1285	0.005
NH_3 (ν_2)	1250 - 705	0.005
HCN (ν_2)	800 - 630	0.005

CHAPTER 7

HIGH SENSITIVITY POINT MONITORING (PM) OF ATMOSPHERIC GASES EMPLOYING TUNABLE DIODE LASERS

7.1 Introduction

Chapters 4 and 5 have been concerned with line-tunable laser sources (CO_2, CO) which were employed to monitor those gases which have absorption lines in close coincidence with the available output wavelength of the lasers [79-82]. Some work on longpath atmospheric absorption has also been reported using tunable diode lasers [10]. Both of these techniques have shown considerable success, but have been somewhat limited in sensitivity. This has resulted in applications being limited to gases which occur naturally at high concentrations. Much greater absorption sensitivities can be attained using acousto-optical techniques [83-85], but the effective pathlength in typical spectrophone cells is less than 1 m. In addition, this approach suffers from interferences from unwanted molecular species, and is somewhat difficult to calibrate [84], [85].

In the present Chapter, a laser absorption spectrometer which combines the sensitivity of the acousto-optical methods with the convenience of direct, longpath optical detection is described. The system is exactly the same one described in Chapter 6. With this system, we can detect absorptions with sensitivity of 3×10^{-8}.

This corresponds to concentrations of 1 part per billion (ppb) of a weakly absorbing molecule such as SO_2 (ν_1 band), or 3×10^{-3} ppb of a strongly absorbing molecule such as CO. This sensitivity, combined with the wavelength tunability of diode lasers, permits trace amounts of almost any gaseous molecular species to be monitored. For example, two diodes have been employed in the present work, which have the capability of detecting ambient levels of many gases commonly found in the atmosphere, such as SO_2, N_2O, H_2O, CO_2 and O_3. Furthermore, the present technique does not suffer from interference from unwanted molecular species, and can be easily calibrated even at the ppb concentration level.

Section 7.2 of this Chapter describes the experimental arrangement, while Section 7.3 explains the modulation techniques used to achieve a high sensitivity. In section 7.4 the applications of the present system to detect O_3, NH_3, and SO_2 in the atmosphere are demonstrated.

7.2 Experimental Apparatus

The apparatus employed is illustrated schematically in Fig. 7.1, and is described in detail in Chapter 6. For point monitoring, two important modifications have been made. In the first modification, in addition to the drive current supplied to the diode, a small high-frequency current modulation is superimposed. This results in a high-frequency modulation (kHz range) of the diode wavelength and it is this modulation which enables us to achieve such high sensitivity. The second modification involves splitting off a portion of the diode laser beam and directing it to a second HgCdTe detector (Detector B in Fig. 7.1). This second beam is used to lock the laser wavelength to the molecular absorption line under investigation. The first diode laser used for the measurements is a $Pb_{1-x}Sn_xSe$ diode supplied by Laser Analytics, (1% Sn) which was selected to give an output covering the range 1050 cm^{-1} to 1150 cm^{-1}, which spans the ν_1 absorption band of SO_2. The second diode is the same one as in Chapter 6 which spans the ν_3 absorption band of O_3.

7.3 Experimental Technique

The first step in attaining the high sensitivity detection of any gas is to determine an operating region in which the laser operates in a single mode, and tunes through several strong absorption lines of the gas under investigation. Accordingly, this gas is placed into the 5 m base White cell if it is available in low concentration (e.g., SO_2 source gas employed was supplied by Matheson with .1 % of SO_2 in dry nitrogen, and ozone which was generated by uv source to obtain ozone with 10 ppm in air). After the gas sample was placed into the laser beam a search was made for strong absorption lines. Using the spectrum available in the literature as a guide, we were able to find several strong lines for each gas. For SO_2, we employed the first diode, a relatively strong concentration of SO_2 is placed in the 5 m White cell, and scanned those wavelength regions covered by the diode laser. The

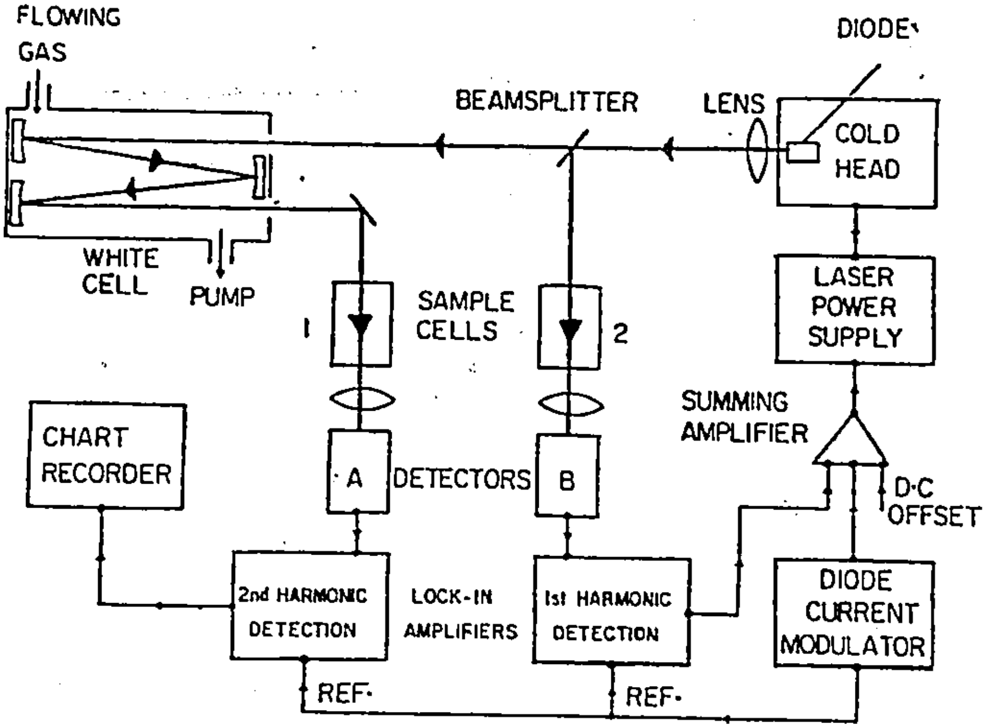

Figure 7.1 Schematic diagram of the Laser Absorption Spectrometer.

gas sample was introduced at a pressure p = 10 Torr and pathlength L = 60 m. This mixture produces ∿80% absorption on the stronger SO_2 lines, as can be seen in Fig. 7.2. The lower trace was obtained from experimental results using conventional detection techniques. The diode laser beam was chopped at 150 Hz and synchronously detected by the HgCdTe detector (A in Fig. 7.1) and a lock-in amplifier. The diode wavelength was tuned over ∿1 cm^{-1} using a combination of temperature and current tuning. Throughout this wavenumber region, the diode was operated in a single mode, thus eliminating the need for a mode-selecting monochromator. The resolution of the diode laser is much less than a Doppler width, but a major problem with all diode-laser spectroscopy is to obtain absolute wavenumber calibration. To some extent we were able to overcome this problem, by using as our reference the accurately-known wavenumbers of several absorption lines of N_2O which lie in this region [26]. We are able to estimate the wavenumbers, ν, of the SO_2 lines in Fig. 7.2 to better than 0.01 cm^{-1}. This enables us to make an accurate comparison with the theoretical predictions of [26] shown in the upper half of Fig. 7.2. In general, the agreement is good, with the predicted wavenumbers rarely being more than 0.01 cm^{-1} different from the experimental measurements. The experimental intensities also agree with the theoretical predictions to better than 20% on the strong lines. Observe, however, that many weak SO_2 absorption lines (a few are indicated by *) which are obtained experimentally, are not predicted from the theoretical compilation. Some of these weak SO_2

lines were confirmed to relate to $^{34}S^{16}O_2$ isotope and the first hot band of $^{32}S^{16}O_2$. This was achieved by using our computer package to generate the whole spectrum of $^{32}S^{16}O_2$ and its isotopic species employing the molecular constants in Ref. [33]. Experimentally (and theoretically), the two strong lines near 1142.0 cm^{-1} were found to be amongst the strongest in the band (indicated by R). They were therefore selected for more detailed study and for SO_2 detection. For NH_3, we employed the same diode laser, which was used in defining SO_2. A 10 cm sample cell containing pure ammonia at pressure $p < 1$ Torr was introduced into the laser beam, and a search was made for strong absorption lines. Using the spectrum compiled by F. W. Taylor [87] as a guide, we were able to find several strong lines near 1140 cm^{-1}, as shown in Fig. 7.3. For this data the diode wavenumber is tuned by varying the current, the laser beam is chopped, and conventional amplitude detection is employed. For O_3, we employed the same diode which was used in ozone high resolution spectroscopy (Chapter 6). We chose to operate the diode laser in the 1052 cm^{-1} region where it was single mode, and tuned through several strong absorption ozone lines. The upper trace of Fig. 7.4 is a scan of a relatively high concentration of ozone (using the same technique as in Chapter 6), taken with the chopper in the laser beam, and employing conventional amplitude detection. The chopper was then removed from the system and a small frequency modulation was superimposed on the diode current ramp. Next, the detector signal is synchronously detected at the modulation frequency. Figure 7.4 (lower scan) shows the recorded second harmonic signal. This second harmonic technique results in a substantial reduction in noise as described by Reid et al. [75], and enables us to detect absorption coefficients with sensitivity as high as 3×10^{-8} m^{-1} [77].

7.4 O_3 Detection and Results

Ambient ozone levels in air are detected by scanning at high sensitivity. For our measurements, air from above the roof of the laboratory building was passed through the White cell at reduced pressure (p = 20 Torr), and the diode laser scanned over the same wavenumber region as in Fig. 7.4. The data is shown in Fig. 7.5 where four strong ozone lines can be clearly seen, as well as several additional lines. The very strong line at 1052.196 cm^{-1} is easily identified as the P(14) line of CO_2. One of the other additional lines is probably the $8_{35} \rightarrow 9_{54}$ line of HDO, listed at 1052.144 cm^{-1} on the AFCRL compilation of [25]. The remaining two lines are caused by some unidentified constituent of the air above our laboratory. Figure 7.5 clearly illustrates one of the problems of using CO_2 lasers for differential absorption measurements to monitor atmospheric ozone. If the P(14) CO_2 line is used as a probe, most of the atmospheric absorption of the laser beam will be caused by the atmospheric CO_2, with only a small contribution from ozone. There can also be additional interferences from HDO, and possibly from the unknown lines (neither O_3 nor HDO) observed near 1052.0 cm^{-1}. Clearly, a complicated calibration procedure is required to account for such interferences.

Our LAS does not suffer from such complications, as the tuning ability of the diode laser enables us to concentrate on those ozone lines which are free from interferences. For example, to monitor ozone in the air, it is sufficient to scan over one isolated ozone line, as shown in Fig. 7.6A. This scan is taken with a 3 s time constant to improve the signal-to-noise ratio. For comparison, we show in Fig. 7.6B the P(14) CO_2 line as observed in air. For the latter, the instrumental sensitivity was reduced by a factor of 20. These lines correspond to A and B in Fig. 7.5. No attempt was made to accurately calibrate the ozone concentrations observed in Fig. 7.5 and 7.6, or to ensure that our samples of air remained uncontaminated by nearby vehicle and air-conditioner exhausts. These scans were simply taken to illustrate the technique and sensitivity. However, one can obtain a reasonable estimate of the ozone concentration by comparing the measured absorption with the known line strength of the observed ozone lines [74]. This procedure gives an ozone concentration of 35 ppb. As a check on this calculation, we compare the measured ozone absorptions directly with the absorption observed on the P(14) CO_2 line. If the atmospheric CO_2 concentration is assumed to be 330 ppm, we estimate that the ozone concentration is 38 ppb, in good agreement with the previous calculation. It follows that the noise level shown in Fig. 7.6 corresponds to ∿0.5 ppb ozone in air.

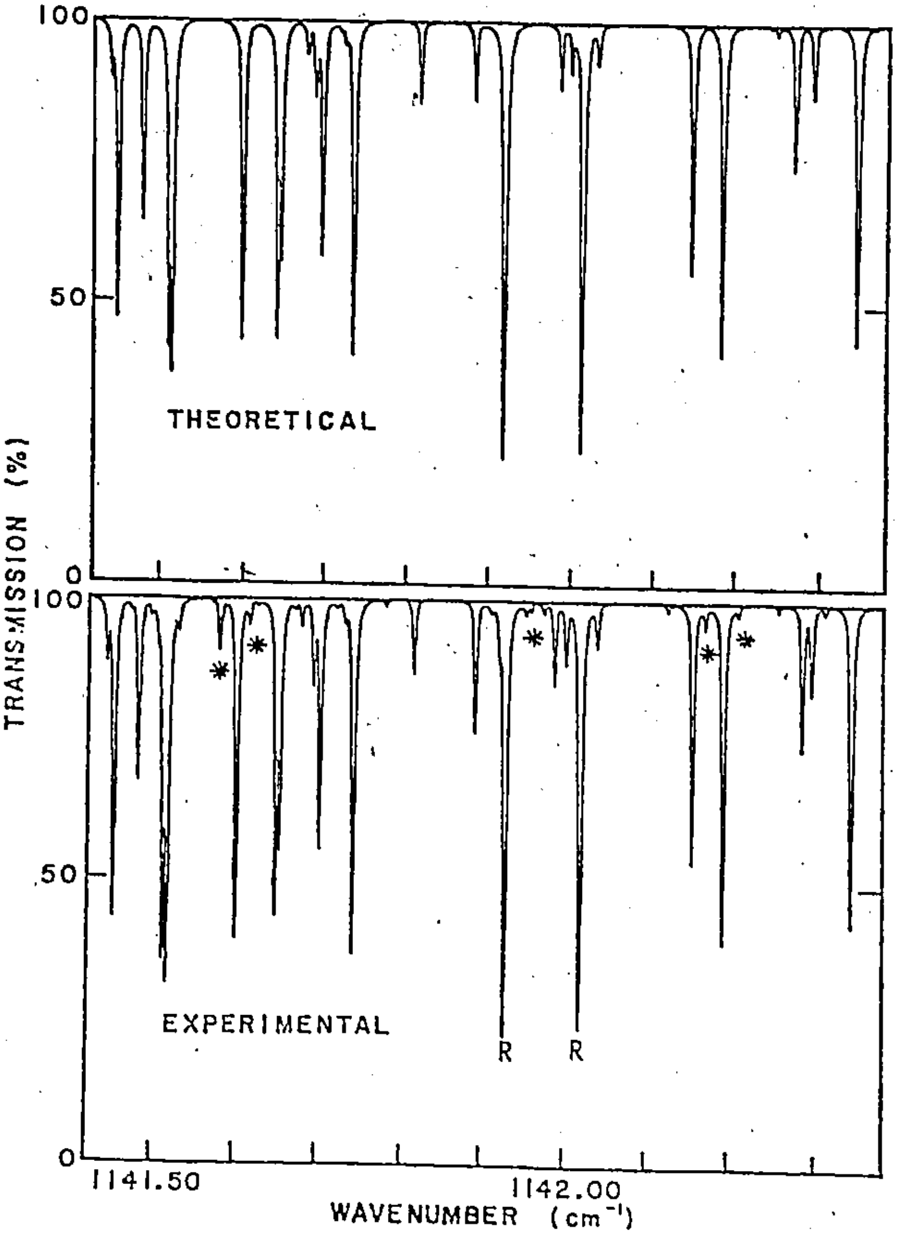

Figure 7.2 Experimental and theoretical transmission spectra for SO_2 in the region 1142 cm^{-1}. A pathlength of 60m is used, with a 1000 ppm mixture of SO_2 in N_2 at a total pressure of 10 Torr. A few of weak absorption lines (marked by *) which are not predicted by the theoretical compilation of [25].

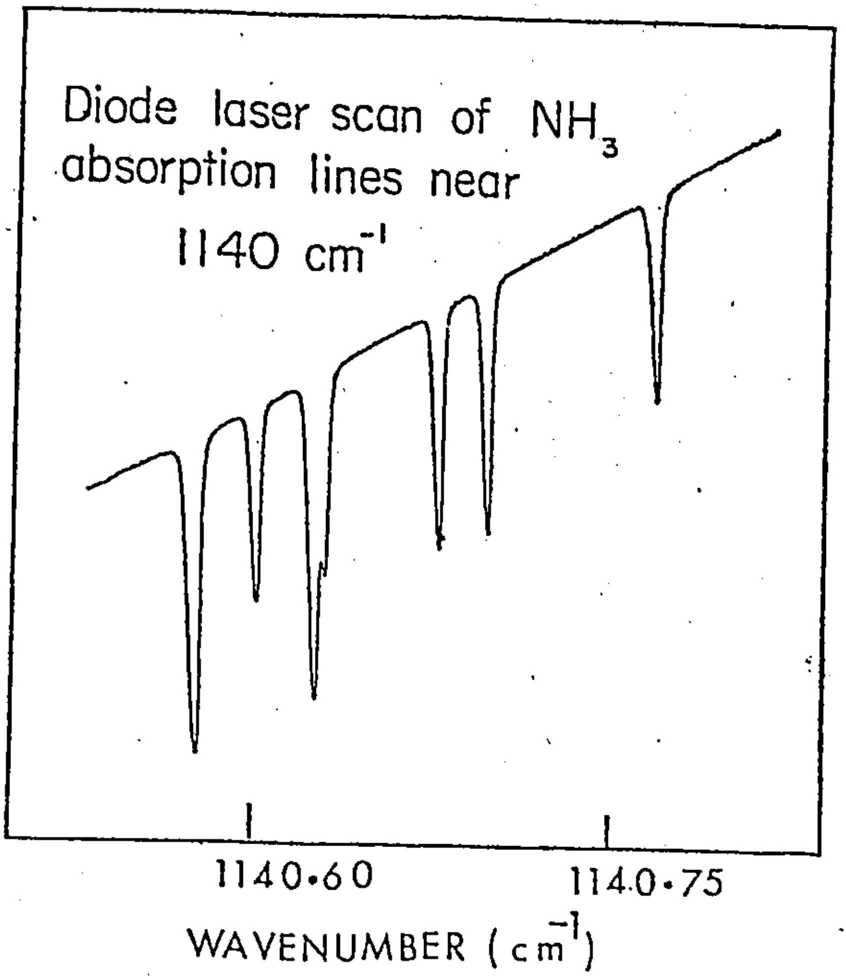

Figure 7.3 Detection of 10 ppb NH_3 in air. A conventional high resolution scan of NH_3 near 1140 cm^{-1} . Pressure is <1Torr, and cell length of 10^3cm are used. These are the same lines used in NH_3 detection in Fig. 7.7.

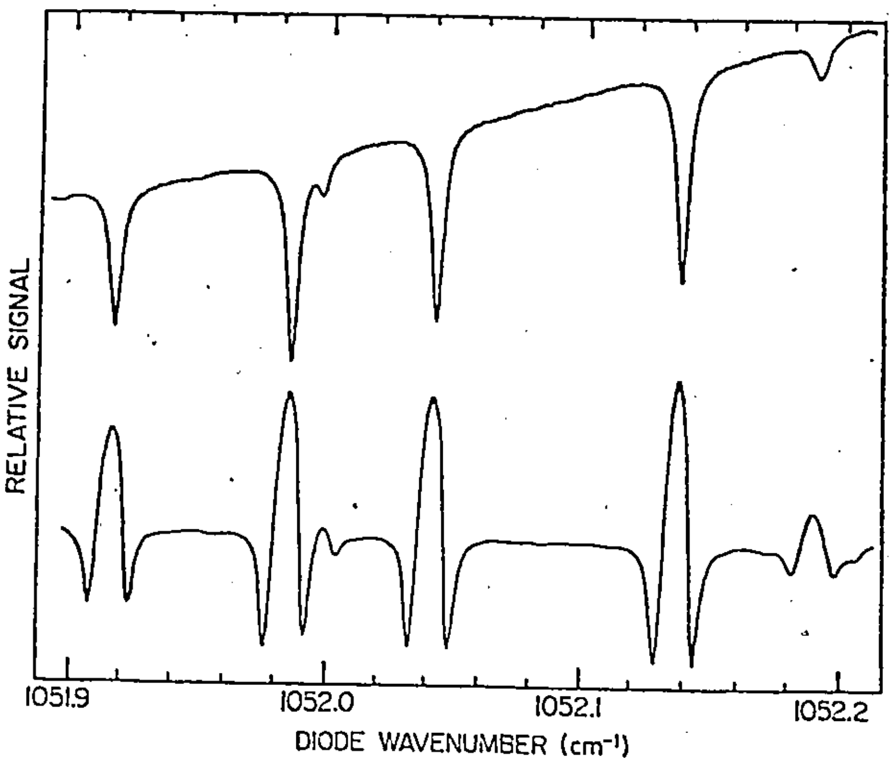

Figure 7.4 High-resolution ozone spectrum near 1052 cm^{-1}. The upper scan is taken with conventional amplitude detection; second harmonic detection is employed for the lower scan. A mixture of 10 ppm ozone in air is flowed through the White cell (240m pathlength) at total pressure of 20Torr.

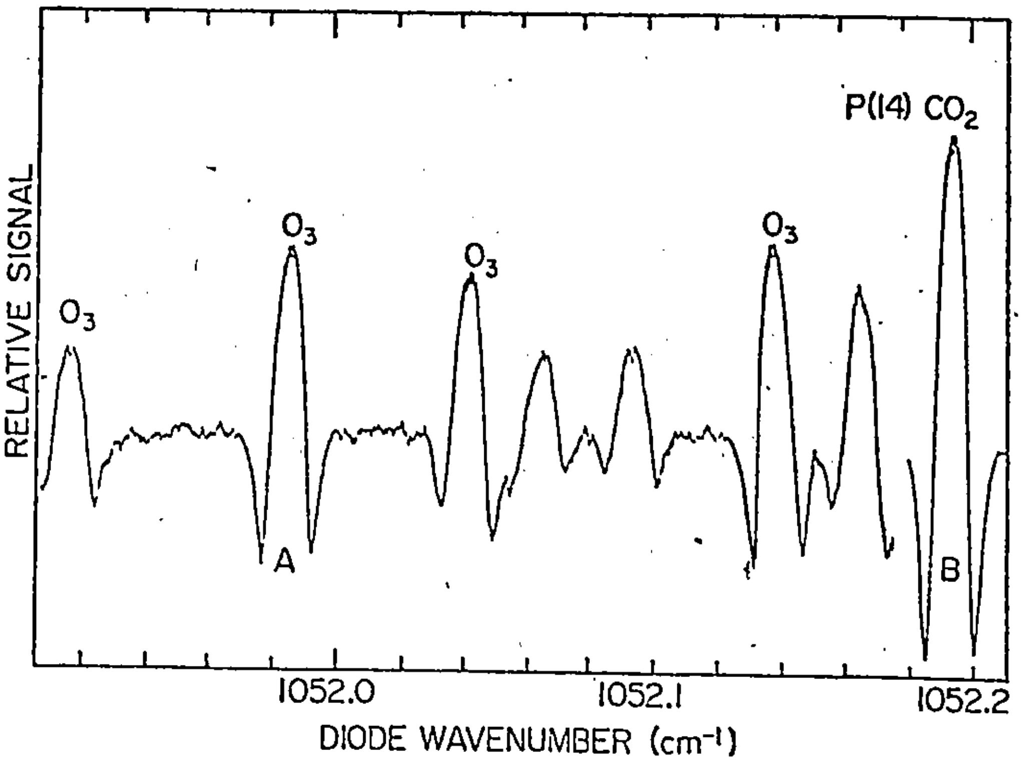

Figure 7.5 Detection of atmospheric ozone. This second harmonic scan is taken over the same wavelength region as in Fig. 7.4 and employed the same pathlength and total pressure. A 1sec time constant is used. The additional lines are described in the text. The estimated ozone concentration is 38ppb. Note that line A and line B are repeated in Fig. 7.6 but in different scale, and the instrumental sensitivity is reduced by a factor of 10 for line B.

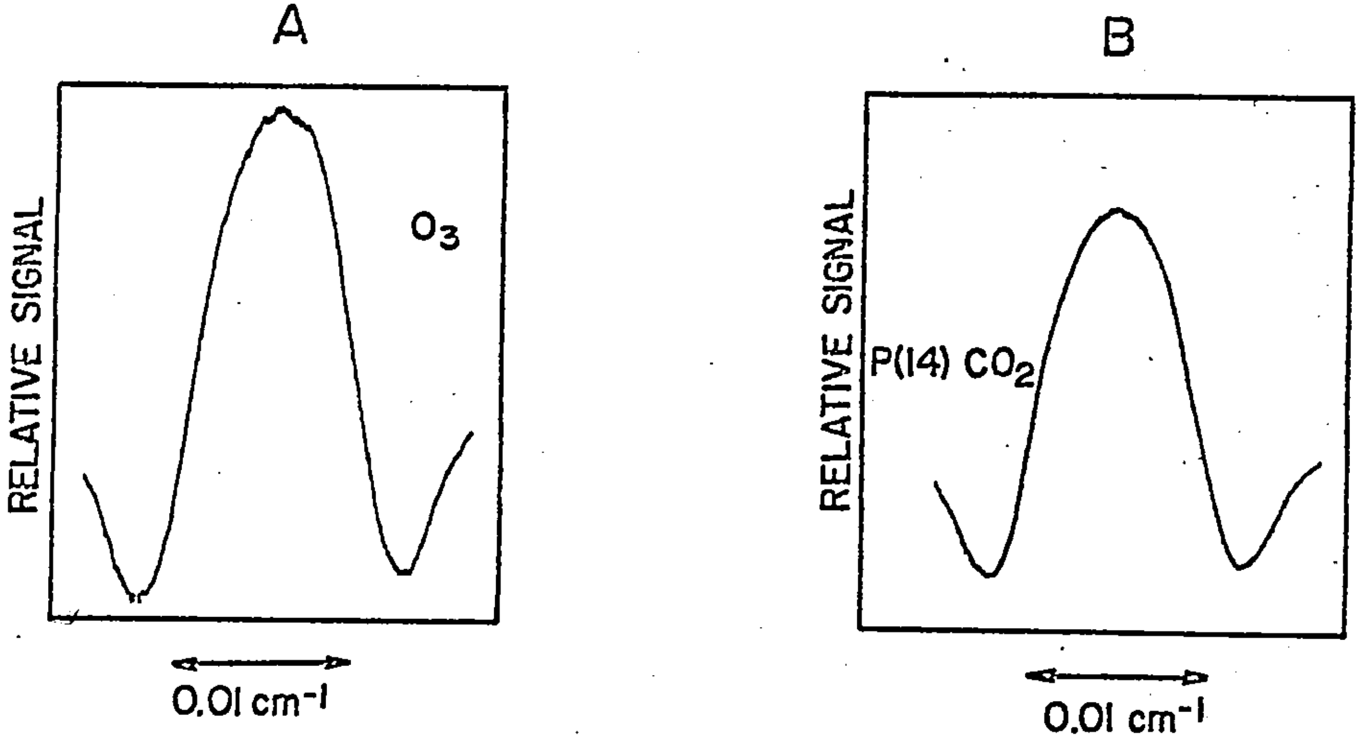

Figure 7.6 Selected lines from Fig. 7.5 taken under the same conditions, except that the instrumental sensitivity for B is a factor of 20 lower than A. The absorption coefficient of the central ozone line is $5 \times 10^{-6} m^{-1}$.

7.5 NH_3 Detection and Results

To detect ammonia in the air, one only needs to scan the selected wavenumber region with very high sensitivity. To obtain sufficiently high sensitivity, the diode wavelength has a small 1 KHz frequency modulation superimposed upon it, and the laser beam is passed through the 5 m White cell to provide a total pathlength of 200 m. Figure 7.7 shows the signal obtained at 2 kHz from HgCdTe detector A, for the same lines in Fig. 7.3. Figure 7.7 clearly illustrates the capability of the system to detect the ammonia in air. There are two additional absorption lines present in this air scan. These were identified as the P(34) $(02^00 - 00^00)$ and the P(24) D $(03^10 - 01^10)$ lines of N_2O at 1140.606 cm^{-1} and 1140.747 cm^{-1} respectively [25]. Using the calibration procedures outlined in section 7.7, the ammonia concentration in the laboratory was determined to be 10 ppb.

Figure 7.7 displays a very convincing demonstration of the detection of ammonia in air, but there is actually no need to scan over several absorption lines. A single isolated line is sufficient to monitor a given gas. One can then increase the sensitivity by scanning very slowly over a single line, and using a long time constant to reduce noise.

7.6 SO_2 Detection Employing a Locking Technique

To ensure that the diode wavelength does not drift during a very slow scan, we have found it convenient to lock the laser wavelength to the relevant absorption line using a beam splitter and the second

HgCdTe detector B. A short cell (Cell 2 in Fig. 7.1) containing pure gas (ammonia or SO_2) at low pressure is placed in this beam, and first harmonic detection is used to give a derivative line-shape. Figure 7.8 shows the first derivative and second derivative of an absorption line. The laser wavelength is then locked to the line center, P, using conventional servo techniques. The wavelength can be scanned by introducing a slow dc ramp into the feed-back loop. This dc shifts the locking point from line center, and allows one to scan slowly from one edge of the line to the other. Another advantage of locking the laser wavelength using a short cell of pure gas is that it confirms the identification of the absorption line being measured in the air. Locking has been carried out on isolated lines in NH_3, SO_2, and N_2O, while monitoring the same absorption lines in air using detector A. Figure 7.9 shows a typical scan when locked to an SO_2 line at 1141.91 cm^{-1}. A time constant of 10 s was used for this trace. The noise level corresponds to ∿2 ppb SO_2 or an absorption sensitivity of $6 \times 10^{-8}\ m^{-1}$.

It takes several minutes to complete the scan shown in Fig. 7.9. A more effective utilization of this time is simply to lock at point p and measure the voltage offset, s, from the baseline. In this manner one can conveniently use time constants as long as 100 s, and continuously monitor changing levels of gas concentration. Figure 7.10 is typical of the results obtained. The diode laser is locked to the center of an SO_2 absorption line, and the second harmonic signal at detector A is recorded on chart paper as the gas mixture in the 5 m White cell is varied. The baseline level is obtained by flowing pure N_2, or simply by evacuating the cell. The system response is calibrated using a known N_2/SO_2 mixture, and the SO_2 concentration in air can easily be determined as 8 ppb. In Fig. 7.10, the noise level corresponds to ∿1 ppb SO_2, or an absorption sensitivity of ∿ 3×10^{-8} m^{-1}. These results are typical of the day-to-day operation of the instrument. We have monitored atmospheric SO_2 concentrations for periods of several hours at a time, and the diode laser has been in trouble-free operation for many months. To change from one gas to another, the diode temperature and current are changed slightly to shift to the correct wavelength, and the gas in sample cell 2 is changed. N_2O was monitored on the overlapping P(28) $(02^{0}0 - 00^{0}0)$ and P(18) C $(03^{1}0 - 01^{1}0)$ lines at 1145.334 cm^{-1} [25] with a sensitivity of ∿1 ppb. The NH_3 lines at 1140 cm^{-1} are much stronger ir transition than those of SO_2 or N_2O in the same wavelength region, and the LAS can detect less than 0.1 ppb NH_3 in air.

7.7 Linearity and Calibration

An important property of any practical pollution monitoring instrument is that its response should be linear, and that it should be easily calibrated. The LAS is based on the measurement of optical absorption, and for the very small optical densities involved, Beer's law should ensure linearity of response. Nevertheless, this linearity was checked under practical conditions. The diode laser was locked to an SO_2 absorption line, and calibrated SO_2 in N_2 mixtures were passed through the White cell. The results are shown in Fig. 7.11. The calibrated mixtures were prepared from an 820 ppb SO_2 in N_2 mixture supplied by Airco Industrial Gases. This standard mixture was then diluted with pure N_2 using a carefully calibrated flow-meter system. Within experimental error, the LAS response was linear over the entire range from 20 to 820 ppb. The experimental error was small, being approximately 1 or 2% of the higher concentrations (limited by the resetability of the flowmeters) and ± 1 ppb at the lower concentrations. These flowmeter results confirm the linearity of the LAS. The absolute calibration clearly depends on the accuracy and stability of the concentration of SO_2 in the standard mixture. The Airco mixture was supplied in a specially coated aluminum cylinder designed to minimize concentration changes with time and temperature [88]. Nevertheless, SO_2 mixtures in the ppb range are notoriously difficult to prepare and store, and an independent check on the calibration is in order. Fortunately, the system can be directly calibrated for mixtures in the ppb range using high SO_2 concentration mixtures which do not suffer from the same preparation and storage problems. Over an interval of several months, two cylinders of ∿ 1000 parts per million SO_2 in N_2 were obtained from Matheson Gas Products. These mixtures were passed, at the same pressure as in the multipass cell, through a 10 cm cell placed in front of the 5 m White cell (cell 1 in Fig. 7.1). With the White cell set for a 160 m pathlength, the system response is equivalent to a mixture of ∿625 ppb flowing through the White cell. These results are also indicated in Fig. 7.11.

The very good agreement obtained with mixtures from two different suppliers, and differing in nominal concentration by 3 orders of magnitude, confirms the absolute calibration of the LAS for the monitoring of SO_2. In principle, one could even eliminate the necessity of obtaining calibrated mixtures by making absorption lines in pure SO_2, i.e., the LAS can be entirely calibrated by optical methods.

The usefulness of these calibration techniques were particularly well illustrated when we attempted to measure the concentration of NH_3 in air. Rough calculations based on the results of Fig. 7.7, and the theoretical linestrengths of the NH_3 lines [90], indicated that the measured NH_3 concentration was $\sim$10 ppb. However, the most dilute concentration commercially available was 50 ppm NH_3 in N_2. By using this mixture in cell 1, and setting the White cell to a 200 m pathlength, we were able to simulate a 25 ppb mixture. This calibration enabled us to determine that the local NH_3 concentration fluctuated in the 6 to 8 ppb range. When the system sampled laboratory air, a somewhat higher reading was obtained due to NH_3 given off by laboratory personnel. If anyone stood close to the air intake tube, the NH_3 emitted by the human body would derive the system off scale. No particular care was taken to eliminate such contamination effects from the measurements taken of the local atmosphere. Hence, the true background level may be somewhat lower than 6-8 ppb NH_3.

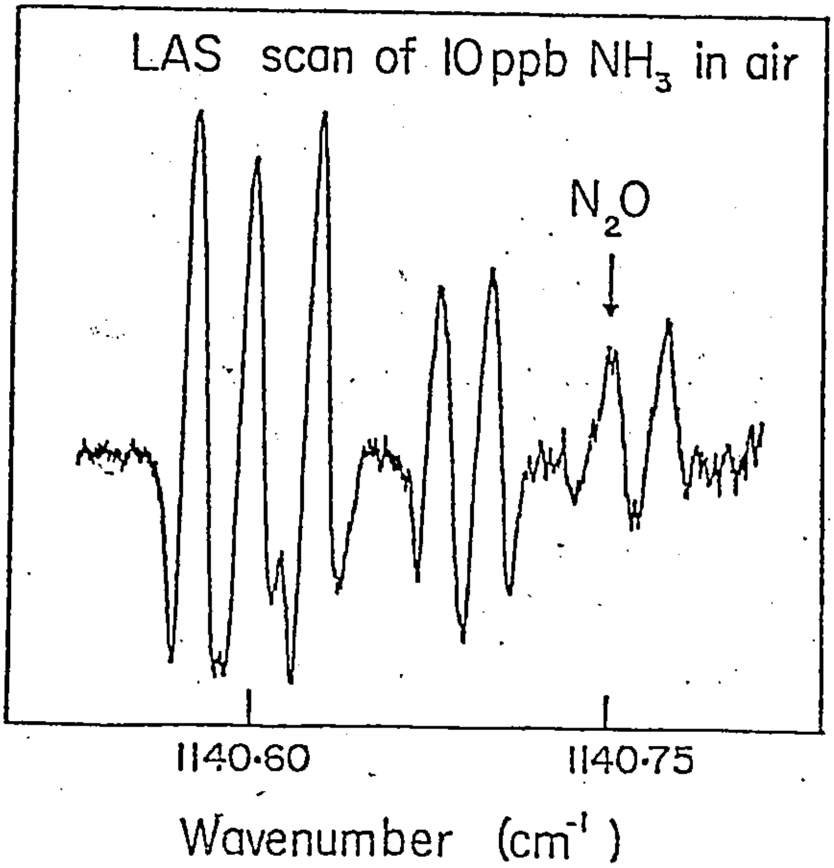

Figure 7.7 Detection of 10 ppb NH_3 in air. Typical results of an LAS scan over the same wavelength region, as in Fig. 7.3, in air. Pathlength is 200m in air at 20Torr, with a time constant of 3sec. The air scan contains two additional lines due to N_2O. One is indicated at 1140.747 cm^{-1}. A second stronger N_2O line is coincident with the NH_3 line at 1140.606 cm^{-1}.

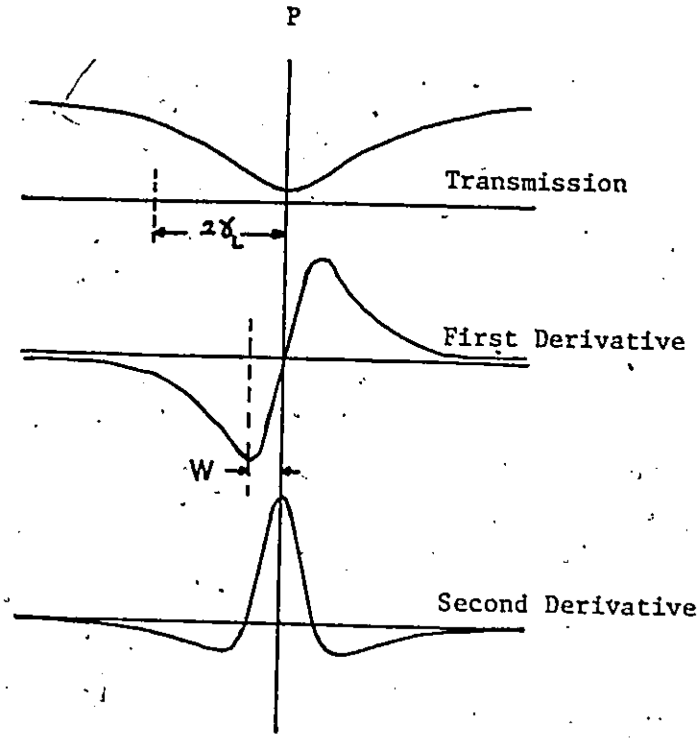

Figure 7.8 Transmission, first, and second derivative assuming Lorentzian line shape; γ_L denotes HWHM for the absorption line. W denotes the inflection point location ($W = \pm \gamma/\sqrt{3}$), P is the locking point.

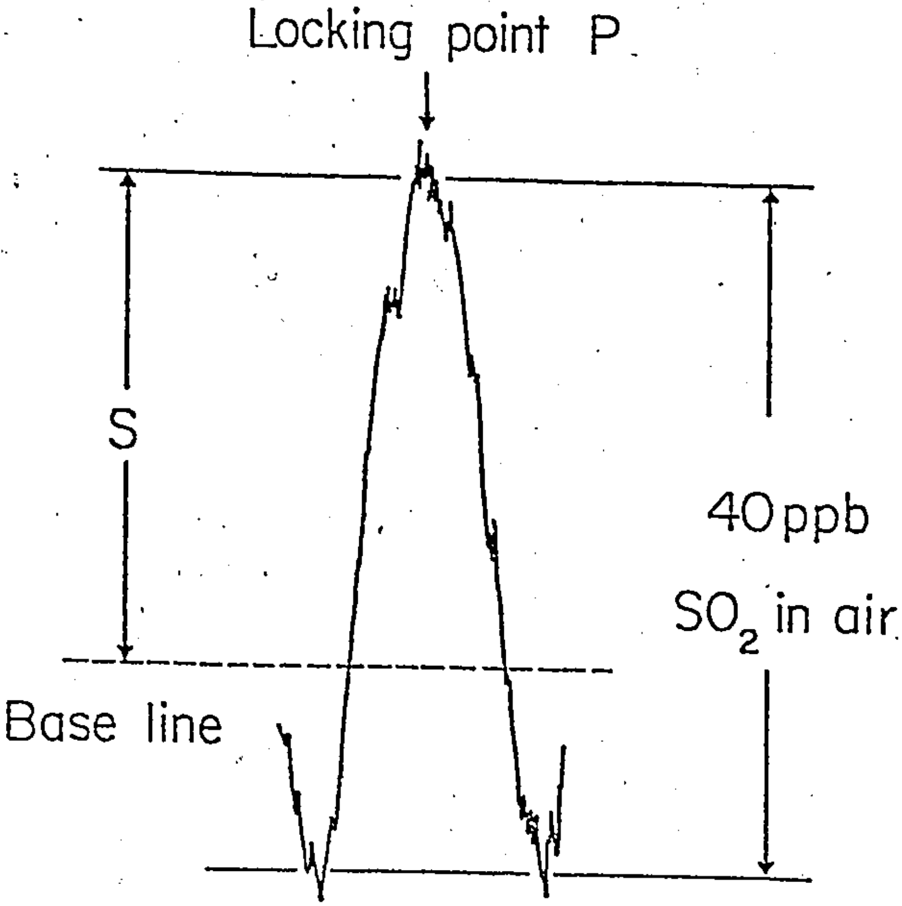

Figure 7.9 Slow scan over the SO_2 line at 1141.91 cm^{-1}. Pathlength in air is 200m, at 11torr pressure, and a time constant of 10sec is used. All the results are taken by locking at point P and measuring the voltage offset S.

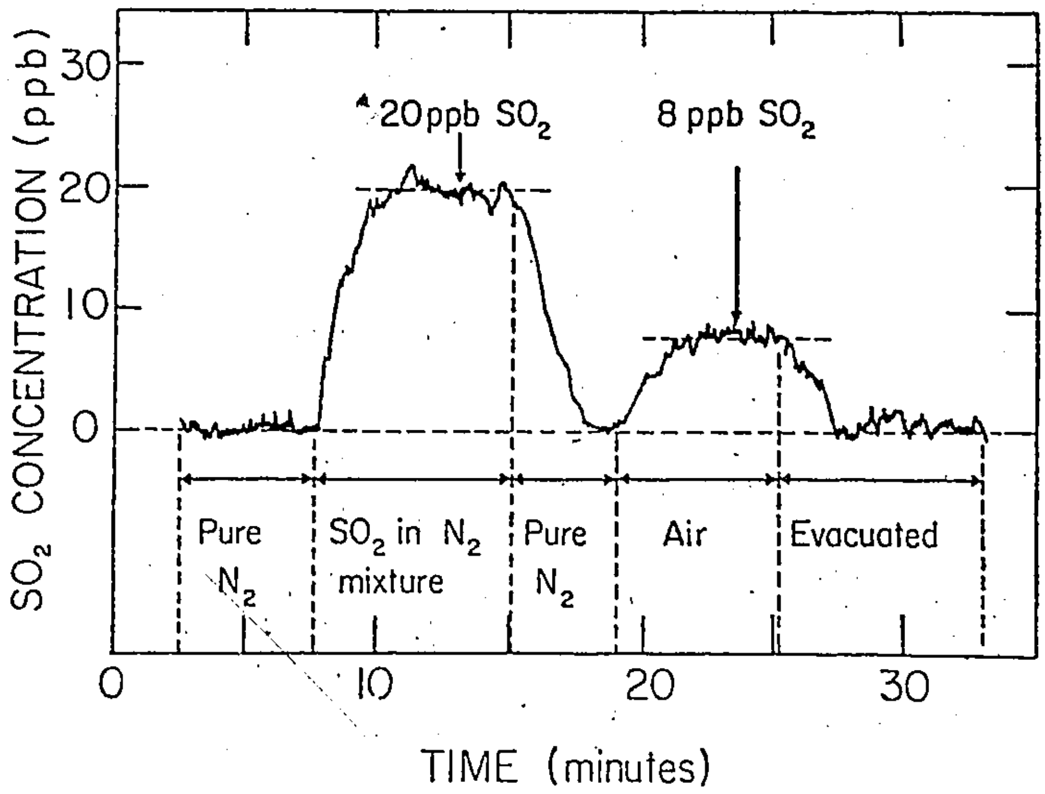

Figure 7.10 A plot of voltage offset S with the diode laser at the center of an SO_2 line. Pathlength in the 5m White cell is 160m, and the gas mixture in the cell is varied with time. Under these conditions, the speed of response of the LAS is limited by the 100sec time constant used with lock-in amplifier A.

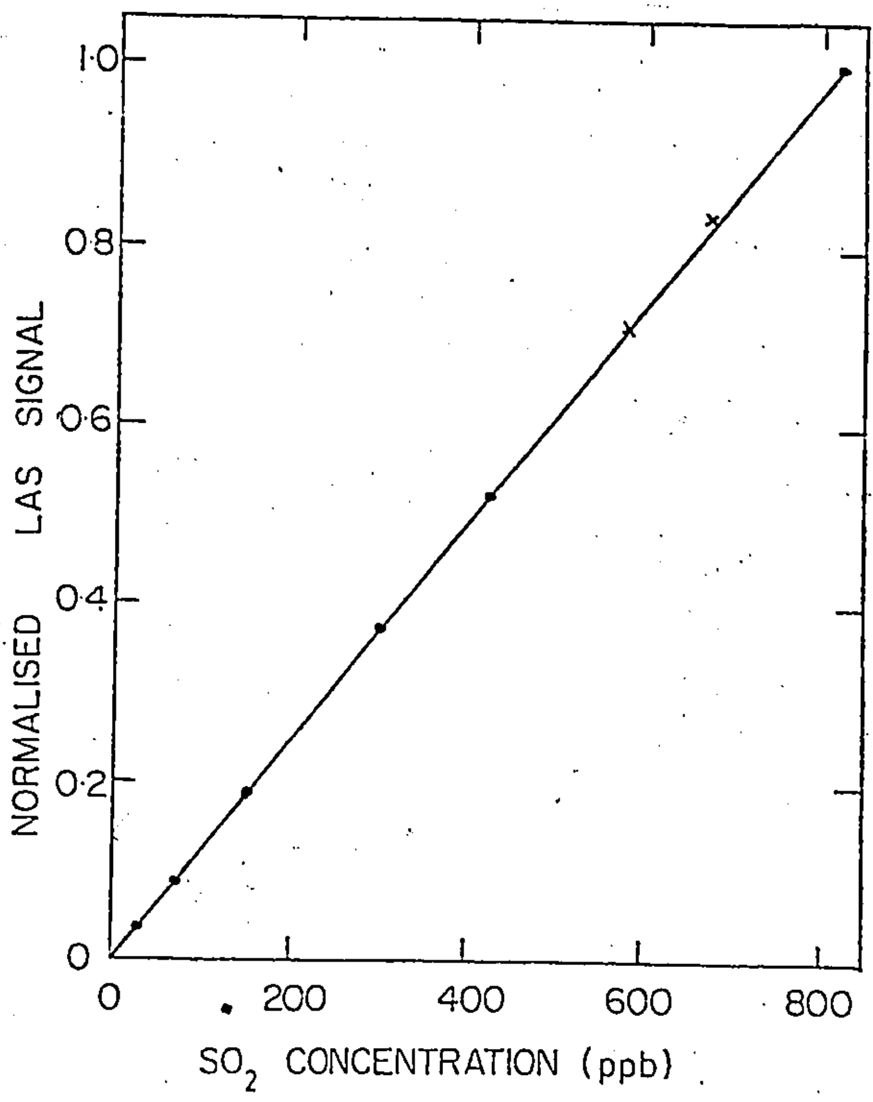

Figure 7.11 Linearity and calibration of LAS. The points marked• are obtained using a 160m pathlength in mixtures prepared from a standard 820ppb SO_2 in N_2 mixture supplied by Airco. This standard mixture was then diluted with pure N_2 using calibrated flowmeters. The two points marked x correspond to 973ppm and 1123ppm SO_2 in N_2 mixtures supplied by Matheson. These high concentration mixtures are placed in sample cell 1 , with a pathlength of only 9.5cm.

CHAPTER 8

REMOTE LONG-PATHLENGTH STATION FOR SO_2 DETECTION

8.1 Introduction

The use of a Laser Absorption Spectrometer (LAS), and gas samples at reduced pressures enabled us to detect absorption coefficients, in the laboratory, with sensitivity of 3×10^{-8} m^{-1}. The performance of the LAS using a shorter White cell has recently been demonstrated, Reid et al [77] obtained a commercial multipass cell (Wilks Variable Long Path Gas Cell) with a single pathlength of 0.75 m, and a capability of pathlengths up to 50 m. This cell was operated with a total pathlength of 40.5 m. Typical results for the detection of SO_2, N_2O, and NH_3 are shown in Fig. 8.1. The Wilks cell is a factor of 7 times shorter in length than the 5 m White cell, and was expected to be a factor of 7 less sensitive. However, it is found that the better mechanical stability of the Wilks cell helps to compensate for the loss of pathlength, and the experimental sensitivity is only reduced by 2. This can be clearly seen by comparing the results for SO_2 in Figs. 7.10 and 8.1. The sensitivity of the LAS using the short Wilks cell is 2.3 ppb of SO_2 or N_2O, and .1 - .2 ppb NH_3. These figures apply to continuous monitoring, (with a 100 S time constant), and to absorption

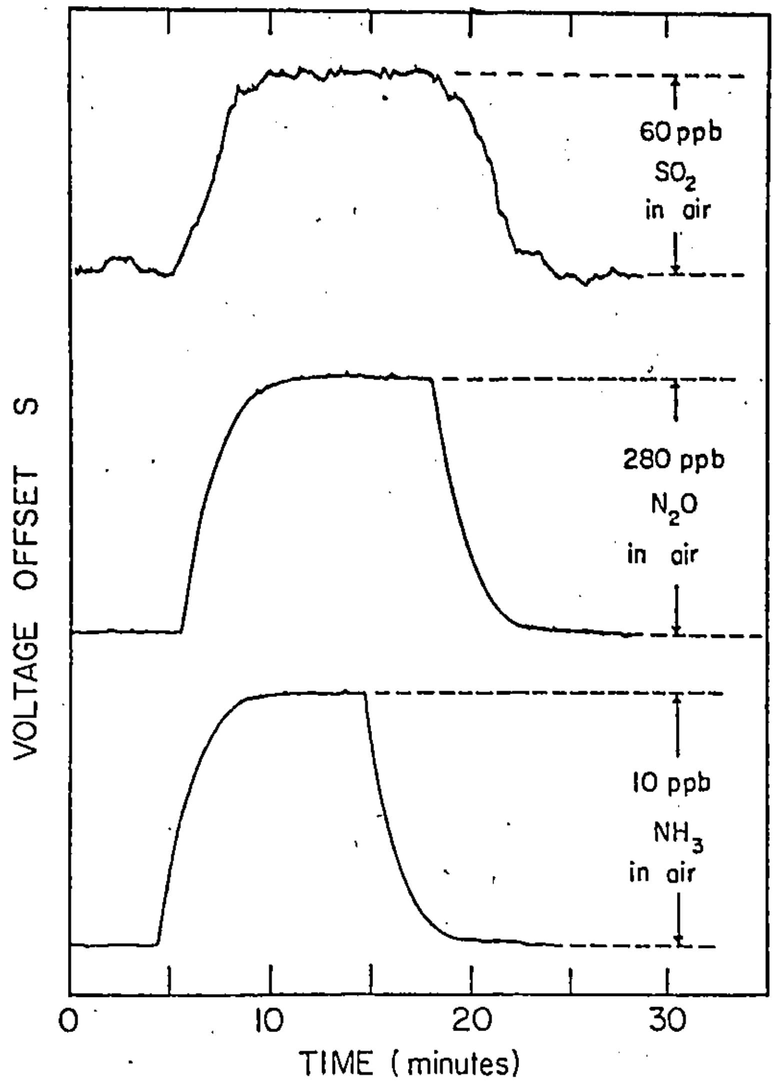

Figure 8.1 LAS performance with 40.5 m pathlength in Wilks White cell. The cell is filled successively with pure N_2, air, and pure N_2, at a total pressure of 20 Torr. The diode laser is locked in turn to SO_2, N_2O, and NH_3 lines near 1140 cm^{-1}, and a 100 s time constant is employed.

coefficients sensitivity 10^{-7} m^{-1}. A prototype portable Point Monitoring (PM) instrument which has been designed in the McMaster University Air Pollution Laboratory is now monitoring SO_2 in Hamilton with great success. This instrument permits the gas pressure to be reduced until the Doppler-broadened ir absorption structure is revealed, thereby making possible very high specificity. However, it is difficult to eliminate entirely the problems associated with the PM of reactive gases such as NO and SO_2, which can be changed during the sampling procedure.

In the present Chapter the use of a LAS in remote Long-Path Monitoring (LPM) is described. Although, LPM sensitivity at the present time is not high as in PM, it has several advantages over PM. LPM produces average values for the pollutants concentration over the path. These average values are of greater overall significance in the ambient air analysis than are point values. In addition, the LPM eliminates entirely the problems associated with the sampling procedure. Furthermore, it is more meaningful for regional data than PM, as well as being more economical in manpower and equipment. Generally, however, remote monitoring is not considered to be a substitute for point monitoring, but an adjunct to it. Nevertheless, in some cases remote sensing represents the only economical or technically feasible technique.

The teasibility of remote long-path laser monitoring of atmospheric pollutants by a derivative absorption techniques has recently been demonstrated by Ku et al. [89] and redesigned for improved performance by Chaney et al [9]. The capability of this technique is limited for simple molecule detection such as with CO.

We report here the first remote long-path monitoring technique for SO_2 detection employing a second harmonic resonance absorption scheme. This technique enabled us to detect SO_2 concentrations as low as 50 ppb employing a diode laser emitting in the ν_1 band of SO_2, and a total pathlength of 1.2 km in the atmosphere which was obtained by using corner cube retroreflectors and an off-axis launching telescope. The basic concept shows promise for measuring SO_2 concentrations as low as 10 ppb in the ν_1 band. This can be achieved by improving the present transmitter-receiver optical system, and the data processing. We also report on absorption data at atmospheric pressure for SO_2, N_2O, NH_3, H_2O and O_3 in the region 1100 - 1200 cm^{-1}. This data is a useful starting point for designing single - or multi-species LPM systems.

The present Chapter includes theoretical and experimental investigations indicating that additional improvements in sensitivity should result from operating in the ν_3 band of SO_2. However, greater care is required in this region (1300 - 1400 cm^{-1}) because of interference from atmospheric H_2O.

8.2 Experimental Apparatus

Figure 8.2 is a schematic diagram of the experimental apparatus; while Fig. 8.3 shows a view of the laboratory optical table. The same PbSnSe diode laser (used in PM of SO_2 in Chapter 7) is mounted on the tip of the cold head (described in Chapter 2). The laser output is

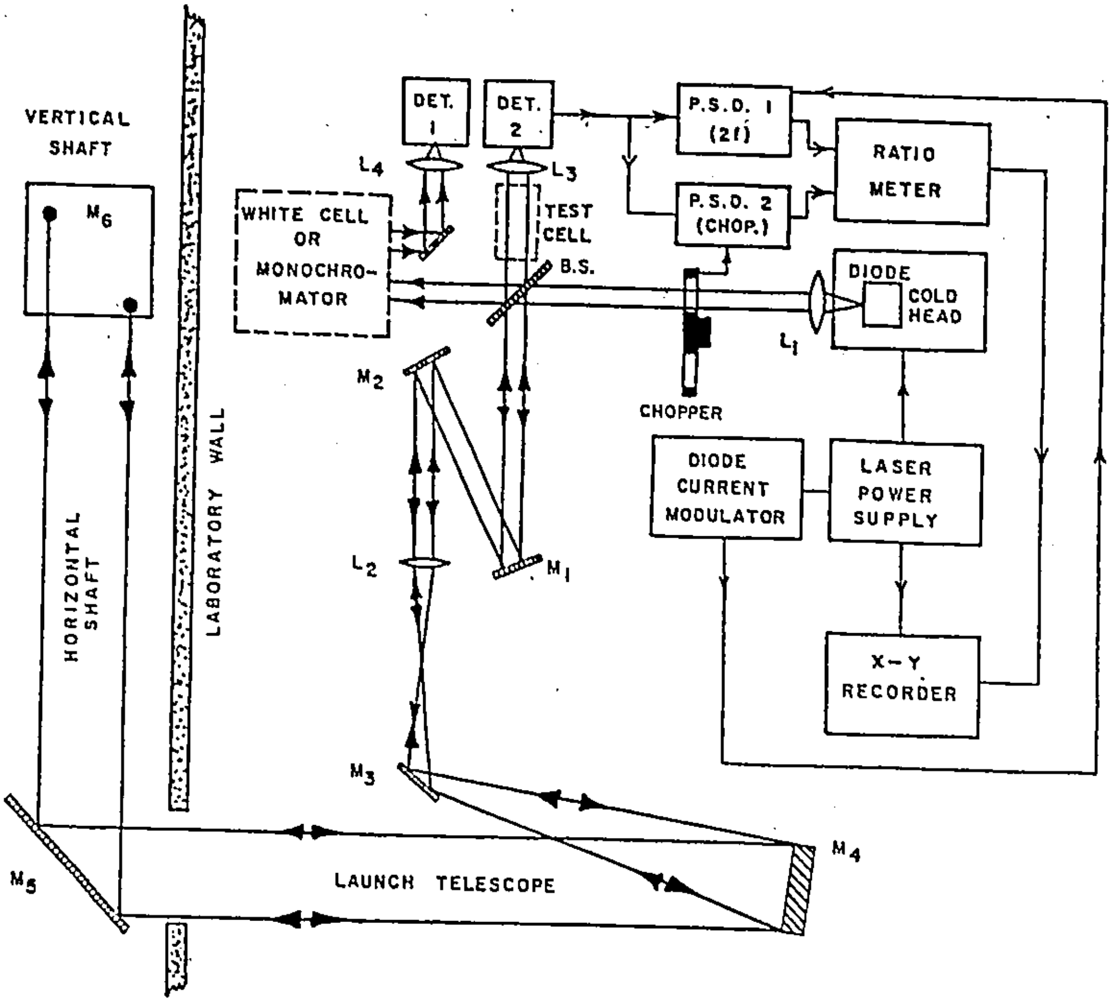

Figure 8.2 . Schematic diagram of the LAS used for remote detection.

Figure 8.3 A view of the laser laboratory showing the optical table, and the optical components; (foreground) from the left He-Ne red laser, He piping, the cold head, the spectrometer, and the CO/CO_2 laser head; (background) from the left the launching telescope, the focussing mirror, the beam-splitter, the calibration (10 cm) cell, detector input lens, the detector, and the 5 m White cell. Also showing, on the laboratory wall, the launching hole, and a mirror which may be used to obtain the zero-pollutant reference signal.

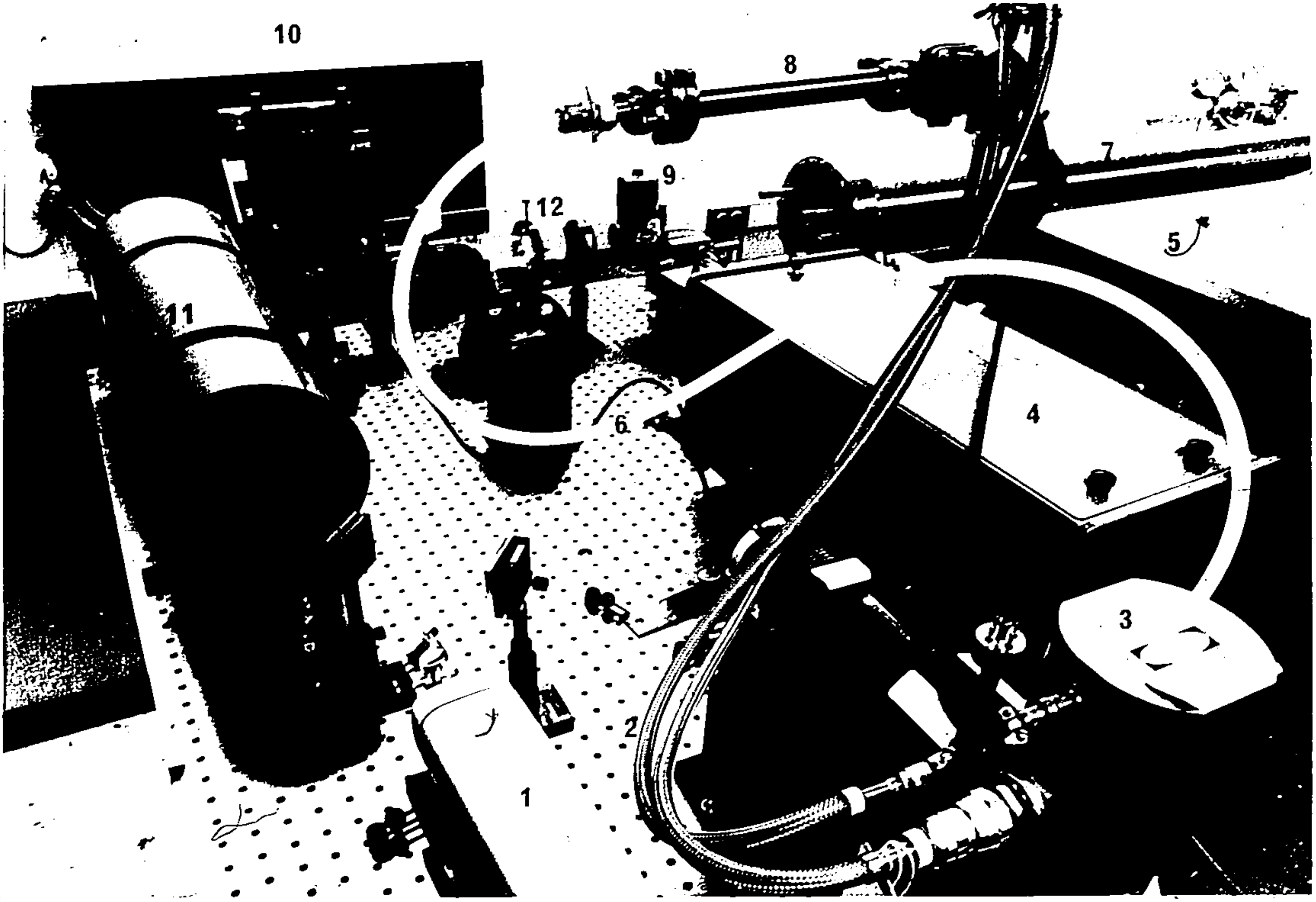
10
8
9
12
7
11
5
6
4
3
2
1

collected by a 5 cm focal-length germanium (Ge) lens, and divided into two beams by a Ge beam-splitter. The reflected beam is focussed by a 2.5 cm focal-length Ge lens at the focal point of a launching telescope (off-axis Hardin Optical Co.). The latter has a 12.5 cm clear aperture and employs an off-axis parabola of 63 cm focal-length. One may use a focussing mirror instead of the 2.5 cm focal-length lens. However, we have found that greater care is required for the configuration that employs a focussing lens, because the reflection from the lens back to the beam-splitter results in a large false signal at the signal detector, and may cause fringes to appear as an optical noise, and also because the Ge lens will not be transparent to the visible beam used for the alignment.

Two mirrors (6 mm x 200 x 250 plate glass) are used to send the expanded beam (12 cm dia.) 28 m to the roof of the laboratory; one to direct the beam vertically and one to dodge past existing piping. The beam is confined to a 15 cm stove-pipe for 23 m vertically. A small over pressure in the building causes a flow of air up the pipe. Approximately 13 cm of clear aperture is available.

A third mirror on the roof, of the same type, is used to direct the beam to targets (see Fig. 8.4). This mirror (aiming mirror) can be remotely controlled from the laser laboratory for fine alignments.

Several methods are available for returning the laser beam

Figure 8.4 A view of the laser beam launch station located on the roof of the McMaster University Medical Centre.

towards its origin. We chose corner reflectors, as a target, because they are compact and require no alignment or maintenance, while "Cat's eye" retroreflector systems are large and subject to misalignment. However, for large permanent installations, "Cat's eyes" are best in offering large aperture at low cost, but for experimental work, inexpensive corner cube retroreflectors are quite adequate. Five small corner cubes, each of 5 cm size, obtained from Edmund Scientific are placed beside each other on a wooden plate and mounted in a wooden box. This box was placed on the roof of another building (Arts II) facing the laboratory roof and the aiming mirror. The distance between the aiming mirror and the retroreflector is 590 m (see Fig. 8.5).

To facilitate precise aiming of the ir beam, the roof mirror is rebuilt with electric motors to provide a very fine motion (as shown in Fig. 8.6). The motion is slow, but not so slow as to prevent motions of several degrees. The drive rate, in both axes, for the beam reflected from the mirror, is 42 μ rad/sec. Backlash is about 2.5 s, and motor stop time is about 1.5 s. The motors are controlled from the laboratory by toggle switches.

Several techniques were conceived and tried out, to find the simplest method of aiming the diode laser ir beam to the distant retroreflector target. A small mirror (1 cm diameter) was placed near the focal point of the launching telescope, away from the beam, and an eye-piece was used to see the image of the target. The He - Ne laser was sent through the beam path and the required adjustment of the optical components on the optical table was made to focus the He - Ne laser beam on the retroreflector image. The beam is returned by the retroreflector along the same path, through the beam-splitter, and then focussed on the HgCdTe signal detector. As a part of the alignment, a retroreflector is placed near the telescope and the detector position is adjusted to obtain a maximum signal. If this is done carefully, a retroreflected signal will be detected when the diode laser beam is launched through the atmosphere. The roof mirror is then used to maximize this signal.

8.3 Experimental Technique

The laser beam is chopped mechanically at ∿ 900 Hz, while the drive current to the diode is simultaneously modulated at a higher frequency, $f = 5$ kHz. The output of the detector is fed into two lock-in amplifiers. One of them is for synchronous detection at twice of the modulation frequency (second harmonic detection); while the other is for synchronous detection of the chopped signal. The outputs from the two lock-in amplifiers are fed to a ratio meter to obtain $\Delta I(\nu)/I(\nu)$, where $I(\nu)$ is the chopped component and $\Delta I(\nu)$ is the frequency-modulated component detected at 2f. These signals are related to the transmitted signal and its second harmonic, respectively. The output of the ratio meter is fed to the Y axis of an X-Y recorder. The X axis signal is proportional to the diode current, hence it is related to the wavelength of the diode power.

The second beam, which is the transmitted part through the

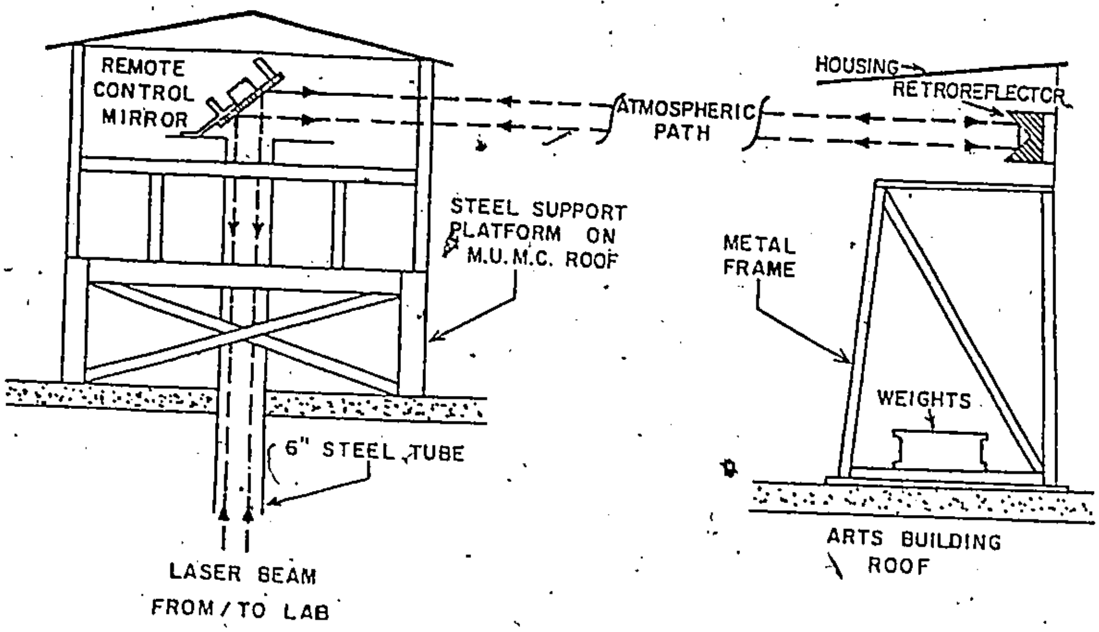

Figure 8.5 Schematic diagram of the launch station on the roof of the laboratory and the retroreflector system on the roof of the Arts Building some 600 m away.

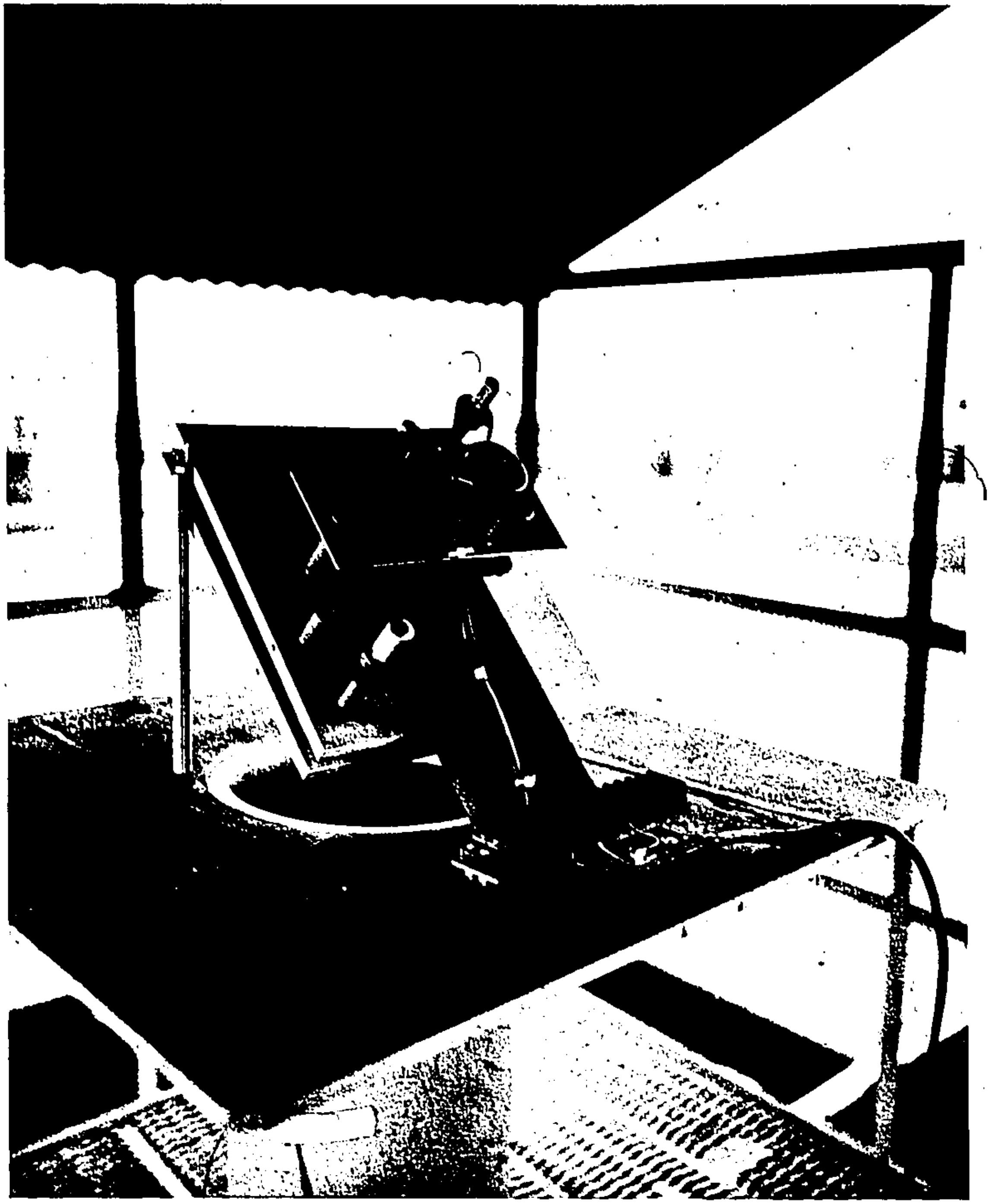

Figure 8.6 A view of the large mirror mount located within the launch station on the roof of the McMaster University Medical Centre. The chain drive to the mirror mount angular alignment adjustment controls can be clearly seen.

beam-splitter, can be focussed into the 0.5 m spectrometer, or into the 5 m White cell. This beam enabled us to perform the measurements described next.

8.3.1 White Cell Experiment: ν_1 Band Results

The following results were obtained by employing the diode laser emitting in the ν_1 band of SO_2, the 5 m White cell, and gas samples of known concentrations. The first step in the detection of any (absorbing) gas concentration in the atmosphere is to obtain a wavelength region which contains strong absorption lines of the target gas and minimal absorption due to other gases. This was achieved by using the line parameter compilation of Ref. [25] as an input to our computer program to generate the desired transmission spectra in the region 1100 - 1200 cm^{-1}. Some results are shown in Fig. 8.7. Here, the upper curve represents the transmission of H_2O due to 1% of H_2O in air and a total pathlength of L = 1 km (i.e., CL = 1000 cm). The remaining curves represent the normalized absorption coefficients for several important absorbing gases. The maximum value of the absorption coefficient for each gas is given in Table 8.1. Also shown in Table 8.1 is the minimum detectable concentration of each gas in the spectral region 1100 - 1200 cm^{-1}. This concentration is calculated using Eqn. 3.2 and the strongest absorption coefficient value of each gas. It is assumed that a pathlength of 1.2 km is employed, and that an absorption of 0.3% can be measured. Our experience indicates that the latter is a reasonable criterion for a practical monitoring system. Figure

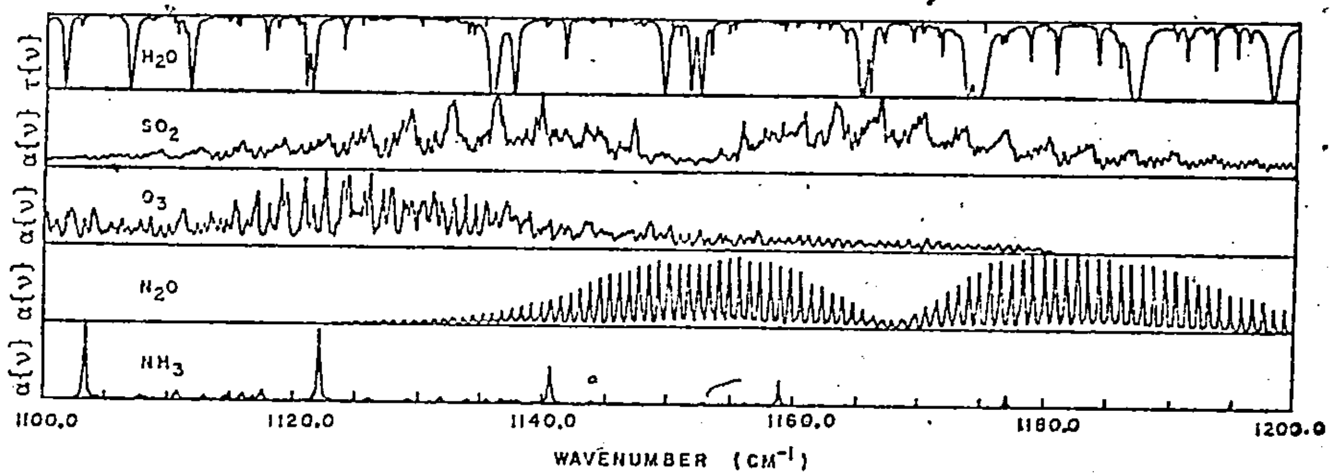

Figure 8.7 A theoretical curve of H_2O transmission and absorption coefficients of different gases in the atmosphere. The value of CL (concentration times pathlength) used for generating H_2O curve is 1000 cm. These traces with Table 8.1 are used in selecting the optimum wavelength region for a gas detection in the presence of the others.

8.7 and Table 8.1 contain sufficient data for determining the optimum spectral region in which to detect a particular gas in the presence of others.

TABLE 8.1 Minimum detectable concentration of different pollutant gases in the region 1100 - 1200 cm^{-1} at atmospheric pressure. The results are quoted for a minimum detectable absorption of .3%.

Pollutant Gas	Maximum Absorption Coefficient (cm^{-1} atm^{-1})	Minimum Detectable Concentration (ppb)
SO_2	2.3	10
O_3	.5	50
N_2O	1.2	20
NH_3	52	.5

For SO_2 detection, the spectral region 1160 - 1161 cm^{-1} has been chosen, where the absorption coefficients of other gases are minimum or approximately constant with the wavelength. In addition, this spectral region was covered by our diode laser which was operating in a single mode. Figure 8.8 shows typical results of the conventional direct transmission scan of the diode current over the selected spectral region. The four scans A, B, C, and D were taken at total pressure of 10, 100, 400, and 760 Torr, respectively to illustrate the broadening of the absorption lines due to increasing the total pressure. A value of CL = .7 cm was used for all the four scans, where C is the concentration of the SO_2/N_2 mixture introduced into the White cell at a pathlength L. After the operating diode current (which is required to scan the diode over the absorption dip, marked by * in Fig. 8.8) is determined, the synchronous detection is switched to the second harmonic one. It was found that a 100 mA current was required to scan our diode over this absorption dip.

To apply the second harmonic detection technique adequately, the modulation frequency and amplitude must be adjusted for the largest 2f signal and minimum noise for a low concentration of SO_2. This was achieved by introducing 1 Torr from an 973 ppm SO_2 in N_2 mixture, and 759 Torr of dry N_2 supplied by Matheson, into the White cell at 40 m pathlength. This combination of SO_2 concentration and pathlength is equivalent to 43 ppb of SO_2 in 1.2 km. The amplitude of the frequency modulation which is necessary to scan our diode over an absorption line at reduced pressure is ∿ 200 mV at f = 3 kHz. In the case of atmospheric pressure, the optimum amplitude of modulation is 3 V, at f = 5 kHz, and near 1160.8 cm^{-1}. This amplitude

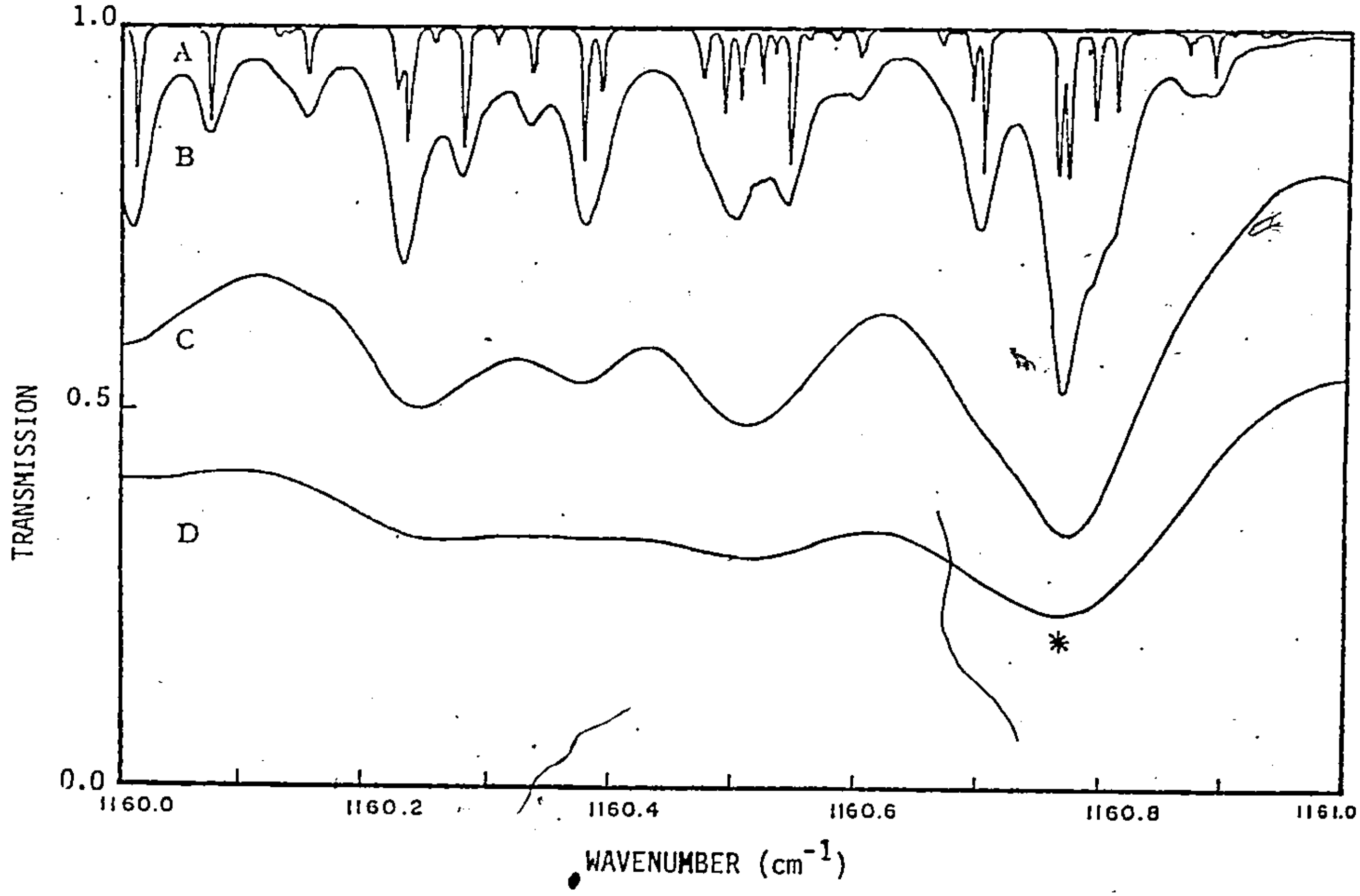

Figure 8.8 Typical results of scanning the laser current over the selected region for SO_2 detection (1160.8 cm^{-1}). A, B, C, and D are taken at 10, 100, 400, and 760 Torr total pressure, respectively. The CL value used for SO_2 mixture is 0.7 cm. Note the region marked by * is the selected region which shows maximum absorption. This region is used for SO_2 detection in the atmosphere.

depends on the width of the absorption dip which may vary for different spectral region.

Since the amplitude of the frequency modulation signal is relatively large, the probability of modulating a curvature portion of the diode laser power is high. This results in a high background (B.G) (i.e., zero-pollutant) signal which is not related to the absorbing pollutant. However, the B.G signal can be measured by scanning the diode current over the same region with the White cell filled with pure N_2, or completely evacuated. We found that the detection sensitivity, depends on how accurate one can produce and measure this zero-pollutant signal and subtract it from the pollutant signal. Figure 8.9 shows the system responses due to 492 ppb, and 246 ppb of SO_2/N_2 mixtures in 1.2 km. Each of these responses is the result of a 2f signal normalization by its chopped signal, and subtraction of its normalized background signal.

During our measurements, two standard SO_2/N_2 mixtures were used: 973 ppm and 1123 ppm of SO_2 in N_2, supplied by Matheson. However, for checking the system linearity, one can employ one standard mixture and change the White cell pathlength to obtain different combinations of CL. From Fig. 8.9, and several measurements which were taken at different CL values, it is found that, the system response is linear and this linearity is valid up to 500 ppb of SO_2 in 1.2 km. This applies only for the spectral region near 1160.8 cm^{-1} and may not be true for different regions.

According to the above calibration procedure, we have prepared

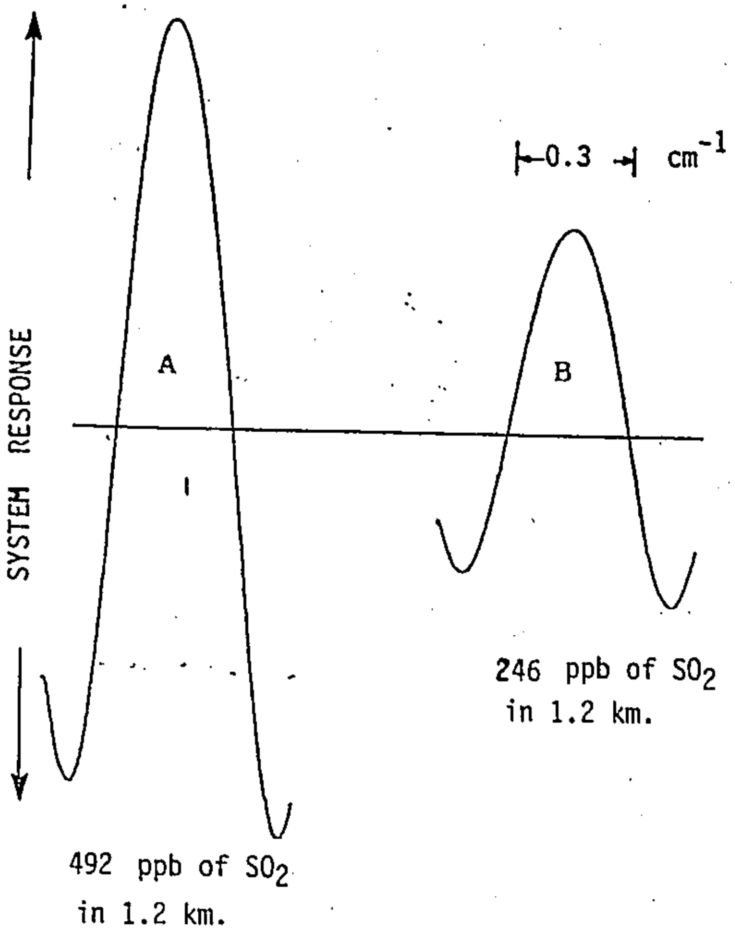

Figure 8.9 A typical result of the second harmonic signal. The diode laser is scanned over the selected region shown in Fig. 8.8. Scan A is taken with the White cell filled with a mixture of 492 ppb of SO_2 in 1.2 km. Scan B is taken after reducing the pathlength used in Scan A by a factor of 2.

two SO_2/N_2 mixtures in 10 cm short cells; one is equivalent to 83 ppb of SO_2 in 1.2 km, while the other is calibrated to be equivalent to 1 ppm of SO_2 in 1.2 km. Two ratios of the system responses to these concentrations are determined experimentally, and we define:

$$R_1 = \frac{\text{normalized 2f signal due to 1 ppm}}{\text{normalized 2f signal due to 83 ppb}} \tag{8.1}$$

$$R_2 = \frac{\text{normalized (2f signal due to 1 ppm + B.G)}}{\text{normalized (2f signal due to 83 ppb + B.G)}} \tag{8.2}$$

The above mixtures, along with the calculated ratios (R_1 and R_2), are used in the adjustment and calibration of the system during the atmospheric measurements.

To check against H_2O and other interferences experimentally, the 83 ppb small cell is placed into the beam, and the White cell (at 400 m pathlength) was evacuated and filled with pure N_2. Then the diode current is scanned over the absorption region, and the 2f signal is recorded. After that, the White cell is evacuated and filled with 1 atm of the roof air. This roof air was flowing through two stages in cascade before it enters the White cell: (1) a tube filled with a ground charcoal to absorb the ambient SO_2; (2) a tube contains a small wet cloth to increase the H_2O concentration in the White cell. Then the diode current is scanned and the response is recorded again. Typical results of the above measurements are shown in Fig. 8.10. These traces indicate that there are no inter-

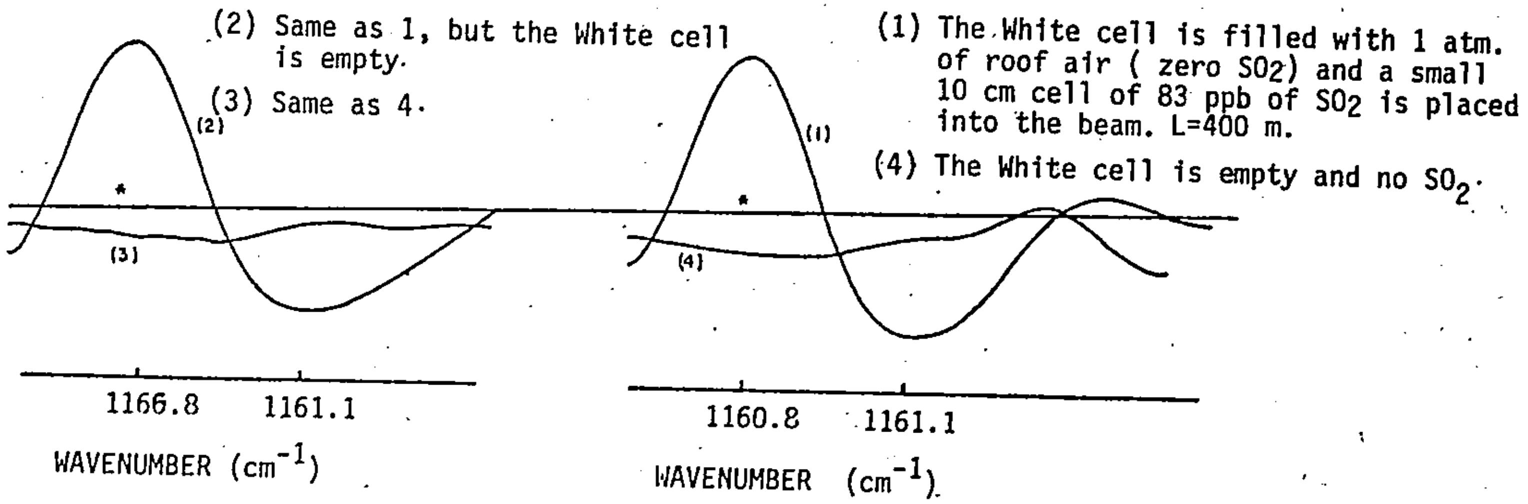

Figure 8.10 Check against interference effects: the 4 second harmonic scans are taken by scanning the laser over the SO_2 absorption dip shown in Fig. 8.8 (marked by *). Note that there is no effect due to the air in the selected region (marked by *).

ference effects in the selected absorption region (marked by * in Figs. 8.10 and 8.8).

Finally, as a word of caution, the accuracy of 2f signal measurement depends on how accurate one can adjust the phase on the 2f lock-in amplifier. It was found that this adjustment may be performed at low pressures, which is accurate and easier. Since the phase setting depends only on the frequency of the modulation, it is only necessary to increase the amplitude of the modulation in the case of measurement at atmospheric pressure.

8.3.2 Atmospheric Measurements (ν_1 Band)

All the measurement results reported in the preceding subsection have been achieved by employing the transmitted beam through the beam-splitter (see Fig. 8.2), and the 5 m White cell. Now, for measurements into the atmosphere, we have employed the reflected beam from the beam-splitter. This beam is launched through the atmosphere by the telescope, and returned back (to a signal detector behind the beam-splitter) by a remote retroreflector. The total pathlength into the atmosphere employing the present optical setup is 1.2 km. The returned signal is synchronously detected at twice the modulation frequency by a lock-in amplifier, and at the chopped frequency by another one. Long-term effects due to atmospheric turbulence and scattering unrelated to absorbing molecules are eliminated electronically by rationing the 2f and the chopped signals, since both are proportionately affected by such influences.

A small cell (10 cm long) is placed permanently into the

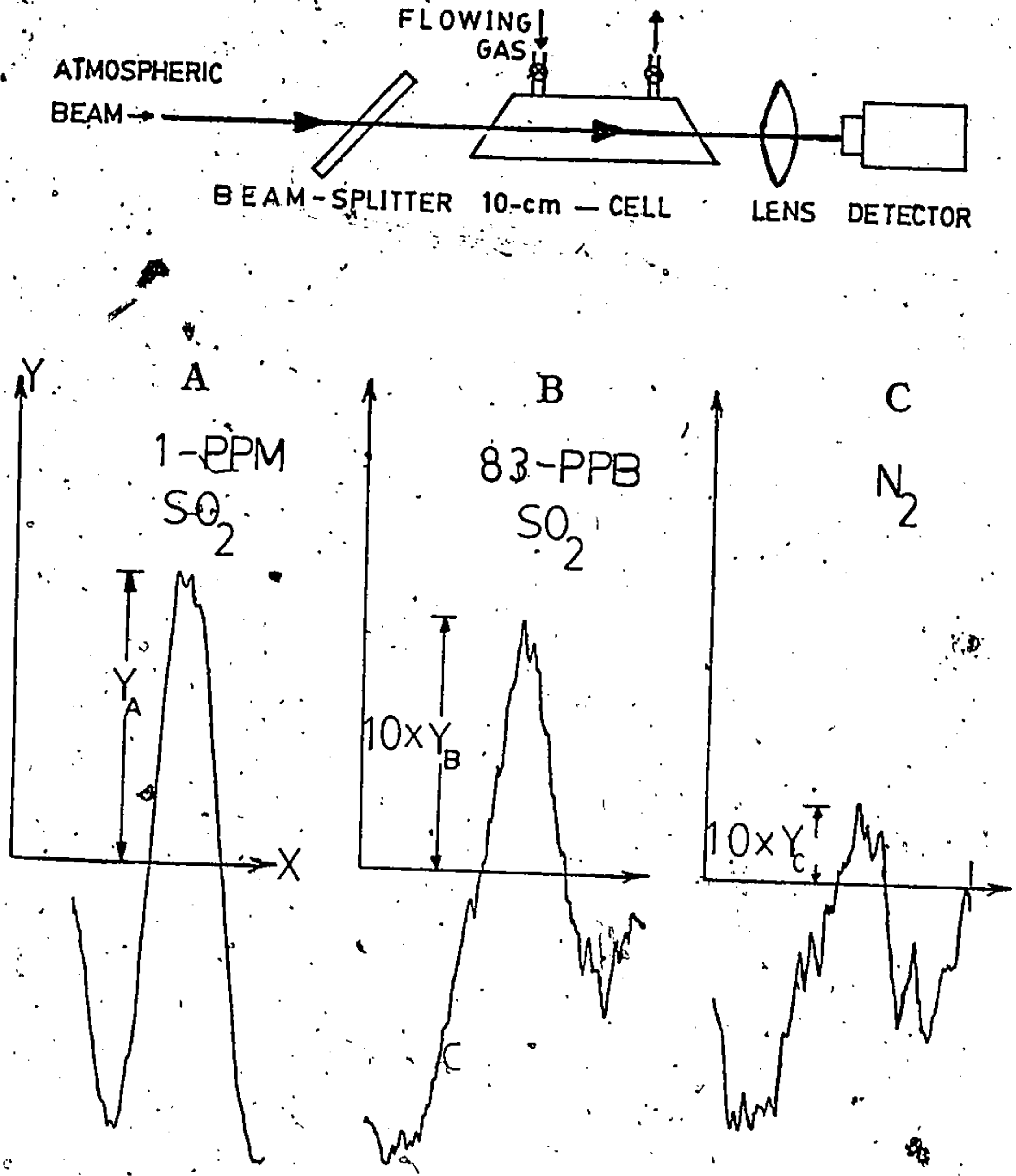

Figure 8.11 Atmospheric SO_2 measurements: the shown scans are taken by scanning the laser over the region near 1160.8 cm^{-1}. Each trace is the ratio of the 2f signal and the chopped signal. The time constant on the Lock-in amplifier is 10 sec. The estimated detectable limit is 50 ppb of SO_2, Traces B and C are taken with the instrumental sensitivity is increased by a factor of 10.

Y_C = the system response in curve C

$$= B.G + S_{N_{atm}} \tag{8.5}$$

where, B.G is the zero-pollutant response (background), and S_{Natm} is the response due to atmospheric pollutant (N_{atm}) assuming zero background.

From Eqns (8.3 - 8.5) and 8.1, the minimum detectable SO_2 concentration is given by

$$N_{min} = \frac{N_B}{n} \sum_{i=1}^{n} \left(\frac{Y_{A_i} - Y_{C_i}}{Y_{B_i} - Y_{C_i}} - R_1 \right) \tag{8.6}$$

where n is the number of measurements which have been taken, and N_B is equal to 83 ppb. The value N_B depends on N_{min} through the relation $N_B > N_{min}$. Primary calculations of the SNR indicated that $N_{min} \approx$ 50 ppb, and for this reason, we have chosen N_B = 83 ppb.

The atmospheric SO_2 concentration, N_{atm}, is calculated using Eqns 8.1 to 8.3, and is given by:

$$N_{atm} = N_B \left(\frac{R_2 Y_B - Y_A}{R_2 - 1} \right) \frac{1}{Y_B - Y_C} \pm N_{min} \tag{8.7}$$

where R_1 and R_2 are defined by Eqns 8.1 and 8.2, respectively.

We report here a sensitivity of 50 ppb for SO_2 detection employing a diode laser emitting in the ν_1 band of SO_2. The present sensitivity is not high enough to monitor SO_2 in ambient levels (∿ 10 ppb), but it is quite enough to monitor SO_2 in stacks and at flare levels. However, the present basic concept shows promise for measuring ambient levels. This can be achieved by:

(1) Improving the present transmitter-receiver optical system. Eng et al [90] concluded that, a large retroreflector allows a greater reduction of noise due to atmospheric turbulence by aperture averaging. Therefore, a 30 cm diameter Cat's eye retroreflector, which has a beam divergence of about 0.15 mrad, is recommended for this application.

(2) Data processing, and fully-controlled measurements. Since the amplitude resolution of the analog ratioing system used was only about two parts in 10^3. This can be improved by using a higher resolution ratio meter or a digital ratioing system. Also, employing a digital system will enable one to perform all the repeatable scans and background substraction accurately.

Theoretical calculations and laboratory measurements (described in the next section) indicate that additional improvements in SO_2 detection sensitivity should result from employing a diode laser emitting in the ν_3 band of SO_2.

8.4 ν_3 Band Measurements

Recently, Laser Analytics has fabricated a diode laser emitting in the ν_3 band of SO_2 (1350 cm^{-1}). This laser is 10 times more powerful than any diode laser previously used in our laboratory. Its threshold current is relatively constant with temperature. A typical value is 0.25 A, and it is easy to find a single mode operation anywhere in the range from 1300 cm^{-1} to 1380 cm^{-1} with a continuous tuning range of $\sim$ 0.5 cm^{-1}. In addition, the SO_2 absorption line intensities in the ν_3 band is about 8 times more stronger than the absorption lines in the ν_1 band. These combined characteristic features of the diode laser and the SO_2 absorption have been exploited to improve the sensitivity of point and long-path monitoring. Great care is required because of the overlapping of very strong H_2O absorption lines in this region. However, since the point monitoring technique permits the gas sample to be extracted at reduced pressure, it is easy to select a strong absorption line of SO_2, free from any overlapping H_2O absorption lines.

We tried to exploit these characteristic features and perform theoretical and experimental investigations about the possibility of launching this laser beam into the atmosphere and detect SO_2 in ambient levels (10 ppb).

8.4.1 Calculations

The transmission spectra of H_2O in the region from 1320 cm^{-1} to 1380 cm^{-1} was generated using our computer program. The value of pathlength times concentration used in these calculations was CL = 1200 cm. The individual line parameters of H_2O were taken from AFRCL compilations [25] after making the necessary corrections. It was found, from several observations, that the H_2O lines wavenumbers in this spectral region must be shifted a value of ∿ 0.03 cm^{-1} towards lower wavenumbers. Our theoretical calculations indicate that the only relatively wide microwindow region is the one near 1331.5 cm^{-1}, where the transmission of H_2O is about 50% for an interval of about 0.5 cm^{-1}. Figure 8.12 shows the calculated absorption spectra in the spectral region 1330 - 1334 cm^{-1}. The absorption spectra of H_2O (heavy curve) was generated using CL = 1200 cm, while the other three curves are the absorption spectra of SO_2, CH_4, and N_2O generated using CL = .12 cm for each gas. Note that decreasing the total pathlength will improve the H_2O transmission, but at the same time it will lower the detection sensitivity. Therefore, a study is required to determine the optimum pathlength prior to designing a system, employing this diode laser, for pollutant detection in the atmosphere. Our observations and calculations indicate that an optimum pathlength of about 500 m is sufficient to increase the atmospheric detection sensitivity to 10 ppb of SO_2 in the ν_3 band.

8.4.2 Experimental Results and Discussions

Figure 8.13 is a typical direct scan of the diode laser current over the theoretically selected region 1330.8 - 1331.8 cm^{-1}. This scan was achieved by placing a small 10 cm cell containing a trace of pure SO_2 at ∿ 1 Torr into the laser beam, and synchronously detecting the "direct" transmission at the chopper frequency. The wavenumbers in this region were calibrated by the aid of SO_2 line

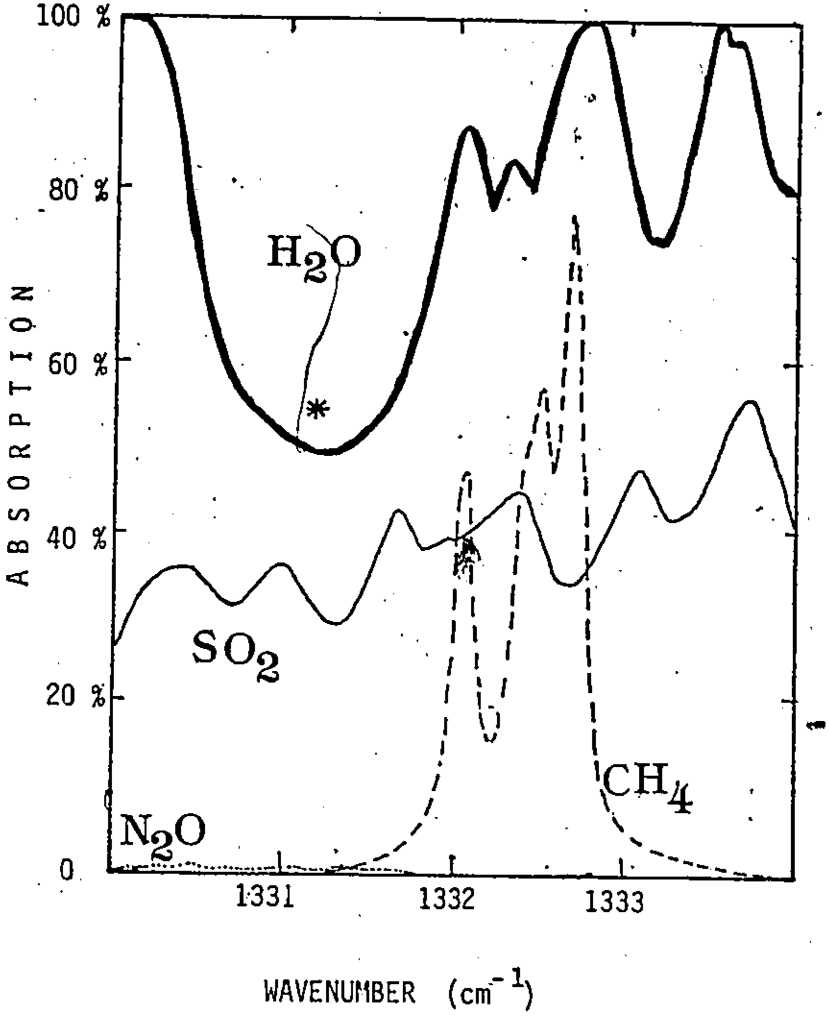

Figure 8.12 Theoretical curves of the H_2O absorption, and SO_2, N_2O, and CH_4 absorption in the microwindow near 1331.5 cm^{-1}. These curves show the possibility of detecting SO_2 in the atmosphere employing diode laser radiating in the ν_3 band of SO_2. The H_2O curve is calculated using cl = 1200 cm, and all the absorption curves are calculated using cl = 0.12 cm. The wavelength marked by * is the proposed region for atmospheric SO_2 monitoring with expecting sensitivity of 10 ppb.

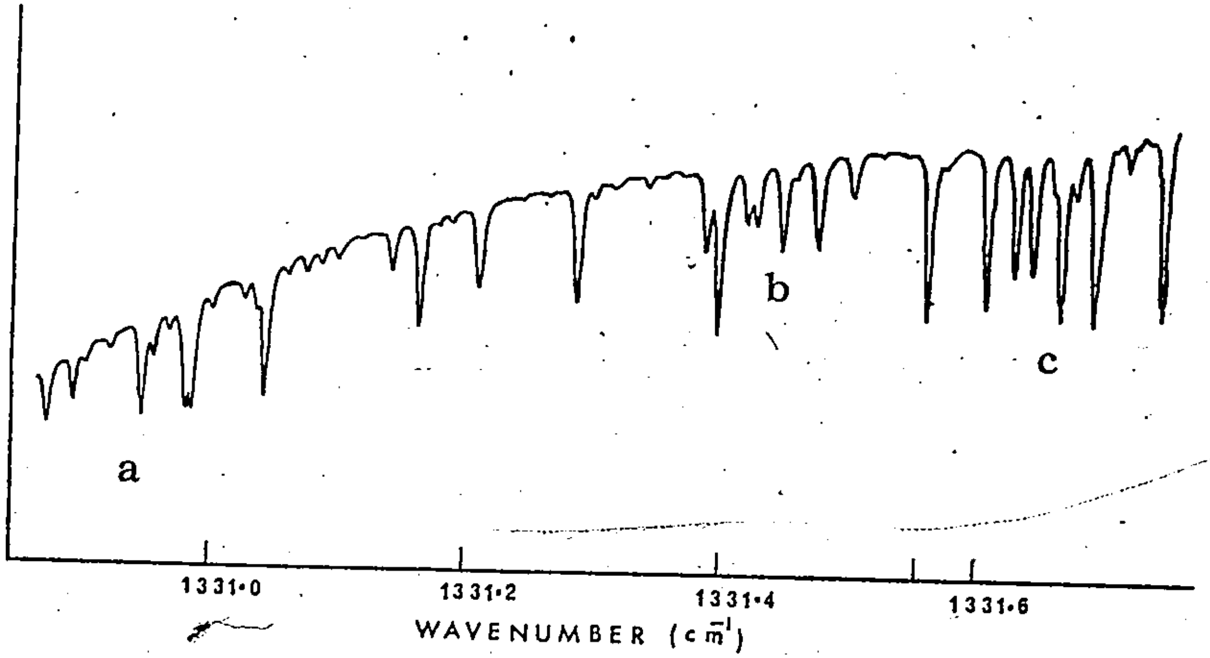

Figure 8.13 A typical direct scan of the diode laser current over the proposed region in Fig. 8.12. This scan is taken by placing a 10 cm cell containing trace of SO_2 at 1 Torr. Note that there are 3 groups of SO_2 lines a, b, and c, each group may produce an absorption dip at atmospheric pressure. The regions b and c are the same regions in Fig. 8.14 marked by 1 and 2, respectively.

parameters listed in Ref. [26]. Figure 8.13 illustrates three groups of SO_2 lines a, b, and c, each group may produce an absorption dip at atmospheric pressure. Figure 8.14 shows the transmission of SO_2/N_2 mixture introduced into the White cell with a CL = .03 cm. The four curves, from the top, illustrate the broadening of the absorption lines with increasing pressure from 10 to 100, 400, and 760 Torr, respectively. Note that there are two absorption dips, marked by 1 and 2 which belong to the absorption lines groups b and c in Fig. 8.13, respectively. One absorption dip, 1, near 1331.35 cm^{-1}; while the other, 2, near 1331.63 cm^{-1}. Employing the second harmonic detection technique (described in subsection 8.3.1) on the absorption region, marked by 2, enabled us to measure a known SO_2 concentration in the White cell with a sensitivity of better than 1 ppb in 1 km.

8.4.3 H_2O Interference Effects

To check experimentally against H_2O interference, the diode laser current is scanned across the selected spectral region with the White cell at 400 m, and filled with roof air. Figure 8.15 shows typical direct scans for total pressures (of the roof air) of 25 Torr (top scan), and 760 Torr (middle scan). The lower scan was taken with a small 10 cm cell, containing pure SO_2 at $p < 1$ Torr, placed into the beam, for wavenumbers calibration. Note that there is an absorption dip due to H_2O (marked by * in the middle scan). Comparing Figs. 8.14 and 8.15, it is clear that the two absorption dips marked by * (due to H_2O) and 2 (due to SO_2) are overlapped;

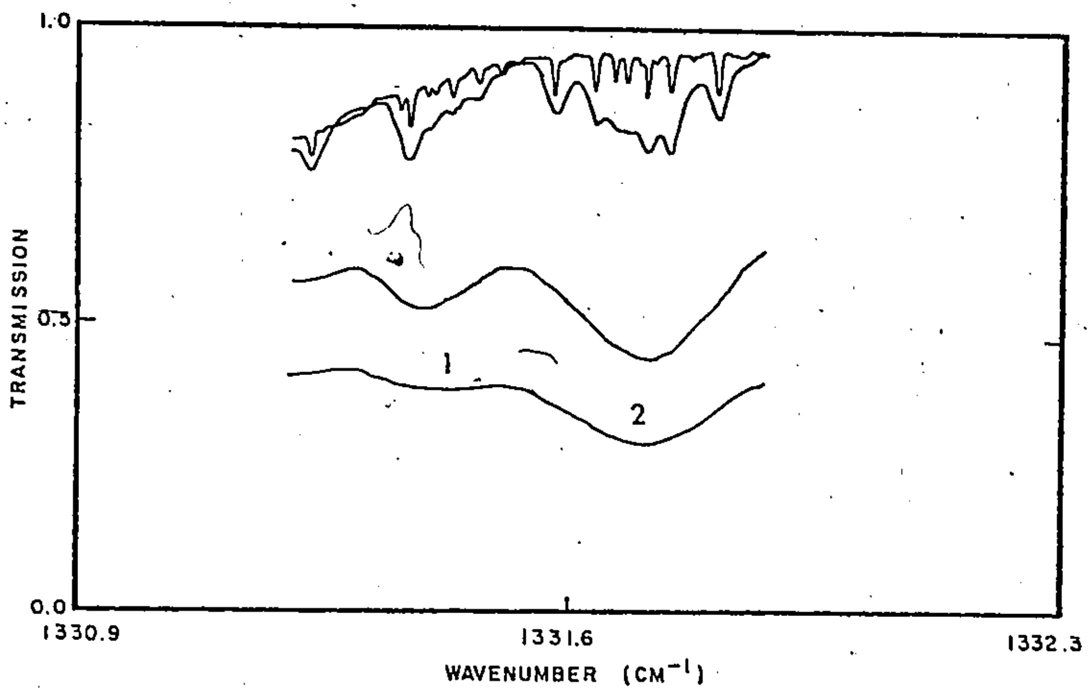

Figure 8.14 Typical direct scans of the diode laser current over the regions b and c in Fig. 8.13 near 1331.5 cm^{-1}. The four curves from the top are taken at 10, 100, 400, and 760 Torr total pressure, respectively. The value of cl used is 0.03 cm.

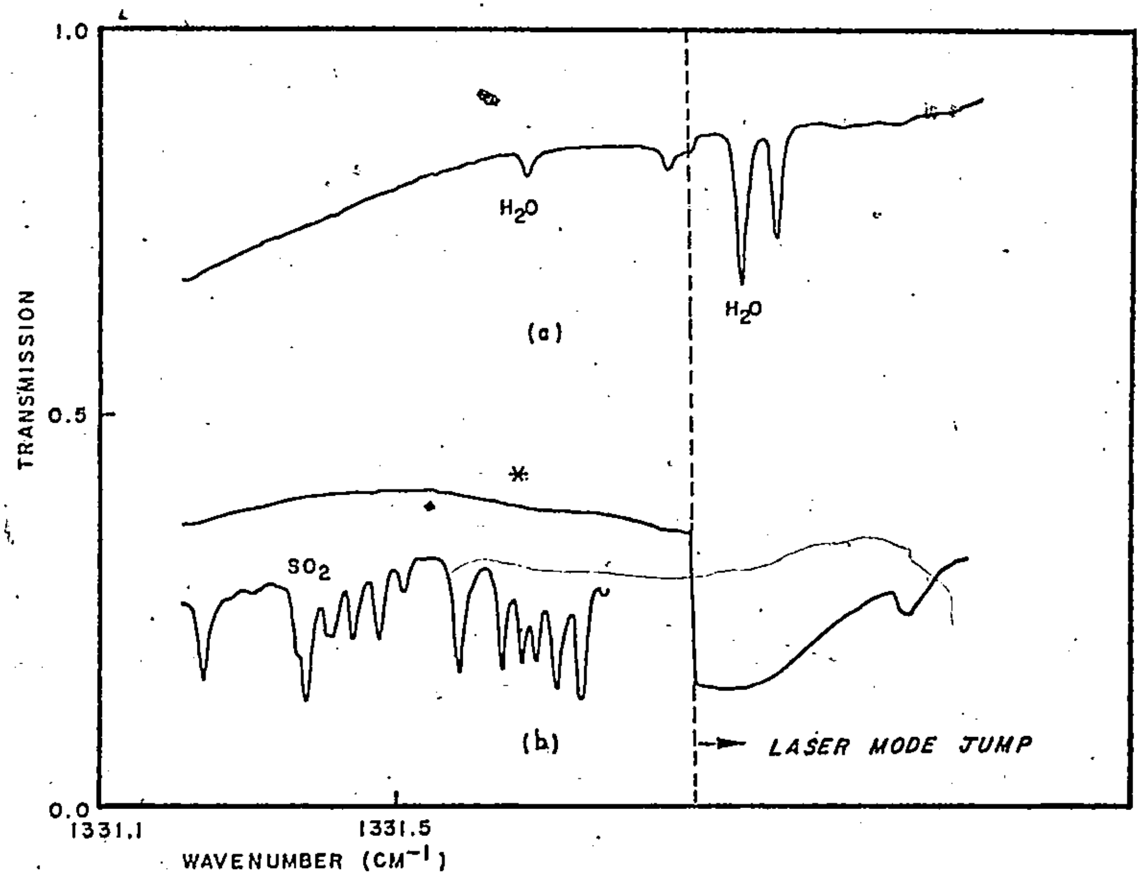

Figure 8.15 Typical direct scans showing the H_2O effect in the proposed region near 1331.5 cm^{-1}. Note that there is H_2O absorption dip (marked by *) overlapping the absorption dip (marked by 2) in Fig. 8.14. The absorption dip marked by 1 is free from H_2O absorption dips. The pathlength used was 400 m.

while the absorption dip marked by 1 is free from H_2O absorption dips. This may not be true at higher CL values of H_2O. However, by scanning the diode current back and forth between these two SO_2 absorption dips 1 and 2, and by knowing the relative absorption coefficients of H_2O and SO_2 at these two regions, one can estimate the SO_2 and H_2O in the path simultaneously. This may be achieved by applying the novel Detection and Estimation Techniques using Linear Weights described by Morgan [91]. The linear weights may be implemented as hardware (analog detection), or as software (digital processing). To demonstrate the absorption effects due to H_2O and SO_2 in these two spectral regions, we employed the White cell at 400 m and the small 10 cm cell which contains 83 ppb of SO_2 in 1.2 km as following:

It is possible to apply a ramp current from an external generator to the laser power supply. The function of this ramp current (together with the frequency modulation) is to produce repeated 2f scans automatically as shown in Fig. 8.16. The crucial parameters of this ramp are: (1) its frequency which control the scanning rate, (2) its amplitude which, together with the setting current value on the laser power supply, control the scanned spectral region. Applying this ramp technique, one can adjust the LAS to monitor a pollutant in the atmosphere continuously. The upper traces in Fig. 8.16 are typical scans over the spectral region marked by 1 in Fig. 8.14; while the lower traces in Fig. 8.16 are for the region marked by 2. The results in Fig. 8.16 agreed with the results in Fig. 8.15 in the sense that, the spectral region marked by 1 is free from H_2O

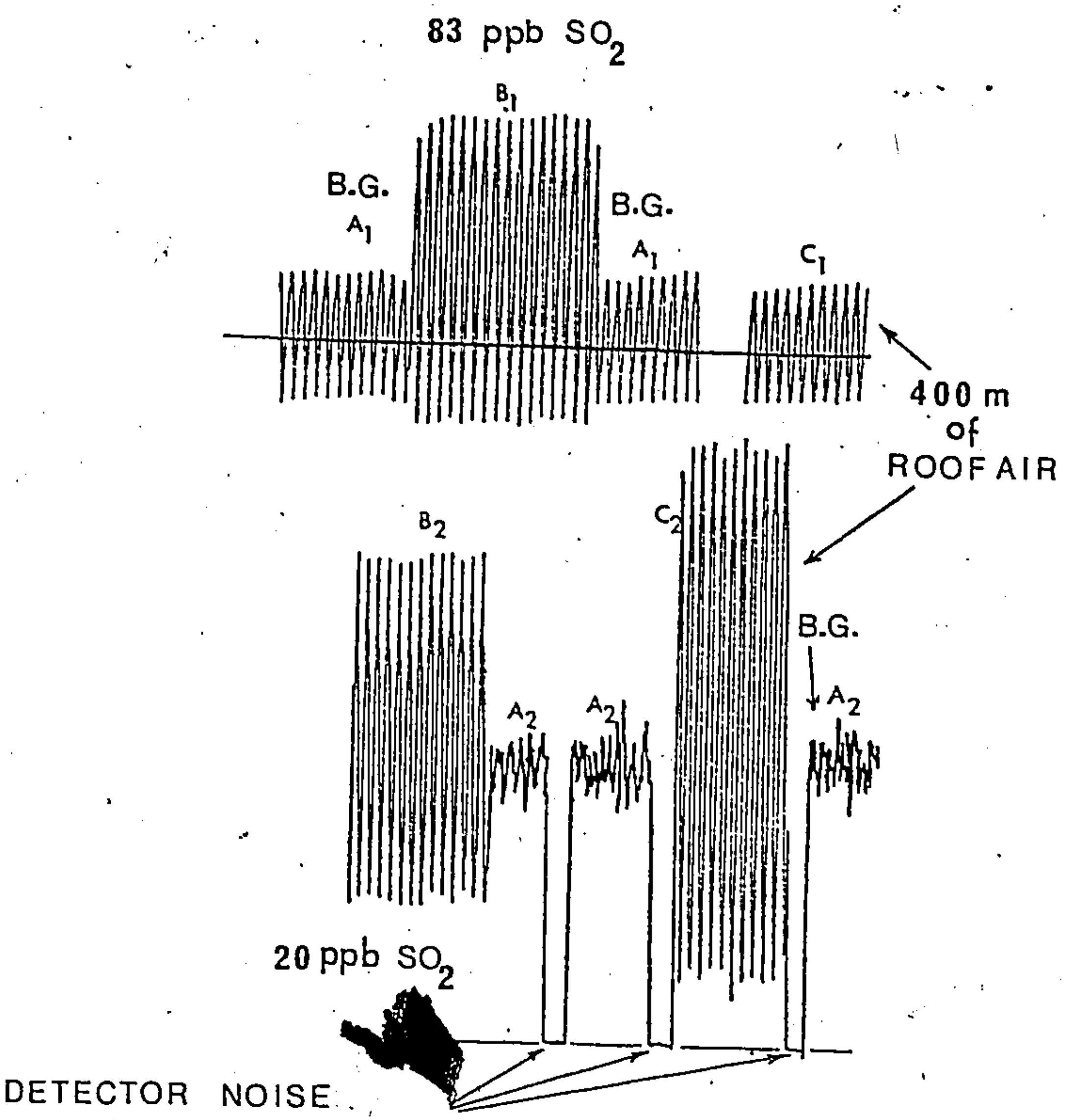

Figure 8.16 A typical repeatable 2f scans over the absorption dips 1 and 2 (see Fig. 8.14). The upper traces are taken in the region 1; the lower are in the region 2. B.G. is the background signal (zero-pollutant signal) taken by flushing the White cell with dry N_2. The instrumental sensitivity is increased by a factor of 2 in the lower traces.

interference. In Fig. 8.16, the background scans (B.G.) were taken when the White cell was evacuated completely and no SO_2 in the beam path. The SO_2 scans were achieved by placing a small 10 cm cell (83 ppb) in the beam, or by introducing a known mixture of SO_2/N_2 into the White cell (20 ppb). The roof air scans were generated when the White cell, at 400 m pathlength, was filled with 1 atm of roof air. The latter was passing through a small tube filled with ground charcoal to absorb the ambient SO_2 before it enters the White cell.

The reported data in the present section may be considered as a starting point for the design of an SO_2 monitor in the atmosphere employing a diode laser emitting in the spectral region near 1331.5 cm^{-1}. Due to overlapping by H_2O absorption, we recommend the use of a fully-controlled instrument and data processing. This may be achieved by following the automatic technique which is described by Max et al [92]. The present investigations show promise for monitoring SO_2 and CH_4 ambient levels in the atmosphere employing a lead-salt semiconductor diode laser radiating in the spectral region near 1332 cm^{-1}.

CHAPTER 9

NOISE REDUCTION AND SYSTEM IMPROVEMENTS

9.1 Introduction

The feasibility of laser monitoring of atmospheric pollutants by the resonance absorption technique has been demonstrated in Chapter 7 for point monitoring, and in Chapter 8 for long-path monitoring. Generally, the sensitivity of a LAS is limited by the ability to detect a small change in the transmitted signal. The major sources of signal fluctuations which limit sensitivity are:

(1) noise due to atmospheric turbulence;
(2) laser source noise;
(3) optical feedback;
(4) signal level fluctuations due to changes in the transmittance of the atmosphere;
(5) laser frequency fluctuations.

By eliminating the effects due to the above noise sources, much higher detection sensitivity than that at the present can be achieved. Noise analysis and reduction is described in the following sections.

9.2 Advantages of Employing Harmonic Detection Technique

Figure 9.1 represents several scans over two SO_2 lines in the 1141.9 cm^{-1} region [75]. The SO_2/N_2 mixture used in the White Cell has been diluted with N_2, and the absorption at the stronger line is now only 10%. It can be seen that, for small absorptions, the direct amplitude detection method (upper scan) produces a very noisy trace. The chief source of this noise is power fluctuations in the laser beam caused by mechanical vibrations of the diode, and consequent beam wander in the optical path. For the purposes of Fig. 9.1, a small aperture was placed in the beam path to enhance such power fluctuations. The regular nature of the "noise" is caused by the cycling of a piston in the diode cold head. It is obvious that direct detection techniques using a mechanical chopper are very susceptible to any type of power fluctuations in the laser beam. Other disadvantages of this technique are the strongly sloping background signal, which make it very difficult to identify small absorptions, and the vulnerability of the scheme to small drifts in the laser output power, in addition to the fact that it is impossible to accurately locate the line center for high resolution spectroscopy (described in Chapter 6). All these problems can be avoided by modulating the diode current at kHz frequencies. We report here an optimum modulation frequency of 3 kHz for point monitoring, and 5 kHz for long-path monitoring. Signals detected at the first and second harmonic of the modulation frequency are also shown in Fig. 9.1. Note the dramatic improvement in SNR in each case. However, it is clear that the second derivative technique results in least noise. This is related to the strongly sloping background in the upper scan of Fig. 9.1. This slope produces a significant dc offset in the first harmonic scan, and the magnitude of this offset is proportional to the laser been diluted with N_2, and the absorption at the stronger line is now only 10%. It can be seen that, for small absorptions, the direct amplitude detection method (upper scan) produces a very noisy trace. The chief source of this noise is power fluctuations in the laser beam caused by mechanical vibrations of the diode, and consequent beam wander in the optical path. For the purposes of Fig. 9.1, a small aperture was placed in the beam path to enhance such power fluctuations. The regular nature of the "noise" is caused by the cycling of a piston in the diode cold head. It is obvious that direct detection techniques using a mechanical chopper are very susceptible to any type of power fluctuations in the laser beam. Other disadvantages of this technique are the strongly sloping background signal, which make it very difficult to identify small absorptions, and the vulnerability of the scheme to small drifts in the laser output power, in addition to the fact that it is impossible to accurately locate the line center for high resolution spectroscopy (described in Chapter 6). All these problems can be avoided by modulating the diode current at kHz frequencies. We report here an optimum modulation frequency of 3 kHz for point monitoring, and 5 kHz for long-path monitoring. Signals detected at the first and second harmonic of the modulation frequency are also shown in Fig. 9.1. Note the dramatic improvement in SNR in each case. However, it is clear that the second derivative technique results in least noise. This is related to the strongly sloping background in the upper scan of Fig. 9.1. This slope produces a significant dc offset in the first harmonic scan, and the magnitude of this offset is proportional to the laser

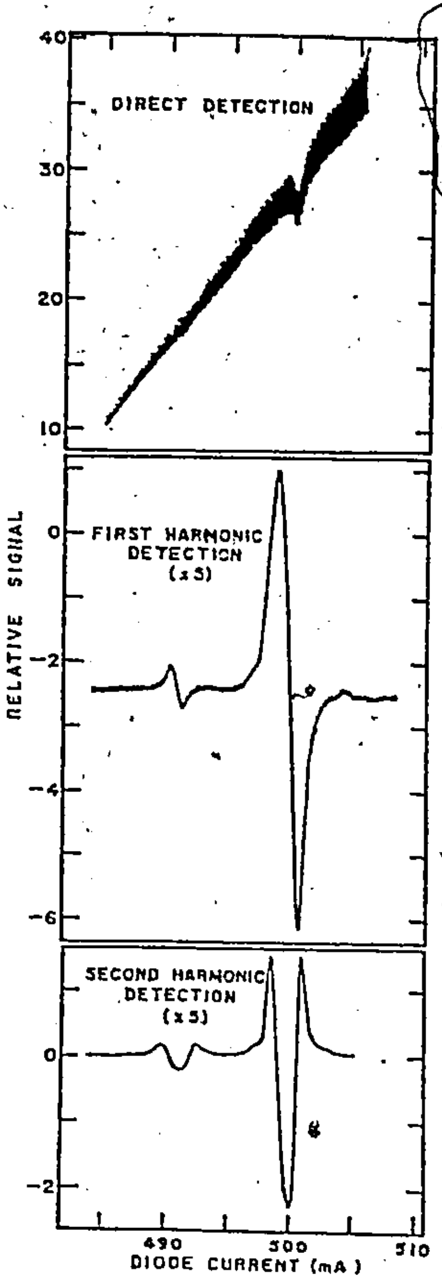

Figure 9.1 Comparison of the three detection schemes at low SO_2 concentrations. The three traces are taken under the same experimental conditions. Note the dramatic noise reduction with second harmonic detection. After [75].

power incident on the detector. Hence, the first harmonic technique is still somewhat susceptible to fluctuations in the laser power. In contrast, detection at the second harmonic produces negligible dc offset, and further reduces the effect of laser power fluctuations. Also, the fact that the second harmonic signal swings around zero greatly facilitates subsequent signal processing. Another advantage of modulating the laser is that, the first or the second harmonic signal can be used to stabilize the laser frequency. The frequency instability, or drift in operating frequency (wavelength), is due primarily to changes in room temperature. Even though the cold finger on which the diode laser is mounted is precisely controlled, the diode temperature will vary with room temperature due to the variation in the radiation falling on the diode. This problem was not apparent when the LAS was used in a temperature-controlled laboratory, but it became very apparent when the portable system was monitoring SO_2 in the field. The conclusion was that the laser frequency had to be controlled at a given frequency on the SO_2 absorption line being used for the measurement. This was achieved by employing the locking technique (described in Chapter 7) on the first harmonic or the technique used on the second harmonic as described by Chaney et al [9].

In harmonic detection, the modulation amplitude must be adjusted to give the largest signal, consistent with no undue broadening of the linewidth. This corresponds to a diode wavelength modulation of the order of the FWHM of the pollutant absorption lines (PM), or absorption dip (LPM). Detection at the first and second harmonic of the modulation frequency is often referred to as taking the first and second derivative of the upper scan in Fig. 9.1. However, a much smaller amplitude of modulation is required for a true derivative signal as described by McClenny et al [93]. The three traces in Fig. 9.1 were taken for the same absorption conditions. Note that the maximum excursion of the harmonic signals from zero is approximately equal to the magnitude of the direct absorption signal in the upper scan. This results from the fact that the direct absorption amplitude represents the maximum swing which can be obtained in a signal transmitted through the absorbing medium. So, from this point of view, we neither lose or gain signal by using the diode modulation techniques.

9.3 Background Signals (Zero-Pollutant-Signal)

For the reasons mentioned above, we have chosen to concentrate on increasing the detection sensitivity using second-harmonic detection. The detection limit of a LAS can be determined by trying to detect a standard low concentration of a pollutant gas. In an initial series of experiments at reduced pressures employing the diode laser setup shown in Fig. 7.1, Reid et al [75] arranged for the total SO_2 absorption in the beam path to be $\sim 10^{-4}$, and tried to detect this using the second harmonic technique. The traces shown in Fig. 9.2 are typical of early results. All traces represent the output of the lock-in amplifier (A in Fig. 7.1) with the second harmonic of the diode modulation frequency as reference, and a time-constant of one second. The upper trace was taken with the laser beam blocked, and represents detector

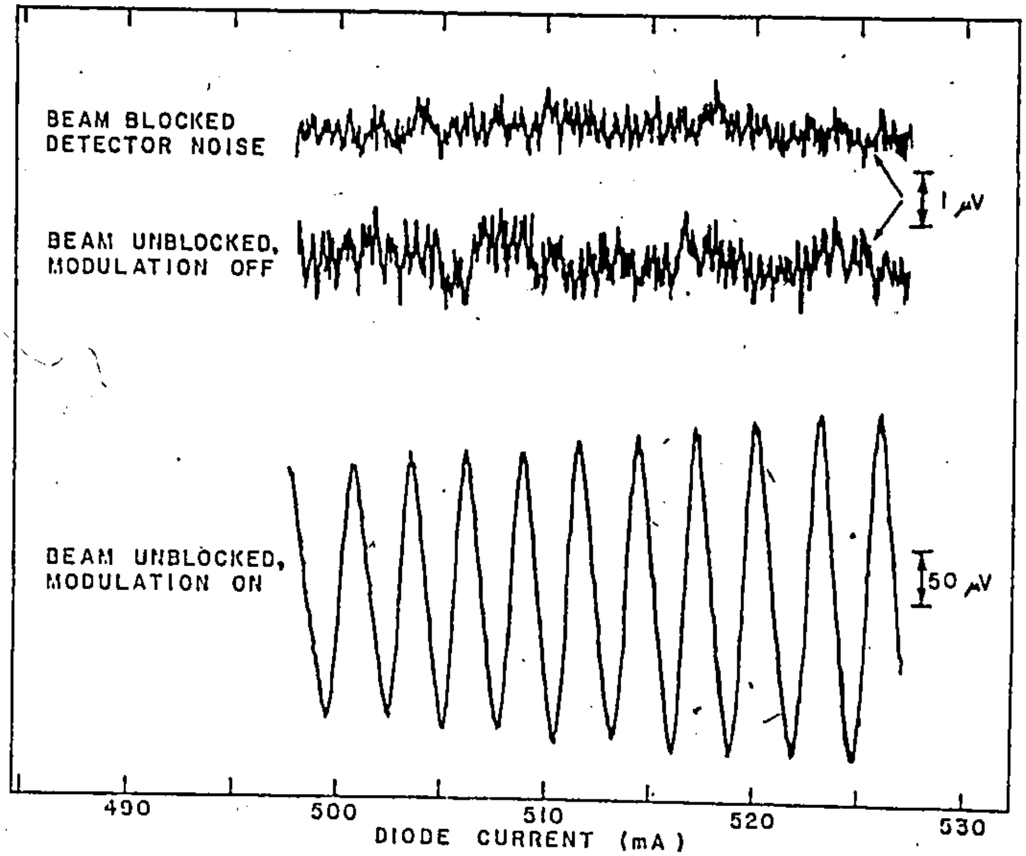

Figure 9.2 Lock-in amplifier output using the second harmonic detection scheme. In the absence of modulation, sensitivity is limited by detector noise. When a 1 kHz modulation is applied to the diode current, the interference fringes in the bottom trace appear. These fringes result from an etalon formed by two anti-reflection coated lenses in the beam path. The etalon spacing is 38 cm, with an effective reflectivity of 10^{-3}. After [75].

noise. The next trace was taken with the laser beam falling on the detector, but with no modulation applied to the diode. Note that there is only a small increase in noise, even though approximately 10 μW of power was incident on the detector. This gave a potential maximum SNR value of > 10^6 with the employed detector. Unfortunately, when modulation was applied to the diode, the bottom trace was obtained. These fringes have amplitudes much greater than detector noise, and correspond to interferences between scattered and reflected beams in the optical path. In a sense, the diode wavelength was being tuned through a series of Fabry-Perot fringes. By measuring the fringe spacing and amplitude we were able to determine the physical elements involved in the "etalon". The fringes in Fig. 9.2 were caused by two anti-reflection coated lenses in the beam, with a lens spacing of 38 cm and effective etalon reflectivity ∿ 10^{-3}.

For detection at atmospheric pressure, we mentioned in Chapter 8 that the sensitivity depends on how accurately one can produce and measure the background (zero-pollutant) signal. The relatively large amplitude of modulation applied at 1 atm produces a large background signal which is not the case at reduced pressures. Therefore, greater care is required to ensure that the resulting signal is a true background due to the laser behaviour and not a wide fringe caused by optical components. To perform these measurements, the White cell was filled with 1 atm of pure N_2, and the laser (which was emitting in the ν_3 band of SO_2) was scanned over a spectral region (e.g., the region marked by 2 in Fig. 8.14) with the modulation on. Figure 9.3 shows typical 2f scans of the diode laser over this region. Traces marked by 1, 2, and 3 were taken with the White cell at 40, 200, and 300 m pathlengths, respectively. Trace 5 was taken at 100 m. It is clear that these traces are not true background but are results of fringes. By measuring the fringe spacing, we found that the only possible physical elements which may cause these fringes were the diode collecting 5 cm lens and a reflecting surface deep inside the cold head. We have confirmed this by blocking part of the beam between the collecting lens and the cold head window. Traces 4, 6, and 7 are the results of blocking part of the beam at different positions. Comparing these traces in Fig. 9.3, we conclude that the left part of the beam is responsible for creating such fringes. Similar fringes were observed involving the windows of the small 10 cm cell, and other optical components in the laser beam.

It is necessary to carefully design the optical beam handling and the absorption cell to minimize such effects. Careful design of the absorption cell, together with slight angular misalignment of the optical elements in the beam path, allows the reduction of these effects.

9.4 Atmospheric Measurements Noise

In the case of pollutants detection in the atmosphere (see Fig. 8.2), the fringes caused by multi-pass White cells do not exist. The total pathlength (1.2 km) is obtained by the laser beam round

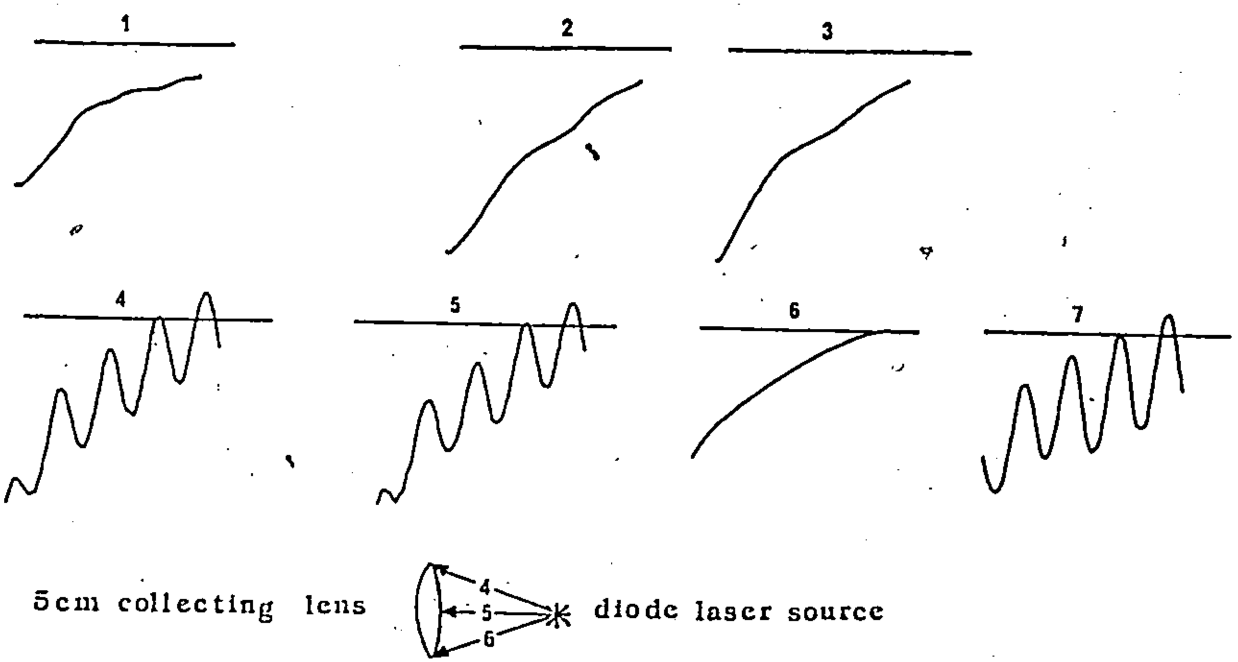

Figure 9.3 Different lock-in amplifier outputs with the modulation on. The top three scans 1, 2, and 3 are taken over the region 1331.5 (see Fig. 8.13) with the White cell at 40, 200, and 300 m pathlength, respectively. All the four traces 4, 5, 6, and 7 are taken with the White cell at 100 m. All the seven scans shown are taken with the White cell filled with dry nitrogen. The difference between these scans in the bottom is the result of blocking part of the laser beam before it enters the 5 cm collecting lens. Note that scan No. 6 is the optimum one and resulted by blocking the part of the beam which creates the shown fringes in scans 4, 5, and 7.

trip into the atmosphere. However, such fringes may be produced by other optical components (e.g., small 10 cm cell, and between the beam-splitter and detector lens), but it is easy to eliminate these fringes. Also, great care is required (to eliminate fringes) when a retroreflector is used near the laser to obtain the background (zero-pollutant) signal. In the following we describe other sources of noise rather than these fringes.

9.4.1 Vibration and Stability

The mounts for shaft mirrors (see Fig. 8.2) were worked to rest on stubby triangular bases; this improved stability to what is probably the limit attainable in the laser laboratory building at McMaster University Medical Centre (MUMC). From beam alignment experiments, it physically appears that MUMC is fairly stable during the night, but bends a few minutes of arc at about 8:30 a.m. and continues to move around until 10:30 p.m. However, if the building is to be seriously used as a laser base, experiments should be made to characterize total image motion and vibration, and to separate building motion from atmospheric effects. In Fig. 9.4, a possible coaxial system for diode lasers is shown. Once aligned, the entire unit is pointed at distant targets. Such a unit could be reasonably portable, compact, and separated from the building vibrations. Coaxial optics offer some advantages over beam-splitters, since there is no scattered light from a partial mirror and the system operates at any wavelength. However, the aperture of the transmitter (or receiver) is restricted to 1/2 or 1/3 that of the other, and the central part of the beam is

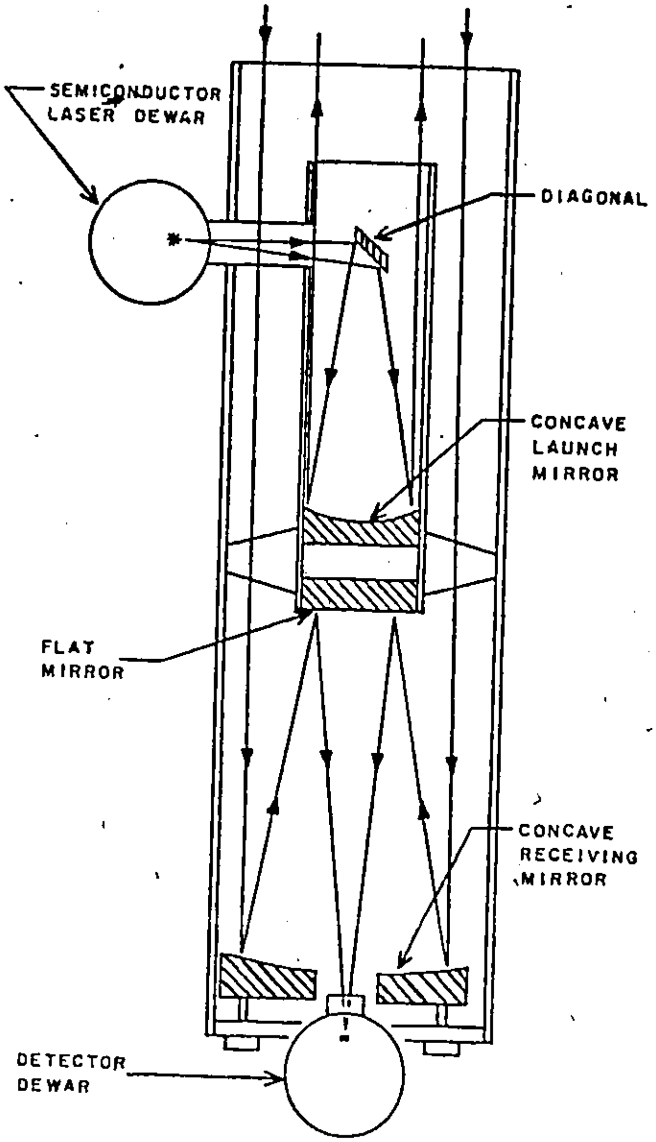

Figure 9.4 A possible coaxial beam launching and receiving telescope containing the semiconductor diode source and detector in one unit. A proposed portable system.

lost.

9.4.2 Beam Focus

It is important to focus the outgoing laser beam on the retroreflector if maximum energy is to be intercepted by the retroreflector. However, early experiments (employing the Molectron CO_2 laser) suggested that the focussed beam might scintillate more than a defocussed beam, presumably caused by the focussed beam wandering off the retroreflector entirely or partly. Thus it was necessary to measure both returned power and noise as a function of focus. It was found that power rises sharply at the best focus, while noise, measured as the peak to peak variation in 120 seconds divided by the average total power, is roughly constant. Under markedly different conditions of turbulence, this may not be true.

9.4.3 Scintillation

Although the second harmonic detection technique, together with the ratioing technique has been proved to be the only feasible method for the reduction of laser power fluctuations falling on a detector, we have found that it is necessary to describe the atmospheric scintillation.

The intensity of a laser beam propagating in the atmosphere is randomly amplitude modulated. Reviews of the literature dealing with this scintillation problem are given in [94] and [95]. Experimental results about CO_2 laser radiation propagation are given in [96]. The variance of σ_I^2 of the natural logarithm of the normalized radiation intensity $\log_e I(R) / \overline{I(R)}$ as a function of range R and wavenumber ν is, by theory, predicted to be

$$\sigma_I^2 = \begin{cases} 12.8\, C_n^2\, l_o^{-7/3}\, R^3 , & (\lambda R)^{1/2} \ll l_o \\ 1.23\, C_n^2\, \nu^{7/6}\, R^{11/6} , & l_o \ll (\lambda R)^{1/2}\, L_o \end{cases} \qquad (9.1)$$

where l_o is the inner and L_o the outer scale size of the turbulence and λ is the wavelength of the laser beam. Plane wave propagation in a homogeneous medium and detection in a point have then been assumed. Typical values of l_o and L_o are 3×10^{-3} m and 10 m, respectively, suggesting a wide range in which Eqn. 9.1 shall hold.

The present launching system when employing a cat's-eye retroreflector will be considered to have transmitting and receiving optics with large aperture areas. This means that the variance of $I(R) / \overline{I(R)}$ is reduced due to aperture averaging (see [94] , [95]). For example, at 10 μm, a 30 cm diam beam is about 3.5D, where D, the transverse correlation distance of the log intensity, is approximately given by the first Fresnel zone diameter $(2 / \pi\lambda R)^{1/2}$. R is the range. For the above conditions, a reduction of about 80% in atmospheric turbulence noise is possible for an average value of the turbulence parameter $C_n^2 \rangle = 1 \times 10^{-4}\ m^{-2/3}$. The noise reduction is more than two times as great as that for a 10 cm beam retroreflected by a 10 cm corner-cube retroreflector.

Figure 9.5 shows the effects of increasing the retroreflector area on the SNR.

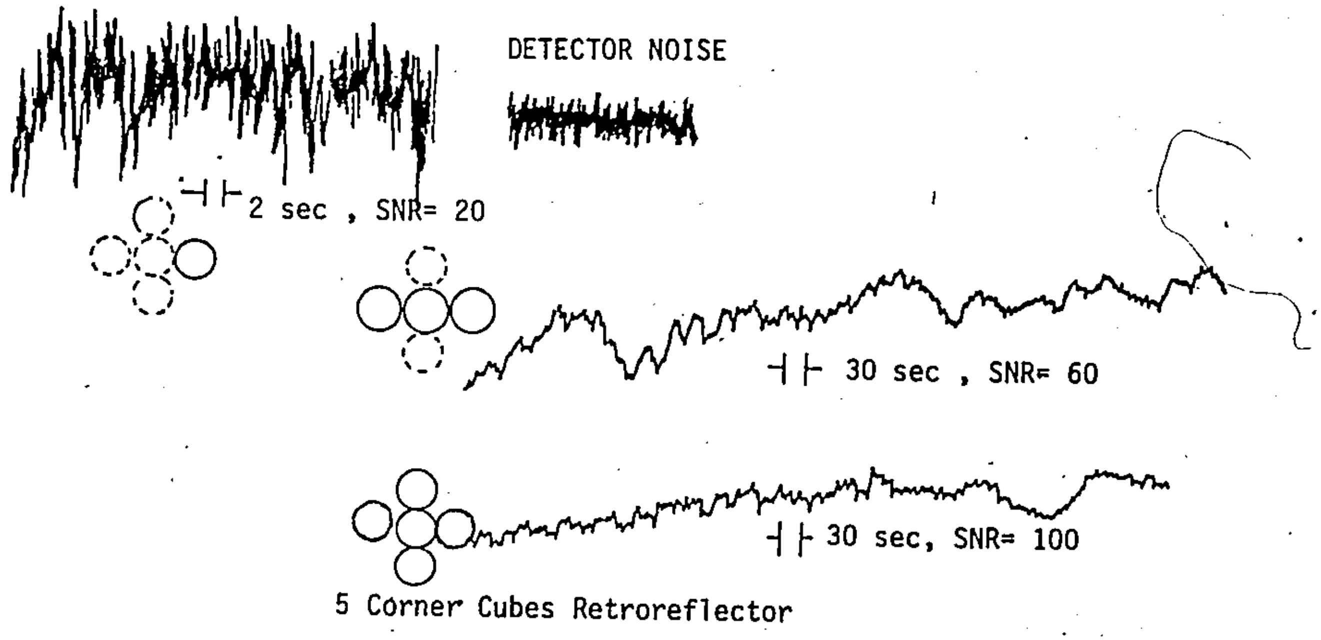

Figure 9.5 Typical results showing the effect of increasing the retroreflector area. Note that as the area of the retroreflector is increased the scintillation decreased.

CHAPTER 10

SUMMARY AND CONCLUSIONS

Employing the resonance absorption scheme, we report theoretical and experimental techniques which are useful in molecular spectroscopic studies and in the development of a Laser Absorption Spectrometer (LAS). This LAS marks a significant step forward in the application of a tunable laser to point and long-path monitoring of atmospheric pollutants.

We have described, in Chapter 1, the advantages of using lasers as a light source in optical monitoring techniques in general, and in a resonance absorption scheme in particular. The latter is advantageous because it is the most sensitive and requires the least amount of laser power. Consequently, it promises to be the simplest and least expensive system.

Both fixed-frequency and tunable lasers have been employed in this Thesis. The distinction between tunable and fixed-frequency lasers is not as clear as one might first believe. A reasonable definition of a tunable laser is one that is continuously tunable over 1 cm^{-1} or more and has a total tuning range of hundreds of cm^{-1}; a fixed-frequency laser is one that cannot be tuned over more than a small fraction of a cm^{-1} (e.g., ~ 0.002 cm^{-1} for a low-pressure CO_2

laser transition). A fixed frequency laser may often be step-tuned from one transition to another - and for this reason these lasers seldom match perfectly with the absorption lines of molecules to be detected. With the availability of tunable ir lasers, it is possible to ideally match pollutant absorption lines. The most useful type of tunable laser for pollution monitoring is the lead-salt semiconductor diode laser because it is simple, and can be made to emit in the infrared "fingerprint" region of most molecules. In addition, it has a narrow linewidth. Very recently, Preier [97] reviewed the fundamental material properties, device technology, laser properties, and applications of lead-salt diode lasers.

In Chapter 2, we described the lasers which have been used in this thesis. An experimental technique for determining semiconductor diode laser characteristics is described. These characteristics (e.g., wavelength coverage, tuning rates, single mode operating regions, and frequency stability) are very important parameters which must be known prior to applying such lasers.

As a starting point in the design of a resonance absorption pollution monitor (especially one which employs a fixed-frequency laser), theoretical calculations of laser transmission through the atmosphere must be carried out. To perform such calculations, it is necessary to know accurately the band spectra of both pollutant gases and normal atmospheric absorbing gases, together with values for their ir absorption coefficients. We review the molecular absorption theory in Chapter 3. This theory enabled us to develop a computer software package which proved to be both accurate and efficient. The three main subroutine subprograms, written in Fortran IV, are as follows:

(1) A subroutine for generating molecular absorption lines positions,

(2) A subroutine for generating lines intensities,

(3) A subroutine for generating absorption (transmission) spectra of any gas within a selected wavelength region, and at any pressure.

Much of the data which can be generated by the first two subroutines is available in the literature. However, the available data is often in a form which cannot be used directly, is not available, or is not accurate enough. Therefore, it is necessary for an air pollution laboratory to have such programs to generate the individual line parameters of a gas from its molecular constants. New data can be obtained experimentally, for special cases, and for relatively narrow spectral regions, by employing lasers. One of our computer subroutine subprograms has been used recently by Taylor et al [98] to generate the CO_2 laser gain code at multiatmosphere pressures.

To establish some useful criteria for pollution monitoring via the "direct" resonance absorption scheme, measurements on ozone with a line-tunable CO_2 laser have been performed and reported in Chapter 4. We conclude that, if fixed frequency laser systems are employed, a frequency mismatch of up to $\Delta\nu_n = 0.001\ cm^{-1}$ can easily be tolerated provided that there are no neighboring absorption lines due to foreign species within ± $0.1\ cm^{-1}$, or that the absorption intensity of such foreign species lines is more than an order of magnitude less than the intensity of the gas species being monitored. Reduced pressure measurements, such as employed in Chapter 4 on ozone, are a useful experimental tool for establishing such criteria. Whether these criteria can be met for every pollutant gas is in doubt, as the measurements on ozone indicate. The density of ozone absorption lines is so great that it appears impossible to find a region where nearest neighbor contributions can be neglected. Although these nearest neighbors are all part of the ozone system, they can serve to represent the effect of interfering foreign species lines. If fixed frequency laser systems are to be effectively employed, monitoring likely has to be carried out at, e.g., two CO_2 transitions such as P(8) and P(12). Thus, the ratio of the absorptions at the two transition frequencies would probably serve as a positive identification of the ozone species. However, the ability to match laser lines with gas species lines to within 0.001 cm^{-1} (30 MHz) may prove difficult for the majority of gases that one would want to detect as pollutants. Consequently, a fully-tunable laser system is probably the best route to follow, with a scan through two or more adjacent absorption lines to ensure that the effects of interference from foreign species is eliminated.

As mentioned previously, the use of "direct" absorption laser techniques for monitoring of a pollutant gas requires an accurate knowledge of a number of spectroscopic parameters. In particular, it is important to have good values for the location and the absorption of suitable pollutant transitions. To provide such information on NO, we have exploited the coincidences between CO laser lines and NO absorption lines to experimentally perform spectroscopic studies. In Chapter 5, we have reported measurements on seventeen NO lines which showed significant absorption with the line-tunable CO laser source. The absolute absorption as a function of pressure has been determined. As a result, we have been able to establish accurate values for the absorption of atmospheric NO at the pertinent CO laser wavelengths. For the experimental data we have also deduced the separation $|\Delta\nu_n|$ between the appropriate NO and CO wavelengths, the NO/N_2 pressure-broadening, the NO band strengths, and the individual NO line strengths. A knowledge of both the absorption and the pressure-broadening parameters is essential for pollutant sensing using either long atmospheric paths or point monitoring employing a multi-pass absorption cell operating at reduced gas pressure. We have determined all the available NO lines suitable for use with the CO laser. Further research is required to establish regions free of interference from other atmospheric gases when direct atmospheric monitoring is employed. However, the data presented in Chapter 5 are sufficient to design a point monitoring system, which is less susceptible to interference from other gases. In particular, water vapor (which is the source of considerable interference over long-pathlengths in this wavelength region) is easily removed prior to measurement.

The technique reported in Chapter 5 is a useful tool when a tunable laser is not available. However, for some applications, as in the case of employing CO_2 laser in ozone detection in the atmosphere, the linewidths of ozone have a HWHM of ∿ 30 MHz. Therefore, their line-center frequencies must be known to better than 10 MHz if the absorption data are to be used properly. For this reason, we have developed a simple technique for high resolution spectroscopy. This technique is described in Chapter 6, where we report the accurate frequency measurement of over 100 lines in the ν_3 band of ozone. These measurements were made with a tunable diode laser, a multi-pass absorption cell, and a temperature-stabilized germanium etalon. Despite the relative simplicity of the technique, we achieved an accuracy of better than 10 MHz in our measurements. This accuracy compares well with that achieved by the more complicated heterodyne techniques of high-resolution spectroscopy. In our measurements we have primarily concentrated on those ozone lines that are close to CO_2 laser lines. We have measured the frequencies of those reasonably strong ozone lines that lie within 6 GHz of the laser lines in the 9.4 μm region. These laser lines include most of the $^{12}C^{16}O_2$ lines and, in addition, selected isotopic and sequence lines, particularly those in close coincidence (< 300 MHz) with ozone lines. Diode lasers have been used previously to measure some individual absorption lines with accuracies of 15 MHz, and to analyze absorption bands with much reduced accuracies. However, we report here the first measurements over an entire absorption band using the full resolution of our tunable diode laser. The data reported in Chapter 6 is more than sufficient for a detailed band analysis of the ν_3 band of ozone. At present, the accuracy of our measurements is still limited by residual drifts of the etalon fringes. Better temperature stabilization or the use of an air-spaced actively-locked etalon will remove this limitation. The estimated accuracy of a tunable diode laser, in combination with a stabilized etalon, would then be limited simply by the accuracy with which one can judge the line center (1-3 MHz). Finally, it should be possible to automate much of the measurement procedure.

Up to this point, experimental and theoretical techniques have been demonstrated for spectroscopic studies of pollutant gases. These studies must be performed prior to the design of any pollution monitor based on the resonance absorption scheme. In Chapter 7, a laser absorption spectrometer which combines the sensitivity of acousto-optical methods with the convenience of direct, long-path optical detection has been demonstrated. This LAS employs tunable lasers and a second harmonic detection technique which has been developed at McMaster University Air Pollution Laboratory (MUAPL) [75]. A dramatic reduction of the system noise was achieved by using the second harmonic detection technique. A sensitivity of 3×10^{-8} m^{-1} is attained. This extremely high sensitivity was reached after locking the diode laser wavelength at the absorption line center and employing longer time constant. We have demonstrated the use of LAS for point monitoring of ambient concentrations of ozone at a sensitivity of 0.5 ppb, employing the same diode laser which was used in Chapter 6, and with the White cell set at 200 m. Employing another diode laser (discussed in Chapter 2), we have detected SO_2, N_2O, and NH_3 in the atmosphere with sensitivities of 2, 3, and 0.2 ppb, respectively. Furthermore, the present technique does not suffer from interference from unwanted molecular species, and can be easily calibrated even at the ppb concentration level. The LAS was zeroed by evacuating the White cell, and calibration was checked using a short cell containing a relatively high concentration mixture. At this time, a fully portable instrument is under development at the MUAPL. This instrument is based on a tunable semiconductor diode laser, and a relatively small commercial White cell capable of 50 m maximum pathlength.

Point monitoring (PM) permits the gas pressure to be reduced until the Doppler-broadened ir absorption structure is revealed, thereby making possible very high specificity along with the very high sensitivity. The present sensitivity of the LAS is more than sufficient for many practical applications, and we are still far from the ultimate limit given by detector noise. However, it is difficult to eliminate entirely the problems associated with PM of reactive gases such as NO and SO_2, which can be changed or converted during the sampling procedure. Remote long-path monitoring (LPM) yields values for the average pollutant concentration over the path, which is generally more meaningful for regional models than point monitoring. In addition, the LPM eliminates entirely the problems associated with the sampling procedure. However, LPM is not generally considered to be a substitute for point monitoring, but an adjunct to it. Nevertheless, in some cases, remote sensing represents the only economical or technically feasible technique.

A long-path station for monitoring atmospheric pollutants has been built and tested. Chapter 8 describes such a station using a second harmonic technique which has been modified to apply on an absorption dip instead of an isolated absorption line. At atmospheric pressure a number of pollutant absorption lines may combine to form an absorption dip of any shape and a relatively wide halfwidth ($\sim 0.2\ \mathrm{cm}^{-1}$). Therefore, the amplitude of the frequency modulation applied to the diode laser is about 15 times more than the one applied at reduced pressures on an isolated absorption line (these values are valid only at $1160.8\ \mathrm{cm}^{-1}$ in the ν_1 band of SO_2, and may be different for another gas or region). The large modulation amplitude resulted in a high zero-pollutant reference signal (background signal). This background signal must be measured accurately in order to attain high detection sensitivity. The response of the system to a pollutant concentration is the result of subtracting two signals, one with zero-pollutant, and the other with the pollutant present. The zero-pollutant reference signal may be obtained by one of the following techniques:

(1) Employ another retroreflector near the laser in a laboratory or in a van (portable type station). The resulted pathlength L is essentially equal to zero. Hence, the recorded system response is due to zero-pollutant concentration.

(2) Tune the diode laser current away from the absorption line. This technique is valid only for monitoring simple, linear, or symmetric-top molecules such as NO, CO, CO_2, N_2O, NH_3, ... etc., where the absorption lines at atmospheric pressure are separated from each

other and the absorption between two adjacent lines is approximately constant or zero.

(3) Employ two short 10 cm cells containing two known pollutant gas concentrations. Chapter 8 describes this technique, which has been used for background compensation.

In Chapter 8, we report theoretical and experimental absorption data for SO_2, N_2O, H_2O, NH_3 and O_3 in the spectral region 1100-1200 cm^{-1}. This data is useful as a starting point in the design of a long-path pollution monitor of single- or multi-pollutants into the atmosphere. Our calculations and observations indicate that the selected region near 1160.8 cm^{-1} is relatively free from H_2O interference effects. Here, an H_2O concentration variation from 25% R.H. to 75% R.H. is equivalent to 5 ppb of SO_2 in 1.2 km. These values may be different for other spectral regions.

The non-perfect reproducibility of the system response to a known low concentration of SO_2 give a limit of 50 ppb on the minimum detectable SO_2 concentration. This concentration is the average value over a 600 m pathlength (one way); the total pathlength which was used in our calculations was 1.2 km (round trip). This pathlength was achieved by employing an off-axis telescope at the laboratory and 5 small corner cubes for the retroreflector placed on the roof of another building at 600 m distance from the laboratory roof building. The most serious limitation was due to the laser beam wandering. This can be reduced by using larger retroreflector. Our calculations and observations indicate that it is possible to obtain a detection sensitivity of 10 ppb of SO_2 in 1.2 km, employing a diode laser radiating in the ν_1 band of SO_2. This higher sensitivity can be achieved by improving the present transmitter-receiver optical system (e.g., switching to a Cat's eye retroreflector system and data processing (e.g., digitalization of the data for processing with a computer).

Chapter 8 also contains theoretical and experimental investigations of SO_2, CH_4, H_2O, and N_2O in the region 1300-1400 cm^{-1} (ν_3 band of SO_2). These investigations indicate that it will be possible to achieve additional improvement in the detection sensitivity by employing a diode laser emitting in the ν_3 band of SO_2. We report an optimum microwindow spectral region near 1331.5 cm^{-1} for SO_2 monitoring in the atmosphere. We report also an optimum pathlength of 500 m and two spectral regions near 1331.35 cm^{-1} and 1331.63 cm^{-1}. The first region is free from H_2O interference effects with 500 m pathlength; the other region suffers from H_2O interference effects. However, one can scan the diode over these two regions and apply an analytical technique to estimate H_2O and SO_2 concentrations simultaneously.

The feasibility of laser monitoring of atmospheric pollutants by the resonance absorption technique has been demonstrated in Chapter 7 for point monitoring, and in Chapter 8 for long-path monitoring. The attained detection sensitivities were achieved after employing the second harmonic detection technique and eliminating the effects due to system noise sources. These sources are described in detail in Chapter 9, where we demonstrate the advantages of employing the second harmonic technique. The main advantage of applying such a technique is the dramatic reduction of the noise which results from laser power fluctuations. However, modulating the diode laser resulted in another kind of noise which is due to optical feedback (fringes). We describe these fringes in Chapter 9, along with a method of eliminating such fringes.

Atmospheric noise, other than that mentioned above, is described in Chapter 9. Long-term effects due to atmospheric turbulence and scattering unrelated to absorbing molecules are eliminated electronically by rationing the second harmonic and the chopped signals, since both are affected similarly by such influences. Finally we describe in Chapter 9 the possibility of improving the stability, sensitivity, and portability of our atmospheric monitoring system.

APPENDIX A

CALCULATIONS OF PARAMETERS OF ABSORPTION LINES FOR ASYMMETRIC ROTORS

"AROTOR" is a Fortran IV computer program which we have developed to generate line positions and intensities of any asymmetric rotor molecule (e.g., SO_2, H_2S, O_3, H_2O, HDO, NO_2, ... etc.). The inputs to the program are the molecular constant, the band strength, the axis of rotation, and the selection rules of the molecule under consideration.

Definitions of Variables

Section A1, The inputs to the program are read in this section as following:

VK1, VK2:	Lower and upper state value of κ, respectively.
OMG:	Band center (cm^{-1}).
OSO:	Abundance of isotopic species (percentage).
SP:	Total band strength (cm^{-2} atm^{-1}).
Q:	Total partition function value.
GO:	Lower state vibrational energy (cm^{-1}).
TEMP:	Temperature ^oK.
CEX:	constant = kT/h.
IBAND:	Number of bands to be performed.

IAXIS:	Rotation axis: a, b, or c. IAXIS = 1 for a, IAXIS = 2 for b, and IAXIS = 3 for c.
JI:	The minimum value of J (Quantum number).
JF:	The maximum value of J.
C1:	$(A_v - C_v)/2$ of the lower state (cm^{-1}).
C2:	$(A_v + C_v)/2$ of the lower state (cm^{-1}). C3 and C4 are the same as C1 and C2, respectively, but for the upper state. Here, A_v, C_v are the molecular vibrational constants.

Section A2

IITOT:	Number of all P, Q, and R transitions.
M1(1):	J number of a lower state, while
M1(2):	J number of its upper state.
ICC:	equal to 0 for Q branch, 1 for R or P branch.

This section generates also the constants H, F, G, and A as described in Table II of reference [30]. We have used type II^{ℓ} in our calculations.

Section A3

In this section, the submatrices E^+, E^-, O^+ and O^- are generated into the subroutine subprogram "SUBMTX" for the lower and upper states. This subroutine evaluates also all the eigenvalues of each matrix. The theory used to generate these matrices is in reference [30]. The outputs of "SUBMTX" are:

TEPD, AB1D: E^+ matrix and its eigenvalues, respectively, for the lower state.

TEND, AB2D: Same for E^-.

TOPD, AB3D: Same for O^+.

TOND, AB4D: Same for O^-.

For all the above and following definitions, we have replaced the last character, D, by U for the same calculations but for the upper state. For example, TEPD is E^+ matrix for the lower state, while TEPU is E^+ for the upper state.

ABTOTD, ABTOTU: Arrays contains all the eigenvalues of the four submatrices E^+, E^-, O^+, and O^-.

BD, BU: Are outputs of the subroutine "ORD" which arrange the arrays ABTOTD and ABTOTU in descending order.

Subroutine "ARRGE" is used in this section to provide each one of the matrices E^+, E^-, O^+, and O^- with its row and column values of K_{-1} and K_{+1}, as following:

NK1D: K_{-1} for the lower state of E^+.

NK2D: K_{-1} for the lower state of E^-.

NK3D and NK4D are for O^+ and O^-, respectively.

NP1D, NP2D, NP3D, NP4D are for K_1 of the lower state of E^+, E^-, O^+, O^-, respectively.

BEPD: Arranged eigenvalues of E^+ in the lower state, while BEND, BOPD, BOND are the same for E^-, O^+, O^- ~~in~~ the lower state.

Subroutine "FINSUB" generates the final matrix T which is described in reference [30].

The generated matrix is "AAV" for each of the matrices E^+, E^-, ..., then each one is stored in its array. For example, AAV of E^+ is stored in the array TEPD, AAV of E^- in the array TEND, ... etc.

Note: In the above definitions, the last character D or U indicates that the calculations are in the lower or upper state.

Section A4

Up to this point, we have calculated the matrices T and T' described in references [30, 32]. To calculate the rotational dipole matrix $|\mu|^2$, we have used the following equation [32],

$$|\mu|^2 = T_1' \quad \Phi_{F_g} \, T_2$$

Φ_{F_g} is the symmetric direction cosines matrix. We have followed the theory described in [99] to calculate Φ_{F_g}. Eighteen different matrices were used according to Table 1 in reference [99]. These eighteen matrices could be constructed using five different subroutines "R1", "R2", "R3", "Q1", and "Q2". These subroutines are classified with respect to the selection rules and the rotation axis IAXIS as described in Fig. 1 in [99]. Subroutine "FRQAST" performs the last calculation which is defined above. This subroutine generates all the desired line positions and strengths for the given transitions. This data needs to be sorted in ascending or descending order with respect to line positions.

Typical output of "AROTOR" is shown in Fig. A-1 for the ν_3 band of $^{32}S^{16}O_2$ molecule. The molecular constants and the absorption data are the same as in reference [100]. Where,

J = Lower state J number.
J1 = Upper state J number.
K = K_{-1}
FRQUENCY = Transition frequency $J \rightarrow J_1$ (cm^{-1}).
ROTA. STR. = Rotational dipole matrix element.
RELAT. STR. = Relative strength.
ABS. STR. = Absolute strength (cm^{-2} atm^{-1} x 1000).
LOW ENG. = Lower state energy (cm^{-1}).
UPP. ENG. = Upper state energy (cm^{-1}).
EIG. LOW. = Eigenvalue used in lower state.
UPP. EIG. = Eigenvalue used in upper state.
LINE ISOTOPIC = Isotopic identification, 3216 is for $^{32}S^{16}O_2$, while 001 refers to v_1 v_2 v_3 and $v_3 = 1$ for the ν_3 band.

Figure A-1 Typical output of "AROTOR" for the ν_3 band of $^{32}S^{16}O_2$.

```
 J.  J1   K    FREQUENCY   ROTA.STR.   RELAT.STR.    ABS.STR.   LOW ENG.   UPP ENG.   EIG.LOW.   UPP EIG.   LINE ISOTOPIC
290

 25  25  10   1375.9109    22.1559      3.6474      42.0351    378.0097   391.8916  -433.3416  -483.9301     32160001
 25  26   8   1376.6033    23.5412      5.2051      59.9867    316.6549   331.2237  -504.1271  -554.7063     32160001
 25  25   6   1377.1642    24.6193      6.8417      78.6479    269.1050   284.2397  -558.9359  -609.5296     32160001
 25  25   4   1377.5664    25.3817      8.2926      95.5697    235.4461   250.9829  -597.8184  -648.3311     32160001
 25  25   2   1377.3165    25.7744      9.4784     109.2354    210.7603   226.0473  -626.2986  -677.4241     32160001
17
 26  27  26   1365.6329     1.9531       .0026        .0304   1377.9826  1381.5861   650.7795   598.3750     32160001
 26  27  24   1367.5136     5.6670       .0173        .1937   1237.2231  1212.7122   453.7784   401.3456     32160001
 26  27  22   1369.2442     9.0746       .0591        .6806   1050.1361  1057.3598   272.5401   220.0815     32160001
 26  27  20   1370.8246    12.1659       .1530       1.3213    905.7675   915.5026   107.0653    54.5838     32160001
 26  27  18   1372.2551    15.0010       .3630       4.1837    776.9435   757.1691   -42.6446   -95.1451     32160001
 26  27  16   1373.5359    17.5197       .7409       8.5382    660.8460   672.3524  -176.5673  -229.1056     32160001
 26  27  14   1374.6675    19.7422      1.3665      15.7430    558.4185   571.0565  -294.7587  -347.2901     32160001
 26  27  12   1375.6506    21.6655      2.2972      26.4740    459.6676   483.2838  -397.1513  -449.6909     32160001
 26  27  10   1376.4871    23.2986      3.5433      40.5355    334.6676   409.0552  -463.7488  -536.2894     32160001
 26  27   8   1377.1813    24.6327      5.0310      57.5806    333.2727   348.4245  -554.5113  -607.0434     32160001
 26  27   6   1377.7479    25.6712      6.5884      75.5269    235.7711   301.4895  -609.3144  -661.8007     32160001
 26  27   4   1378.3596    26.4268      7.9397      91.4914    253.0599   269.3906  -647.0536  -699.2520     32160001
 26  27   4   1361.9770      .0328       .0097        .1121    253.0599   253.0074  -647.0536  -718.3660     32160001
 26  27   2   1394.8324      .0499       .0164        .1892    236.5871   269.3906  -666.0584  -699.2520     32160001
 26  27   2   1378.4498    26.7555      8.7003     100.2678    216.5871   253.0074  -666.0584  -718.3660     32160001
 26. 27   0   1377.5223    26.9200      9.8011     112.9543    212.8771   228.3699  -693.4128  -747.1111     32160001
17
 26  27  25   1366.5921     3.8521       .0079        .2724   1290.8975  1295.4601   550.3086   497.8897     32160001
 26  27  23   1368.3977     7.4078       .0333       1.1520   1126.9742  1133.3424   361.1089   308.7429     32160001
 26  27  21   1370.0531    10.6673       .0938       3.4161    975.7138   984.7375   197.6322   135.3618     32160001
 26  27  19   1371.5586    13.6305       .2435       8.4174    840.1173   849.6464    30.2396   -22.2527     32160001
 26  27  17   1372.9142    16.2974       .5256      18.1738    717.1663   728.0710  -111.5970  -164.0974     32160001
 26  27  15   1374.1203    18.6640      1.0131      35.2007    607.9232   620.0146  -237.6448  -290.1702     32160001
 26  27  13   1375.1775    20.7424      1.7912      51.9257    512.3329   525.4805  -347.9281  -400.4643     32160001
 26  27  11   1376.0870    22.5256      2.8332      99.6941    430.4249   444.4824  -442.4261  -494.9673     32160001
 26  27   9   1376.8515    24.0026      4.2554     147.4719    352.2205   377.0428  -521.1138  -573.6508     32160001
 26  27   7   1377.4784    25.1859      5.9154     201.0634    307.7783   323.2277  -583.9239  -636.4391     32160001
 26  27   5   1378.0116    26.0807      7.3134     252.8540    267.3551   283.3372  -630.5611  -682.9734     32160001
 26  27   5   1355.0793      .0119       .0033        .1136    267.3551   260.4046  -630.5611  -709.7352     32160001
 26  27   3   1378.6602    26.7036      8.3393     290.0521    243.7741   259.4048  -657.7667  -709.7352     32160001
 26  27   3   1360.6508      .0182       .0056        .1952    243.7741   242.3954  -657.7667  -730.7472     32160001
 26  27   1   1395.9343      .0287       .0039        .3426    226.5000   260.4048  -677.6959  -709.7352     32160001
 26  27   1   1377.9249    26.7893      9.1339     315.9672    225.5000   242.3954  -677.6959  -730.7472     32160001
15
 27  28  27   1365.2076     1.9644       .0016        .0545   1435.6888  1408.8669   702.8094   648.4640     32160001
 27  28  25   1367.1635     5.6789       .0107        .3699   1308.1040  1313.2390   497.9283   443.5534     32160001
 27  28  23   1368.9692     9.1077       .0377       1.3046   1144.1818  1151.1215   308.8098   254.4080     32160001
 27  28  21   1370.6247    12.2505       .1045       3.6136    993.9229  1002.5151   135.4548    81.0257     32160001
 27  28  19   1372.1303    15.1051       .2436       8.5938    857.3283   867.4292   -22.1355   -76.5829     32160001
 27  28  17   1373.4862    17.6799       .5252      18.1536    734.3999   745.5566  -163.9591  -218.4247     32160001
 27  28  15   1374.6926    19.9658      1.0130      34.6763    625.1406   637.8037  -290.0125  -344.4927     32160001
 27  28  13   1375.7503    21.9651      1.7471      60.4042    529.5550   543.2758  -400.2992  -454.7796     32160001
 27  28  11   1376.6605    23.6308      2.7323      96.5337    447.6572   462.2882  -494.7765  -549.2710     32160001
 27  28   9   1377.4263    25.1101      4.1034     142.0732    379.4691   394.8659  -573.4458  -627.9342     32160001
 27  28   7   1378.0559    26.2541      5.5313     192.9673    325.0594   341.0858  -636.2187  -693.6839     32160001
 27  28   5   1378.5627    27.1119      7.0308     242.0452    284.6204   301.1536  -682.8736  -737.2708     32160001
 27  28   3   1378.6588    27.6322      9.1667     282.3555    256.4997   273.1293  -715.3166  -769.9676     32160001
 27  28   1   1379.0640    27.9194      9.4121     325.4141    228.9918   245.0264  -747.0527  -802.7558     32160001
15
 27  28  26   1366.2043     3.8574       .0048        .0551   1335.1866  1399.3634   598.3386   544.0391     32160001
 27  28  24   1368.0851     7.4290       .0209        .2412   1224.4351  1230.4906   401.3387   347.0130     32160001
 27  28  22   1369.8157    10.7143       .0542        .7402   1067.3444  1075.1306   220.1618   165.7475     32160001
 27  28  20   1371.3963    13.7152       .1535       1.8331    923.9175   933.2842    54.6390      .2518     32160001
 27  28  18   1372.8270    16.4297       .3562       4.2206    794.1557   804.9532   -95.0183  -149.4752     32160001
 27  28  16   1374.1080    18.8565       .7345       8.4653    679.0614   690.1339  -228.9574  -283.4307     32160001
```

```
      PROGRAM AROTOR(INPUT,OUTPUT,TAPE5=INPUT,TAPE6=OUTPUT)
      DIMENSION AAV(26,26)
      DIMENSION VL(2),M1(2)
      DIMENSION FI(26,26)
      DIMENSION TEPD(26,26),TEND(26,26),TOPD(26,26),TOND(26,26)
      DIMENSION TEPU(26,26),TENU(26;26),TOPU(26,26),TONU(26,26)
      DIMENSION AB1D(26),AB2D(26),AB3D(26),AB4D(26)
      DIMENSION AB1U(26),AB2U(26),AB3U(26),AB4U(26)
      DIMENSION ABTOTD(101),ABTOTU(191),BD(101),BU(101)
      DIMENSION BEPD(26),BEND(26),BOPD(26),BOND(26)
      DIMENSION BEPU(26),BENU(26),BOPU(26),BONU(26)
      DIMENSION NK1D(26),NP1D(26),NK2D(26),NP2D(26),NK3D(26),NP3D(26)
      DIMENSION NK4D(26),NP4D(26),NK1U(26),NP1U(26),NK2U(26),NP2U(26)
      DIMENSION NK3U(26),NP3U(26),NK4U(26),NP4U(26)
C
CCCCC                                   SECTION A1
C
      WRITE(6,1)
    1 FORMAT(2X,*J.*,1X,*J1*,2X,*K *,2X,*FRQUENCY*,3X,*ROTA STR  *,2X,*R
     1ELAT STR  *,3X,*ABS STR  *,3X,*LOW ENG *,3X,*UPP ENG*,3X,*EIG LOW*
     2,3X,*UPP EIG*,3X,*LINE ISOTOPIC*)
      READ(5,*)IAXIS,IBANDS
      READ(5,*)OSO,CEX,QR,TEMP
      DO 1020 IIKK=1,IBANDS
      READ(5,*)JF,JI,C1,C2,C3,C4
      READ(5,*)VK1,VK2,SP,OMG,CO,IDNT
      SO=OSO*SP/100.
      ITRAC=IDNT
C
CCCC                                    SECTION A2
C
      N1=(JF-JI)+1
      N2=N1-1
      IITOT=3*JF-3*JI+1
      DO 7770 IKI=1,IITOT
      IF(IKI.LE.N1) GO TO 1919
      GO TO 2929
 1919 M1(1)=JI-1+IKI
      M1(2)=M1(1)
      ICC=0
      GO TO 5959
 2929 IF(IKI.LE.(N1+N2)) GO TO 3939
      GO TO 4949
 3939 M1(1)=IKI-N1+JI-1
      M1(2)=M1(1)+1
      ICC=0
      GO TO 5959
 4949 M1(2)=IKI-(N1+N2)+JI-1
      M1(1)=M1(2)+1
      ICC=1
 5959 VL(1)=VK1
      VL(2)=VK2
      DO 9010 IK=1,2
      J=M1(IK)
      VK=VL(IK)
      H=1.
      F=0.
      G=VK
      A=0.
      C=VK
C
C
CCCC                                    SECTION A3
C
C
      IF(IK.EQ.2) GO TO 9000
      CALL SUBMTX(H,F,C,G,J,TEPD,TEND,TOPD,TOND,NEPD,NEND,NOPD,NOND,AB1D
     1,AB2D,AB3D,AB4D)
      GO TO 9010
 9000 CALL SUBMTX(H,F,C,G,J,TEPU,TENU,TOPU,TONU,NEPU,NENU,NOPU,NONU,AB1U
     1,AB2U,AB3U,AB4U)
 9010 CONTINUE
      DO 9100 I=1,NEPD
```

```
 9100 ABTOTD(I)=AB1D(I)
      DO 9200 I=1,NEND
 9200 ABTOTD(I+NEPD)=AB2D(I)
      DO 9300 I=1,NOND
 9300 ABTOTD(I+NEPD+NEND)=AB4D(I)
      DO 9400 I=1,NOPD
 9400 ABTOTD(I+NEPD+NEND+NOND)=AB3D(I)
      J=M1(1)
      J0=2*J+1
      J1=M1(2)
      DO 9101 I=1,NEPU
 9101 ABTOTU(I)=AB1U(I)
      DO 9201 I=1,NENU
 9201 ABTOTU(I+NEPU)=AB2U(I)
      DO 9301 I=1,NONU
 9301 ABTOTU(I+NEPU+NENU)=AB4U(I)
      DO 9401 I=1,NOPU
 9401 ABTOTU(I+NEPU+NENU+NONU)=AB3U(I)
      J01=2*J1+1
      CALL ORD(ABTOTD,BD,J0)
      CALL ORD(ABTOTU,BU,J01)
      CALL ARRGE(J,BD,BEPD,BEND,BOPD,BOND,NK1D,NP1D,NK2D,NP2D,NK3D,NP3D,
     1NK4D,NP4D,NEPD,NEND,NOPD,NOND)
      CALL ARRGE(J1,BU,BEPU,BENU,BOPU,BONU,NK1U,NP1U,NK2U,NP2U,NK3U,NP3U
     1,NK4U,NP4U,NEPU,NENU,NOPU,NONU)
      CALL FINSUB(TEPD,NEPD,BEPD,AAV)
 1002 DO 1111 IR=1,NEPD
      DO 1111 IC=1,NEPD
      ICR=IC
 1111 TEPD(IR,IC)=AAV(IR,ICR)
      CALL FINSUB(TEPU,NEPU,BEPU,AAV)
 1004 DO 1112 IR=1,NEPU
      DO 1112 IC=1,NEPU
      ICR=IC
 1112 TEPU(IR,IC)=AAV(IR,ICR)
      CALL FINSUB(TEND,NEND,BEND,AAV)
 1006 DO 2220 IR=1,NEND
      DO 2220 IC=1,NEND
      ICR=IC
 2220 TEND(IR,IC)=AAV(IR,ICR)
      CALL FINSUB(TENU,NENU,BENU,AAV)
 1008 DO 2229 IR=1,NENU
      DO 2229 IC=1,NENU
      ICR=IC
 2229 TENU(IR,IC)=AAV(IR,ICR)
      CALL FINSUB(TOPD,NOPD,BOPD,AAV)
      DO 3333 IR=1,NOPD
      DO 3333 IC=1,NOPD
 3333 TOPD(IR,IC)=AAV(IR,IC)
      CALL FINSUB(TOPU,NOPU,BOPU,AAV)
      DO 3334 IR=1,NOPU
      DO 3334 IC=1,NOPU
 3334 TOPU(IR,IC)=AAV(IR,IC)
      CALL FINSUB(TOND,NOND,BOND,AAV)
      DO 4444 IR=1,NOND
      DO 4444 IC=1,NOND
 4444 TOND(IR,IC)=AAV(IR,IC)
      CALL FINSUB(TONU,NONU,BONU,AAV)
      DO 4445 IR=1,NONU
      DO 4445 IC=1,NONU
 4445 TONU(IR,IC)=AAV(IR,IC)
C
C
CCCC                                   SECTION A4
C
C

      L=ICC
      IF(IAXIS.EQ.1) GO TO 9991
      IF(IAXIS.EQ.2) GO TO 9993
      IF(J.NE.J1) GO TO 8881
      CALL Q1(1,0,1,M,N,J,FI)
      CALL FROAST(NK1D,NP1D,NK3U,NP3U,J,J1,TEPD,TOPU,BEPD,BOPU,FI,M,N,L)
      CALL Q1(2,0,1,M,N,J,FI)
```

```
      CALL FRQAST(NK2D,NP2D,NK4U,NP4U,J,J1,TEND,TONU,BEND,BONU,FI,M,N,L)
      GO TO 7770
 8881 IF(ICC.EQ.1) GO TO 8882
      CALL R2(1,1,1,M,N,J1,FI)
      CALL FRQAST(NK1D,NP1D,NK4U,NP4U,J,J1,TEPD,TONU,BEPD,BONU,FI,M,N,L)
      CALL R2(2,1,1,M,N,J1,FI)
      CALL FRQAST(NK2D,NP2D,NK3U,NP3U,J,J1,TEND,TOPU,BEND,BOPU,FI,M,N,L)
      CALL R2(2,1,1,M,N,J1,FI)
      CALL FRQAST(NK3D,NP3D,NK4U,NP4U,J,J1,TOPD,TEND,BOPD,BENU,FI,M,N,L)
      CALL R2(1,1,1,M,N,J1,FI)
      CALL FRQAST(NK4D,NP4D,NK1U,NP1U,J,J1,TOND,TEPU,BOND,BEPU,FI,M,N,L)
      GO TO 7770
 8882 CALL R3(1,1,1,M,N,J1,FI)
      CALL FRQAST(NK4U,NP4U,NK1D,NP1D,J1,J,TONU,TEPD,BONU,BEPD,FI,M,N,L)
      CALL R3(2,1,1,M,N,J1,FI)
      CALL FRQAST(NK3U,NP3U,NK4D,NP4D,J1,J,TOPU,TEND,BOPU,BEND,FI,M,N,L)
      CALL R2(2,1,1,J1,FI)
      CALL FRQAST(NK4U,NP4U,NK3D,NP3D,J1,J,TENU,TOPD,BENU,BOPD,FI,M,N,L)
      CALL R2(1,1,1,M,N,FI)
      CALL FRQAST(NK1U,NP1U,NK4D,NP4D,J1,J,TEPU,TOND,BEPU,BOND,FI,M,N,L)
      GO TO 7770
 9993 IF(J.NE.J1) GO TO 7771
      CALL Q1(1,1,-1,M,N,J,FI)
      CALL FRQAST(NK1D,NP1D,NK4U,NP4U,J,J1,TEPD,TONU,BEPD,BONU,FI,M,N,L)
      CALL Q1(2,1,-1,M,N,J,FI)
      CALL FRQAST(NK2D,NP2D,NK3U,NP3U,J,J1,TEND,TOPU,BEND,BOPU,FI,M,N,L)
      GO TO 7770
 7771 IF(ICC.EQ.1) GO TO 7772
      CALL R2(1,0,1,M,N,J1,FI)
      CALL FRQAST(NK1D,NP1D,NK3U,NP3U,J,J1,TEPD,TOPU,BEPD,BOPU,FI,M,N,L)
      CALL R2(2,0,1,M,N,J1,FI)
      CALL FRQAST(NK2D,NP2D,NK4U,NP4U,J,J1,TEND,TONU,BEND,BONU,FI,M,N,L)
      CALL R3(1,0,1,M,N,J,FI)
      CALL FRQAST(NK3D,NP3D,NK1U,NP1U,J,J1,TOPD,TEPU,BOPD,BEPU,FI,M,N,L)
      CALL R3(2,0,1,M,N,J,FI)
      CALL FRQAST(NK4D,NP4D,NK2U,NP2U,J,J1,TOND,TENU,BOND,BENU,FI,M,N,L)
      GO TO 7770
 7772 CALL R3(1,0,1,M,N,J1,FI)
      CALL FRQAST(NK1U,NP1U,NK3D,NP3D,J1,J,TEPU,TOPD,BEPU,BOPD,FI,M,N,L)
      CALL R3(2,0,1,M,N,J1,FI)
      CALL FRQAST(NK2U,NP2U,NK4D,NP4D,J1,J,TENU,TOND,BENU,BOND,FI,M,N,L)
      CALL R2(1,0,1,M,N,J,FI)
      CALL FRQAST(NK3U,NP3U,NK1D,NP1D,J1,J,TOPU,TEPD,BOPU,BEPD,FI,M,N,L)
      CALL R2(2,0,1,M,N,J,FI)
      CALL FRQAST(NK4U,NP4U,NK2D,NP2D,J1,J,TONU,TEND,BONU,BEND,FI,M,N,L)
      GO TO 7770
 9991 IF(J.NE.J1) GO TO 6661
      CALL Q2(1,2,M,N,J,FI)
      CALL FRQAST(NK1D,NP1D,NK2U,NP2U,J,J1,TEPD,TENU,BEPD,BENU,FI,M,N,L)
      CALL Q2(2,1,M,N,J,FI)
      CALL FRQAST(NK3D,NP3D,NK4U,NP4U,J,J1,TOPD,TONU,BOPD,BONU,FI,M,N,L)
      GO TO 7770
 6661 IF(ICC.EQ.1) GO TO 6662
      CALL R1(0,1,J,M,N,FI)
      CALL FRQAST(NK1D,NP1D,NK1U,NP1U,J,J1,TEPD,TEPU,BEPD,BEPU,FI,M,N,L)
      CALL R1(1,2,J,M,M,FI)
      CALL FRQAST(NK3D,NP3D,NK3U,NP3U,J,J1,TOPD,TOPU,BOPD,BOPU,FI,M,N,L)
      CALL R1(1,3,J,M,N,FI)
      CALL FRQAST(NK4D,NP4D,NK4U,NP4U,J,J1,TOND,TONU,BOND,BONU,FI,M,N,L)
      CALL R1(2,4,J,M,N,FI)
      CALL FRQAST(NK2D,NP2D,NK2U,NP2U,J,J1,TEND,TENU,BEND,BENU,FI,M,N,L)
      GO TO 7770
 6662 CALL R1(0,1,J1,M,N,FI)
      CALL FRQAST(NK1U,NP1U,NK1D,NP1D,J1,J,TEPU,TEPD,BEPU,BEPD,FI,M,N,L)
      CALL R1(1,2,J1,M,N,FI)
      CALL FRQAST(NK3U,NP3U,NK3D,NP3D,J1,J,TOPU,TOPD,BOPU,BOPD,FI,M,N,L)
      CALL R1(1,3,J1,M,N,FI)
      CALL FRQAST(NK4U,NP4U,NK4D,NP4D,J1,J,TONU,TOND,BONU,BOND,FI,M,N,L)
      CALL R1(2,4,J1,M,N,FI)
      CALL FRQAST(NK2U,NP2U,NK2D,NP2D,J1,J,TENU,TEND,BENU,BEND,FI,M,N,L)
 7770 CONTINUE
 1020 CONTINUE
 9770 STOP
      END
```

```
      SUBROUTINE FRQAST(N1D,N2D,N1U,N2U,J,J1,TD,TU,B1D,B2U,FI,M,N,IK)
      DIMENSION N1D(1),N2D(1),N1U(1),N2U(1)
      DIMENSION FI(26,1),TD(26,1),TU(26,1)
      DIMENSION R(26,26),RG(26,26)
      DIMENSION B1D(1),B1U(1),B2D(1),B2U(1)
      DIMENSION JJ1(150),JJ(150),KK1(150),KK2(150),KK3(150),KK4(150)
      DIMENSION EED1(150),SS(150),SS1(150)
      DIMENSION EEU2(150),AAA1(150),AAA2(150)
      DIMENSION FF1(150),IJI(150)
      DIMENSION SSR(150)
      COMMON /ABC/ ITRAC
      COMMON /AAA/ C1,C2,C3,C4,OMG,SO,CEX,QR,VK1,VK2,CO
C
  202 JD=J*(J+1)
      J1D=J1*(J1+1)
      DO 100 IR=1,M
      DO 100 IC=1,N
      R(IR,IC)=0.
  100 RG(IR,IC)=0.
      IF(J.EQ.J1) GO TO 300
      IF(J.GT.J1) GO TO 400
      CO=1./(4.*(J+1))
      GO TO 500
  300 CO=(2.*J+1)/(4.*J*(J+1))
      GO TO 500
  400 CO=1./(4.*J)
  500 DO 600 IR=1,M
      DO 600 IC=1,N
      DO 600 I=1,M
  600 R(IR,IC)=R(IR,IC)+TD(I,IR)*FI(I,IC)
      DO 700 IR=1,M
      DO 700 IC=1,N
      DO 700 I=1,N
  700 RG(IR,IC)=RG(IR,IC)+R(IR,I)*TU(I,IC)
      ICOUNT=0
      DO 800 IR=1,M
      DO 800 IC=1,N
  303 K1=N1D(IR)
      K2=N2D(IR)
      K3=N1U(IC)
      K4=N2U(IC)
      IT=J+K1+K2
      KN=K3-K1
      KP=K4-K2
      VKP=KP
      VKP=ABS(VKP)
      VKN=KN
      VKN=ABS(VKN)
      IF(VKN.GT.2.OR.VKP.GT.3) GO TO 800
      KT=KN+KP
 1002 BD=B1D(IR)
      BU=B2U(IC)
      IF(IK.EQ.1) GO TO 2001
      ED1=C1*JD+C2*BD
      EU2=C3*J1D+C4*BU
      AA1=BD
      AA2=BU
      GO TO 3001
 2001 ED1=C1*J1D+C2*BU
      EU2=C3*JD+C4*BD
      AA1=BU
      AA2=BD
 3001 F1=OMG+(EU2-ED1)
      S=RG(IR,IC)**2*CO
      IF(S.LT..01) GO TO 800
      IF(K1.NE.IO(K1)) GO TO 909
      C=.25
      GO TO 808
  909 C=.75
  808 EDE=ED1+CO
      S1=S*SO*F1*EXP(-EDE/CEX)*1000.*C/(3.1415927*QR*OMG)
      SR=S*F1*EXP(-EDE/CEX)/OMG
      ICOUNT=ICOUNT+1
      I=ICOUNT
```

```
      AAA1(I)=AA1
      AAA2(I)=AA2
      EEU2(I)=EU2
      JJ1(I)=J1
      JJ(I)=J
      KK1(I)=K1
      KK2(I)=K2
      KK3(I)=K3
      KK4(I)=K4
      SSR(I)=SR
      EED1(I)=EDE
      SS(I)=S
      SS1(I)=S1
      FF1(I)=F1
      IJI(I)=ITRAC
  800 CONTINUE
      ITPE=ICOUNT
      WRITE(9)ITPE
      WRITE(6,*)ITPE
      IF(IK.EQ.0) GO TO 1009
      DO 1109 K=1,ITPE
       WRITE(9)JJ1(K),JJ(K),KK1(K),FF1(K),SS(K),SSR(K),SS1(K),EED1(K),EE
     1U2(K),AAA1(K),AAA2(K),IJI(K)
      IF(FF1(K).LT.1401.AND.FF1(K).GT.1299) GO TO 9011
      GO TO 1109
 9011 WRITE(6,1108)JJ1(K),JJ(K),KK1(K),FF1(K),SS(K),SSR(K),SS1(K),EED1(K
     2),EEU2(K),AAA1(K),AAA2(K),IJI(K)
 1109 CONTINUE
      RETURN
 1009 DO 1209 K=1,ITPE
       WRITE(9)JJ(K),JJ1(K),KK1(K),FF1(K),SS(K),SSR(K),SS1(K),EED1(K),EE
     1U2(K),AAA1(K),AAA2(K),IJI(K)
      IF(FF1(K).LT.1401.AND.FF1(K).GT.1299) GO TO 9022
      GO TO 1209
 9022 WRITE(6,1108)JJ(K),JJ1(K),KK1(K),FF1(K),SS(K),SSR(K),SS1(K),EED1(K
     2),EEU2(K),AAA1(K),AAA2(K),IJI(K)
 1209 CONTINUE
 1108 FORMAT(1X,2(1X,I2),2X,I2,2X,F10.4,7(1X,F10.4),2X,I10)
  707 RETURN
      END
```

```
      SUBROUTINE Q1(IA,IB,IM,MR,MC,J,FI)
      DIMENSION FI(26,1)
      DO 500 IR=1,MR
      DO 500 IC=1,MC
  500 FI(IR,IC)=0.
      IF(IA.EQ.2) GO TO 700
      DO 800 IC=1,MC
      IQ=2*IC-2
      FI(IC,IC)=J*(J+1)-IQ*(IQ+1)
  800 FI(IC,IC)=SQRT(FI(IC,IC))
      FI(1,1)=FI(1,1)*SQRT(2.)
      GO TO 900
  700 DO 100 IC=2,MC
      IQ=2*IC-2
      IR=IC-1
      FI(IR,IC)=J*(J+1)-IQ*(IQ+1)
  100 FI(IR,IC)=SQRT(FI(IR,IC))
  900 IF(IA.EQ.2) GO TO 200
      DO 300 IR=2,MR
      IC=IR-1
      IQ=IR+IC-2
      IF(IB.EQ.0) GO TO 400
      FAC=-1.
      GO TO  510
  400 FAC=1.
  510 FI(IR,IC)=J*(J+1)-IQ*(IQ+1)
  300 FI(IR,IC)=FAC*SQRT(FI(IR,IR-1))
      GO TO 610
  200 DO 710 IR=1,MR
```

```
      IQ=2*IR-1
      FI(IR,IR)=J*(J+1)-IQ*(IQ+1)
      IF(IB.EQ.0) GO TO 810
      FAC=-1.
      GO TO 710
  810 FAC=1.
  710 FI(IR,IR)=FAC*SQRT(FI(IR,IR))
  610 DO 111 IR=1,MR
      DO 111 IC=1,MC
  111 FI(IR,IC)=FI(IR,IC)*IM
      RETURN
      END
      SUBROUTINE R2(IA,IB,IM,M,N,J1,FI)
      DIMENSION FI(26,1)
      DO 600 IR=1,M
      DO 600 IC=1,N
  600 FI(IR,IC)=0.
      IF(IA.EQ.2) GO TO 700
      DO 800 IR=1,M
      IQ=2*IR-2
      FI(IR,IR)=(J1+IQ)*(J1+IQ+1)
      IF(IB.EQ.0) GO TO 1000
      FAC=-1.
      GO TO 2000
 1000 FAC=1.
 2000 FI(IR,IR)=FAC*SQRT(FI(IR,IR))*IM
  800 CONTINUE
      DO 1100 IR=2,M
      IC=IR-1
      IQ=IR+IC-2
      FI(IR,IC)=(J1-IQ)*(J1-(IQ+1))
 1100 FI(IR,IC)=SQRT(FI(IR,IC))*IM
      FI(1,1)=FI(1,1)*SQRT(2.)
      RETURN
  700 DO 1200 IR=1,M
      IQ=2*IR-1
      FI(IR,IR)=(J1-IQ)*(J1-(IQ+1))
 1200 FI(IR,IR)=IM*SQRT(FI(IR,IR))
      DO 1300 IC=2,N
      IR=IC-1
      IQ=2*IR
      FI(IR,IC)=(J1+IQ)*(J1+IQ+1)
      SI=SQRT(FI(IR,IC))
      IF(IB.EQ.0) GO TO 1400
      FAC=-1.
      GO TO 1500
 1400 FAC=1.
 1500 FI(IR,IC)=FAC*SI*IM
 1300 CONTINUE
      RETURN
      END
      SUBROUTINE Q2 (ID,IRD,MR,MC,J,FI)
      DIMENSION FI(26,1)
      IF(ID.EQ.2) GO TO 700
      MR=IFIX(0.5*(J+2))
      MC=IFIX(0.5*J)
      DO 500 IR=1,MR
      DO 500 IC=1,MC
  500 FI(IR,IC)=0.
      GO TO 600
  700 MR=IFIX(0.5*(J+2))
      MC=IFIX(0.5*(J+1))
      DO 800 IR=1,MR
      DO 800 IC=1,MC
  800 FI(IR,IC)=0.
  600 DO 900 IR=1,MR
      DO 900 IC=1,MC
      MM=IR-IC
      IF(MM.NE.1) GO TO 900
      FI(IR,IC)=4.*(IRD+2.*(IR-2))**2
  900 CONTINUE
      END
```

```
      SUBROUTINE R1 (IR,ID,J,M,N,FI)
      DIMENSION FI(26,1)
      GO TO (100,200,200,400) , ID
  100 M=IFIX(0.5*(J+3))
      N=IFIX(0.5*(J+2))
      GO TO 500
  200 M=IFIX(0.5*(J+2))
      N=IFIX(0.5*(J+1))
      GO TO 500
  400 M=IFIX(0.5*(J+1))
      N=IFIX(0.5*J)
  500 DO 600 I=1,N
      DO 600 K=1,M
  600 FI(I,K)=0.
      DO 700 I=1,N
      DO 700 K=1,M
      IF(I.NE.K) GO TO 700
      IQ=I
      FI(I,I)=4.*(J**2-(IR+2*IQ)**2)
  700 CONTINUE
      RETURN
      END
      SUBROUTINE ARRGE(J,B0,B1,B2,B3,B4,NK1,NP1,NK2,NP2,NK3,NP3,NK4,NP4,
     1N1,N2,N3,N4)
      DIMENSION B0(1),B1(1),B2(1),B3(1),B4(1),N1N(101),N2N(101)
      DIMENSION NK1(1),NP1(1),NK2(1),NP2(1),NK3(1),NP3(1)
      DIMENSION NK4(1),NP4(1)
      J0=2*J+1
      CALL ACG(J,N1N,N2N)
      IF(J.EQ.IO(J)) GO TO 1000
      DO 200 I=1,N1
      K=4*I-2
      B1(I)=B0(K)
      NK1(I)=N1N(K)
  200 NP1(I)=N2N(K)
      DO 300 I=1,N2
      K=4*I
      B2(I)=B0(K)
      NK2(I)=N1N(K)
  300 NP2(I)=N2N(K)
      DO 400 I=1,N3
      K=4*I-3
      B3(I)=B0(K)
      NK3(I)=N1N(K)
  400 NP3(I)=N2N(K)
      DO 500 I=1,N4
      K=4*I-1
      B4(I)=B0(K)
      NK4(I)=N1N(K)
  500 NP4(I)=N2N(K)
      RETURN
 1000 DO 600 I=1,N1
      K=4*I-3
      B1(I)=B0(K)
      NK1(I)=N1N(K)
  600 NP1(I)=N2N(K)
      DO 700 I=1,N2
      K=4*I-1
      B2(I)=B0(K)
      NK2(I)=N1N(K)
  700 NP2(I)=N2N(K)
      DO 800 I=1,N3
      K=4*I-2
      B3(I)=B0(K)
      NK3(I)=N1N(K)
  800 NP3(I)=N2N(K)
      DO 900 I=1,N4
      K=4*I
      B4(I)=B0(K)
      NK4(I)=N1N(K)
  900 NP4(I)=N2N(K)
      RETURN
      END
```

```
      SUBROUTINE SUBMTX(H,F,C,G,J,TEP,TEN,TOP,TON,NEP,NEN,NOP,NON,AB1,AB
     12,AB3,AB4)
      DIMENSION AB1(1),AB2(1),AB3(1),AB4(1)
      DIMENSION Z(26,26),WK(40)
      DIMENSION TEP(26,1),TEN(26,1),TOP(26,1),TON(26,1)
      DIMENSION A1(26,26),A2(26,26),A3(26,26),A4(26,26)
      DIMENSION G1(26),G2(26),G3(26),G4(26),G5(26)
      DIMENSION W(40)
      COMPLEX W
      NZ=26
      JD=J*(J+1)
      A=F*JD
      IF(J.EQ.IO(J)) GO TO 3333
      N1=(J+1)/2
      N2=(J-1)/2
      N3=N1
      N4=N1
      GO TO 2222
 3333 N1=(J+2)/2
      N2=J/2
      N3=N2
      N4=N2
 2222 DO 1000 IR=1,N1
      DO 1000 IC=1,N1
      TEP(IR,IC)=0.
 1000 A1(IR,IC)=0.
      DO 2000 IR=1,N2
      DO 2000 IC=1,N2
      TEN(IR,IC)=0.
 2000 A2(IR,IC)=0.
      DO 3000 IR=1,N3
      DO 3000 IC=1,N3
      TOP(IR,IC)=0.
 3000 A3(IR,IC)=0.
      DO 4000 IR=1,N4
      DO 4000 IC=1,N4
      TON(IR,IC)=0.
 4000 A4(IR,IC)=0.
C
C
      BB=G-F+F*JD
      CC=H*FN(J,0)**.5
      BC1=BB+CC
      BC2=BB-CC
      DO 1001 IR=2,N3
      IC=IR-1
      L=2*IC
      TR=FN(J,L)*H**2
      A3(IR,IC)=SQRT(TR)
 1001 TOP(IR,IC)=TR
      JC=1
      DO 1002 IR=2,N3
      TR=A+(IR+JC)**2*C
      A3(IR,IR)=TR
      TOP(IR,IR)=TR
 1002 JC=JC+1
      DO 1003 IC=2,N3
      IR=IC-1
      A3(IR,IC)=1.
 1003 TOP(IR,IC)=1.
      A3(1,1)=BC1
      TOP(1,1)=BC1
      DO 1004 IR=1,N4
      DO 1004 IC=1,N4
      TON(IR,IC)=TOP(IR,IC)
 1004 A4(IR,IC)=A3(IR,IC)
      TON(1,1)=BC2
      A4(1,1)=BC2
      DO 1005 IR=2,N1
      IC=IR-1
      L=2*(IC-1)+1
      TR=FN(J,L)*H**2
      A1(IR,IC)=SQRT(TR)
```

```
1005 TEP(IR,IC)=TR
     JC=-1
     DO 1006 L=1,N1
     TR=A+(L+JC)**2*C
     A1(L,L)=TR
     TEP(L,L)=TR
1006 JC=JC+1
     A1(2,1)=SQRT(2.)*A1(2,1)
     TEP(2,1)=2.*TEP(2,1)
     DO 1007 IC=2,N1
     IR=IC-1
     A1(IR,IC)=1.
1007 TEP(IR,IC)=1.
     NM=N2-1
     DO 1008 IR=1,NM
     IC=IR+1
     A2(IR,IC)=1.
1008 TEN(IR,IC)=1.
     DO 1009 IR=1,N2
     I=(2*IR)**2
     TR=I*C+A
     A2(IR,IR)=TR
1009 TEN(IR,IR)=TR
     DO 2001 IR=2,N2
     IC=IR-1
     I=2*IC+1
     TR=FN(J,I)*H**2
     A2(IR,IC)=SQRT(TR)
2001 TEN(IR,IC)=TR
     NEP=N1
     NEN=N2
     NOP=N3
      NON=N4
     T=48.
     FX=2.**(-T)
     CALL EA02B(N1,26,A1,G1,G2,G3,G4,G5,FX)
     DO 3001 IP=1,N1
3001 AB1(IP)=A1(IP,IP)
     CALL EA02B(N2,26,A2,G1,G2,G3,G4,G5,FX)
     DO 3002 IP=1,N2
3002 AB2(IP)=A2(IP,IP)
     CALL EA02B(N3,26,A3,G1,G2,G3,G4,G5,FX)
     DO 3003 IP=1,N3
3003 AB3(IP)=A3(IP,IP)
     CALL EA02B(N4,26,A4,G1,G2,G3,G4,G5,FX)
     DO 3004 IP=1,N4
3004 AB4(IP)=A4(IP,IP)
     RETURN
     END
     FUNCTION IO(L)
     Y=FLOAT(L)
     Z=Y/2.
     M=Z
     M2=2*M
     IO=M2
     RETURN
     END
     SUBROUTINE ORD(X,Y,JO)
     DIMENSION X(1),Y(1)
     J=1
  30 TERM=-1.E20
     DO 10 I=1,JO
     IF(X(I).GT.TERM) GO TO 20
     GO TO 10
  20 TERM=X(I)
     M=I
  10 CONTINUE
     Y(J)=TERM
     X(M)=-1.E20
     J=J+1
     IF(J.GT.JO) GO TO 2222
     GO TO 30
2222 RETURN
     END
```

```
      SUBROUTINE FINSUB(T,N,TB,AAV)
      DIMENSION AL(26,26),AN(26,26),AV(26,26),AP(26,26),R(26,26)
      DIMENSION T(26,1),TB(1),AAV(26,1),VKM(26),VBM(26)
C
      NORD=N
      VKO=T(1,1)
      DO 3000 IR=2,N
      IC=IR-1
 3000 VBM(IC)=T(IR,IC)
      DO 3001 IR=2,N
      II=IR-1
 3001 VKM(II)=T(IR,IR)
      DO 1000 IR=1,N
      DO 1000 IC=1,N
      AL(IR,IC)=0.
 1000 AN(IR,IC)=0.
      AL(1,1)=1.
      IF(N.LT.2) GO TO 1002
      TERM=1.
      DO 1001 I=2,N
      TERM=TERM/SQRT(VBM(I-1))
 1001 AL(I,I)=TERM
 1002 DO 1003 I=1,N
 1003 AV(1,I)=1.
      IF(N.LT.2) GO TO 1007
      DO 1004 I=1,N
      AV(2,I)=-(VKO-TB(I))
 1004 AP(2,I)=-AV(2,I)
      IF(N.LT.3) GO TO 1007
      DO 1005 I=1,N
      AV(3,I)=(VKM(1)-TB(I))*(-AV(2,I))-VBM(1)
 1005 AP(3,I)=AV(3,I)
      IF(N.LT.4) GO TO 1007
      DO 1006 J=4,N
      SIG=(-1)**(J-1)
      DO 1006 I=1,N
      AP(J,I)=(VKM(J-2)-TB(I))*AP(J-1,I)-VBM(J-2)*AP(J-2,I)
 1006 AV(J,I)=AP(J,I)*SIG
 1007 DO 1008 IR=1,N
      DO 1008 IC=1,N
 1008 R(IR,IC)=0.
      DO 1009 KR=1,N
      DO 1009 KC=1,N
      DO 1009 I=1,N
 1009 R(KR,KC)=R(KR,KC)+AL(KR,I)*AV(I,KC)
      DO 1011 I=1,N
      SUM=0.
      DO 1010 J=1,N
 1010 SUM=SUM+R(J,I)**2
 1011 AN(I,I)=1./SQRT(SUM)
      DO 1012 IR=1,N
      DO 1012 IC=1,N
 1012 AAV(IR,IC)=0.
      DO 1013 KR=1,N
      DO 1013 KC=1,N
      DO 1013 I=1,N
 1013 AAV(KR,KC)=AAV(KR,KC)+R(KR,I)*AN(I,KC)
      RETURN
      END
```

```
      FUNCTION FN(M,N)
      FN=(M*(M+1)-N*(N+1))*(M*(M+1)-N*(N-1))/4.
      RETURN
      END
```

```
      SUBROUTINE R3(IA,IB,IM,M,N,J1,FI)
      DIMENSION FI(26,1)
      DO 600 IR=1,M
      DO 600 IC=1,N
  600 FI(IR,IC)=0.
      IF(IA.EQ.2) GO TO 700
      DO 800 I=1,M
      IQ=2*I-2
      FI(I,I)=(J1-IQ)*(J1-(IQ+1))
      FI(I,I)=SQRT(FI(I,I))*IM
  800 CONTINUE
      FI(1,1)=FI(1,1)*SQRT(2.)
       DO 900 IC=2,N
       IR=IC-1
      IQ=IR+IC-2
      FI(IR,IC)=(J1+IQ)*(J1+(IQ+1))
      SI=SQRT(FI(IR,IC))
      IF(IB.EQ.0) GO TO 1000
      FAC=-1.
      GO TO 900
 1000 FAC=1.
  900 FI(IR,IC)=FAC*SI*IM
      RETURN
  700 DO 1100 I=1,M
      IQ=2*I-1
      FI(I,I)=(J1+IQ)*(J1+(IQ+1))
      SI=SQRT(FI(I,I))
      IF(IB.EQ.0) GO TO 1200
      FAC=-1.
      GO TO 1100
 1200 FAC=1.
 1100 FI(I,I)=FAC*SI*IM
      DO 1300 IR=2,M
      IC=IR-1
      IQ=IR+IC-1
      FI(IR,IC)=(J1-IQ)*(J1-(IQ+1))
      SI=SQRT(FI(IR,IC))
 1300 FI(IR,IC)=IM*SI
      RETURN
      END
      SUBROUTINE ACC(J,N1,N2)
      DIMENSION N1(1),N2(1)
      I=1
      M2=0
       M1=0
 1000 N1(I)=J-M1
      N2(I)=M2
      N1(I+1)=N1(I)
       N2(I+1)=N2(I)+1
      M2=M2+1
      M1=M1+1
      I=I+2
      IF(I.GT.2*J) GO TO 1001
      GO TO 1000
 1001 N1(2*J+1)=0
      N2(2*J+1)=J
      RETURN
      END
```

APPENDIX B

SUBROUTINE SUBPROGRAM FOR MOLECULAR SPECTRA GENERATION

"ABSORP" is a computer program which we have developed to plot the absorption spectra in a selected wavelength region at any pressure. The resolution of the scanning is assumed to be infinity which is suitable for employing lasers (i.e., the line-width of the laser is much smaller than the narrowest absorption line-width of the considered molecule).

List of Variables

FMAX:	Is the upper frequency limit of the spectral region (cm^{-1}).
FMIN:	Is the lower frequency limit (cm^{-1}).
P:	The total pressure of the gas or the mixture (Torr).
WDO:	Doppler-broadening HWHM per 1 cm^{-1}.
WLO:	Lorentz-broadening HWHM (at $P = 760$ Torr), cm^{-1}.
NO:	Number of absorption lines in the selected spectral region.
F(I):	Absorption line positions, $I = 1 \ldots I = NO$, in cm^{-1}.
S(I):	Absorption line intensity ($cm^{-2}\ atm^{-1}$).

W(I)	HWHM (Lorentz) for transition I if it is available (cm^{-1}). For most of the calculations we have considered W(I) having the same value (i.e., equal to WLO).

The above parameters are inputs to "ABSORP". F(I), S(I), and W(I) may be available in the literature or can be calculated by "AROTOR" in Appendix A.

DFMX:	Is a frequency limit around any absorption line, at which the absorption is to be considered as zero, i.e., absorption at (F(I) ± DFMX) equal 0.

FFO(I), SSO(I), WWO(I), I = 1, N, are parameters of the contributing absorption lines in the selected spectral region (i.e., from FMIN to FMAX).

The calculations of the absorption coefficient, Y(M), at a frequency, X(M), due to all contributing absorption lines depends on the total pressure. We have divided the pressure scale, from 1 Torr and below up to 760 Torr, to three regions: 1) $P < 10$ Torr, the profile used is purely Doppler, 2) $P > 40$ Torr, the profile is mainly Lorentzian, and 3) between 10 and 40 Torr we have used Voit profile. We have checked the transitions from one profile to another.

The calculation of Y(M) is done at each frequency by adding the absorptions of all the contributing lines, then increment the frequency by DF and repeat the calculations. Now, we have an (X, Y) array of size NN. Y(I) must be normalized to its maximum value, YN.

Plotting the results depends upon the available plotting subroutines, the plotting statements listed in Appendix B may be only useful at McMaster University Computer Center. We have used the following subroutines from the Computer Center library:

1) "EA02B" for eigenvalues generation of any symmetrical matrix of N×N.
2) "PLOT" used to plot a continuous curve between the points Y(I) at X(I).
3) "UNITTO" to convert from data point to plotter units.
4) "INCH TO" to convert from inches to data points.

A typical output of "ABSORP" is shown in Fig. 8.7.

```
      PROGRAM ABSORP (INPUT,OUTPUT,TAPE5=INPUT,TAPE6=OUTPUT)
      DIMENSION F(3000),S(3000),W(3000)
      DIMENSION FO(1000),SO(1000),WO(1000)
      DIMENSION FFO(1000),SSO(1000),WWO(1000)
      DIMENSION X(4000),Y(4000)
      DIMENSION XS(2),YS(2)
C
C
C
C
C
C
      READ(5,*) FMAX,FMIN,P,WDO,WLO,NO
      READ(5,101)(F(I),S(I),W(I),I=1,NO)
  101 FORMAT(3 F10.4    )
C
C     PICK UP ALL THE LINENES IN THE SPECTRAL REGION
C
      FLMT=(P/40.)*WLO
      DFMX=2.*FLMT
      J=1
      DO 100 I=1,NO
      IF(F(I).GT.(FMAX+FLMT).OR.F(I).LT.(FMIN-FLMT))GO TO 100
      FO(J)=F(I)
      SO(J)=S(I)
      WO(J)=W(I)
      J=J+1
  100 CONTINUE
      N=J-1
C
C     ORDERING THE LINES IN INCREASING WAY
C
      L=N
  200 TERM=0.
      DO 300 I=1,L
      IF(FO(I).GT.TERM) GO TO 300
      TERM=F(I)
      M=I
  300 CONTINUE
      FFO(J)=FO(M)
      SSO(J)=SO(M)
      WWO(J)=WO(M)
      FO(M)=FO(L)
      SO(M)=SO(L)
      WO(M)=WO(L)
      L=L-1
      IF(L.EQ.0) GO TO 400
      GO TO 200
C
C     CALCULATING THE ABSORPTION COEFFICIENT AT DIFFERENT FREQUENCY
C     THE LINE PROFILE WILL DEPEND ON THE PRESSURE  1) P.LT.10 TORR
C        DOPPLER BROADEN.  2) P.LT.40 TORR IT WILL BE VOICT PROFILE 3)
C     P.GT.40 IT WILL BE COLLISION BROADEN.
C
C
  400 J=1
  500 MM=(J-1)*4
      DF=(FFO(J+1)-FFO(J))/5.
      DO 600 K=1,5
      M=K+J-1+MM
      X(M)=FFO(J)+DF*(K-1)
      FRQ=X(M)
      SUM=0.
      DO 990 I=1.N
      XX=ABS(FRQ-FFO(I))
      IF(XX.GT.DFMX) GO TO 500
      SS=SSO(I)
      WW=WLO*P/760.
      WD=WDO*FFO(I)
      IF(P.LT.10.) GO TO 600
      IF(P.LT.40.) GO TO 700
      PROF=SS*WW*P/(3.1415927*760.*(XX**2+WN**2))
      GO TO 800
```

```
 600 PROF=SS*P*ALOG(2.)**.5*EXP(-XX**2*ALOG(2.)/WD**2)/(WD*3.1415927**.
    15*760.)
     GO TO 800
 700 XO=XX*ALOG(2.)**.5/WD
     YO=WW*ALOG(2.)**.5/WD
     PROF=SS*P*ALOG(2.)**.5*RO(XO,YO)/(760.*3.1415927**.5*WD)
 800 SUM=SUM+PROF
 900 CONTINUE
     Y(M)=SUM
     J=J+1
     IF(J.GT.(J-1)) GO TO 1000
     GO TO 500
1000 NN=(N-1)*5+1
C
C    CALCULATE THE MAX. ABSORBTION  COEFFICIENT  YN=Y(I) MAX. AND THEN
C    NORMALIZE ALL THE ABS. TO YN
C
     TERM=0.
     DO 1100 J=1,NN
     IF(Y(J).LT.TERM) GO TO 1100
     TERM=Y(J)
     M=J
1100 CONTINUE
     YN=Y(M)
     DO 1200 I=1,NN
1200 Y(I)=Y(I)/YN
C
C    NOW WE HAVE NN POINTS OF X AND Y AND THE FOLLOWING STEPS  FOR PLOT
C    NN POINTS  THE FOLLOWING DEPENDS ON THE COMPUTER USED AND IS ONLY
C    WHEN USING CDC MCMASTER COMPUTER   ..............................
C
     XS(1)=FMAX
     XS(2)=FMIN
     YS(1)=1.
     YS(2)=0.
     XL=5.+20.
     YL=3.+6.5
     XNDIV=20.
     YNDIV=5.
     CALL MAP(XS,YS,2,XL,YL,XNDIV,YNDIV)
     CALL CURVE(X,Y,NN)
     CALL PLOT(5,0.0,999)
     STOP
     END



     SUBROUTINE CURVE(X,Y,N)
     DIMENSION X(1),Y(1)
     MM=N-1
     X1=X(1)
     Y1=Y(1)
     CALL UNITTO(X1,Y1,XX,YY)
     CALL PLOT(XX,YY,3)
     DO 100 I=1,MM
     CALL UNITTO(X(I+1),Y(I+1),XM,YM)
     CALL PLOT(XM,YM,2)
 100 CONTINUE
     RETURN
     END
```

```
      SUBROUTINE MAP (X,Y,M,XL,YL,XNDIV,YNDIV)
      DIMENSION X(M),Y(M)
      CALL PLOT(0.,0.,-3)
      CALL DATE(D1)
      CALL LETTER(10,.3,270.,1.,10.,10HELSHERBINY)
      CALL LETTER(10,.3,270.,2.,10.,D1)
      CALL PLOT(5.,0.0,-3)
      XMARG=5.
      YMARG=3.
      CALL FACTOR(M,X,Y,XL,YL,XMARG,YMARG)
      CALL PLOT(XMARG,YMARG,3)
      CALL PLOT(XL,YMARG,2)
      CALL PLOT(XL,YL,1)
      CALL PLOT(XMARG,YL,1)
      CALL PLOT(XMARG,YMARG,1)
      YSTEP=(YL-YMARG)/YNDIV
      XOR=XMARG
      YOR=YMARG
      NDIVX=IFIX(XNDIV+1.)
      NDIVY=IFIX(YNDIV+1.)
      DO 100 KY=1,NDIVY
      CALL PLOT(XOR,YOR,3)
      CALL PLOT(XOR+.1,YOR,2)
      CALL PLOT(XL-.1,YOR,3)
      CALL PLOT(XL,YOR,2)
      CALL INCHTO(XMARG,YOR,XP,YP)
      ENCODE(5,3,YD) YP
      CALL LETTER(5,.1,0.0,4.1,YOR-.05,YD)
      YOR=YOR+YSTEP
  100 CONTINUE
      XSTEP=(XL-XMARG)/XNDIV
      DO 200 KX=1,NDIVX
      CALL PLOT (XOR,YMARG,3)
      CALL PLOT (XOR,YMARG+.1,2)
      CALL PLOT (XOR,YL-.1,3)
      CALL PLOT (XOR,YL,2)
      CALL INCHTO (XOR,YMARG,XH,YH)
      ENCODE(7,4,XD) XH
      CALL LETTER(7,.1,0.0,XOR-.2,2.815,XD)
      XOR=XOR+XSTEP
  200 CONTINUE
      RETURN
    3 FORMAT(F6.2)
    4 FORMAT(F7.2)
      END
```

```
      FUNCTION RO (X,Y)
      COMMON W(10),T(10),Y2
      W(1)=4.6224367E-1
      W(2)=2.86675505E-1
      W(3)=1.09017206E-1
      W(4)=2.48105209E-2
      W(5)=3.24377334E-3
      W(6)=2.28338636E-4
      W(7)=7.80255648E-6
      W(8)=1.08606937E-7
      W(9)=4.39934099E-10
      W(10)=2.22939365E-13
      T(1)=0.245340708
      T(2)=.737473729
      T(3)=1.23407622
      T(4)=1.73853771
      T(5)=2.254974
      T(6)=2.78880606
      T(7)=3.34785457
      T(8)=3.94476404
      T(9)=4.60368245
      T(10)=5.38748089
      Y2=Y**2
      IF(Y.LT.1.0.AND.X.LT.4.OR.Y.LT.1.8/(X+1.))  GO TO 333
      IF(Y.LT.2.5.AND.X.LT.4.0)  GO TO 222
  111 RO=R3(X,Y)
      RETURN
  222 RO=R2(X,Y)
      RETURN
  333 RO=R1(X,Y)
      RETURN
      END
      FUNCTION R1 (X,Y)
      DIMENSION C(34)
      F3(T)=EXP(T**2-X**2)
      Y2=Y**2
      IF((X**2-Y**2).GT.70.)  GO TO 22
      U1=EXP(-X**2+Y2)*COS(2.*X*Y)
      GO TO 55
   22 U1=0.0
   55 IF(X.GT.5.)  GO TO 1111
      C(1)=.199999999997
      C(2)=-.18400000000299
      C(3)=.15583999999965
      C(4)=-.12166400000044
      C(5)=.08770815999404
      C(6)=-.05851412480087
      C(7)=.03621573016240
      C(8)=-.020849764398
      C(9)=.011196011635
      C(10)=-.5623189627E-2
      C(11)=.2648763417E-2
      C(12)=-.1173267076E-2
      C(13)=.48995199781E-3
      C(14)=-.19336308015E-3
      C(15)=.7228774468E-4
      C(16)=-.23655125E-4
      C(17)=.8662073684E-5
      C(18)=-.278763797E-5
      C(19)=.8566873627E-6
      C(20)=-.2518433784E-6
      C(21)=.709360221E-7
      C(22)=-.191732257E-7
      C(23)=.49801256E-8
      C(24)=-.12447734E-8
      C(25)=.2997777E-9
      C(26)=-.6964450E-10
      C(27)=.156262E-10
      C(28)=-.33897E-11
      C(29)=.7116E-12
      C(30)=-.1447E-12
      C(31)=.285E-13
      C(32)=-.55E-14
```

```
      C(33)=.1E-14
      C(34)=-.2E-15
      BNO1=0.00
      BNO2=0.00
      X1=X/5.00
      COEF=4.00*X1**2-2.00
      DO  20 I = 1 , 34
      II=35-I
      BN=COEF*BNO1-BNO2+C(II)
      BNO2=BNO1
   20 BNO1=BN
  330 F=X1*(BN-BNO2)
  440 DNO1=1.0-2.0*X*F
 1100 DNO2=F
      GO TO 1200
 1111 DNO1=-(.5/X**2+.75/X**4+1.875/X**6+6.5625/X**8+29.53125/X**10+.162
     14218/X**12+1055.7421/X**14)
      DNO2=(1.00-DNO1)/(2.*X)
 1200 FUNCT=Y*DNO1
      IF(Y.LE.1.0E-08)  GO TO 2500
      Q=1.0
      YN=Y
      DO 2000 I =2,50
      DN=(X*DNO1+DNO2)*(-2.)/FLOAT(I)
      DNO2=DNO1
      DNO1=DN
      IF(MOD(I,2)) 2000,2000,1500
 1500 Q=-Q
      YN=YN*Y2
      G=DN*YN
      FUNCT=FUNCT+Q*G
      IF(ABS(G/FUNCT).LE.1.0E-08)  GO TO 2500
 2000 CONTINUE
 2500 R1=U1-1.12837917*FUNCT
      RETURN
      END
      FUNCTION R2(X,Y)
      COMMON W(10),T(10),Y2
      G=0.0
      DO 100 I=1,10
      RR=T(I)-X
      S=T(I)+X
  100 G=G+(4.*T(I)**2-2.)*(RR*ATAN(RR/Y)+S*ATAN(S/Y)-.5*Y*(ALOG(Y2+RR**2
     1)+ALOG(Y2+S**2)))*W(I)
      R2=0.318309886*G
      RETURN
      END
      FUNCTION R3(X,Y)
      COMMONW(10),T(10),Y2
      G=0.0
      DO 100 I =1,10
  100 G=G +(1.0E0/((X-T(I))**2+Y2)+1.E0/((X+T(I))**2+Y2))*W(I)
      R3=0.318309886*Y*G
      RETURN
      END
```

The following are subroutines available from the author and not listed here:

1) Subroutine for absorption lines generation of symmetric-top molecules.

2) Subroutine for diatomic molecules.

3) Subroutine for CO_2 laser gain spectra including all the hot bands, the isotopic species bands, and their sequence bands.

REFERENCES

[1] P. L. Hanst, "Infrared spectroscopy and infrared lasers in air pollution research and monitoring", Appl. Spectrosc., Vol. 24, pp. 161-174, 1970.

[2] C. B. Ludwig, M. Griggs, and E. R. Bartle, "Remote sensing of air pollution", J. Opt. Soc, Amer., Vol. 60, pp. 731-732, 1970.

[3] H. Kildal and R. L. Byer, "Comparison of lasers methods for the remote detection of atmospheric pollutants", Proc. IEEE, Vol. 59, pp. 1644-1663, Dec. 1971.

[4] Lars-Göran Rosengren, "Analysis of a long-distance system measuring the concentration of atmospheric gaseous pollutants", IEEE Trans. on Aerospace and Elect. Syst., Vol. AE-9, No. 5, pp. 725-731, 1973.

[5] P. L. Kelley, R. A. McClatchey, R. K. Long, and A. Snelson, "Molecular absorption of infrared laser radiation in the natural atmosphere", Opt. and Quant. Elect., Vol. 8, pp. 117-144, 1976.

[6] E. R. Murray, J. E. Vander Laan, and J. G. Hawley, "Remote measurement of HCL, CH_4, and N_2O using a single ended chemical-laser lidar system", Appl. Opt. Vol. 15, pp. 3140-3148, 1976.

[7] L. B. Kreuzer and C. K. N. Patel, "NO pollution: Detection by optoacoustic spectroscopy", Appl. Opt., Vol. 173, pp. 45-47, July 1971.

[8] E. D. Hinkley, "Laser spectroscopic instrumentation and techniques: long-path monitoring by resonance absorption", Opt. and Quant. Elect., Vol. 8, pp. 155-167, 1976.

[9] L. W. Chaney, D. G. Rickel, G. M. Russwurm, and W. A. McClenny, "Long-path laser monitor of carbon monoxide: system improvements", Appl. Opt., Vol. 18, pp. 3004-3009, 1979.

[10] E. D. Hinkley, Ed., "Laser monitoring of the atmosphere", Topics in Appl. phys., Vol. 14, 380 pages, Springer-Verlag, 1976.

✓

[11] C. R. Stanley, "Carbon dioxide lasers - an introduction to their characteristics and design", Optics and Laser Techn., Vol. 3, pp. 12-17, 1971; and A. Yariv, "Introduction to optical electronics", Eds. Holt, Rinehart, and Winston, New York, 1971.

[12] A. R. Calawa, "Small bandgap lasers and their uses in spectroscopy", J. Luminescence, Vol. 7, pp. 477-500, 1973; or I. Melngailis, "The use of lasers in pollution monitoring", IEEE Trans. on Geoscience Electronics, GE-10, pp. 7-17, 1972.

[13] R. B. Dennis, C. R. Pidgeon, S. C. Smith, B. S. Wherrett, and R. A. Wood, "Stimulated spin-flip raman scattering: a magnetically tunable ir laser", Proc. Roy. Soc. London, Vol. A331, pp. 203-236, 1972.

[14] D. C. Hanna, B. Luther-Davies, and R. C. Smith, "Singly resonant proustite parametric oscillator tuned from 1.22 to 8.5 μm", Appl. Phys. Letters, Vol. 22, pp. 440-442, 1973.

[15] S. E. Harris, "Tunable optical parametric oscillators", Proc. IEEE, Vol. 57, pp. 2096-2113, 1969.

[16] N. G. Basov, E. M. Belenov, V. A. Danilychev, and A. F. Suchkov, "Possibility of producing tunable ir gas lasers", JETP Letters, Vol. 14, pp. 375-376, 1971.

[17] E. D. Hinkley, "High-resolution ir spectroscopy with a tunable diode laser", Appl. Phys. Letters, Vol. 16, pp. 351-354, 1970.

[18] K. W. Nill, A. J. Strauss, and F. A. Blum, "Tunable cw $Pb_{0.98}Cd_{0.02}S$ diode lasers emitting at 35 μm: Applications to ultrahigh-resolution spectroscopy", Appl. Phys. Letters, Vol. 22, pp. 677-679, 1973.

[19] K. W. Nill, F. A. Blum, A. R. Calawa, and T. C. Harman, "Infrared spectroscopy of CO using a tunable PbSSe diode laser", Appl. Phys. Letter, Vol. 19, pp. 79-82, 1971.

[20] J. F. Butler, "Magnetoemission experiments in $Pb_{1-x}Sn_xTe$", Solid State Comm., Vol. 7, pp. 909-915, 1969.

[21] E. D. Hinkley, K. W. Nill, and A. Blum, "Tunable lasers in the infrared", Laser Focus, April, pp. 47-51, 1976.

[22] J. F. Butler and A. R. Calawa, "Physics of Quantum Electronics", P. L. Kelley, B. Lax, and P. E. Tanenwald, Eds., McGraw-Hill, N. Y., pp. 458, 1966.

[23] A. R. Calawa, J. O. Dimmock, T. C. Harman, and I. Melngailis, "Magnetic field dependence of laser emission in $Pb_{1-x}Sn_xSe$ diodes", Phys. Rev. Letter, Vol. 23, pp. 7-13, 1969.

[24] J. M. Besson, W. Paul, and A. R. Calawa, "Tuning of PbSe laser by hydrostatic pressure from 8 to 22 μ", Phys. Rev., Vol. 173, pp. 699-713, 1968.

[25] R. A. McClatchey, W. S. Benedict, S. A. Clough, D. E. Burch, R. F. Calfee, K. Fox, L. S. Rothman, and J. S. Garing (H_2O, CO_2, N_2O, O_2, O_3, NH_3, ...) 1973 Magnetic Tape.
and

[26] L. S. Rothman, S. A. Clough, R. A. McClatchey, L. G. Young, D. E. Snider, and A. Goldman (SO_2, NO, CH_4, ...) 1977 Magnetic Tape, "AFCRL Atmospheric absorption line parameters compilation".

These two tapes are available from National Climatic Center of NOAA, Federal Building, Asheville, North Carolina 28801, each tape can be purchased from them for a service charge of $60.00.

[27] J. H. Park, "Atlas of Infrared Absorption Lines", NASA Contractor Report No. 2925.

[28] W. S. Benedict, R. Herman, G. E. Moore, and S. Silverman, "The strengths, widths, and shapes of Infrared lines", Can. J. Phys., Vol. 34, pp. 830-848, 1956.

[29] W. F. Kolbe, H. Busher, and B. Leskovar, "Microwave absorption coefficients of atmospheric pollutants and constituents", J.Q.S.R.T., Vol. 18, pp. 47-64, 1977.

[30] G. W. King, R. M. Hainer, and P. C. Cross, "The Assymmetric Rotor I", J. Chem. Phys., Vol. 11, pp. 27-43, 1943.

[31] W. Gordy and R. L. Cook, "Microwave Molecular Spectra", Wiley, Ed, N. Y., 1970.

[32] P. C. Cross and R. M. Hainer, "The Asymmetric Rotor II", J. Chem. Phys., Vol. 12, pp. 210-245, 1944.

[33] M. Osumi and T. Kunitomo, "Calculation of absorption coefficient for the ν_1 band of SO_2", J.Q.S.R.T., Vol. 15, pp. 1055-1065, 1975.

[34] B. K. Garside, E. A. Ballik, M. Elsherbiny, and J. Shewchun, "Resonance absorption measurements of NO with a line-tunable CO laser: Spectroscopic data for pollution monitoring", Appl. Optics, Vol. 16, pp. 398-402, 1977.

[35] G. Birnbaum, "Intermolecular Forces", Adv. Chem. Phys., J. O. Hirchfelder, Ed., Vol. 12, pp. 487-548, Wiley N. Y., 1964.

[36] G. D. T. Tejwani, "Calculation of pressure-broadened line-width of SO_2 and NO_2", J. Chem. Phys., Vol. 57, pp. 4676-4681, 1972.

[37] Krishnaji and V. Prakash, "Width of rotational lines of an asymmetric-top molecule of SO_2", J. Chem. Phys., Vol. 52, pp. 4674-4677, 1970.

[38] G. D. T. Tejwani and E. S. Yeung, "Pressure-broadened line widths of ozone", J. Chem. Phys., Vol. 63, pp. 1513-1517, 1973.

[39] D. V. Bates, G. M. Bell, C. D. Burnham, M. Hazucha, J. Mantha, L. D. Pengelly, and F. Silverman, "Short term effect of ozone on the lungs", J. Appl. Physiol., Vol. 32, pp. 176-181, 1972.

[40] R. E. Munn, "Scope report 3, International council of scintific unions, scientific committee on problems of the environment", Royal SOC., London, pp. 110, 1973.

[41] W. A. McClenny, R. E. Baumgardner, Jr., F. W. Baity, Jr., and R. A. Gray, "Methodology for comparison of open-path monitors with point monitors", J. Air Pollut. Control Assoc., Vol. 24, pp. 1044-1046, 1974.

[42] R. R. Patty, G. M. Russwurm, W. A. McClenny, and D. R. Morgan, "CO_2 laser absorption coefficients for determining ambient levels of O_3, NH_3 and C_2H_4, Appl. Opt., Vol. 13, pp. 2850-2854, 1974.

[43] K. Asai and T. Igarashi, "Detection of ozone by differential absorption using CO_2 laser", Opt. Quant. Elect., Vol. 7, pp. 211-214, 1975.

[44] S. A. Clough and F. X. Kneizys, "Coriolis interaction in the ν_1 and ν_3 fundamental of ozone", J. Chem. Phys., Vol. 44, pp. 1855-1861, 1966.

[45] J. V. White, "Long optical paths of large aperture", J. Opt. SOC. Am., Vol. 32, pp. 285-288, 1942.

[46] K. M. Baird, H. D. Riccius, and K. J. Siemsen, "CO_2 wavelengths and the velocity of light", Opt. Commun., Vol. 6, pp. 91-95, 1972.

[47] S. A. Clough and F. X. Kneizys, "Ozone line compilation", A.F.C.R.L., Report A.F.C.R.L. 65-862, 1965.

[48] G. N. Plass and D. I. Fivel, "Influence of Doppler effect and damping on line-absorption coefficient and atmospheric radiation transfer", Astrophys. J., Vol. 117, pp: 225-233, 1953.

[49] T. F. Deutsch, "NO Molecular laser", Appl. Phys. Lett., Vol. 9, pp. 295-297, 1966.

[50] R. H. Gillette and E. H. Eyster, "The fundamental rotation-vibration band of nitric oxide", Phys., Rev., Vol. 56, pp. 1113-1119, 1939.

[51] D. B. Keck and C. D. Hause, "High resolution study of Nitric Oxide near 5.4 microns", J. Mol. Spectrosc., Vol. 26, pp. 163-174, 1968.

[52] J. H. Shaw, "Nitric Oxide fundamental", J. Chem. Phys., Vol. 24, pp. 399-402, 1956.

[53] R. O'B. Carpenter and M. A. Franzosa, "Line strengths and spectral emissivities of NO as functions of temperature and amount of gas", J.Q.S.R.T., Vol. 5, pp. 465-493, 1965.

[54] C. Chackerian, Jr., and H. F. Weisbach, "Amplified laser absorption: detection of NO", J. Opt. SOC. Amer., Vol. 63, 342-345, 1973.

[55] J. Reid, Private Communication, Measurements made at NRC, Ottawa, employing a Spin-Flip-Raman laser (1977).

[56] T. R. Todd, C. M. Clayton, W. B. Telfair, T. K. McCubbin, Jr., and J. Pliva, "Infrared Emission of $^{12}C^{16}O$, $^{13}C^{16}O$, and $^{12}C^{18}O$, J. Mol. Spectrosc., Vol. 62, pp. 201-227, 1976.

[57] K. Hakuta and H. Vehara, "Laser magnetic resonance for the $v = 1 \leftarrow 0$ transition of NO ($^2\Pi_{3/2}$) by CO laser", J. Mol. Spectrosc., Vol. 58, pp. 316-322, 1975.

[58] J. W. C. Johns, NRC Ottawa; Private Communication.

[59] L. L. Abels and J. H. Shaw, "Widths and strengths of vibration-rotation lines in the fundamental band of NO", J. Mol. Spectrosc., Vol. 20, pp. 11-27, 1966.

[60] R. E. Richton, "NO line parameters measured by CO laser transmittance", Appl. Optics, Vol. 15, pp. 1686-1687, 1976.

[61] P. Varanasi and S. S. Penner, "Absolute ir intensity measurements on the fundamental of NO", J.Q.S.R.T., Vol. 7, pp. 279-282, 1967.

[62] N. G. Nereson and H. Flicker, "Wavenumber measurements of weak CO_2 laser lines around 10.6 μm", Opt. Commun., Vol. 23, pp. 171-176, 1977.

[63] P. Brockman, C. H. Bair, and F. Allario, "High resolution spectral measurement of the HNO_3 11.3 μm band using tunable diode lasers", Appl. Optics, Vol. 17, pp. 91-99, 1978.

[64] J. Reid and K. Siemsen, "Laser power and gain measurements on the sequence bands of CO_2", J. Appl. Phys., Vol. 48, pp. 2712-2717, 1977.

[65] F. R. Petersen, D. G. McDonald, J. D. Cupp, and B. L. Danielson, in Proc. of Laser Spectroscopy Conference, Vail, Colorado, pp. 25-29, June, 1973.

[66] C. Freed, R. G. O'Donnell, and A. H. M. Ross, "Absolute frequency calibration of the CO_2 isotope laser transitions", IEEE Trans. Instrum. Meas., Vol. IM-25, pp. 431-437, 1976.

[67] C. Freed, A. H. M. Ross, and R. G. O"Donnell, "Determination of laser line frequencies and vibrational-rotational constants of the $^{12}C^{18}O_2$, $^{13}C^{16}O_2$, and $^{13}C^{18}O_2$ isotopes from measurements of cw beat frequencies with fast HgCdTe photodiodes and microwave frequency counters", J. Mol. Spectros., Vol. 49, pp. 439-453, 1974.

[68] K. J. Siemsen and B. G. Whitford, "Heterodyne frequency measurements of CO_2 laser sequence-band transitions", Opt. Commun., Vol. 22, pp. 11-16, 1977.

[69] R. P. Edwin, M. T. Dudermel, and M. Lamare, "Refractive index measurements of Ge sample", Appl. Optics, Vol. 17, pp. 1066-1068, 1978.

[70] H. Flicker, J. P. Aldridge, H. Filip, N. G. Neresou, M. J. Reisfeld, and W. H. Weber, "Wavenumber calibration of tunable diode lasers using etalon", Appl. Opt., Vol. 17, pp. 851-852, 1978.

[71] A. R. Chraplyvy, "Diode laser spectra with simultaneous frequency calibration", Appl. Optics, Vol. 17, pp. 2674-2675, 1978.

[72] T. L. Worchesky, K. J. Ritter, J. P. Sattler, and W. A. Riessler, "Heterodyne measurements of ir absorption frequencies of D_2O", Opt. Lett., Vol. 2, pp. 70-71, 1978.

[73] J. J. Hillman, T. Kostiuk, D. Buhl, J. L. Faris, J. C. Navaco, and M. J. Mumma, "Precision measurements of NH_3 spectral lines near 11 μm using the ir heterodyne technique", Opt. Lett., Vol. 1, pp. 81-83, 1977.

[74] A. Barbe, C. Secroun, P. Jouve, N. Monnanteuil, J. S. Depannemaecker, B. Duterage, J. Bellet, and P. Pinson, "Infrared and microwave high-resolution spectrum of the ν_3 band of ozone", J. Mol. Spectrosc., Vol. 64, pp. 343-364, 1977.

[75] J. Reid, J. Shewchun, B. K. Garside, and E. A. Ballik, "High sensitivity pollution detection employing tunable diode lasers", Appl. Opt., Vol. 17, pp. 300-307, 1978.

[76] J. Shewchun, B. K. Garside, E. A. Ballik, C. C. Y. Kwan, M. M. Elsherbiny, G. Hogenkamp, and A. Kazandjian, "Pollution monitoring system based on resonance absorption measurements of ozone with a tunable CO_2 laser: some criteria", Appl. Optics, Vol. 15, pp. 398-405, 1977.

[77] J. Reid, B. K. Garside, J. Shewchun, M. M. Elsherbiny, and E. A. Ballik, "High sensitivity point monitoring of atmospheric gases employing tunable diode lasers", Appl. Optic, Vol. 17, pp. 1806-1810, 1978 and M. Elsherbiny, E. A. Ballik, J. Shewchun, B. K. Garside, and J. Reid, "High sensitivity point monitoring of ozone, and high resolution spectroscopy of the ν_3 band of ozone using a tunable semiconductor diode laser", Appl. Optics, Vol. 18, pp. 1198-1203, 1979.

[78] A. R. H. Cole, "Tables of wavenumbers for the calibration of IR spectrometers", Pergamon Press, 1977.

[79] P. L. Hanst, "Optical measurements of atmospheric pollutants: accomplishments and problems", Optical and Quant. Electron., Vol. 8, pp. 87-93, 1976.

[80] R. T. Menzies, "Use of CO and CO_2 lasers to detect pollutants in the atmosphere", Appl. Optics, Vol. 10, pp. 1532-1538, 1971.

[81] R. T. Menzies and M. T. Chahine, "Remote atmospheric sensing with an airborne laser absorption spectrometer", Appl. Optics, Vol. 13, pp. 2840-2849, 1974.

[82] R. T. Menzies and M. S. Shumate, "Remote measurements of ambient air pollutants with a biastatic laser system", Appl. Optics, Vol. 15, pp. 2080-2084, 1976.

[83] L. B. Kreuzer, N. D. Kenyon, and C. K. N. Patel, "Air pollution: Sensitive detection of ten pollutant gases by CO and CO_2 lasers", Science, Vol. 177, pp. 347-349, 1972.

[84] T. F. Deaton, D. A. Depatie, and T. W. Walker, "Absorption coefficient measurements of N_2O and CH_4 at DF laser", Appl. Phys. Letter, Vol. 26, pp. 300-303, 1975.

[85] M. S. Shumate, R. T. Menzies, J. S. Margolis, and L. G. Rosengren, "Water vapor absorption of CO_2 laser radiation", Appl. Optics, Vol. 15, pp. 2480-2488, 1976.

[86] C. Amiot and G. Guelachvili, "Extension of the 10^6 samples Fourier spectroscopy to the indium antimonide region: vibration-rotation bands of $^{14}N_2{}^{16}O$: 3.3-5.5 μm region", J. Mol. Spectrosc., Vol. 59, pp. 171-190, 1976.

[87] F. W. Taylor, "Spectral data for the ν_2 bands of ammonia with applications to radiative transfer in the atmosphere of Jupiter", J.Q.S.R.T., Vol. 13, pp. 1181-1217, 1973.

[88] S. G. Wechter, "Preparation of stable pollution gas standard using treated aluminum cylinders", paper presented at the ASTM Calibration Symposium, Boulder, Colorado, Aug. 1975.

[89] R. T. Ku, E. D. Hinkley, and J. O. Sample, "Long-path monitoring of atmospheric carbon monoxide with tunable diode laser system", Appl. Optics, Vol. 14, pp. 854-861, 1975.

[90] R. S. Eng, A. W. Mantz, and T. R. Todd, "Improved sensitivity of tunable diode laser open-path trace gas monitoring systems", Appl. Optics, Vol. 18, pp. 3438-3442, 1979.

[91] D. R. Morgan, "Spectral absorption pattern detection and estimation. I. Analytical techniques", Appl. Spectrosc., Vol. 31, pp. 404-415, 1978.
and
D. R. Morgan, "Spectral absorption pattern detection and estimation. II. System application and design", Appl. Spectrosc., Vol. 31, pp. 415-423, 1978.

[92] E. Max, and S. T. Eng, "A diode laser system for long-path, automatic monitoring of SO_2", Optical and Quant. Electron., Vol. 11, pp. 97-101, 1979.

[93] W. A. McClenny, and G. M. Russwurm, "Laser-based, long-path monitoring of ambient gases - analysis of two systems", Atmosph. Environ., Vol. 12, pp. 1443-1453, 1978.

[94] E. Brookner, "Atmosphere propagation and communication channel model for laser wavelengths", IEEE Trans. Commun. Tech., Vol. COM-18, pp. 396-416, 1970.

[95] M. Cuisenier and J. Pinard, "New methods of instrumental spectroscopy", CNRS International Symposium 161, Gordon and Breach, eds, N. Y., 1972.

[96] R. S. Laurence, and J. W. Strohbehn, "A survey of Clear air propagation effects relevant to optical communications", Proc. IEEE, Vol. 58, pp. 1523-1545, Oct. 1970.
and
M. W. Fitzmaurice, J. L. Bufton, and P. O. Minott, "Wavelength dependence of laser beam scintillation", J. Opt. SOC. Amer., Vol. 59, No. 1, pp. 7-10, 1969.

[97] H. Preier, "Recent advances in lead-chalocogenide diode lasers", Appl. Phys., Vol. 20, pp. 189-206, 1979.

[98] R. S. Taylor, A. J. Alcock, W. J. Sarjeant, and K. E. Leopold, "Electrical and gain characteristics of a multiatmosphere uv-preionized CO_2 laser", IEEE of Quant. Elec., Vol. QE-15, pp. 1131-1140, Oct. 1979.

[99] R. H. Schwendeman, "The matrix elements of the direction cosines in the Wang Symmetric rotor basis", J. Mol. Specrosc., Vol. 7, pp. 280-286, 1961.

[100] V. Dana and J. C. Fontanella, "Etude de la structure rotationnelle de la bande ν_3 de $^{32}S^{16}O_2$ de 1334 à 1382 cm^{-1}", Mol. Phys,, Vol. 30, pp. 1473-1479, 1975.
OR
M. Osumi and T. Kunitomo, "Calculation of absorption coefficient for the ν_2 and ν_3 band of sulfur dioxide", J. Quant. Spec. Rad. Trans., Vol. 17, pp. 493-499, 1977.

[101] "Widely-tunable" lasers, while operating CW at temperatures above 77°K are available commercially, but are quite expensive.